Dissertation

Characterization of the initial-state and propagation of fluctuations in heavy-ion collisions

Hendrik Roch

Supervisor and 1st Reviewer:
Prof. Dr. N. Borghini

2nd Reviewer:
Prof. Dr. S. Schlichting

Universität Bielefeld
Fakultät für Physik

June 13, 2022

Gedruckt auf alterungsbeständigem Papier ISO 9706

Abstract

The aim of this thesis is to develop an initial state characterization for heavy-ion collisions as well as a characterization of fluctuations arising from the initial-state energy density and their propagation into the final state.

In the first main part of the thesis we will set the stage and introduce the physics addressed in heavy-ion collisions and introduce different initial state models, namely the Glauber and Saturation model. Then we will derive the Boltzmann equation and introduce a numerical framework to solve it in two dimensions for an ideal gas of massless particles. The motivation for this new framework is the following: In small systems or peripheral collisions the number of interactions is small and the applicability of hydrodynamics is still under debate.

The second main part will study how fluctuations in anisotropic transverse flow occur due to a finite number of rescatterings during the system evolution within the numerical approach. Initial geometries from a Monte Carlo Glauber model are used to study how flow coefficients fluctuate about their mean value for a given initial-state eccentricity. Additionally we study for the first time how the distributions of the second and third event planes of anisotropic flow about their participant planes in the initial state evolve with the mean number of rescatterings in the system.

In the third part of the thesis we will study the generation of an anisotropic flow signal and spatial eccentricities in more detail, especially at early times using different particle-based transport approaches and a fixed initial condition. We study the onset of anisotropic flow as a function of the number of rescatterings from the few-rescatterings case to the hydrodynamic regime using a power-law ansatz and an exponent varying with the number of rescatterings. The numerical results are compared to semi-analytical calculations based on an expansion in powers of time and cross section in the few-rescatterings regime. Additionally, we will test the effectiveness of the "escape mechanism" to create anisotropic flow in two numerical scenarios with a $2 \to 2$ and $2 \to 0$ collision kernel respectively, and we compare the results to analytical calculations using only the loss term in the Boltzmann equation. This reveals that the even flow harmonics behave similarly, while the odd ones show a significant difference.

The fourth part of this thesis develops a general decomposition of an initial state density profile ensemble using an average state and independent orthonormal fluctuation modes. Event-by-event fluctuations are encoded in the modes forming a basis. Using Glauber and Saturation type initial conditions, we quantify different types and probabilities of event-by-event fluctuations and their impact on initial-state characteristics. Using dynamical simulations within KøMPøST and MUSIC, we investigate the impact of single modes on final-state observables and their corre-

lations. A comparison to event-by-event simulations is used to quantify the accuracy of the mode-by-mode approach.

Contents

Chapter 1

Heavy-ion collisions

It's a warm summer evening, circa 600 BC. You've finished your shopping at the local market, or agora ... and you look up at the night sky. There you notice some of the stars seem to move, so you name them planets or wanderer. – *Sheldon Lee Cooper (The Big Bang Theory)*

In the quote above Sheldon tries to explain physics to Penny. He begins his explanation with knowledge that was already acquired in ancient Greece. Since this would go beyond the scope of this thesis, we will start in the 60s of the last century. There the theory of strong interaction was developed, which is the reason why later in 1974 during a workshop at Bear Mountain physicists came up with the idea to use heavy-ion collisions to probe matter under extreme conditions, at high baryon and energy densities, where the strong force is the dominant interaction [1].

On the next pages we want to describe the physics of heavy-ion collisions briefly. As this field of research is a broad subject with many interesting aspects, the interested reader is referred to the books [2, 3] and the reviews [4, 5], as we cannot cover all aspects here. The following chapter is strongly inspired by these references.

1.1 What is a heavy-ion collision?

An ultra relativistic heavy-ion collision is the head-on collision of two beams of heavy elements, e.g., Pb, Au and Xe, which are completely ionized and accelerated to very high energies, such that the ions move with a velocity close to the speed of light.[1] The beams which are accelerated in a circular collider experiment are steered by strong magnets in such a way that they collide in the detectors which detect the particles emitted from the center of the collision. In the center of momentum frame the ions are Lorentz contracted such that they look like colliding pancakes. During the collision of the nuclei there is a medium with high energy density created between the pancakes. For the characterization of different collisions the total collision energy $\sqrt{s_{\mathrm{NN}}}$ per nucleon-nucleon pair, one from each beam, in the center of mass frame is used. Currently there are two large facilities where heavy-ion collisions are performed:

- The Relativistic Heavy Ion Collider (RHIC) at Brookhaven National Laboratory (BNL) in New York which performs measurements since 2000. At RHIC, a variety of ions are used, e.g., Au, U, but also lighter ones like Ru, Cu and Zr. The circular accelerator has a circumference of around 3.8 km and can accelerate gold ions to $\sqrt{s_{\mathrm{NN}}} = 200$ GeV. The emitted particles from the collisions are currently measured in STAR (Solenoidal Tracker At RHIC) and PHENIX (Pioneering High Energy Nuclear Interactions eXperiment). Since 2010 there was a multi-step program called Beam Energy Scan (BES) I and BES II whose aim was to probe the collisions with lower beam energy and therefore higher baryon chemical potential μ_{B}.

- The Large Hadron Collider (LHC), located near Geneva on the border between Switzerland and France, is performing heavy-ion collisions since 2010. The research program at CERN is mainly dedicated to high energy particle physics experiments, which try to probe the physics of the standard model or find physics beyond this model. However, there is some beamtime during the year where heavy-ions are injected into the accelerator with about 27 km circumference. The LHC heavy-ion program uses, for example, Pb or Xe ions for their measurements. Other systems, e.g., O, are planned for future runs. The experiments which collect the data are ATLAS (A Toroidal LHC ApparatuS), ALICE (A Large Ion Collider Experiment), CMS (Compact-Muon-Solenoid-Experiment) and LHCb (Large Hadron Collider beauty). The ALICE detector is especially built and designed for heavy-ion experiments. Within the LHC it is possible to collide nucleus on nucleus (A+A), as well as proton on nucleus

[1] Head-on does not mean that two nuclei overlap perfectly, which is in further detail described in Sec. 1.4.3.1 by the concept of centrality.

(p+A) and proton on proton (p+p) at the same energies. Currently the LHC is the collider with the highest beam energies in the world, which is of the order of a few TeV.

In the future there will be further experiments with heavy-ions built:

- The Facility for Antiproton and Ion Research (FAIR) will be constructed at the GSI Helmholtzzentrum für Schwerionenforschung in Darmstadt (Germany) and will perform measurements at even higher baryon chemical potential than the ones performed at RHIC. FAIR is expected to start operating in 2025.
- A second planned facility is the Electron Ion Collider (EIC), which will be built at BNL and which will probe ions with point-like electrons to explore the structure of protons and nuclei. The planned start of operation is around 2030.
- Then there is also the Nuclotron-based Ion Collider fAcility (NICA) currently built at the Joint Institute for Nuclear Research (JINR) in Dubna. The experiments planned are also going into the direction of high baryon chemical potentials. Commissioning is planned for 2023.

1.2 Why do we perform heavy-ion collisions?

As mentioned in the beginning of this chapter, the theory of the strong interaction, i.e., Quantum Chromo-Dynamics (QCD), was developed in the 60s, and in the 80s physicists came up with the idea to probe QCD matter with heavy-ion collisions. To get a better idea why we perform heavy-ion collisions, we will first have a short look at QCD. We will just focus on the aspects of QCD which are important for heavy-ion collisions, as the details of this quantum gauge theory are beyond the scope of this work.

By today it is known that a nucleus, which has a typical size of several femtometers (10^{-15} m), consists of nucleons, namely positively charged protons and charge neutral neutrons. This implies that there are many positively charged objects in a very small volume, which brings up the question which attractive force is overcoming the electromagnetic repulsion and binds the nucleons in the nuclei. In 1961 Gell-Mann introduced a geometrical model called “eightfold way” based on group theoretical considerations which arranged the particles according to their charge and strangeness. Until 1964 there was no explanation why the particles fit in this scheme. Then Gell-Mann and Zweig proposed that hadrons are composed of smaller constituents, the quarks. Within this quark model they were able to reproduce the results of the eightfold way and built all the hadrons from a small number of quarks. At that time three quark flavors, called up, down and strange, were known. Today we know that there exist three more flavors, namely charm, bottom and top. So the force between the nucleons is actually a force between their constituents, i.e., quarks and gluons described by a $SU(3)_f$ flavor group. This model of the hadron substructure was confirmed by Deep Inelastic Scattering (DIS) experiments.[2]

[2]DIS is extending the Rutherford scattering experiment to higher energies. This gives the opportunity to resolve smaller length scales to study the structure of the proton.

Since the quark model can be used to reproduce the hadrons, which are physically measurable, in the eightfold way, the quarks have to be fermions with spin 1/2. In the eightfold way there are particles like the Δ^{++}, which consists of three up-quarks. According to the Pauli principle, which is an important result from quantum field theory, this particle is not allowed to exist as the quarks are all in the same quantum state. This puzzle was solved in 1964 by Greenberg who introduced an additional quantum number, the color, which is the charge of QCD. The existence of the Δ^{++} gives us a minimal number of three color charges. An upper bound, which leads to an exact number of three colors, can be obtained through the comparison of total cross-section measurements between $e^- + e^+ \rightarrow$ hadrons and $e^- + e^+ \rightarrow \mu^- + \mu^-$. As quarks and gluons carry a color charge with three possible states, e.g., green, blue and red, and the fact that in nature only colorless states can be observed, baryons composed of three quarks and mesons consisting of a quark-antiquark pair are the only possibility to build the observed particles. All anti-particles are made of anti-quarks which carry an anti-color. The quark interactions are mediated by eight different massless and color charged gauge bosons, the gluons, leading to more freedom for interactions than in Quantum Electro-Dynamics (QED). In QCD the gluons can self-interact between three or four gluons. As no color-charged object has ever been measured, the concept of confinement was introduced: It states that there is no way to isolate a single quark (or gluon).

A second interesting feature, one of the reasons why heavy-ion collisions are an interesting probe of QCD, is that of asymptotic freedom related to the strong coupling constant α_S. This coupling describes the strength of the strong interactions. Within QCD the coupling can be computed as a function of the energy scale Q. In Fig. 1.1 measurements and calculations of α_S are shown. The coupling for small energy scales (large distances) is very large, hence the quarks are confined in the hadrons. With increasing energy scale Q (decreasing distance) the coupling decreases and eventually for $Q \rightarrow \infty$ will be zero. This leads to asymptotically free quarks.

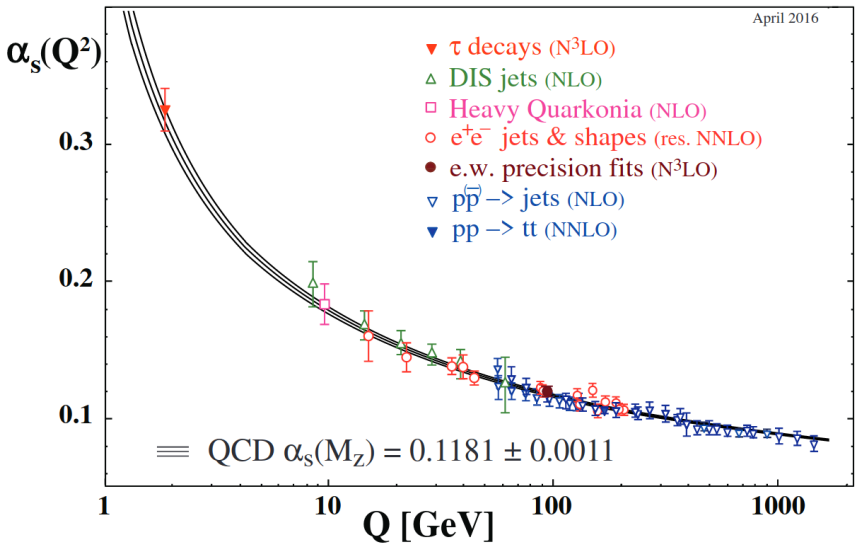

Figure 1.1: Measurements of the strong coupling constant α_S for different energy scales Q (points) and a QCD calculation (lines). The plot is taken from [6].

For physicists this was one reason to perform heavy-ion experiments. In a nuclear collision the nuclear matter is highly compressed, leading to high temperatures and baryon densities. This phenomenon is depicted in Fig. 1.2, where one can see that heating up nuclear matter leads to an overlap of the individual nucleons and than above some critical temperature T_c to a medium of quasi-free quarks and gluons. This medium is called a Quark-Gluon-Plasma (QGP). With heavy-ion collisions this matter, which has a temperature of more then 10^5 times the temperature of the Sun's core, becomes accessible in the laboratory.

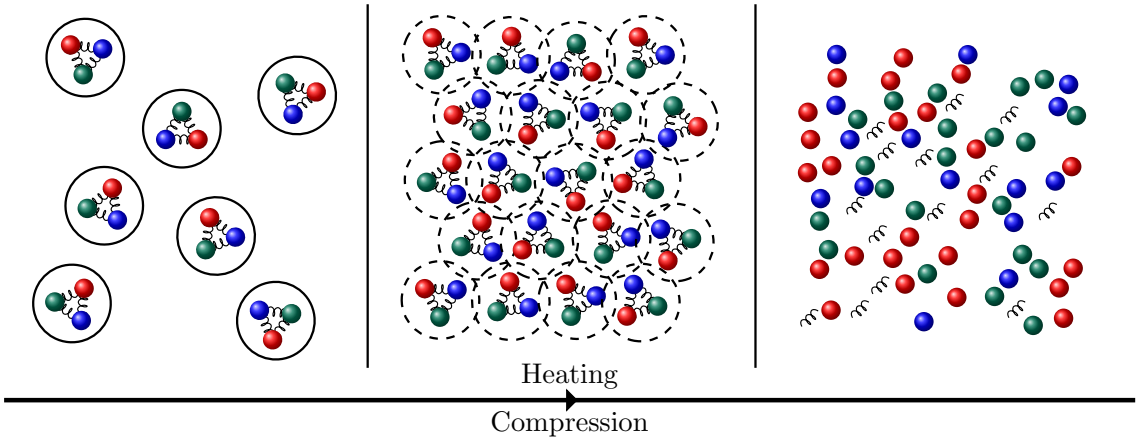

Figure 1.2: The picture shows what happens to nuclear matter if it is heated up/compressed. At low temperatures/densities (left) the quarks are confined inside the nucleons. If the temperature/density increases the nucleons start to overlap and above some critical temperature/density the quarks of individual nucleons are so close to each other that they are quasi free in the medium (right). This illustration is inspired by [7].

In the following two subsections we will have a closer look at two very important applications of results from heavy-ion collisions.

1.2.1 QCD in the early Universe

As we know today, the Universe was filled with a QGP for a short time after the Big Bang. The temperature was too high for the formation of hadrons. Therefore, the small droplet of QGP created in heavy-ion collisions is a direct probe of matter in the early Universe. In analogy to the Big Bang a heavy-ion collision is often called Little Bang. Heavy-ion collisions are one tool to directly obtain information about the matter in the early Universe.[3] One of the most important results from the studies of heavy-ion collisions is that the QGP is a liquid. In the QGP there are no hadrons, but only quarks and gluons. These are strongly coupled to their neighbors.

[3] A long time it was believed that heavy-ion collisions are the only way to obtain information about primordial QCD matter, as there was no first order phase transition that could have lead to fluctuations on length scales larger than the fm-scale and leave an imprint in the visible Universe today. However, it was pointed out by Schwarz in Ref. [8] that a drastic change in the degrees of freedom caused by the QCD transition leaves an imprint in the gravitational-wave background, which could be detected by pulsar timing arrays.

An important finding was that the liquidness of the QGP characterized by the shear viscosity to entropy density ratio η/s is close to the theoretical lower bound of $1/4\pi$. This bound can be computed in infinitely strong coupled gauge theories that are akin to QCD and have a dual gravitational description in a 4+1-dimensional Anti-de-Sitter space.

1.2.2 The phase diagram of QCD

The equilibrium phase diagram of QCD matter (Fig. 1.3) as a function of temperature T and baryon chemical potential μ_B is a second important reason to study heavy-ion collisions. For the early Universe as well as for the mid-rapidity regions

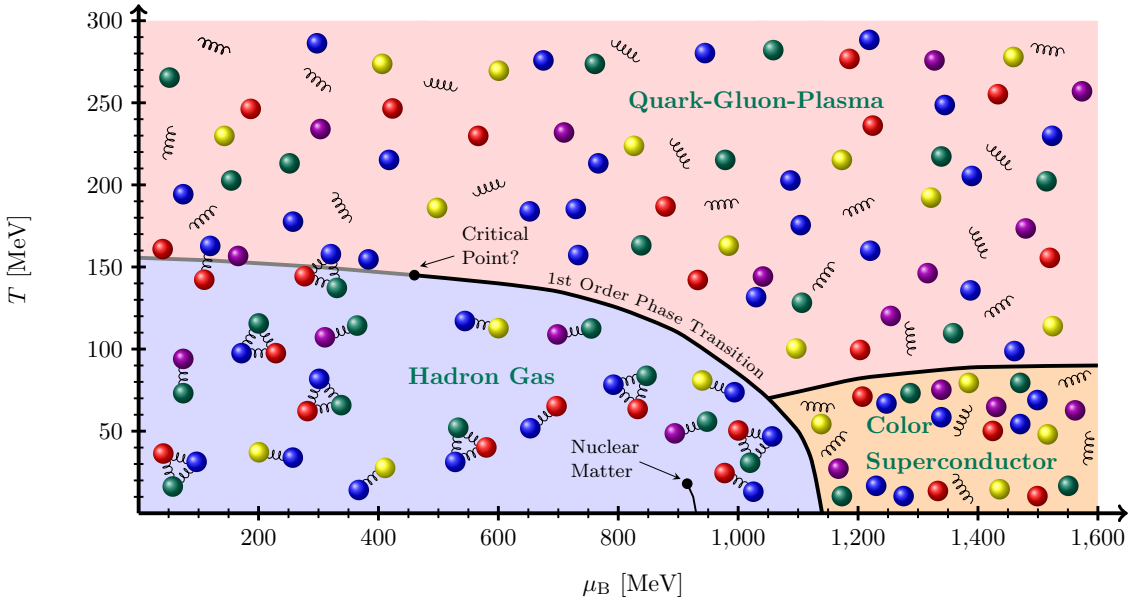

Figure 1.3: The equilibrium phase diagram of QCD matter as a function of temperature T and baryon chemical potential μ_B. The graph was inspired by the phase diagram in Ref. [9].

of high energy heavy-ion collisions the approximation $\mu_B = 0$ is applicable, where a smooth crossover from QGP to hadrons takes place.[4] This crossover is indicated by the gray line in Fig. 1.3. To study QCD matter with higher μ_B, i.e., an excess of

[4]For heavy-ion collisions the concept of rapidity y, which is additive under boosts in the beam direction, is used instead of the particle speed in units of the speed of light. The rapidity is defined by

$$y = \frac{1}{2} \ln \left(\frac{E_{\mathbf{p}} + p_{\parallel}}{E_{\mathbf{p}} - p_{\parallel}} \right), \tag{1.1}$$

where $E_{\mathbf{p}}$ is the energy and $p_{\parallel}$ the three-momentum in the longitudinal (beam) direction of the emitted particles. For the highest energies the masses of the particles can be neglected. Then one can define the pseudorapidity η as

$$\eta = \frac{1}{2} \ln \left(\frac{|\mathbf{p}| + p_{\parallel}}{|\mathbf{p}| - p_{\parallel}} \right). \tag{1.2}$$

quarks over antiquarks, would be possible if the detectors could measure the debris of the collision at very high rapidity. Due to the construction of the present detectors this is not possible. Another possibility to increase μ_B is to perform collisions at lower energies and scan the phase diagram in the BES I and BES II programs at RHIC. With the collisions at lower energies one wants to answer the question if the crossover turns into a first order phase transition line for larger values of μ_B which has a critical point at its end. Within QCD there exist models that predict such a critical point but accessing the region with higher μ_B/T using lattice calculations suffers from the sign problem and problems with the continuum limit. Up to today there is no proof of existence for a critical point but there are strong motivations to answer this question in the next years when the statistics of the observables proposed for the critical point is sufficient.

The region of small temperatures and high baryon chemical potential is some state of matter where it is not made of separate nucleons. They are brought together so close that they can form a color superconductor, where the quarks form pairs analogous to Cooper pairs in solid state physics. Lab experiments at such high μ_B are not possible. The only place where such high densities could exist in the Universe is in the center of neutron stars. Measurements of gravitational waves from neutron star collisions will give information about transport properties of cold dense quark matter in the future.

Indeed, this equilibrium phase diagram is not the whole truth. There exist also theories which tell us that we do not measure the matter in thermodynamic equilibrium. It is possible to obtain effects measured in experiment also in models where no equilibration happened. One prominent example for heavy-ion collisions is elliptic flow [10].[5]

So in general the phase diagram shown in Fig. 1.3 has to be taken with a grain of salt. At the moment the only confirmed parts of it are the cross over line and the nuclear liquid-gas transition line. All other lines might turn out to not exist or their positions in the diagram might change in the future. There is still a lot to explore.

1.3 History of a heavy-ion collision

In heavy-ion physics the only certainly known things about the initial state is the type of the colliding nuclei and the collision energy. Much later in QCD time scales, the particles are measured in the detector. The problem here is that the detectors cannot cover the full solid angle and neutral particles are not measured. Nevertheless, the community of heavy-ion physics researchers developed theoretical models to extract a whole range of information from the measured particle spectra.

In the following we will shortly go through the stages of the established spacetime diagram shown in Fig. 1.4.

At the bottom of Fig. 1.4 the two nuclei are approaching each other at almost the speed of light, which causes a Lorentz contraction in the longitudinal direction. The collision is happening at $t = 0$ fm/c, when the nuclei start to interpenetrate. Then individual collisions of the nuclei constituents happen. Nucleons which do not

[5]The concept of elliptic flow will be introduced in Sec. 1.4.

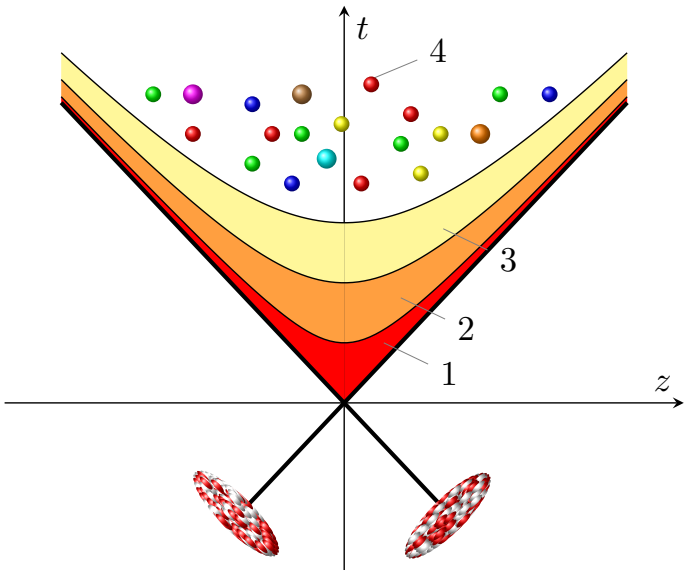

Figure 1.4: Spacetime evolution of a heavy-ion collision. First the pre-equilibrium stage (1), then the quark-gluon plasma (2), the chemical freeze-out (3) and the thermal/ kinetic freeze-out (4). The z-direction is the longitudinal (beam) axis.

collide, e.g., if the nuclei perform a peripheral collision, are called spectators. All nucleons colliding at least once are called participants.

By passing through each other the nuclei leave behind a debris of excited matter which further expands into the longitudinal direction. In this phase the system is far away from local thermal equilibrium, but from phenomenology we know that at a time of the order 1 fm/c [5] the plasma is so close to equilibrium that a further evolution of the system can be described by viscous hydrodynamics.[6] This is indicated by the first stage in Fig. 1.4, where different models exist for the description. In the string decay picture the nucleons form color strings while passing each other. These energy carrying strings can decay into quarks and gluons or directly into hadrons. At very high energy this model breaks down, as the strings start to overlap and cannot be seen as different entities. Then there is the parton cascade model, where nuclei are modeled as collections of quarks and gluons which perform hard scatterings, described by a relativistic Boltzmann equation including dominant perturbative QCD interactions. As perturbation theory breaks down for collisions at low momentum transfers, the model is only applicable for high-energy heavy-ion collisions. In the Color Glass Condensate description (CGC), a small coupling α_S is assumed due to the rapidly rising gluon density for small length scales. It is assumed that the hadrons at very high energy consist of densely packed gluons with color charges evolving slowly compared to other time scales in the collision process. In the Lorentz contracted nuclei color electric and magnetic fields are produced, which form sheets in the transverse plane. By flying through each other these sheets produce longitudinal fields and a medium which is called glasma. Compared to the string model, here only color electric fields are present, which can decay back into

[6]Further details about the process of thermalization can be found in the review [11] by Schlichting and Teaney.

gluons in a pair creation process. The pre-equilibrium stage can then be further evolved in time by the assumption that the coupling is weak and effective kinetic theory is applicable until the system is (nearly) thermalized.

If the momentum distribution of the system has almost isotropized, viscous relativistic hydrodynamics can be used as an effective theory to describe the further time evolution of the QGP until the freeze-out temperature is reached and hadrons are formed. Relativistic hydrodynamics as an effective theory simplifies the description of the system with the cost that one needs an equation of state to close the set of equations. Lattice QCD can provide this equation of state and connect first principle QCD calculations with the effective description. Over the last years relativistic hydrodynamics has been very successful in describing the collected data in experiments, especially the anisotropic flow signals. Hydrodynamics is one possible description to convert anisotropies in position space into anisotropies in momentum space, which is needed to explain the anisotropic flow signals. Due to the low η/s the momentum anisotropies in the medium survive the further evolution. Instead of using the usual versions of relativistic hydrodynamics, which assume a perfect isotropic local thermal equilibrium, there is also the possibility to apply anisotropic relativistic hydrodynamics starting at even earlier times, when the transversal pressure $\mathcal{P}_{\mathrm{T}}$ is much larger then the longitudinal pressure $\mathcal{P}_{\mathrm{L}}$ in the local rest frame of the QGP. The framework of anisotropic hydrodynamics (aHydro) was first derived in 2010 in two independent papers from an anisotropic distribution in momentum space by Florkowski and Ryblewski [12] and Martinez and Strickland [13]. It was additionally shown in [13] that this framework can reproduce the ideal hydrodynamics limit, where $\eta/s = 0$ and the free-streaming limit, where $\eta/s = \infty$. For $\mathcal{P}_{\mathrm{L}} \approx \mathcal{P}_{\mathrm{T}}$ viscous hydrodynamics is recovered. Another possibility in which the knowledge of the thermalization or hydrodynamization time is not required is the usage of relativistic kinetic theories like the Boltzmann equation for the whole evolution. Using the Boltzmann equation is in general more complicated than the effective theory of relativistic hydrodynamics and computationally more expensive.

After the chemical freeze-out, which is defined as the moment when the particles in the system stop interacting inelastically, they can still interact elastically and exchange momentum. Dominant elastic processes are, e.g., $\pi + \pi \to \rho \to \pi + \pi$, $\pi + n \to \Delta \to \pi + n$ and strong decays of more massive resonances.

The thermal or kinetic freeze out is the point in the evolution of the QGP, where the hadrons will not interact any more.[7] At this point the strongly coupled system transforms to a weakly coupled system with actually free-streaming particles. If the time scale of the particle interaction overcomes the time scale of the expansion the kinetic freeze out happens. In reality the kinetic freeze-out does not happen at a hypersurface but in a spacetime volume, as particles with different cross sections have different freeze-out points.

At the end of the evolution the particles are detected and identified in a variety of different detectors. The momenta and charges are determined and then traced back by computer algorithms to determine the trajectories. Calorimeters measure the particle energies and the spatial tracks are measured by time projection chambers,

[7]The denomination "thermal" is due to the fact that the freeze-out is a fast process and the momentum distributions of the non-interacting particles does not change any more.

where the charges are determined with the help of strong magnetic fields. The properties of the detectors are very important for the comparison between theoretical calculations and experimental results, as the detectors cover only a finite rapidity region and low energy particles are not able to penetrate the vacuum vessel, leading to a low energy threshold for the detection.

1.4 What can we observe from heavy-ion collisions?

In this section we want to go through the different types of observables in heavy-ion collisions, which can give us insight into the QGP. The origin of these observables depending on temperature is depicted in Fig. 1.5.

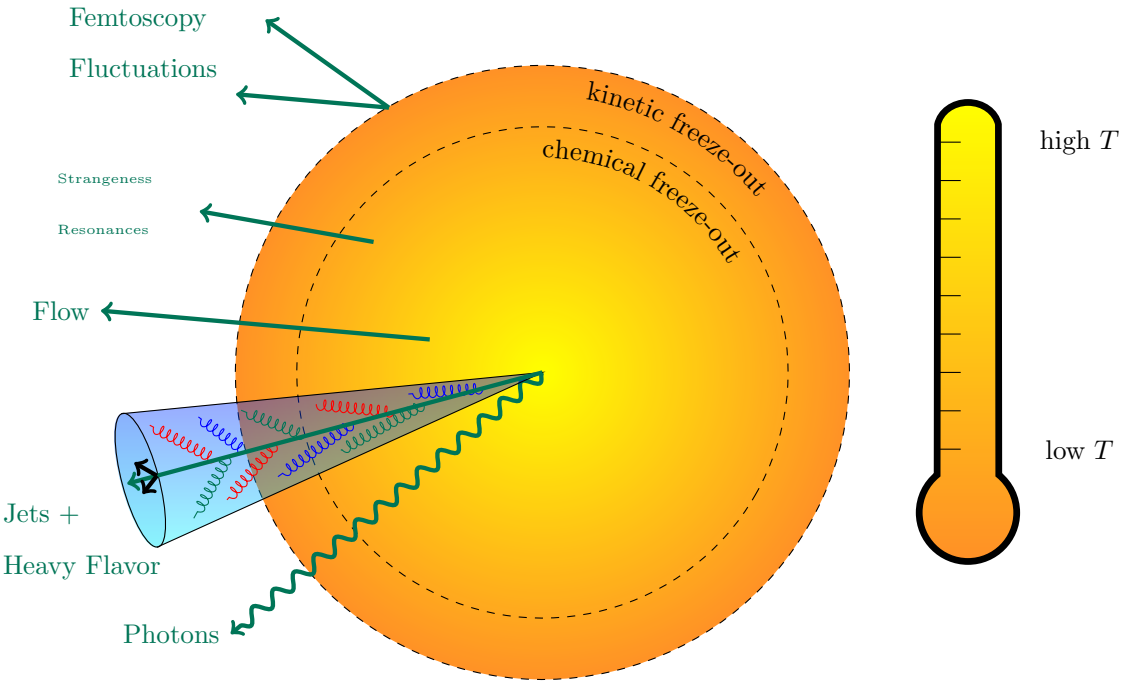

Figure 1.5: The origin of the observables in a heavy-ion collision as a function of temperature. The figure is strongly inspired by [14].

1.4.1 Photons

Photons belong to the group of electromagnetic probes. They are important observables as they only interact electromagnetically. In the evolution process of a heavy-ion collision photons are emitted during the whole time. For the characterization of the QGP one is only interested in the photons produced through collision processes, i.e., direct photons. In experiments it is hard to distinguish between the direct photons and the background produced by hadronic decays. Photons are interesting in that they can be generated in the pre-equilibrium phase. The difficulty is to distinguish them from the thermal photons produced in the phase where the QGP is locally equilibrated.

1.4.2 Jets and heavy flavor

During the initial hard scattering processes massive particles like quarkonia, e.g., charmonia ($c\bar{c}$) or bottomonia ($b\bar{b}$) can be produced. Another possibility is the creation of a jet, which consists of two or more quarks or gauge bosons with very high transverse momentum p_{T}.[8] In heavy-ion collisions the jets shoot through the expanding medium which gives information about the whole evolution of the QGP. For quarkonia this is also the case.

1.4.3 Anisotropic flow

The azimuthal particle distribution of the emitted particles is one of the most important observables in heavy-ion physics. If two nuclei collide with a non-zero impact parameter, then an anisotropic medium in the participant region in position space is produced. During the evolution of this anisotropic medium the collisions between constituent particles of the QGP translate the spatial anisotropy into a momentum anisotropy. This momentum anisotropy is called anisotropic flow.[9] The final state momentum anisotropy of the invariant particle distribution is usually decomposed into a Fourier series as [15]

$$E_{\mathbf{p}}\frac{\mathrm{d}^3N}{\mathrm{d}^3\mathbf{p}} = \frac{\mathrm{d}^3N}{p_{\mathrm{T}}\mathrm{d}p_{\mathrm{T}}\mathrm{d}\varphi_{\mathbf{p}}\mathrm{d}y} = \frac{1}{2\pi}\frac{\mathrm{d}^2N}{p_{\mathrm{T}}\mathrm{d}p_{\mathrm{T}}\mathrm{d}y}\sum_{n=-\infty}^{\infty} v_n(p_{\mathrm{T}},y)e^{-\mathrm{i}n(\varphi_{\mathbf{p}}-\Psi_n)}, \tag{1.3}$$

where Ψ_n is the n-th "event-plane" angle. In this work we assume that the events considered do all have the same impact parameter. In experiments this is not possible to realize, such that the concept of centrality is introduced, which is presented in Sec. 1.4.3.1. A direct measurement of Ψ_n is not possible, but there exist some methods to extract it from the data. The first proposed method by Ollitrault had the disadvantage of introducing some unwanted correlations [16, 17]. This problem was solved by the methods of Borghini et al., which use multiparticle-cumulants [18] or Lee-Yang zeros [19].

The (differential) anisotropic flow coefficients are given by

$$v_n(p_{\mathrm{T}},y) \equiv \left\langle e^{\mathrm{i}n(\varphi_{\mathbf{p}}-\Psi_n)}\right\rangle_{\mathbf{p}} \tag{1.4}$$

$$= \frac{\int \frac{\mathrm{d}^3N}{p_{\mathrm{T}}\mathrm{d}p_{\mathrm{T}}\mathrm{d}\varphi_{\mathbf{p}}\mathrm{d}y}e^{\mathrm{i}n(\varphi_{\mathbf{p}}-\Psi_n)}\,\mathrm{d}\varphi_{\mathbf{p}}}{\int \frac{\mathrm{d}^3N}{p_{\mathrm{T}}\mathrm{d}p_{\mathrm{T}}\mathrm{d}\varphi_{\mathbf{p}}\mathrm{d}y}\,\mathrm{d}\varphi_{\mathbf{p}}}. \tag{1.5}$$

Notice that the particle distributions are real valued such that $v_{-n} = v_n^*$. Integrating

[8] The transverse momentum is the momentum in the plane perpendicular to the beam direction. In principle one could use the absolute value of the three-momentum, but particles with large longitudinal momenta can not be detected, as they are to collimated with the beam.

[9] The denomination "flow" is due to the fact that hydrodynamics naturally translates spatial anisotropies into momentum anisotropies for small transverse momenta.

over the rapidity as well as the transverse momentum gives the integrated flow v_n:

$$v_n e^{in\Psi_n} = \left\langle e^{in\varphi_{\mathbf{p}}} \right\rangle_{\mathbf{p}} \tag{1.6}$$

$$= \frac{\int \frac{\mathrm{d}^3N}{p_{\mathrm{T}}\mathrm{d}p_{\mathrm{T}}\mathrm{d}\varphi_{\mathbf{p}}\mathrm{d}y} e^{in\varphi_{\mathbf{p}}}\, p_{\mathrm{T}}\mathrm{d}p_{\mathrm{T}}\mathrm{d}\varphi_{\mathbf{p}}\mathrm{d}y}{\int \frac{\mathrm{d}^3N}{p_{\mathrm{T}}\mathrm{d}p_{\mathrm{T}}\mathrm{d}\varphi_{\mathbf{p}}\mathrm{d}y}\, p_{\mathrm{T}}\mathrm{d}p_{\mathrm{T}}\mathrm{d}\varphi_{\mathbf{p}}\mathrm{d}y}. \tag{1.7}$$

The coefficient v_1 is called directed flow, v_2 elliptic flow, v_3 triangular flow, etc., as there exists a geometrical interpretation which becomes more obvious if the spatial eccentricities are introduced for the initial state in Sec. 2.4.1.

1.4.3.1 Centrality

The impact parameter of a nucleus-nucleus collision is not a direct observable in experiments. However, it is an important quantity as it controls the geometric size, shape and the orientation of the transverse overlap zone. For an estimation of the impact parameter a simple estimate can be obtained by measuring the multiplicity, i.e., the amount of particles emitted from the collision.[10]

In Fig. 1.6 we see a schematic multiplicity distribution, i.e., the likelihood that an event produces N_{ch} charged hadrons. The distribution has a similar shape as

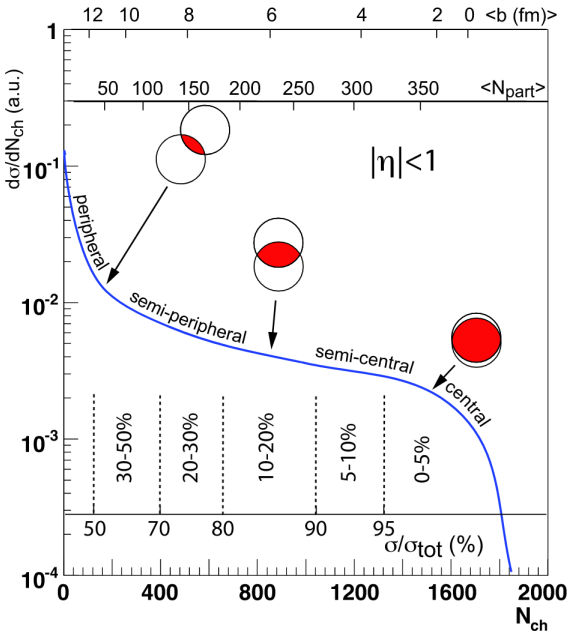

Figure 1.6: Schematic example (no measurements) of the charged hadron multiplicity correlation with the impact parameter b and the number of participants $N_{\mathrm{part.}}$. The plot is taken from [20].

the experimentally measured ones. We assume that the impact parameter is monotonically related to the multiplicity at mid- and forward rapidity. If the impact

[10] This measurement is typically performed in a (pseudo-)rapidity window, as the detectors do not cover the whole solid angle.

parameter is now large, then the event is "peripheral" such that the number of particles at mid-rapidity is small and there is a large number of spectators at beam rapidity. On the other side, if the impact parameter is small, then the event is "central" and we expect many particles at mid-rapidity, so few spectator nucleons at beam rapidity.

In practice the charged particle multiplicity is measured for an ensemble of events and then the total integral of the distribution is computed. Afterwards the distribution is binned into fractions of the total integral (dashed lines in Fig. 1.6 show examples).

From the theoretical side one can use a Glauber model to compute the same distribution with the same binning.[11] This gives the possibility to relate the mean number of participants $\langle N_{\text{part.}} \rangle$ or the impact parameter to the experimentally derived centrality classes.[12]

1.4.4 Femtoscopy

Adapting a method to measure the spatial extent of stars called Hanbury Brown-Twiss (HBT) interferometry, one can extract the HBT radii from two-particle correlations. With these HBT radii one can characterize the size of regions of homogeneity in the kinetic freeze-out volume.

1.5 Why is this work important/necessary?

In this thesis we want to address the question how fluctuations in the anisotropic flow coefficients are related to fluctuations in the initial state energy density. This question is of great importance, because in heavy ion collisions only the final state is directly measurable. Everything that happens before and what is known about the created QGP medium so far was deduced from the observation of the final state. The second known thing is, up to a certain degree, the very initial state of the collision. Here, the knowledge is limited to the beam energy and the ion type of the experiment. A complete (quantum mechanical) characterization of the incoming nuclei is not yet possible, as this is a quantum many-body system. Therefore, physicists came up with different models for the initial state of the collision and how the QGP medium is propagated in time. These models are able to reproduce many of the features seen in the data. Using these models and bringing the fluctuations of anisotropic flow in relation to the fluctuations in the initial state energy density can give us a new method to extract information about the initial state of heavy-ion collisions indirectly.

[11] The Glauber model will be introduced in Sec. 2.1.

[12] In reality the situation is more complicated by event selection methods, uncertainties in the total measured cross section, fluctuations in the distributions and finite kinematic acceptance of the detectors. The interested reader is referred to Ref. [21] for more details.

Chapter 2

Modelling the initial state of the heavy-ion collision

A theory has only the alternative of being right or wrong. A model has a third possibility: it may be right, but irrelevant. – Manfred Eigen

In Sec. 2.1.2 we want to introduce the Monte Carlo (MC) Glauber model which has been very successful in heavy-ion physics to describe geometric quantities like the impact parameter b, the number of participating nucleons $N_{\text{part.}}$ or the number of binary nucleon-nucleon collisions $N_{\text{coll.}}$ and can serve as an initial condition for simulations. Therefore, we mainly follow the review [20] and the books [2,3]. Then we will shortly discuss how to generate energy-density profiles from the MC Glauber quantities (Sec. 2.2) and introduce a second initial state model — the Saturation model — more related to QCD (Sec. 2.3).

Afterwards, we will discuss two possibilities to characterize the initial state via spatial eccentricities and Bessel-Fourier coefficients in Sec. 2.4.

2.1 The Glauber model

The original version of the Glauber model was developed in the 1950s and used quantum many body techniques to solve scattering problems of high energetic composite systems analytically. Therefore, the assumption is made that the scatterers have such a high energy that their wavelengths are much longer than the interaction range. Thus, the incoming particle only deviates little from its path such that the problem can be solved using small angle approximations. This assumption that the nuclei and their constituent nucleons move along straight lines, even during the interaction between the two nuclei, defines an interaction zone for each impact parameter of the two incoming nuclei.

2.1.1 Optical Glauber model

Within the original Glauber model one can write down analytical expressions for cross sections, the number of collisions or the number of participating nucleons in the colliding nuclei. The Glauber model needs two important inputs from the experiments. First, the nuclear charge density distributions, which are measured via electron scatterings in low-energy scattering experiments. Second, the energy dependence of the inelastic nucleon-nucleon cross section is needed.

For large nuclei the nucleon density can be parametrized by a Fermi-/Woods-Saxon-distribution [22] with three parameters:

$$\rho(r) = \frac{\rho_0 \left(1 + w \left(\frac{r}{R}\right)^2\right)}{1 + \exp\left(\frac{r-R}{a}\right)}. \tag{2.1}$$

The parameter ρ_0 is the nucleon density at the center of the nucleus, R the radius and a is the "skin depth". The parameter w takes radial distortions from spherical shape into account [20]. For Pb collisions this parameter is not relevant, as the nucleus is spherical.[1] Additional deformations for prolate or oblate nuclei could be taken into account by additional spherical harmonics in the exponential.

For the second input, i.e., the inelastic nucleon-nucleon cross section $\sigma_{\mathrm{NN}}^{\mathrm{inel}}$, we cannot rely on theoretical calculations from perturbative QCD. The reason is that the cross section includes processes with low momentum transfer, where perturbation theory breaks down.

In the following we consider two nuclei, A (target) and B (projectile), moving along the z-direction and colliding with an impact parameter $\mathbf{b}$. If we now select a tube along the z-axis displaced by $\mathbf{s}$ from the center of nucleus A, then $\mathbf{s} - \mathbf{b}$ is the distance from the center of nucleus B. Assuming now that the nucleons move along straight lines, the tubes along the z-axis will overlap in a collision of the nuclei. We can calculate the probability per transverse area to find a nucleon inside the tube of nucleus A/B by [20]

$$\hat{T}_{A/B}(\mathbf{s}) = \int \hat{\rho}_{A/B}\left(\mathbf{s}, z_{A/B}\right) \, \mathrm{d}z_{A/B}, \tag{2.2}$$

[1] One example, where w deviates from zero is for O nuclei.

which is called "thickness function". The hat indicates that the nucleon density from Eq. (2.1) is normalized to unity, giving the probability per unit volume for finding a nucleon at the position $\left(\mathbf{s}, z_{A/B}\right)$. Thus, $\hat{T}_A(\mathbf{s})\,\hat{T}_B(\mathbf{s}-\mathbf{b})\;\mathrm{d}^2\mathbf{s}$ is the joint probability to find a nucleon in the tubes with area $\mathrm{d}^2\mathbf{s}$. An integral over all displacements $\mathbf{s}$ leads then to [20]

$$\hat{T}_{AB}(\mathbf{b}) = \int \hat{T}_A(\mathbf{s})\,\hat{T}_B(\mathbf{s}-\mathbf{b})\;\mathrm{d}^2\mathbf{s}, \tag{2.3}$$

which is called "nuclear overlap" function and has units of an inverse length squared.

Considering only inelastic collisions, which have a larger energy loss than elastic ones, leads to an interaction probability given by $\hat{T}(\mathbf{b})\,\sigma_{\mathrm{NN}}^{\mathrm{inel}}$. The probability for n interactions is expressed through a binomial distribution [20]

$$p(n,\mathbf{b}) = \binom{AB}{n}\left[\hat{T}_{AB}(\mathbf{b})\,\sigma_{\mathrm{NN}}^{\mathrm{inel}}\right]^n\left[1-\hat{T}_{AB}(\mathbf{b})\,\sigma_{\mathrm{NN}}^{\mathrm{inel}}\right]^{AB-n}, \tag{2.4}$$

where A and B denote the nuclei as well as their nucleon numbers.[2]

From this we can now compute the total number of collisions at a given impact parameter using [20]

$$N_{\mathrm{coll.}}(\mathbf{b}) = \sum_{n=1}^{AB} n\,p(n,\mathbf{b}) = AB\,\hat{T}_{AB}(\mathbf{b})\,\sigma_{\mathrm{NN}}^{\mathrm{inel}}. \tag{2.5}$$

All interacting nucleons are either called "participants" or "wounded nucleons". At a given impact parameter this number is given by [20]

$$N_{\mathrm{part.}}(\mathbf{b}) = A\int \hat{T}_A(\mathbf{s})\left(1-\left[1-\hat{T}_B(\mathbf{s}-\mathbf{b})\,\sigma_{\mathrm{NN}}^{\mathrm{inel}}\right]^B\right)\;\mathrm{d}^2\mathbf{s} \tag{2.6}$$

$$+\,B\int \hat{T}_B(\mathbf{s}-\mathbf{b})\left(1-\left[1-\hat{T}_A(\mathbf{s})\,\sigma_{\mathrm{NN}}^{\mathrm{inel}}\right]^A\right)\;\mathrm{d}^2\mathbf{s}. \tag{2.7}$$

2.1.2 Monte Carlo Glauber model

In contrast to the optical Glauber model, which is based on a continuous density distribution, the MC Glauber model uses the nucleon density distribution in Eq. (2.1) to sample the nucleon positions. The appealing thing about this numerical approach is its simplicity.

Using Eq. (2.1) the nucleon positions for nucleus A and B are sampled. In the next step the impact parameter is sampled according to the distribution $\mathrm{d}\sigma/\mathrm{d}b = 2\pi b$. Note, that for many results presented in this work the impact parameter is fixed. The centers of the nuclei are then shifted to $(-b/2,0,0)$ and $(b/2,0,0)$ along the x-axis. Assuming now that the collisions of the nucleons are independent of each other and that they move in straight lines (optical approximation) along the z-axis, a collision takes place if

$$d \leq \sqrt{\frac{\sigma_{\mathrm{NN}}^{\mathrm{inel}}}{\pi}}. \tag{2.8}$$

[2] The first part gives the number of combinations for n collisions out of AB possibilities for interactions between nucleons. The second and the last part give the probability for exactly n collisions resp. $AB-n$ misses.

d is the distance between the two nucleons, which are checked for a collision, and $\sigma_{\mathrm{NN}}^{\mathrm{inel}}$ is again the total inelastic nucleon-nucleon cross section. Thus, we need the same initial information as for the optical Glauber model.

To improve the model, one can include a minimum separation distance of the nucleons to mimic the Fermi repulsion of the nucleons. Another possibility is to use two different distributions for protons and neutrons in neutron-rich nuclei emulating the neutron skin effect [23].

2.1.3 Comparison of the optical and the MC Glauber model

We can now compare the results of the optical and MC Glauber model as a function of the absolute value of the impact parameter in Fig. 2.1. As an example system we

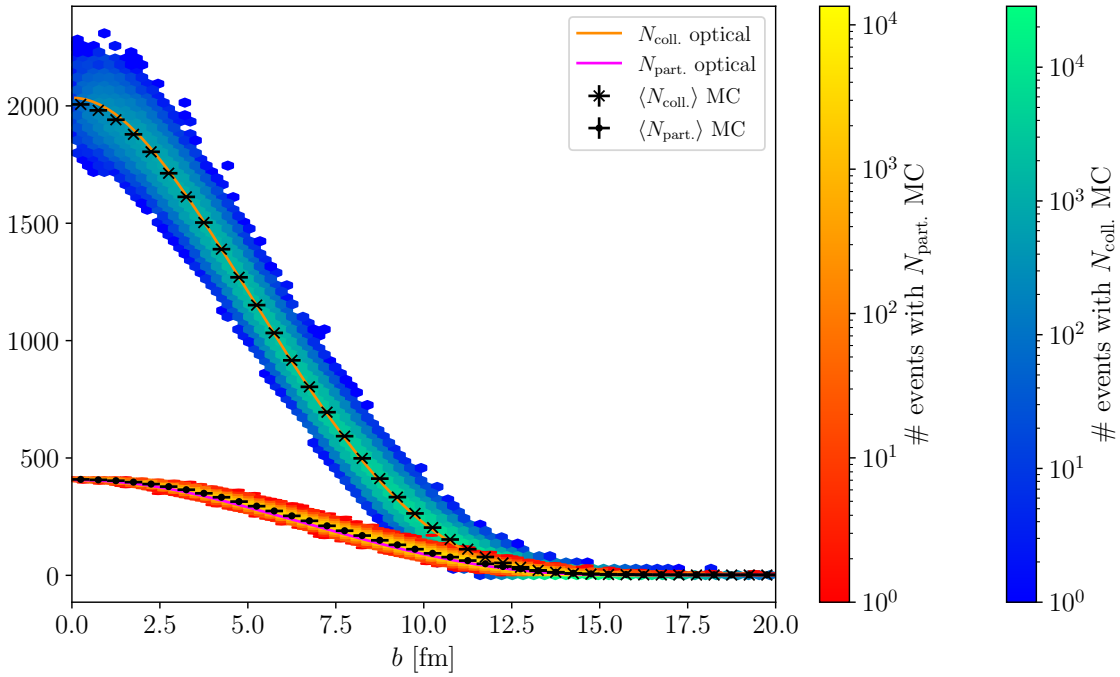

Figure 2.1: $N_{\mathrm{coll.}}$ and $N_{\mathrm{part.}}$ for the optical Glauber model (full lines) compared to 10^6 MC Glauber events (histograms). The black points indicate the impact parameter bin averaged values of the MC Glauber results.

have chosen Pb–Pb collisions at $\sqrt{s_{\mathrm{NN}}} = 5.02$ TeV with $\sigma_{\mathrm{NN}}^{\mathrm{inel}} = 67.6$ mb [24]. In the MC Glauber model 10^6 of these events were sampled and their $N_{\mathrm{part.}}$ and $N_{\mathrm{coll.}}$ are displayed as histograms. To simplify a comparison with the optical Glauber model the MC Glauber results were binned and the values were averaged in bins of 0.5 fm width. The error bars, which are smaller than the points, were calculated with a delete-d Jackknife algorithm (see Appendix G.3). The optical results are given by the full lines using $N_{\mathrm{coll.}}(|\mathbf{b}|)$ (Eq. (2.5)) and $N_{\mathrm{part.}}(|\mathbf{b}|)$ (Eq. (2.7)) implemented in a Mathematica notebook by Klaus Reygers [21].

We find that there is an overall good agreement between the optical Glauber and the MC Glauber model. For $N_{\mathrm{coll.}}$ the averaged bins and the full curve nicely agree. Looking at $N_{\mathrm{part.}}$ we can see that there is also a good agreement between the two models.

One may notice small deviations for $N_{\text{coll.}}$ for central collisions of for $N_{\text{part.}}$ at intermediate values of the impact parameter. It was checked that the minimum nucleon separation d_{min} introduced in the MC Glauber model has not a noticeable influence on the results. An explanation for the differences might be that in the optical Glauber model the opacity of the nuclei is encoded in the cross section. This is also the reason why for perfectly central collisions the number of participants is less then $2A$ which one would naïvely expect. In the MC Glauber there are also nucleons which do not collide in a central collision. Additionally the skin depth of the nuclear distribution is an important parameter for the differences between the models. Nucleons sampled far away from the center do not have the same probability to undergo a collision as the ones in the center. This causes some sort of radial dependence of the nuclear opacity and thus could explain our findings.

2.2 Generating energy-density profiles from the MC Glauber model

We will now discuss how to produce an initial energy-density profile from a MC Glauber model which is either used as initialization for a pure two-dimensional evolution or a longitudinally boost invariant one.

Assuming that the nuclei have been sampled and shifted according to the criteria in Sec. 2.1.2 we go now a step further then in the previous part, where the number of participating and colliding nucleons were simply counted globally. For the generation of a density profile it is however important at which position (x, y) the interaction — and therefore the energy deposition — happens. This is why we introduce a two-dimensional grid with spacing of 0.1 fm. On this grid we store the local number of participating nucleons $N_{\text{part.}}(x, y)$ using the grid points closest to the nucleon centers. For the local number of collisions $N_{\text{coll.}}(x, y)$ we use the grid point which is closest to the halfway point between the two colliding nucleons.

Using these two fields we can now use the ansatz that the initial energy density profile is proportional to a linear combination of soft processes, represented by $N_{\text{part.}}(x, y)$ and hard processes, represented by $N_{\text{coll.}}(x, y)$ [23]:[3]

$$e_{\text{d}}(x, y) \propto (1 - \alpha)\frac{N_{\text{part.}}(x, y)}{2} + \alpha N_{\text{coll.}}(x, y) \tag{2.9}$$

using an amount of $\alpha = 0.2$ hard scatterings. Representing such an energy density profile graphically reveals that it consists of multiple delta distributions located at the grid points and it has large differences between neighboring points. Such a delta-like profile is not useful for a further dynamical evolution, as the large gradients would lead for example to shock fronts in the hydrodynamical evolution. To obtain a smooth profile, we employ a Gaussian smearing $\propto \exp\left[\{(x - x_i)^2 + (y - y_j)^2\}/(2\sigma^2)\right]$ of e_{d} at each point (x_i, y_j), where we use a typical width of $\sigma = 0.4$ fm [25]. Now we have a smoothed density profile $e(x, y)$ suitable for the dynamical evolution, which is needed to fix the proportionality constant in Eq. (2.9) such that the charged hadron

[3] In principle one can initialize an energy density or an entropy density with a linear combination of $N_{\text{part.}}(x, y)$ and $N_{\text{coll.}}(x, y)$, as they can be related by the QCD equation of state.

multiplicity in central events is matched after the identification of $e(x, y)$ with the energy density at midrapidity

$$e(x, y) \equiv \left. \frac{\mathrm{d}E}{\tau_0 \mathrm{d}^2\mathbf{x}\mathrm{d}\eta} \right|_{\eta=0} . \tag{2.10}$$

The parameter τ_0 is the initialization time of the system leading to densities in units of GeV/fm^3.

2.3 Saturation model

The initial-state model which we will describe in this section goes one step further than the Glauber model introduced above. Instead of looking at nucleonic degrees of freedom, it goes deeper into the structure of the individual nucleons and acts on the partonic level, such that it can be used for proton-proton collisions as well.

As we only consider high-energy heavy-ion collisions we can use the CGC effective field theory for QCD at high energies [26, 27]. This theory describes cross sections (and other inclusive observables) in all kinds of colliding systems by using correlators of light-like Wilson lines $V_{\mathbf{x}}$.[4] The most basic one of these correlators is the fundamental color dipole

$$D_{\mathrm{fun}}(x, \mathbf{r}, \mathbf{b}) = \frac{1}{N_c} \left\langle \mathrm{tr} \left[V_{\mathbf{b}+\frac{\mathbf{b}}{2}} V^{\dagger}_{\mathbf{b}-\frac{\mathbf{b}}{2}} \right] \right\rangle_x \tag{2.11}$$

describing the scattering of a color dipole off a hadronic target, as depicted in Fig. 2.2.[5] There a virtual photon fluctuates into a quark antiquark pair which

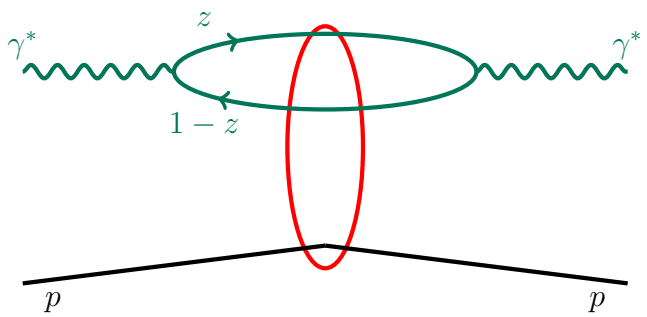

Figure 2.2: Interacting color quark antiquark dipole with a proton. Adapted from [28].

then probes the proton. The quantity z is the longitudinal momentum fraction of the photon carried by the quark.

For this initial-state model we use the Golec-Biernat and Wüsthoff (GBW) parametrization of the fundamental color dipole [29]

$$D_{\mathrm{fun}}(x, \mathbf{r}, \mathbf{b}) = \exp\left(-\frac{Q^2_{s,\mathrm{fun}}(x, \mathbf{b})\mathbf{r}^2}{4} \right), \tag{2.12}$$

[4] A Wilson line can be seen as a connection between two spacetime points to make derivatives, which act on two positions, gauge invariant.

[5] The notation $\langle \cdot \rangle_x$ denotes an average over a fixed value of the Bjorken $x \ll 1$. N_c denotes the number of colors.

where $Q^2_{s,\mathrm{fun}}(x,\mathbf{b})$ is the fundamental saturation scale. This saturation scale depends on the Bjorken x and the transverse position $\mathbf{b}$ within the nucleon or nucleus.[6] It can be parametrized by

$$Q^2_{s,A}(x,\mathbf{b}) = Q^2_{s,p}(x)\,\sigma_0 T_A(\mathbf{b}), \tag{2.13}$$

where $Q^2_{s,p}(x)$ is the average proton saturation scale which obeys the condition $Q^2_{s,p}(x) = \sigma_0^{-1}\int \mathrm{d}^2\mathbf{b}\; Q^2_{s,p}(x,\mathbf{b})$ and $T_A(\mathbf{b})$ is the nuclear thickness function we have introduced in Sec. 2.1.1.

Using then a MC Glauber model to sample the nucleon positions inside a nucleus, we can compute the thickness function of a nucleus by

$$T_A(\mathbf{b}) = \sum_i T_p(\mathbf{b}-\mathbf{b}_i), \tag{2.14}$$

where the sum runs over all nucleons in the nucleus and $T_p(\mathbf{s})$ is the thickness function of a proton approximated by a Gaussian [30]:

$$T_p(\mathbf{s}) = \frac{1}{2\pi B_G} e^{-\frac{\mathbf{s}^2}{2B_G}}. \tag{2.15}$$

$B_G = 4\ \mathrm{GeV}^{-2}$ is the width of the gluon distribution from HERA fits [28, 31]. The $\sigma_0 = 2\pi B_G$ is chosen such that the factor $\sigma_0 T_A(\mathbf{b})$ in Eq. (2.13) counts the effective number of nucleons at the transverse coordinate $\mathbf{b}$. The average saturation scale of the proton can be parametrized by

$$Q^2_{s,p}(x) = Q^2_{s,0} x^{-\lambda}(1-x)^{\delta}, \tag{2.16}$$

where $Q^2_{s,0}$, λ and δ can be extracted from fits to DIS data.

Due to geometrical fluctuations the impact parameter, and therefore the overlap of the gluon distributions vary in $p+p$ collisions. As the impact parameter fluctuation distribution can not be computed using first principles, it is convenient to use an eikonal approximation. There the overlap of two protons at a given impact parameter $b = |\mathbf{b}|$ is given by

$$T_{pp}(b) = \frac{1}{4\pi B_G} e^{-\frac{\mathbf{b}^2}{4B_G}}. \tag{2.17}$$

An explicit calculation of the overlap function $T_{pp}(b)$ is given in Appendix A.1.1

For the inclusive deep-inelastic scattering cross section at leading order it is sufficient to use the fundamental dipole (Eq. (2.11)). This is not enough when it comes to energy deposition in hadronic collisions. Then the un-integrated gluon distribution defined by

$$\Phi_{(U)}(x,\mathbf{b},\mathbf{k}) = \frac{\pi(N_c^2-1)}{g^2} D^{(1)}_{(U)}(x,\mathbf{b},\mathbf{k}) \tag{2.18}$$

[6] Within the description of inclusive deep inelastic scattering data the $\mathbf{b}$ dependence is often neglected. For our purpose it is of course extremely important if we want to compute the energy deposition in a heavy-ion collision.

with $D^{(1)}_{(U)}(x,\mathbf{k},\mathbf{b})$ the Fourier transformed adjoint dipole distribution

$$D^{(1)}_{(U)}(x,\mathbf{b},\mathbf{k}) = \frac{\mathbf{k}^2}{N_c}\int \mathrm{d}^2\mathbf{r}\ \frac{1}{N_c^2-1}\,\mathrm{tr}\left[V^{\mathrm{adj}}_{\mathbf{b}+\frac{\mathbf{r}}{2}}V^{\dagger,\mathrm{adj}}_{\mathbf{b}-\frac{\mathbf{r}}{2}}\right]e^{\mathrm{i}\mathbf{k}\cdot\mathbf{r}} \tag{2.19}$$

is used. In the GBW model the un-integrated gluon distribution is given by [29]

$$\Phi_{(U)}(x,\mathbf{b},\mathbf{k}) = 4\pi^2\frac{N_c^2-1}{g^2N_c}\frac{\mathbf{k}^2}{Q^2_{s,\mathrm{adj}}(x,\mathbf{b})}e^{-\frac{\mathbf{k}^2}{Q^2_{s,\mathrm{adj}}(x,\mathbf{b})}}, \tag{2.20}$$

while assuming a Casimir scaling of the fundamental color dipole distribution with $Q^2_{s,\mathrm{adj}}(x,\mathbf{b}) = (C_A/C_F)\ Q^2_{s,\mathrm{fun}}(x,\mathbf{b})$ denoting the adjoint saturation scale.[7]

In high-energy QCD an appropriate tool to compute the initial energy deposition in a heavy-ion collision is the CGC effective theory which computes the solutions of the classical Yang-Mills equations. If additionally saturation effects in one of the colliding nuclei are negligible, then there is a k_{T}-factorization of the gluon spectrum of the initially produced gluons per unit transverse area [32, 33]

$$\frac{\mathrm{d}N_g}{\mathrm{d}^2\mathbf{b}\mathrm{d}^2\mathbf{P}\mathrm{d}y} = \frac{\alpha_{\mathrm{S}}N_c}{\pi^4\mathbf{P}^2(N_c^2-1)}\int\frac{\mathrm{d}^2\mathbf{k}}{(2\pi)^2}\Phi_A(x_A,\mathbf{b}+\mathbf{b}_0/2,\mathbf{k})\Phi_B(x_B,\mathbf{b}-\mathbf{b}_0/2,\mathbf{P}-\mathbf{k}). \tag{2.21}$$

In leading order kinematics we use $x_{A/B} = \mathbf{P}e^{\pm y}/\sqrt{s_{\mathrm{NN}}}$ and the un-integrated gluon distributions $\Phi_{A/B}$ (Eq. (2.20)) of the nuclei A and B. The vector $\mathbf{b}_0$ is the impact parameter of the collision and $\alpha_{\mathrm{S}} \equiv g^2/(4\pi)$.[8]

Integrating out the transverse momentum dependence $\mathbf{P}$ one can obtain the initial state energy per unit rapidity with

$$(e\tau)_0 = \left(\frac{\tau\mathrm{d}E}{\mathrm{d}^2\mathbf{b}\mathrm{d}\eta}\right)_0 = \int\mathrm{d}^2\mathbf{P}\ |\mathbf{P}|\frac{\mathrm{d}N_g}{\mathrm{d}^2\mathbf{b}\mathrm{d}^2\mathbf{P}\mathrm{d}y}\bigg|_{y=\eta}. \tag{2.22}$$

The x dependence of the un-integrated gluon distributions within the GBW model can be approximated as

$$x = \frac{Q_{s,A/B}(x,T_{A/B}(\mathbf{b}))e^{\pm y}}{\sqrt{s_{\mathrm{NN}}}}. \tag{2.23}$$

This parametrization is similar to the one in the IP-Glasma model and it leads to

$$(e\tau)_0 = \frac{(N_c^2-1)}{4g^2N_c\sqrt{\pi}}\frac{Q_A^2Q_B^2}{(Q_A^2+Q_B^2)^{5/2}}\left[2Q_A^4+7Q_A^2Q_B^2+2Q_B^4\right] \tag{2.24}$$

for the initial energy per unit rapidity, while using Eqs. (2.13) and (2.23) to obtain a self consistent solution of $Q_{s,A/B}(x,\mathbf{b})$. As the result in Eq. (2.24) is computed in leading order, we allow for an additional rescaling factor K of order 1. A more extensive derivation of Eq. (2.24) is given in Appendices A.1.2-A.1.3, where we also comment on the self consistent solution of Eqs. (2.13) and (2.23) (Appendix A.1.4).

In Appendices A.1.5-A.1.6 we discuss how the number of participants is computed, which is used in the code to characterize if an interaction has happened and to accept the sampled event. This is especially important for proton-proton collisions, small systems or peripheral events.

[7] The Casimir operators are given by $C_A = N_c$ and $C_F = (N_c^2-1)/(2N_c)$.

[8] From numerical simulations it is known that higher order saturation corrections to Eq. (2.21) are small, especially at high momenta [33, 34].

2.4 Characterization of the initial state

The initial state energy density in the transverse plane can be characterized in different ways.[9] First, the characterization via eccentricities, where the definition is quite similar to that of anisotropic flow. Second, with Bessel-Fourier coefficients. With the latter method it is also possible to characterize the initial density profile in much more detail depending on the number of coefficients used in the expansion.

2.4.1 Spatial eccentricities

The eccentricity of any spatial distribution in the transverse plane is defined by [36–38]

$$\begin{aligned} \varepsilon_1^{\mathbf{x}} e^{\mathrm{i}\Phi_1} &\equiv -\frac{\int r^3 e^{\mathrm{i}\theta} f(r,\theta)\, r\mathrm{d}r\mathrm{d}\theta}{\int r^3 f(r,\theta)\, r\mathrm{d}r\mathrm{d}\theta} = -\frac{\left\langle r^3 e^{\mathrm{i}\theta}\right\rangle_{\mathbf{x}}}{\langle r^3\rangle_{\mathbf{x}}}, \\ \varepsilon_n^{\mathbf{x}} e^{\mathrm{i}n\Phi_n} &\equiv -\frac{\int r^n e^{\mathrm{i}n\theta} f(r,\theta)\, r\mathrm{d}r\mathrm{d}\theta}{\int r^n f(r,\theta)\, r\mathrm{d}r\mathrm{d}\theta} = -\frac{\left\langle r^n e^{\mathrm{i}n\theta}\right\rangle_{\mathbf{x}}}{\langle r^n\rangle_{\mathbf{x}}} \quad (n>1), \end{aligned} \tag{2.25}$$

where $\varepsilon_n^{\mathbf{x}}$ is the absolute value of the spatial anisotropy and Φ_n is the participant plane (PP) angle with respect to the reaction plane (RP) as depicted in Fig. 2.3 for the case $n = 2$. It is important to note that this formula considers the spatial distribution f centered around its mean already.[10] In practice the distribution function

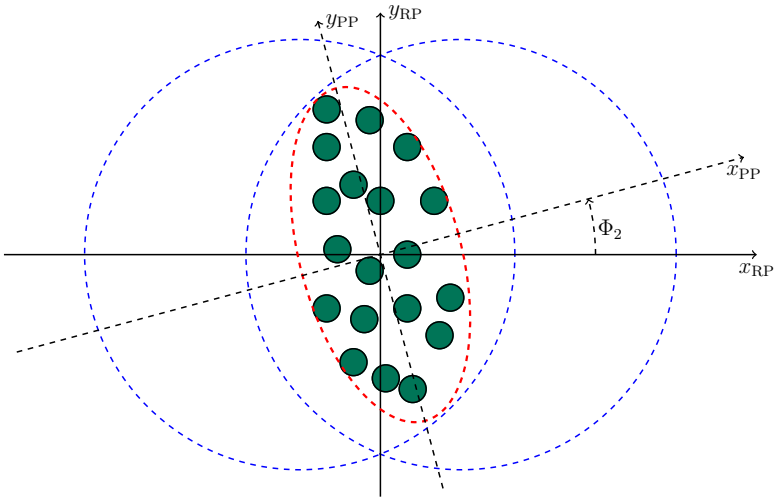

Figure 2.3: Two overlapping spherical nuclei (blue) in the reaction plane (RP). Since the nuclei are made of nucleons with fluctuating positions they can form for example an elliptic shape (red) characterized by $\varepsilon_2^{\mathbf{x}}$ in the participant plane (PP), which can be rotated with respect to the RP by an angle Φ_2.

[9] In this work we initialize our simulations with an energy-density profile. Initialization with an entropy profile is also performed by some groups, as the entropy is related to the amount of produced particles in the final state [35].

[10] From this we can follow a vanishing $\varepsilon_1^{\mathbf{x}}$ immediately if one would use the lower definition in Eq. (2.25). Thus, its definition differs from the one for the higher harmonics.

f can be for example an energy density, entropy density, particle-number density or even an enthalpy density profile. The momentum part of the distribution is already integrated out. That means that the single particle distribution function $f(t, \mathbf{x}, \mathbf{p})$ which is considered in later chapters will be integrated over the whole position and momentum space.

Another way to modify the given definition is to introduce eccentricities which have a larger radial weight if one wants to investigate core-corona effects. Higher powers in r would then lead to a higher sensitivity to the deformations in the outer regions of the given distribution.

The eccentricities of 10^4 MC Glauber events for different impact parameters are shown in the left panel of Fig. 2.4. In contrast to an optical Glauber model the

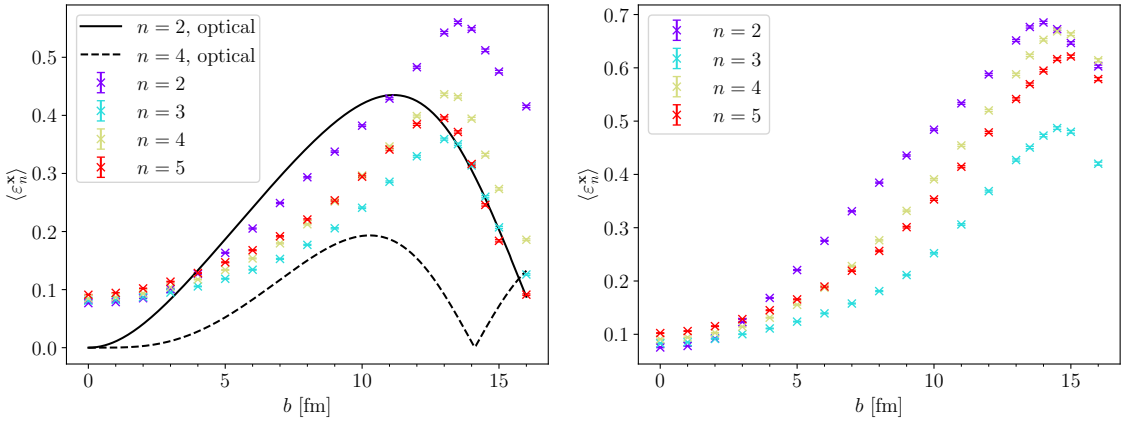

Figure 2.4: The mean of the absolute values of the spatial eccentricities $\langle \varepsilon_n^{\mathbf{x}} \rangle$ with $n \in \{2, 3, 4, 5\}$ for different impact parameters of 10^4 MC Glauber events (left panel) and the same amount of events generated with the Saturation model (right panel). The error bars are generated with a delete-d Jackknife algorithm. In the left panel the full and the dashed line show the absolute values of the $\varepsilon_2^{\mathbf{x}}$ resp. $\varepsilon_4^{\mathbf{x}}$ signal in the optical Glauber model.

eccentricities do not vanish for $b = 0$ fm, as the positions of the nucleons are fluctuating. Additionally the odd eccentricities, which vanish by symmetry arguments in the optical Glauber model, are non-zero in the MC Glauber model as well. $\langle \varepsilon_2^{\mathbf{x}} \rangle$ is the smallest eccentricity at $b = 0$ fm, as the overlap of the nuclei is more or less a circle with fluctuations. This is also why the higher harmonics have larger values in this case. For small impact parameters it is less likely that the nucleon positions fluctuate along only one direction. With increasing impact parameter the elliptical geometry of the overlap region becomes more and more prominent, resulting in a large $\langle \varepsilon_2^{\mathbf{x}} \rangle$ value and smaller spatial anisotropies of higher order. If we look at the optical Glauber model we notice that the maxima of $\varepsilon_2^{\mathbf{x}}$ and $\varepsilon_4^{\mathbf{x}}$ in the optical Glauber model are at smaller impact parameter compared to the MC Glauber. This effect can be explained by the nucleon fluctuations in the MC Glauber case. These fluctuations can even at large impact parameters cause a large spatial anisotropy, while in the optical case the elongation in the y-direction becomes smaller when the impact parameter becomes larger, leading to a decrease in the ellipticity. The kink in the $\varepsilon_4^{\mathbf{x}}$ curve around $b \approx 14$ fm is caused by a sign change. Our findings for the comparison of the optical and MC Glauber model match the results in Ref. [39].

Comparing the Saturation model results (right panel) to the ones from the MC Glauber model we find similar results at small impact parameters. For mid-central or peripheral collisions the results differ in shape and magnitude. In the Saturation model we obtain in general larger eccentricities for all harmonics, which coincides with the findings in Ref. [40]. The maximum of $\varepsilon_2^{\mathrm{x}}$ is approximately at the same b in both models, while the higher harmonics have their maxima at slightly larger impact parameters.

2.4.2 Bessel-Fourier series

For a more accurate characterization of the initial state energy density the expansion into a Bessel-Fourier series is appropriate. In contrast to the eccentricities, which mainly capture the geometry in the azimuthal direction, the Bessel-Fourier coefficients additionally contain information about the radial direction in the sense of length scales on which different azimuthal harmonics occur.

To characterize the energy density in the transverse plane by a Fourier-Bessel series, we follow Ref. [41] and introduce the orthonormal set of basis functions

$$\chi_{n,k}(r,\theta) = \frac{1}{J_{|n|+1}(j_{n,k})} J_n\left(\frac{r}{r_0} j_{n,k}\right) e^{\mathrm{i}n\theta} \tag{2.26}$$

on a disk with radius r_0, $n \in \mathbb{Z}$ and k a positive integer. The function J_n is the n-th Bessel function of first kind and $j_{n,k}$ is the k-th zero of the Bessel function. The radius r_0 is the expansion radius in which the density is supposed to fall off to zero for every point with $r = r_0$. Eq. (2.26) defines a complete orthonormal set of basis functions on a space with the (complex) scalar product

$$\langle a, b\rangle \equiv \frac{1}{\pi r_0^2} \int_0^{2\pi}\int_0^{r_0} a(r,\theta) b^*(r,\theta)\, r\mathrm{d}r\mathrm{d}\theta. \tag{2.27}$$

Any given function $f(r,\theta)$ in the transverse plane can then be expanded using

$$f(r,\theta) = \sum_{k=1}^{\infty}\sum_{n=-\infty}^{\infty} A_{n,k}\chi_{n,k}(r,\theta), \tag{2.28}$$

where the complex valued coefficients $A_{n,k}$ are given by

$$A_{n,k} = \langle f(r,\theta), \chi_{n,k}(r,\theta)\rangle \tag{2.29}$$

$$= \frac{1}{\pi r_0^2}\iint f(r,\theta)\chi^*_{n,k}(r,\theta)\, r\mathrm{d}r\mathrm{d}\theta. \tag{2.30}$$

For our applications the function $f(r,\theta)$ is the real valued energy density distribution in the transverse plane, such that the coefficients obey $A_{n,k} = A^*_{-n,k}$.

The interpretation of the Bessel-Fourier coefficients is straight forward. By the value of n one can directly see which eccentricities are present in the decomposed density distribution, as the exponential in Eq. (2.26) gives a basis on $L^2([0,2\pi])$ already. With the Bessel part in Eq. (2.26) the radial direction is completely characterized. Thus, displaying $|A_{n,k}|$ in the (n,k)-plane can give a very intuitive picture

which eccentricities are present at which length scales of the decomposed density distribution.

In the upper left panel of Fig. 2.5 we can see an example event from the MC Glauber model at impact parameter $b = 0$ fm. It has some distinct areas with

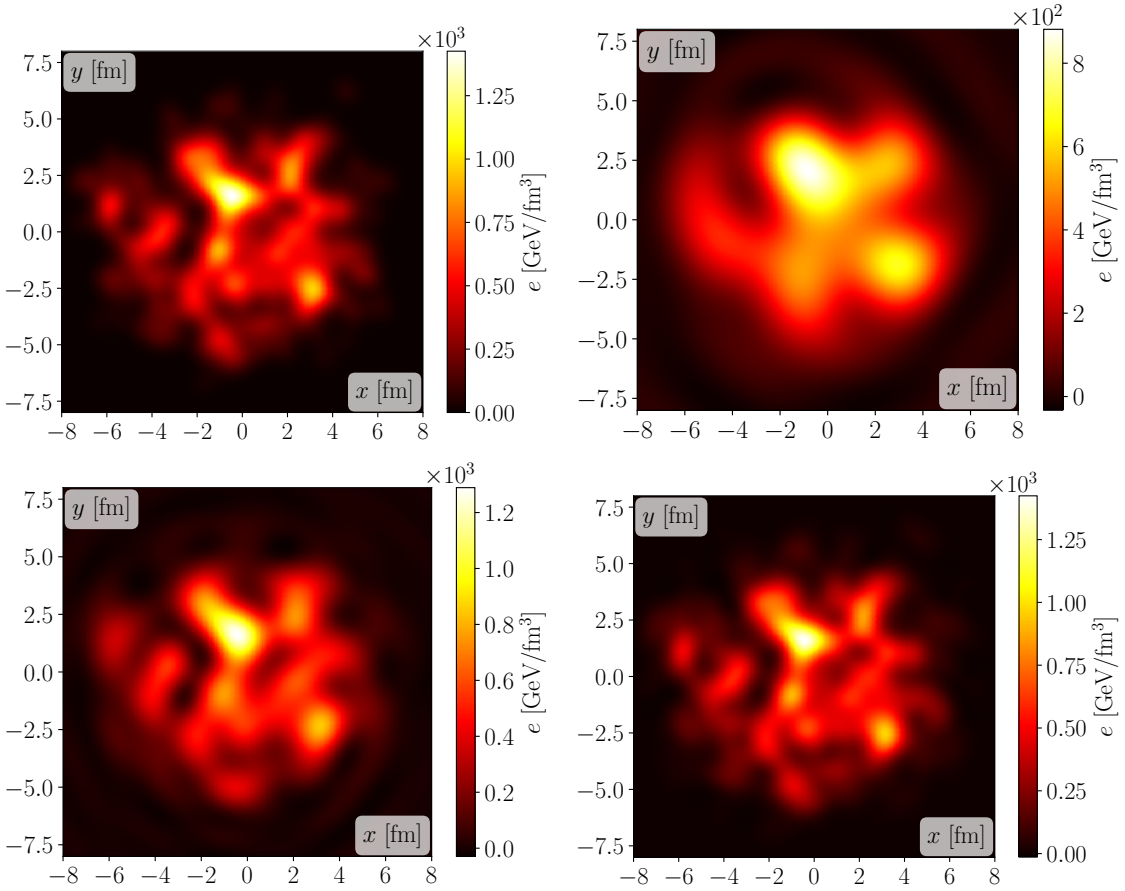

Figure 2.5: The upper left panel shows the energy density of an example event from the Glauber model at $b = 0$ fm (Pb-Pb, 5.02 TeV). All other energy densities are reconstructed from the Bessel-Fourier coefficients $A_{n,k}$ with $|n| \leq 5$, $k \leq 5$ (upper right), $|n| \leq 10$, $k \leq 10$ (lower left) and $|n| \leq 20$, $k \leq 20$ (lower right).

high energy density, so called "hot spots", and some regions with very low energy densities, even close to the center. This density profile is very different from the one generated by the overlap of two Woods-Saxon density profiles due to the fluctuations in the nucleon positions. Decomposing this density profile with the Bessel-Fourier series and reconstruct the profile with different upper bounds $k_{\max}$ and $|n_{\max}|$ in Eq. (2.28) results in the densities shown in the upper right, lower left and lower right panel with $k_{\max} = |n_{\max}| = 5$ resp. $k_{\max} = |n_{\max}| = 10$ resp. $k_{\max} = |n_{\max}| = 20$ coefficients. We can see that with the lowest number of coefficients the main structures of the hot spots are resolved but they are not really distinct structures. Including more coefficients leads to a better resolution of the hot spots but one can see still some differences in the low density regions at the edges. These are resolved for $k_{\max} = n_{\max} = 20$, where a difference between the original and reconstructed profile is not visible by eye. As the Bessel-Fourier coefficients

fulfill the identity $A_{n,k} = A^*_{-n,k}$, the amount of coefficients needed to reconstruct the event is of the order of 420. This estimate is very conservative, as we can see the absolute value of the coefficients in the lower left panel of Fig. 2.6 drops over several orders of magnitude in the (n, k)-plane and thus many of the coefficients do not really contribute to the reconstruction of the density. We find that there are

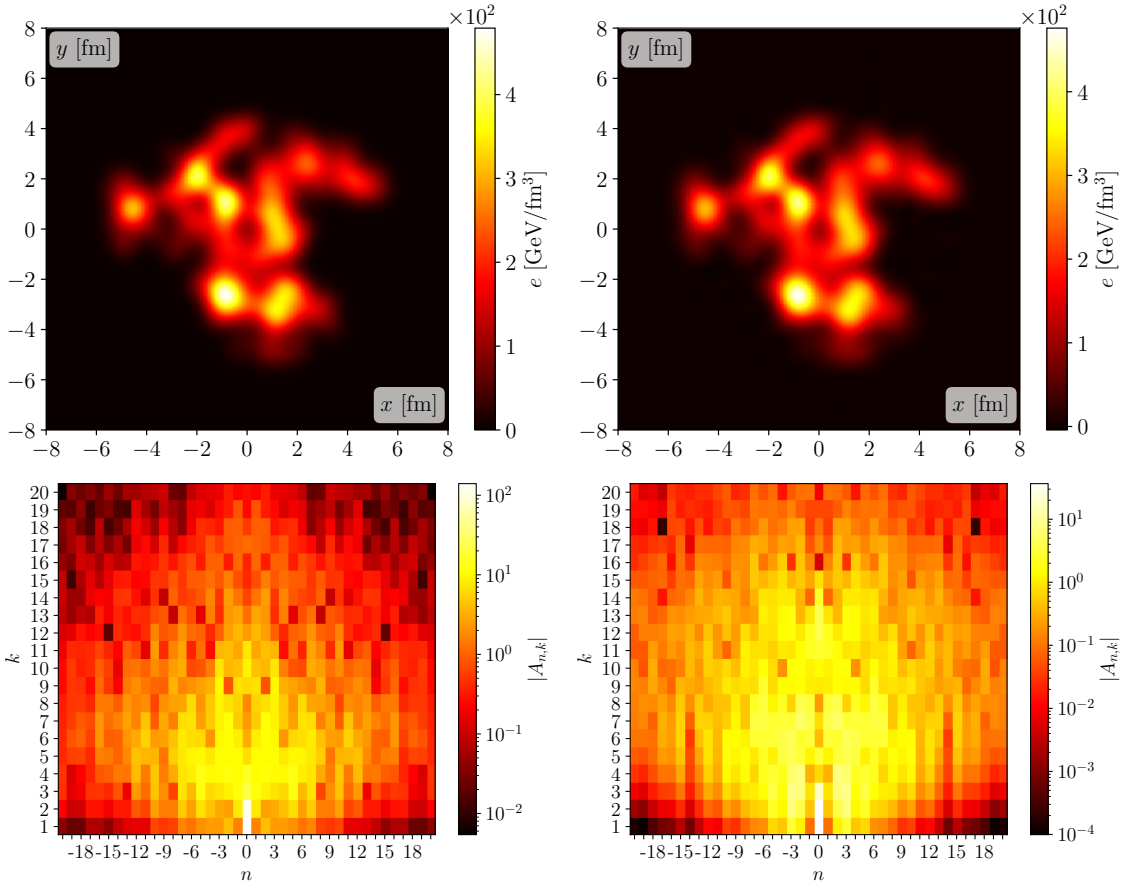

Figure 2.6: The upper left panel shows the energy density of an example event from the Glauber model at $b = 9$ fm (Pb–Pb, 5.02 TeV). In the upper right panel the reconstruction with $|n| \leq 20$, $k \leq 20$ is shown. The lower panel shows the Bessel-Fourier coefficients $A_{n,k}$ for the example event at $b = 0$ fm (see Fig. 2.5) on the left and for the event at $b = 9$ fm on the right.

two large radially symmetric components $A_{0,1}$, $A_{0,2}$ and then a variety of different harmonics at smaller length scales, i.e., larger k-values. However, these are already one or more orders of magnitude smaller, such that of the order of a few tens of coefficients would be sufficient to store a reasonable approximation of the sampled energy density.[11]

Going now to an event at impact parameter $b = 9$ fm shown in the upper left panel of Fig. 2.6 we can see that the system is now much more elongated along the y-axis. This matches the larger ellipticity $\varepsilon_2^{\mathbf{x}}$ from Fig. 2.4 at larger impact parameters compared to central collisions. In contrast to the optical Glauber model

[11] The expansion of the energy density in a Bessel-Fourier series can be used as a data reduction technique for initial state profiles. We will return to this in Sec. 7.1.4.2.

we can see a triangular structure as well, which is on a large length scale. The upper right panel is again the reconstruction with $k_{\max} = |n_{\max}| = 20$ which yields again a result which is indistinguishable from the original density by eye. In the (n, k)-plane (lower right panel) we can see again some large radial contributions but also for the largest radial structures ($k = 1$) we find a considerably large contribution for the harmonics $n = 2, 3$, which is exactly what we can see by eye in the density plot. Another thing to notice is that the absolute numbers of the coefficients are smaller than in the $b = 0$ fm case, which is due to the fact that the values for the density themselves are smaller for the non-central collision.

Chapter 3

Solving the Boltzmann equation

Nothing is more practical than a good theory. – Ludwig Boltzmann

This derivation of the Boltzmann transport equation in Newtonian systems (Sec. 3.2) and in relativistic systems (Sec. 3.3) is strongly inspired by the derivation in Ref. [42]. Sec. 3.3, which extends the classical Boltzmann equation to the relativistic one, additionally uses Ref. [43]. Before we derive the Boltzmann equation, let us have a look in which limit the Newtonian version of kinetic theory is applicable in Sec. 3.1. In the whole chapter we consider systems which consist of one particle species and where particles are indistinguishable.[1] The reason why we introduce the Newtonian kinetic theory first is that most of the concepts can be transferred to the relativistic

[1] The generalization to a multi-component system is straight forward and can be performed by using one distribution function for each particle species and for the exchange terms of the different species.

regime. In Sec. 3.4 we will discuss how one can find numerical solutions to the Boltzmann equation, in which we go into more detail on the Lattice Boltzmann Method (LBM) in Sec. 3.4.1 and the test particle method in Sec. 3.4.2.

3.1 When is a quantum mechanical description necessary?

Kinetic theory describes the evolution of a system of N particles which can interact with each other in the sense that they are freely moving and not bound in a lattice for example. If we want the system to be described by a classical version of kinetic theory, then the ratio λ_{DB}/l between the de Broglie wavelength of each particle and the typical separation l between the particles should be $\ll 1$.[2] Then the wave functions evolve separately according to the Schrödinger equation like classical particles. This is known as Ehrenfest's theorem, which says that the N particles are described by their positions and momenta which evolve due to the laws of classical mechanics.

3.2 Kinetic theory of Newtonian systems

Although the system could in principle be described by classical mechanics, this approach is in the limit of large N not very practicable and it is therefore more convenient to switch to a statistical approach based on a distribution function $f(t, \vec{x}, \vec{u})$ depending on time t, position $\vec{x}$ and coordinate velocity $\vec{u}$. The distribution function is the particle number density at time t in the six-dimensional phase space $(\vec{x}, \vec{u})$. All the dynamics is then encrypted in the time evolution of the distribution function, which is an advection in phase space if there are no collisions. For a system with interactions between the particles the evolution of the distribution function is non-trivial. The equation which describes the evolution of the distribution function is the Boltzmann equation.

The distribution function gives us the probability to find a particle at time t at position $\vec{x}$ and with velocity $\vec{u} = \vec{p}/m$ in the velocity-space element $\mathrm{d}^3\vec{u}$ at $\vec{u}$ and in the volume element $\mathrm{d}^3\vec{x}$ at $\vec{x}$. This leaves us with the total particle number N if we integrate over the whole six-dimensional phase space:

$$N = \int_{-\infty}^{\infty} \mathrm{d}^3\vec{x} \int_{-\infty}^{\infty} \mathrm{d}^3\vec{u}\, f(t, \vec{x}, \vec{u}). \tag{3.1}$$

In Sec. 3.2.1 we will first derive the collisionless Boltzmann equation and in Sec. 3.2.2 we will derive its form in the presence of collisions. The denomination "collision" in this context means any type of particle interaction.

[2] In the case in which the ratio is $\gtrsim 1$ the wave functions of the particles overlap and the system would be described by the Schrödinger equation and the N-particle wave function.

3.2.1 Collisionless Boltzmann equation

In a system where the particles do not interact, they just follow a linear trajectory in position space, while there is no change in momentum space. This behavior is depicted in Fig. 3.1, where the trajectories in position and velocity space are sketched. The evolution of the spatial distribution $f(t, \vec{x})$ is shown in green and the evolution of the velocity distribution $f(t, \vec{u})$ is shown in blue. If the system is

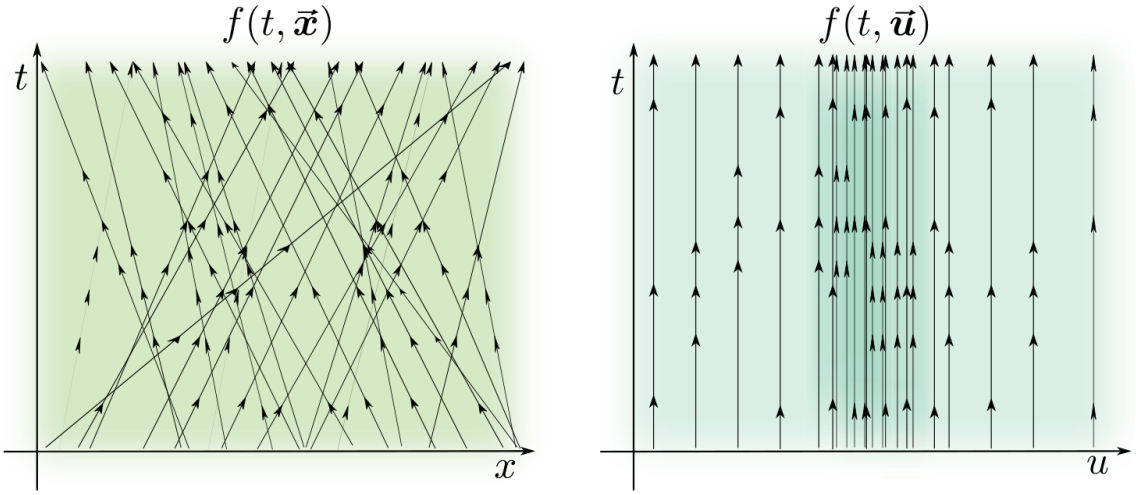

Figure 3.1: Depiction of the phase space trajectories for a particle system without collisions. On the left the trajectories in position space are sketched and the evolution of the spatial distribution $f(t, \vec{x})$ is given by the green color. On the right the trajectories in velocity space are sketched and the evolution of the velocity distribution $f(t, \vec{u})$ is given by the blue color. Due to the fact that there are no collisions the distributions remain unchanged in time and it is assumed that there are no external forces. The picture is taken from [42].

exposed to an external force $\vec{F}$ acting on every particle with mass m all particles in the phase space cell at $(\vec{x}, \vec{u})$ would have traveled into the cell $(\vec{x}+\vec{u}\,\mathrm{d}t, \vec{u}+\vec{F}/m\,\mathrm{d}t)$ with volume element $\mathrm{d}^3\vec{x}'\mathrm{d}^3\vec{u}'$ after the time $\mathrm{d}t$. This tells us that the number of particles contained in one phase space cell is invariant if there are no interactions between the particles, represented by

$$f\left(t + \mathrm{d}t, \vec{x} + \vec{u}\,\mathrm{d}t, \vec{u} + \frac{\vec{F}}{m}\,\mathrm{d}t\right)\,\mathrm{d}^3\vec{x}'\mathrm{d}^3\vec{u}' = f(t, \vec{x}, \vec{u})\,\mathrm{d}^3\vec{x}\mathrm{d}^3\vec{u}. \tag{3.2}$$

So the position and velocity change is given by the coordinate transformation

$$\vec{x}\,' = \vec{x} + \vec{u}\,\mathrm{d}t, \tag{3.3}$$

$$\vec{u}\,' = \vec{u} + \frac{\vec{F}}{m}\,\mathrm{d}t. \tag{3.4}$$

The Jacobian of this transformation is $J = 1+\mathcal{O}(\mathrm{d}t^2)$ which implies that $\mathrm{d}^3\vec{x}'\mathrm{d}^3\vec{u}' = J\,\mathrm{d}^3\vec{x}\mathrm{d}^3\vec{u} = \mathrm{d}^3\vec{x}\mathrm{d}^3\vec{u} + \mathcal{O}(\mathrm{d}t^2)$ [44]. Then a Taylor expansion of the left hand side of Eq. (3.2) up to first order in $\mathrm{d}t$ leaves us with

$$\frac{\partial f(t, \vec{x}, \vec{u})}{\partial t} + \vec{u} \cdot \vec{\nabla} f(t, \vec{x}, \vec{u}) + \frac{\vec{F}}{m} \cdot \vec{\nabla}_{\vec{u}} f(t, \vec{x}, \vec{u}) = 0. \tag{3.5}$$

This equation is the collisionless Boltzmann equation which describes the conservation of $f(t, \vec{x}, \vec{u})$ when there are no particle interactions. Rewritten in the form

$$\frac{\mathrm{d}}{\mathrm{d}t} f\left(t, \vec{x}, \frac{\vec{p}}{m}\right) = \frac{\partial f(t, \vec{x}, \vec{p}/m)}{\partial t} + \dot{\vec{x}} \cdot \frac{\partial f(t, \vec{x}, \vec{p}/m)}{\partial \vec{x}} + \dot{\vec{p}} \cdot \frac{\partial f(t, \vec{x}, \vec{p}/m)}{\partial \vec{p}} = 0 \quad (3.6)$$

with $\vec{F}/m = \partial\vec{p}/\partial t = \dot{\vec{p}}$ and $\vec{u} = \partial\vec{x}/\partial t = \dot{\vec{x}}$ this conservation of the distribution function is more obvious.

3.2.2 Collisional Boltzmann equation

In this part we will focus on a system with binary elastic collisions due to short range forces between the particles. Since there is now not only the possibility of advection between one cell to a neighboring one, but also the possibility that collisions will populate or depopulate this neighboring cell, we have to change Eq. (3.2) to

$$f\left(t + \mathrm{d}t, \vec{x} + \vec{u}\,\mathrm{d}t, \vec{u} + \frac{\vec{F}}{m}\,\mathrm{d}t\right)\,\mathrm{d}^3\vec{x}'\mathrm{d}^3\vec{u}' = f(t, \vec{x}, \vec{u})\,\mathrm{d}^3\vec{x}\mathrm{d}^3\vec{u} + \mathcal{C}[f(t, \vec{x}, \vec{u})]\,\mathrm{d}^3\vec{x}\mathrm{d}^3\vec{u}, \quad (3.7)$$

where the term $\mathcal{C}[f(t, \vec{x}, \vec{u})]\,\mathrm{d}^3\vec{x}\mathrm{d}^3\vec{u}$ is the net change, per unit time, of the particle number in the cell around $(\vec{x}, \vec{u})$ caused by collisions between particles. Then Eq. (3.5) has to be changed to

$$\frac{\partial f(t, \vec{x}, \vec{u})}{\partial t} + \vec{u} \cdot \vec{\nabla} f(t, \vec{x}, \vec{u}) + \frac{\vec{F}}{m} \cdot \vec{\nabla}_{\vec{u}} f(t, \vec{x}, \vec{u}) = \mathcal{C}[f(t, \vec{x}, \vec{u})] = \left(\frac{\partial f(t, \vec{x}, \vec{u})}{\partial t}\right)_{\mathrm{coll}}, \quad (3.8)$$

which is the collisional Boltzmann equation derived by Ludwig Boltzmann in 1872.

Fig. 3.2 depicts the trajectories in position and velocity space when we allow for collisions in the system. The difference to Fig. 3.1 is that the collisions change the trajectories of the particles in phase space with each collision. One can show that if the system is out of equilibrium, the distribution functions $f(t, \vec{x})$ and $f(t, \vec{u})$ evolve in time till they approach the equilibrium value f_{eq}. In Sec. 3.2.3 the properties of this equilibrium distribution will be specified further. The right hand side of Eq. (3.8) is called collision integral or collision kernel and contains the effects of the collisions between the particles.

If there are only binary collisions considered in the system and the particles have velocities $\vec{u}$ and $\vec{u}_1$ and furthermore, there is no external force $\vec{F}$, then the collision integral counts the net number of particles which enter or leave a phase space volume and has the form

$$\begin{aligned}\left(\frac{\partial f(t, \vec{x}, \vec{u})}{\partial t}\right)_{\mathrm{coll}} = \int \mathrm{d}^3\vec{u}_1 \int \mathrm{d}^2\Omega\, \frac{\mathrm{d}^2\sigma(\theta, \phi)}{\mathrm{d}^2\Omega} |\vec{u} - \vec{u}_1| \\ \times \left(f(t, \vec{x}, \vec{u}_1{}')f(t, \vec{x}, \vec{u}\,') - f(t, \vec{x}, \vec{u}_1)f(t, \vec{x}, \vec{u})\right).\end{aligned} \quad (3.9)$$

The distribution functions with the unprimed variables are the ones before the collision at time t and position $\vec{x}$ and the primed ones are the distribution functions after

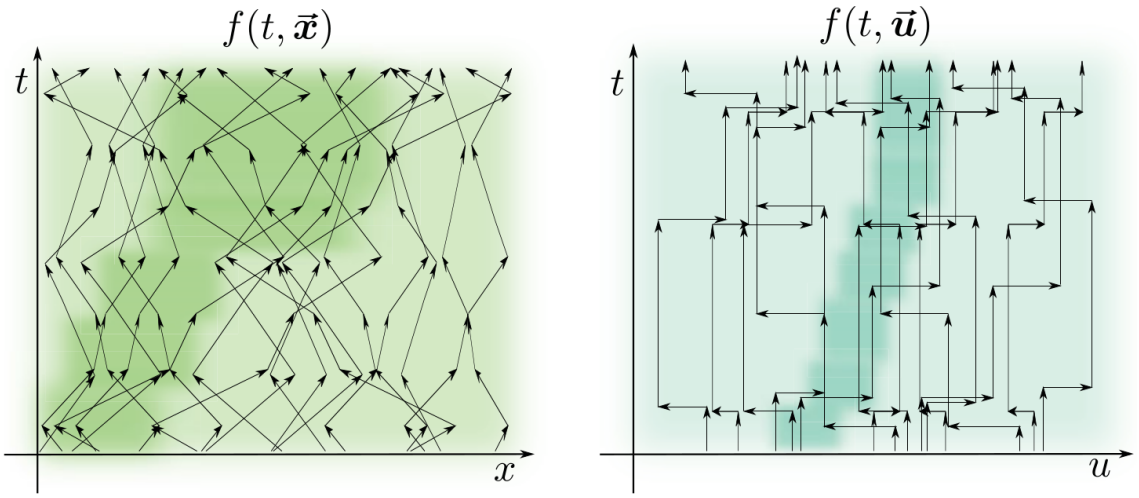

Figure 3.2: Depiction of the phase space trajectories for a particle system with collisions. On the left the trajectories in position space are sketched and the evolution of the spatial distribution $f(t,\vec{x})$ is given by the green color. On the right the trajectories in velocity space are sketched and the evolution of the velocity distribution $f(t,\vec{u})$ is given by the blue color. Here the distributions change until they reach an equilibrium distribution $f_{\text{eq.}}$. It is assumed that there are no external forces. The picture is taken from [42].

the collision. The collision is encoded in the differential cross section $\mathrm{d}^2\sigma(\theta,\phi)$ over the solid angle $\mathrm{d}^2\Omega$, which accounts for the short-range interaction responsible for collisions. The structure of the collision integral is further investigated and derived in Appendix B.1.

We can see from the Equations (3.8) and (3.9) that the Boltzmann equation is a non-linear integro-differential equation. Therefore, the complexity of this equation often requires a numerical solution.

3.2.3 H-theorem

In this subsection we discuss the role of the equilibrium distribution function f_{eq} which is the asymptotic state approached by a system evolving with the collisional Boltzmann equation (3.8) and independent of t.

The H-theorem will give us the form of the stationary and uniform f_{eq}. If we evaluate the collision integral (Eq. (3.9)) for the equilibrium distribution function we obtain

$$\frac{\partial f_{\text{eq}}}{\partial t} = \int \mathrm{d}^3\vec{u}_1 \int \mathrm{d}^2\Omega \, \frac{\mathrm{d}^2\sigma(\theta,\phi)}{\mathrm{d}^2\Omega} |\vec{u} - \vec{u}_1| \left[f_{\text{eq}}(\vec{u}_1{}') f_{\text{eq}}(\vec{u}\,') - f_{\text{eq}}(\vec{u}_1) f_{\text{eq}}(\vec{u}) \right] = 0. \tag{3.10}$$

To solve this equation means that we have to solve

$$f_{\text{eq}}(\vec{u}_2{}') f_{\text{eq}}(\vec{u}_1{}') - f_{\text{eq}}(\vec{u}_2) f_{\text{eq}}(\vec{u}_1) = 0, \tag{3.11}$$

which is a sufficient condition. For the proof that this expression is also a necessary

condition for Eq. (3.10) one has to define the functional $H(t)$ as

$$H(t) \equiv \int \mathrm{d}^3\vec{u}\; f(t,\vec{u}) \ln(f(t,\vec{u})). \tag{3.12}$$

With some algebra one can show that if a distribution function $f(t,\vec{x},\vec{u})$ solves the Boltzmann equation then

$$\frac{\mathrm{d}H(t)}{\mathrm{d}t} \leq 0 \tag{3.13}$$

and that Eq. (3.11) is equivalent to $\mathrm{d}H(t)/\mathrm{d}t = 0$. For the non-relativistic and the relativistic case this proof is described in more detail in [42, 43].

The H-theorem provides us with important consequences. First, it is also shown in [42] that Eq. (3.11) leads to an equilibrium distribution of the form

$$f_{\mathrm{eq}}(\vec{u}) = C \cdot e^{-A(\vec{u}-\vec{u}_0)^2}, \tag{3.14}$$

where C and A are two system specific constants. Second, the definition of the Boltzmann entropy $H(t)$ can be related to the usual entropy definition by

$$S(t) \equiv -k_{\mathrm{B}} V H(t) = -k_{\mathrm{B}} V \int \mathrm{d}^3\vec{u}\; f(t,\vec{x},\vec{u}) \ln(f(t,\vec{x},\vec{u})). \tag{3.15}$$

Third, Eqs. (3.13) and (3.15) are a microscopic formulation of the second law of thermodynamics and explain that entropy has to increase.[3] If we consider a system out of equilibrium then collisions will bring the system back to equilibrium, i.e. $\mathrm{d}H(t)/\mathrm{d}t = 0$, until the distribution f_{eq} is reached.

3.3 Kinetic theory of relativistic systems

As the particles which are created in heavy-ion collisions have velocities in the relativistic regime, it is necessary to extend the Boltzmann equation (3.8) to the case of relativistic particles.

In this work we use the pseudo-metric tensor with $\mathrm{diag}(-1,+1,+1,+1)$ and we set the speed of light c to 1. We denote the components of the position four-vector by x^μ and the ones of the four-momentum of a particle with rest mass m by $p^\mu = mu^\mu = (p^0, p^i)$. The four vectors itself are denoted by x, p. The momenta are normalized by the condition $p^\mu p_\mu = -m^2$. Again we can write the number of particles contained in a phase space volume as

$$f(t,\vec{x},\vec{p})\; \mathrm{d}^3\vec{x}\mathrm{d}^3\vec{p} = f(t,\vec{x},\vec{p})\; \mathrm{d}x^1\mathrm{d}x^2\mathrm{d}x^3\mathrm{d}p^1\mathrm{d}p^2\mathrm{d}p^3. \tag{3.16}$$

If an observer $\mathcal{O}'$ is in the local rest frame of the particles and a second observer $\mathcal{O}$ moves with respect to $\mathcal{O}'$ with a certain velocity in x^1-direction, then the length contraction leads to

$$\mathrm{d}^3\vec{x}\,' = \gamma\; \mathrm{d}^3\vec{x} \tag{3.17}$$

[3] This does not mean that the entropy cannot decrease locally in time.

and

$$\frac{\mathrm{d}^3\vec{p}'}{p_{0'}} = \frac{\mathrm{d}^3\vec{p}}{p_0}, \tag{3.18}$$

where the latter is Lorentz invariant. In the local rest frame we have $p_{1'} = 0$ and therefore $p_{0'} = \gamma^{-1} p_0$. This results with Eqs. (3.17)-(3.18) in the Lorentz invariance of the product

$$\mathrm{d}^3\vec{x}\,'\mathrm{d}^3\vec{p}\,' = \mathrm{d}^3\vec{x}\,\mathrm{d}^3\vec{p}. \tag{3.19}$$

As this product is Lorentz invariant, the number of particles in a phase space element is the same in all reference inertial frames. Thus, the distribution function has to be a Lorentz invariant quantity, i.e.,

$$f'\left(\mathsf{x}', \mathsf{p}'\right) = f\left(\mathsf{x}, \mathsf{p}\right). \tag{3.20}$$

With this knowledge the derivation of the relativistic Boltzmann equation is the same as in the Newtonian case (see Sec. 3.2).

The equation reads

$$p^\mu \frac{\partial f(\mathsf{x}, \mathsf{p})}{\partial x^\mu} + m \frac{\partial \left(F^\mu f(\mathsf{x}, \mathsf{p})\right)}{\partial p^\mu} = \mathcal{C}\left[f(\mathsf{x}, \mathsf{p})\right], \tag{3.21}$$

where F^μ is an external four-force acting on the system and $\mathcal{C}\left[f(\mathsf{x}, \mathsf{u})\right]$ is the relativistic version of the collision integral, which is of the form

$$\begin{aligned}\mathcal{C}\left[f(\mathsf{x}, \mathsf{p})\right] = \left(\frac{\partial f(\mathsf{x}, \mathsf{p})}{\partial t}\right)_{\text{coll}} = E \int \mathrm{d}^3\vec{p}_1 \int \mathrm{d}^2\Omega \, \frac{\mathrm{d}^2\sigma\left(\theta, \phi\right)}{\mathrm{d}^2\Omega} u_{\text{Møller}} \\ \times \left(f_1(\mathsf{x}, \mathsf{p}_1') f(\mathsf{x}, \mathsf{p}') - f_1(\mathsf{x}, \mathsf{p}_1) f(\mathsf{x}, \mathsf{p})\right)\end{aligned} \tag{3.22}$$

if only binary collisions are considered.[4] This form is also quite similar to the Newtonian case of the collision integral with the difference that the relative velocity is substituted by the Møller velocity. The motivation for this and a derivation is presented in Appendix B.2.

3.4 Solving the Boltzmann equation numerically

There exist different approaches to find numerical solutions to the Boltzmann equation. Two common approaches are the Lattice Boltzmann Method which is briefly explained in Sec. 3.4.1 and the test particle method, which we use for our simulations, explained in Sec. 3.4.2.

[4] One has to include a factor 1/2 if the particles are indistinguishable.

3.4.1 The lattice Boltzmann method

The LBM discretizes, in contrast to other methods like the test particle method, the distribution function and does not track individual particles. Therefore, it is based on a strong physical fundament, namely the Boltzmann equation itself, which is solved in a discretized version. As there exists a connection between its dynamics and the macroscopic conservation laws of fluid dynamics, this method is also a second-order precise solver for the Navier-Stokes equation [45]. The LBM can also be used in the relativistic case to solve the Navier-Stokes equation. This has been performed first in 2010 for mildly relativistic systems [46, 47] and then extended to ultra-relativistic systems in general spacetime geometries [48]. This LBM formalism can then be used to reproduce the results from second-order relativistic hydrodynamics. However, there is one caveat. In the formulation of the LBM one approximates the collision kernel using the relaxation time approximation (RTA). This assumes that the distribution relaxes to the equilibrium distribution on a timescale τ_{R}. When using RTA one has to be careful, as the first introduction from 1974 by Anderson and Witting [49] for relativistic systems is incompatible with microscopic and macroscopic conservation laws. These problems are solved in modern formulations of RTA [50].

3.4.2 Test particle method

For the simulation of relativistic heavy-ion collisions the test particle method was extensively used already before the LBM was upgraded to ultra-relativistic systems. One of the first codes was the Zhang Parton Cascade (ZPC) [51] in 1997 which included gluon-gluon elastic scatterings. In 2000 the Molnár Parton Cascade (MPC) [52] was published which introduced a parton subdivision technique for a better preservation of covariance than in ZPC. Also in 2000 the Poincaré-Covariant Parton Cascade (PCPC) [53] was introduced, which treats the whole dynamics in a Poincaré-covariant way. As the test particle method uses a particle formulation it is inherently a non quantum mechanical description of the system. To obtain a completely covariant system the only possibility is that the particles do not interact, as prescribed by the No-Interaction-Theorem formulated by Currie et al. [54]. PCPC introduces a new Poincaré-invariant parameter controlling the time ordering of interactions. Thus, the system is covariant in contrast to other codes involving actions at a distance. By introducing the many-times-formalism the covariance problem is still not solved, as the consistent Poincaré-covariant formulation of statistical mechanics is still missing in this model. In 2005 the Boltzmann Approach of Multi-Parton Scatterings (BAMPS) [55] was introduced which introduced, besides of $2 \to 2$ processes, also inelastic $2 \leftrightarrow 3$ processes. Therefore, the stochastic collision algorithm was introduced by Xu and Greiner, since the geometrical picture in a $3 \leftrightarrow 2$ process is more difficult.

The approach which we will use for the simulations in this thesis was introduced in 2008 by C. Gombeaud and J.-Y. Ollitrault [56]. It takes into account the Lorentz contraction of the hard sphere particles to oblate spheroids. As the Boltzmann equation requires a system which is dilute, the violations of covariance due to instantaneous collisions at a finite distance are small. In contrast to the ZPC

algorithm, the time of the collision is determined in the laboratory frame and not in the center-of-mass frame.

As we want to investigate the transport of fluctuations from the initial state of a heavy-ion collision to the final state anisotropic flow, we will consider a two dimensional system of massless test particles in the following. The restriction to two dimensions will not affect the qualitative behavior of the results, as this setup is sufficient to produce an anisotropic flow signal in the final state [56]. Furthermore, the advantage over a hydrodynamic simulation is that our study is not limited to systems with small mean free path and that no modeling of the freeze-out is required.

The following part about the relevant parameters and the dynamics in the transport code was described in the PhD thesis of C. Gombeaud [57] and in Ref. [56]. We will briefly go through the main aspects of the code and will describe the individual derivations in Appendix B.3 in more detail.

3.4.3 Important parameters

As we restrict our system to two dimensions with massless test particles, the particles travel at the speed of light.[5] Therefore, the Lorentz contraction in the direction of motion contracts them to rods. Assuming the test particles have size r. Then we can assume the collision to happen between one particle of size $2r$ and a pointlike particle to obtain the same result. Hence, the total cross section, which has the dimension of a length, is given by $\sigma = 2r$. There are three inherent length scales in the problem, which one can see in Fig. 3.3. First, the size R of the whole system.

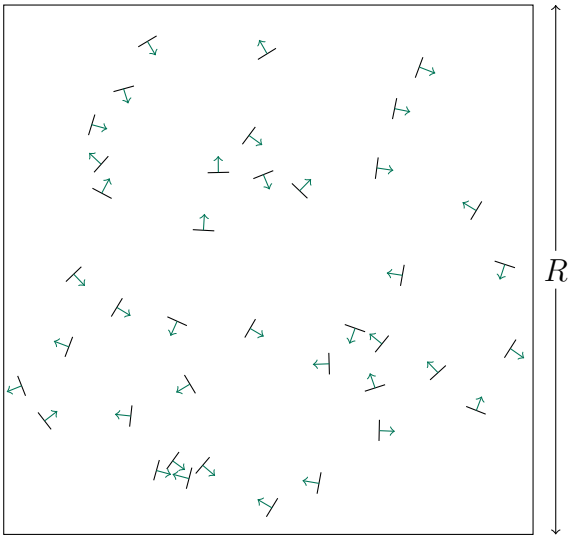

Figure 3.3: Sketch of the two-dimensional system of massless test particles. Figure adapted from [57].

Second, the average distance between two particles $\bar{d}$, which is in an ideal gas in two dimensions given by $\bar{d} = 1/\sqrt{n}$ with the particle number density n of the gas. The third length scale is the mean free path $\lambda_{\text{mfp}} = 1/(\sigma n)$ of the particles.

[5] Thus, in an equilibrated system the particles would obey two-dimensional thermodynamics implying a speed of sound which has a value of $c_s = 1/\sqrt{2}$.

With these three lengths it is possible to form two dimensionless control parameters for the system. The first one is the dilution coefficient D, which is given by the ratio

$$D \equiv \frac{\bar{d}}{\lambda_{\mathrm{mfp}}} = \sigma\sqrt{n}. \tag{3.23}$$

It has to fulfill $D \ll 1$ to assure the applicability of Boltzmann kinetic theory. Further, locality and covariance are only recovered in this limit. The second dimensionless number is the Knudsen number Kn, which is defined by

$$\mathrm{Kn} \equiv \frac{\lambda_{\mathrm{mfp}}}{R} = \frac{1}{\sigma n R}. \tag{3.24}$$

Using the Knudsen number we can control the number of collisions in the system. A Knudsen number in the limit $\mathrm{Kn} \to 0$ corresponds to the hydrodynamic limit, where the particles interact very often. The other limit $\mathrm{Kn} \to \infty$ corresponds to the limit of free-streaming particles. In the transport algorithm the two dimensionless numbers are no direct input parameters, but they can be steered by the number of test particles N_{p} and their cross section σ.

3.4.4 Dynamical system evolution

In this part we will briefly introduce the main parts of the transport algorithm which includes the propagation of the particles, the collision criteria, calculation of the final state momenta of a scattering process and the implementation into the numerical code.

3.4.4.1 Propagation of particles

Particles which do not interact in a time step $\mathrm{d}t$ during the system evolution of the transport algorithm are propagated freely due to

$$\vec{x}\,' = \vec{x} + \vec{v}\,\mathrm{d}t \tag{3.25}$$

from the initial position $\vec{x}$ to the final position $\vec{x}\,'$ with the velocity $\vec{v}$.

3.4.4.2 Collision criteria

To decide whether a particle collides the algorithm uses a geometrical approach. A first criterion which has to be fulfilled is that the particle trajectories cross. Additionally it has to be checked if the collision happens in the given time step. In Fig. 3.4 a sketch of the collision is given. A collision in the frame where the velocities are anti-parallel occurs if the impact parameter b, which is a Lorentz scalar, fulfills the condition $|b| \leq r$. The impact parameter is given by

$$b = \frac{\vec{\mathsf{e}}_z \cdot [(\vec{x}_2 - \vec{x}_1) \times (\vec{v}_2 - \vec{v}_1)]}{\vec{v}_1 \cdot \vec{v}_2 - 1}. \tag{3.26}$$

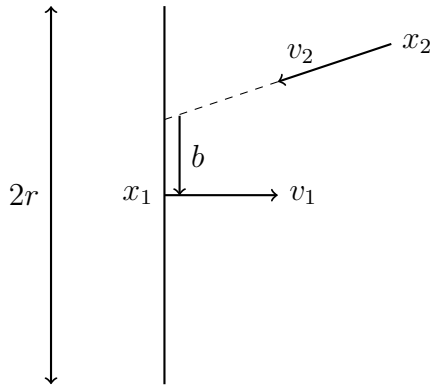

Figure 3.4: Schematic representation of a collision between a particle of size $2r$ and a pointlike particle in the reference frame of the collision. The figure is taken from Ref. [56].

A derivation for this expression is given in Appendix B.3.1 including a proof of the Lorentz invariance of the expression.

For the numerical solution it is important to note that the time in the algorithm is a discrete quantity in time steps of length $\mathrm{d}t$. Thus, a collision is only possible if the positions $\vec{x}_2$ and $\vec{x}_1$ of two particles are such that the time

$$\tau = \frac{(\vec{x}_2 - \vec{x}_1) \cdot \vec{v}_1}{1 - \vec{v}_2 \cdot \vec{v}_1} \tag{3.27}$$

fulfills the criterion $\tau \leq \mathrm{d}t$. This equation is derived in Appendix B.3.1 as well.

3.4.4.3 Changes in momenta

For the calculation of the final state momenta it is convenient to change the reference frame to simplify the algebra. A more detailed derivation is given in Appendix B.3.2. The starting point for this is the Lorentz invariant expression

$$(\mathsf{p}_1 + \mathsf{p}_2 - \mathsf{p}_1')^2 = 0 = (\mathsf{p}_1 + \mathsf{p}_2)^2 - 2\mathsf{p}_1' (\mathsf{p}_1 + \mathsf{p}_2)\,. \tag{3.28}$$

The prime indicates quantities after the scattering process. In the reference frame we want to use to express the kinematics, the scattering angle is given by $\theta = \angle(\vec{\mathsf{e}}_x, \vec{p}_1{}')$, where $\vec{\mathsf{e}}_x$ is the unit vector along the x-axis in that frame. This angle, as well as $\left|\vec{p}_1{}'\right|$ can be determined from the Lorentz invariant expression above. In combination with the Mandelstam variables s and t — which are itself Lorentz invariant quantities — one obtains

$$[(\mathsf{s} + \mathsf{t})\,\vec{p}_1 + \mathsf{t}\vec{p}_2] \cdot \vec{u} = (\mathsf{s} + \mathsf{t})\,|\vec{p}_1| + \mathsf{t}|\vec{p}_2| \tag{3.29}$$

$$\Leftrightarrow \quad \vec{v} \cdot \vec{u} = (\mathsf{s} + \mathsf{t})\,|\vec{p}_1| + \mathsf{t}|\vec{p}_2|. \tag{3.30}$$

The vector $\vec{u}$ is defined as $\vec{p}_1{}' = \left|\vec{p}_1{}'\right|\vec{u}$ and the vector $\vec{v}$ defines the x-axis of the frame we want to describe the collision in.

Going into the center-of-momentum frame we fix the scattering angle to be

$$\theta^* = \pi \left(1 + \frac{b}{r}\right), \tag{3.31}$$

with the absolute value of the impact parameter b (Eq. (3.26)) and the size of the particles r. This scattering angle corresponds to an isotropic cross section and makes sure that there are no double collisions. These double collisions are explained in more detail in Appendix B.3.3.

Now, after fixing θ^*, it is possible to fix the final momenta of the particles. In the collision frame the scattering angle is given by

$$\cos\theta = \frac{(\mathsf{s}+\mathsf{t})\,|\vec{p}_1| + \mathsf{t}|\vec{p}_2|}{|\vec{v}|} \tag{3.32}$$

and again the Mandelstam variables can be used to find $\left|\vec{p}_1{}'\right|$:

$$\left|\vec{p}_1{}'\right| = \frac{\mathsf{t}}{2\,[|\vec{p}_1| - \vec{p}_1 \cdot \vec{u}]}. \tag{3.33}$$

By the energy momentum conservation laws the other final state momentum components can be determined.

3.4.5 Code structure

The first ingredient for the code is the initial condition for the particle positions and their according momenta. As we use different initial conditions throughout this thesis, we will introduce them in the corresponding chapters later on.

Then the main idea of the code is to follow all test particle trajectories, as already mentioned in Sec. 3.4.2. We consider the system as a box with side lengths L and the time is discretized in steps $\mathrm{d}t$. Checking for collisions within a given time step requires checking a possible collision of each particle with all other particles in the system. This introduces a numerical complexity of N_p^2. Reducing the numerical complexity is possible by introducing N_cells^2 cells with side lengths L/N_cells. There exists an optimal value for N_cells which minimizes the errors and the runtime of the code.

Dividing the system into smaller cells has also an influence on the time step, as this one is chosen such that the particles can only scatter with particles in their own cell or a cell directly adjacent to their own. With this restriction the time step is given by

$$\mathrm{d}t = \frac{L}{2N_\mathrm{cells}}. \tag{3.34}$$

At each step in time the code identifies which particles are in which cell. Then the particles in each box are tested for collisions within the same box and then in a next step for collisions with particles in the neighboring boxes.[6] Particles not undergoing a collision during a given time step are propagated according to Eq. (3.25).

The introduction of the cells has decreased the numerical complexity drastically. However, we have to optimize the parameter N_cells such that the code has optimal performance. We can identify two contributions to the runtime of the code.

[6] To avoid a double counting of collisions with particles in neighboring cells, only four of the eight surrounding boxes are checked for collisions.

The first one is the check of the N_{cells}^2 cells during each time step. Then there is a macroscopic time scale for the system evolution which is proportional to the macroscopic system size L. Therefore, one has to consider N_{cells} times the time step, which results in a N_{cells}^3 contribution from scanning the cells for collisions during the time evolution.

A second contribution is arising due to the scattering processes themselves. The probability to have an interaction in a cell is proportional to $(N_{\text{p}}/N_{\text{cells}}^2)^2$. Thus, the runtime of the code is proportional to $(N_{\text{p}}/N_{\text{cells}}^2)^2 N_{\text{cells}}^3$.

Finally we obtain

$$t_{\text{run}} \propto \alpha N_{\text{cells}}^3 + \beta \frac{N_{\text{p}}^2}{N_{\text{cells}}} \tag{3.35}$$

as a runtime estimate t_{run}. Optimizing the given expression with

$$\frac{\mathrm{d}t_{\text{run}}}{\mathrm{d}N_{\text{cells}}} = 3\alpha N_{\text{cells}}^2 - \beta \frac{N_{\text{p}}^2}{N_{\text{cells}}^2} \stackrel{!}{=} 0 \tag{3.36}$$

leads to $N_{\text{cells}} \propto \sqrt{N_{\text{p}}}$. By numerical adjustment one finds a proportionality factor of ≈ 1.4.

3.4.6 Simulating a $2 \to 0$ collision kernel

For the studies which will be described in Chs. 5 and 6 we will need a code version which can simulate a $2 \to 0$ collision kernel, i.e., the loss term in the collision kernel of the Boltzmann equation only. This version of the Code was developed by Benedikt Bachmann in his Bachelor thesis project [58].

The implementation of the $2 \to 0$ collision kernel is straight forward by introducing the labels "active" and "passive" to each particle. A collision between two particles is then only possible between two particles which are "active". After a collision the two participants are labeled as "passive" for the rest of the time evolution of the system. From the time of the collision on the particles are also no longer considered for the computation of observables.

Obviously all conservation laws — energy, momentum and particle number — are violated in this version of the code.

Chapter 4

Fluctuations of anisotropic flow from the finite number of rescatterings

The important thing is to never stop questioning. – Albert Einstein

The following part will explain the importance of anisotropic flow fluctuations and their characterization, which is a crucial part in heavy-ion collision phenomenology. When two nuclei collide the energy deposition in the overlap region yields a highly fluctuating profile due to the random nucleon positions at the moment of the collision and the underlying quarks and gluons with their associated color fields. Taking into account the inhomogeneity of the initial density profile is crutial for the proper estimate of the eccentricity in a given harmonic [36, 59]. In our work we used a MC Glauber model (see Sec. 2.1.2) to implement the randomness in the nucleon positions. A better understanding of the density fluctuations and their mapping to the initial state can give further insight into the structure of the latter. This is of great importance, as the initial state is not directly accessible in experiments. In

experiments the anisotropic flow coefficients are measured as an average over many events with varying initial geometries. These geometry fluctuations will also lead to a fluctuation in the final state anisotropic flow signal, which can be studied for a given initial state model [60]. This sort of flow fluctuations was extensively studied in experiments [61–64] as well as in theoretical studies [39, 65–74].

Most of these phenomenological studies use relativistic hydrodynamics, which is very successful in describing the bulk observables, especially anisotropic flow, for the main stage in the time evolution of the system [75]. Performing a study of fluctuation propagation one might argue that using relativistic hydrodynamics might be too deterministic for such an investigation. If there is an underlying microscopic particle based description the hydrodynamic regime corresponds to the limit where the particles undergo many scatterings. In this sense deterministic hydrodynamics does not capture the effects caused by a finite number of rescatterings per particle, which might be small in systems with small nuclei, where anisotropic flow and its fluctuations are well established [76].

Here we will study these anisotropic flow fluctuations about their mean value at the corresponding eccentricity for several scattering cross sections, i.e., different number of rescatterings $N_{\text{resc.}}$ in the system. Additionally, we will investigate the evolution of distributions of the second and third participant plane in the initial geometry as a function of the number of rescatterings in the system.

Section 4.1 will give a short overview over the setup used for this study. In Sec. 4.2 we will describe flow fluctuations using the Elliptic-Power law. Furthermore, we will discuss the disadvantages of this approach which leads to an alternative description using conditional probabilities introduced in Sec. 4.3. This conditional probability approach and the event-plane angle distributions discussed in Sec. 4.4 are based on Ref. [77]:

- *Fluctuations of anisotropic flow from the finite number of rescatterings in a two-dimensional massless transport model*
  H. Roch, N. Borghini
  Eur. J. Phys. C 81 (2021) 380

In this chapter we study the v_n distribution for a given ε_n, i.e., $p_{v|\varepsilon}(v_n|\varepsilon_n)$ and its dependence on $N_{\text{resc.}}$, which extends a previous study in Ref. [78].

4.1 Setup of the simulations

The initial state lead nuclei for our simulations are generated via the MC Glauber code TGlauberMC [79]. We used a cross section of $\sigma_{NN}^{\text{inel}} = (67.6 \pm 0.6)$ mb for inelastic nucleon-nucleon collisions at $\sqrt{s_{NN}} = 5.02$ TeV. The steps in the Glauber code to create the nuclei were previously described in Sec. 2.1.2. For our study we used sets of 10^4 events, where each set is at fixed impact parameter $b = 0$, 6 or 9 fm fixed along the x-axis.

The nucleon positions in the transverse plane are then used to compute the local number of participants $N_{\text{part.}}(x, y)$ and the local number of binary collisions $N_{\text{coll.}}(x, y)$. Both quantitites are then used to create a density profile according to

Eq. (2.9) with $\alpha = 0.15$. The overall scale factor was chosen such that the hot spots have a temperature of about 800 MeV. As this density would be of a histogram shape with sharp towers, we smear it with a Gaussian distribution with a width of

$$R_{\mathrm{N}} = \frac{1}{2}\sqrt{\frac{\sigma_{\mathrm{NN}}^{\mathrm{inel}}}{\pi}}, \tag{4.1}$$

where $R_{\mathrm{N}} \approx 0.7$ fm for our system.[1]

The next step after the creation of the initial energy density profile is the "particlization", which is needed for the transport algorithm. Therefore the particle density $n(x, y)$ is computed according to the formula for a two-dimensional ideal gas of massless particles in thermal equilibrium without a fugacity. From the particle density the positions of the particles are sampled using an acceptance-rejection algorithm. For the simulations we used $N_{\mathrm{p}} = 5 \times 10^5$ test particles for each event. Trying to implement local energy conservation most accurately and at the same time reducing the computational costs, we coarse grained the grid of the particle density from 0.01 fm used for the computation of the energy density profile to a grid with 0.1 fm spacing. By this procedure it is less likely to have cells with sizable energy but no particle sampled in them, while having not too large values of N_{p}.

For the transport algorithm an initial condition in momentum space is needed as well. The particle momenta are created in such a way that the energy content in each cell is evenly distributed to the test particles inside that cell. Afterwards the particle momenta are rotated randomly in the transverse plane to obtain an isotropic initial condition in momentum space. As the code can only deal with a finite test particle number, the initial momentum distribution cannot be isotropic within one single event. However, we ensure the absence of a global momentum event by event, i.e., a vanishing v_1. Anisotropies of higher harmonics of the order $N_{\mathrm{p}}^{-1/2}$ are unavoidable. This is discussed in more detail in Sec. 4.3.2.

As pointed out above, we want to study the distribution $p_{v|\varepsilon}(v_n|\varepsilon_n)$ as a function of $N_{\mathrm{resc.}}$. Therefore it would be the preferred solution to use a fixed geometry instead of fluctuating geometries event-by-event. There are two reasons why we did not perform such simulations: First, we tried to use "more simplistic" initial conditions in the sense of distorted Gaussians used in Ref. [80, 81]. These profiles led to a v_2 response with a $\mathcal{K}_{2,222} < 0$ in Eq. (4.12), while this response is positive with more realistic initial conditions [66] (see also Tab. C.4). A problem with using a few "realistic" initial profiles generated from the Monte Carlo Glauber code in the transport simulations might be the risk that the chosen initial density distributions are special ones, which do not lead to the general behavior. As the overall results which we find are consistent over the whole eccentricity range we probe with the fixed-impact parameter events, we can claim that the approach is valid.

All simulation results presented in this chapter are performed with the transport algorithm described in Secs. 3.4.2-3.4.5. For the simulations used for the results in this chapter we used a dilution parameter, defined in Eq. 3.23, which fulfills $D \lesssim 0.1$. According to Ref. [56] this corresponds to the dilute regime which preserves covariance and locality in the transport algorithm.

[1] This length R_{N} is the same as used in the Glauber model to decide if a collision between nucleons happens (see Eq. (2.8)).

To decrease the noise of the anisotropic flow signals we perform $N_{\text{iter.}} = 10$ samplings from one initial energy-density profile, which is then evolved. The flow coefficients are then averaged over the $N_{\text{iter.}}$ iterations after their independent evolution.[2] This gives us according to

$$\delta v_n = \frac{1}{\sqrt{N_{\text{iter.}} \cdot N_{\text{p}}}} \tag{4.2}$$

an uncertainty on v_n of the order $\delta v_n \simeq 4.5 \times 10^{-4}$. The uncertainty is actually a factor $\sqrt{2}$ smaller according to Ref. [15].

The following results are based on 10^4 Monte Carlo energy-density distributions at impact parameter $b = 0, 6$ and 9 fm. Each of these initial conditions is evolved in time using the transport algorithm three times with different cross sections σ_{tot}.

We use the Knudsen number (Eq. (3.24)) to characterize the simulations with different cross sections. Therefore we need the characteristic length scale R of the system. Here, we use the root mean square radius of the initial energy-density distribution. This gives us a characteristic system size varying from event to event, as well as the mean free path varies. Finally we obtain a Knudsen number which is fluctuating about a mean value $\langle \text{Kn} \rangle$ for each cross section. The relative fluctuation of the Knudsen number about its mean value is less than 5%, thus it is ignored in the following and we only use the mean value.[3]

As already mentioned in Sec. 3.4.3, the inverse Knudsen number is related to the average number of rescatterings per particle $\langle N_{\text{resc.}} \rangle$ by the linear relation

$$\langle N_{\text{resc.}} \rangle \simeq 0.866 \langle \text{Kn} \rangle^{-1}, \tag{4.3}$$

where we averaged over events with a fixed impact-parameter value. The relation is illustrated in Fig. 4.1.

The value of $\langle N_{\text{resc.}} \rangle$ depends on the lifetime of the system. Our time evolution was performed until 15 fm/c for all cross sections and impact parameters. We checked that the results for the flow coefficients are not affected when using longer lifetimes. This would only lead to a slightly larger coefficient in Eq. (4.3), as the particles have more time to interact. However, the system becomes very dilute at late times which supresses the probability for interactions heavily.

The three different cross sections we use correspond to different anisotropic flow regimes, which is illustrated in Fig. 4.2 for v_2 and v_3 divided by ε_2 resp. ε_3 as a function of $\langle \text{Kn} \rangle^{-1}$ for the three different impact parameters.

We also show two fit curves defined as follows: A fit function for v_2/ε_2 is given by [82]

$$v_2 = \frac{v_2^{\text{hydro}}}{1 + A_2 \text{Kn}}. \tag{4.4}$$

In Ref. [56] it was checked that this function describes v_2 as a function reasonably while keeping the dilution parameter fixed. In our case the dilution parameter

[2] This is computationally cheaper than simulating one event with $N_{\text{iter.}} \cdot N_{\text{p}}$ test particles, as the simulation time grows with $N_{\text{p}}^{3/2}$.

[3] The value of $\langle \text{Kn} \rangle$ depends on the impact parameter of the collision.

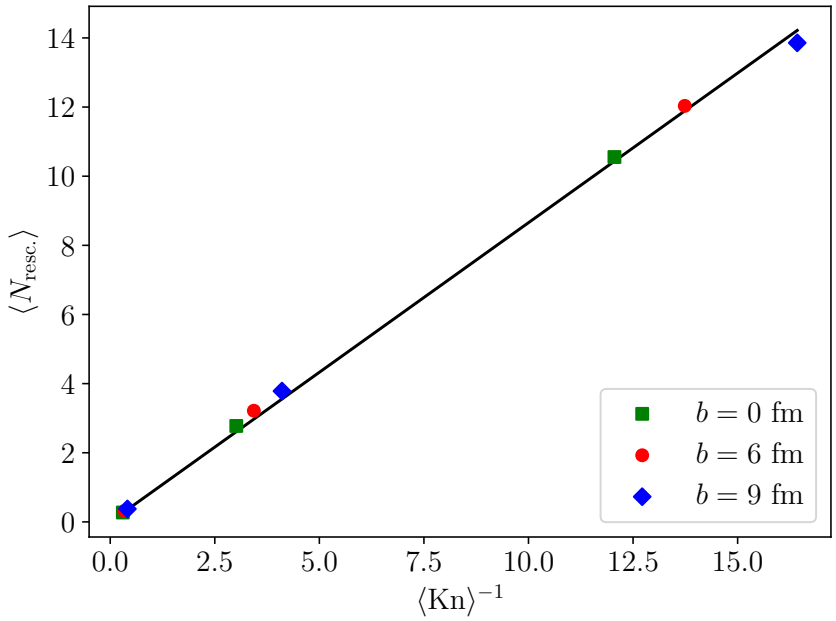

Figure 4.1: The average number of rescatterings per particle $\langle N_{\text{resc.}} \rangle$ vs. the inverse mean Knudsen number $\langle \text{Kn} \rangle^{-1}$ for simulations at $b = 0, 6, 9$ fm and with three different cross sections. The black line is the linear fit (4.3).

depends on the Knudsen number but it varies in a range, where the v_2 value is not affected. We find $v_2^{\text{hydro}}/\varepsilon_2 = 0.2621$ and $A_2 = 1.1967$ in the fit. The behavior of v_3 depending on the Knudsen number is given by a higher-order Padé approximant [83]

$$v_3 = \frac{v_3^{\text{hydro}}(1 + B_3 \text{Kn})}{1 + (A_3 + B_3)\text{Kn} + C_3 \text{Kn}^2}. \tag{4.5}$$

We obtain the parameters $v_3^{\text{hydro}}/\varepsilon_3 = 0.2096$, $A_3 = 0.6973$, $B_3 = 1.7922$, and $C_3 = 13.945$ from the fit used in Fig. 4.2.

Fig. 4.2 visualizes the three different flow regimes. Looking at the largest number of rescatterings, the hydrodynamic values are almost reached. The second simulation with the middle average Knudsen number are in the intermediate flow regime and the third simulation at large $\langle \text{Kn} \rangle$ is the few-collisions regime. We find that triangular flow v_3 needs more rescatterings per particle than elliptic flow v_2 to develop [83, 84] and it has a steeper rise with increasing $\langle N_{\text{resc.}} \rangle$. Notice, that for the intermediate cross section the values for the triangular flow are further away from the hydrodynamic limit than those of the elliptic flow and that for the largest $\langle \text{Kn} \rangle$ its values are at the subpercent level, corresponding to the far-from-equilibrium regime.

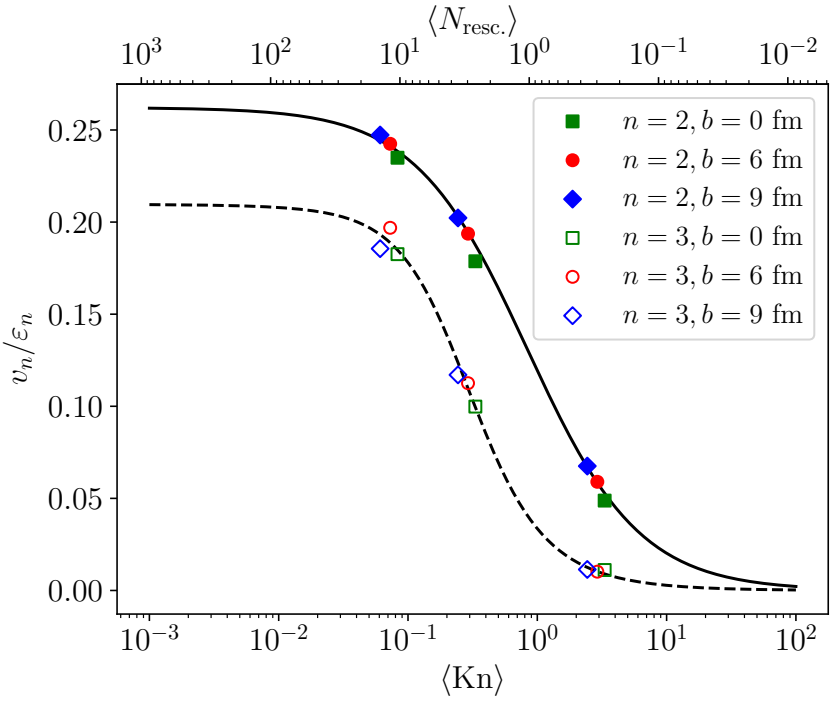

Figure 4.2: Anisotropic flow v_n with $n = 2, 3$ divided by the corresponding initial state eccentricity as a function of the average Knudsen number for three different cross sections. The curves are fits with Eq. (4.4) (full curve) resp. (4.5) (dashed curve).

4.2 Elliptic-Power law

Historically the Elliptic-Power law is an improvement of the previously used Bessel-Gaussian distribution [85]

$$p(\varepsilon_n) = \frac{2\varepsilon_n}{\sigma^2} I_0\left(\frac{\varepsilon_n \varepsilon_0}{\sigma^2}\right) \exp\left(-\frac{\varepsilon_n^2 + \varepsilon_0^2}{\sigma^2}\right), \tag{4.6}$$

where ε_0 is the mean eccentricity in the reaction-plane, σ is the magnitude of anisotropies around ε_0 and I_0 is the modified Bessel function of first kind. Note, that for $\varepsilon_0 = 0$ this distribution reduces to a Gaussian distribution. This is the case if the ansiotropy is only caused by fluctuations.

The Elliptic-Power distribution was first introduced in Ref. [86] as

$$\begin{aligned} p(\varepsilon_n) &= \frac{2\alpha\varepsilon_n}{\pi}\left(1-\varepsilon_0^2\right)^{\alpha+\frac{1}{2}} \int_0^\pi \mathrm{d}\phi \, \frac{\left(1-\varepsilon_n^2\right)^{\alpha-1}}{\left(1-\varepsilon_0\varepsilon_n\cos\phi\right)^{2\alpha+1}} \\ &= 2\varepsilon_n\alpha\left(1-\varepsilon_n^2\right)^{\alpha-1}\left(1-\varepsilon_n\varepsilon_0\right)^{-1-2\alpha}\left(1-\varepsilon_0^2\right)^{\alpha+\frac{1}{2}} \\ &\quad \times {}_2F_1\left(\frac{1}{2}, 1+2\alpha; 1; \frac{2\varepsilon_n\varepsilon_0}{\varepsilon_n\varepsilon_0 - 1}\right) \end{aligned} \tag{4.7}$$

to describe the initial state eccentricity distribution at fixed centrality or impact parameter. It is a two parameter distribution on the compact interval $[0, 1]$, where

the parameter α characterizes the fluctuations and ε_0 has the same interpretation as for the Bessel-Gaussian distribution. The function ${}_2F_1$ is the hypergeometric function. This distribution fits the eccentricity distributions also for larger centralities or impact parameters, whereas the Bessel-Gaussian distribution does not work in this regime.

For anisotropies only due to fluctuations, i.e., for ultra-central collisions, the two-parameter distribution from Eq. (4.7) reduces to the one-parameter Kumaraswamy distribution

$$p(\varepsilon_n) = 2\alpha\varepsilon_n \left(1 - \varepsilon_n^2\right)^{\alpha-1}, \tag{4.8}$$

which is closely related to the Beta distribution.

We show the probability distributions of the eccentricities calculated from 10^4 energy density distributions created from the MC Glauber model described in Sec. 2.2 within Fig. 4.3. The fits are then performed using the Bessel-Gaussian distribution from Eq. (4.6), the Elliptic-Power law from Eq. (4.7) or the Power law from Eq. (4.8). Here the Elliptic-Power law was only used when necessary, i.e., when

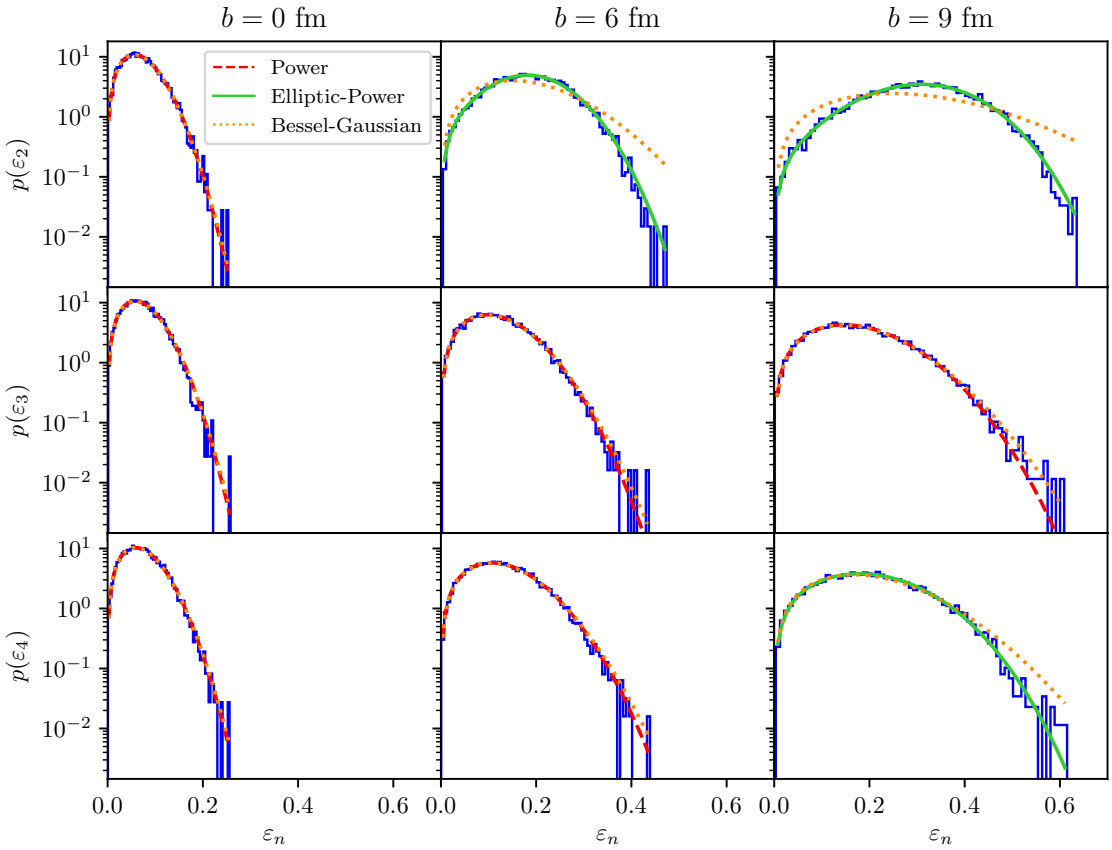

Figure 4.3: Probability distributions of initial state eccentricities ε_2 (top), ε_3 (middle), ε_4 (bottom) for three different impact parameters $b = 0$ fm (left), $b = 6$ fm (center) and $b = 9$ fm (right). The fits are performed using a Bessel-Gaussian distribution Eq. (4.6) (orange), an Elliptic-Power law Eq. (4.7) (green) or a Power law Eq. (4.8) (red).

$\varepsilon_0 \approx 0$ is not a good assumption. This is especially the case for the distributions

of ε_2 and ε_4 at large impact parameters. For ε_3 the assumption $\varepsilon_0 = 0$ is valid for all impact parameters, as the triangularity is purely due to fluctuations of the nucleon positions in the initial state, which are small compared to the effect of the overall geometry. From Fig. 4.3 we can reproduce the finding in Ref. [86] that the Bessel-Gaussian fails to describe the distributions at larger impact parameters.

Tab. 4.1 shows the corresponding fit parameters for the curves shown in Fig. 4.3. In the cases where $\varepsilon_0 = 0$ is written the fit value of the parameter was a very small number with a large uncertainty given by the fit routine. Nevertheless, it is visible by eye, that the (Elliptic-)Power law describes the distributions better. By the increase in the parameter α with increasing impact parameter we can see that for all ε_n the distributions become wider.

Table 4.1: Fit parameters for the eccentricity distributions in Fig. 4.3. If $\varepsilon_0 = 0$ is written, the value is basically vanishing but numerically the fit error becomes large.

Bessel-Gaussian	$b = 0$ fm	$b = 6$ fm	$b = 9$ fm
$p(\varepsilon_2)$	$\sigma = 0.0561 \pm 0.0004$ $\varepsilon_0 = 0$	$\sigma = 0.151 \pm 0.004$ $\varepsilon_0 = 0$	$\sigma = 0.248 \pm 0.010$ $\varepsilon_0 = 0$
$p(\varepsilon_3)$	$\sigma = 0.0576 \pm 0.0004$ $\varepsilon_0 = 0$	$\sigma = 0.0968 \pm 0.0007$ $\varepsilon_0 = 0$	$\sigma = 0.1435 \pm 0.0009$ $\varepsilon_0 = 0$
$p(\varepsilon_4)$	$\sigma = 0.0588 \pm 0.0004$ $\varepsilon_0 = 0$	$\sigma = 0.1054 \pm 0.0006$ $\varepsilon_0 = 0$	$\sigma = 0.166 \pm 0.002$ $\varepsilon_0 = 0$
Elliptic-Power / Power	$b = 0$ fm	$b = 6$ fm	$b = 9$ fm
$p(\varepsilon_2)$	$\alpha = 159 \pm 2$	$\alpha = 62 \pm 2$ $\varepsilon_0 = 0.159 \pm 0.002$	$\alpha = 28.1 \pm 0.7$ $\varepsilon_0 = 0.274 \pm 0.002$
$p(\varepsilon_3)$	$\alpha = 150 \pm 2$	$\alpha = 52.9 \pm 0.7$	$\alpha = 23.9 \pm 0.3$
$p(\varepsilon_4)$	$\alpha = 144 \pm 2$	$\alpha = 44.6 \pm 0.5$	$\alpha = 27 \pm 2$ $\varepsilon_0 = 0.131 \pm 0.006$

We consider the relation between initial state eccentricity ε_n and anisotropic flow v_n as linear, i.e., $v_n = \mathcal{K}_{n,n}\varepsilon_n$ for the moment. Then the relation between the probability distributions of these quantities is given by [60]

$$p(v_n) = \frac{1}{\mathcal{K}_{n,n}} p\left(\frac{v_n}{\mathcal{K}_{n,n}}\right), \tag{4.9}$$

with the Jacobian $\mathrm{d}\varepsilon_n/\mathrm{d}v_n = 1/\mathcal{K}_{n,n}$. This rescaling gives the possibility to relate the fluctuations in the final state to the ones in the initial state eccentricities by a simple rescaling.

Indeed, the harmonics with $n = 2, 3$ obey a linear relation [36, 37, 39, 65, 87–89]:

$$v_2 \simeq \mathcal{K}_{2,2}\varepsilon_2, \tag{4.10}$$

$$v_3 \simeq \mathcal{K}_{3,3}\varepsilon_3, \tag{4.11}$$

while in periperal collisions, which have large ε_2, there is also a cubic contribution in v_2 [66]:

$$v_2 \simeq \mathcal{K}_{2,2}\varepsilon_2 + \mathcal{K}_{2,222}\varepsilon_2^3. \tag{4.12}$$

These scalings have been confirmed in various model studies in the references above, which use either hydrodynamics (ideal or dissipative) or transport approaches.

Using again our set of events from above and evolving them in time with the transport algorithm, we obtain the distributions shown Fig. 4.4. For the transport simulations the afore mentioned three different cross sections were used to see the effect on the final state anisotropic flow probability distributions. We see that the distributions become broader if there are more rescatterings during the evolution of the system.

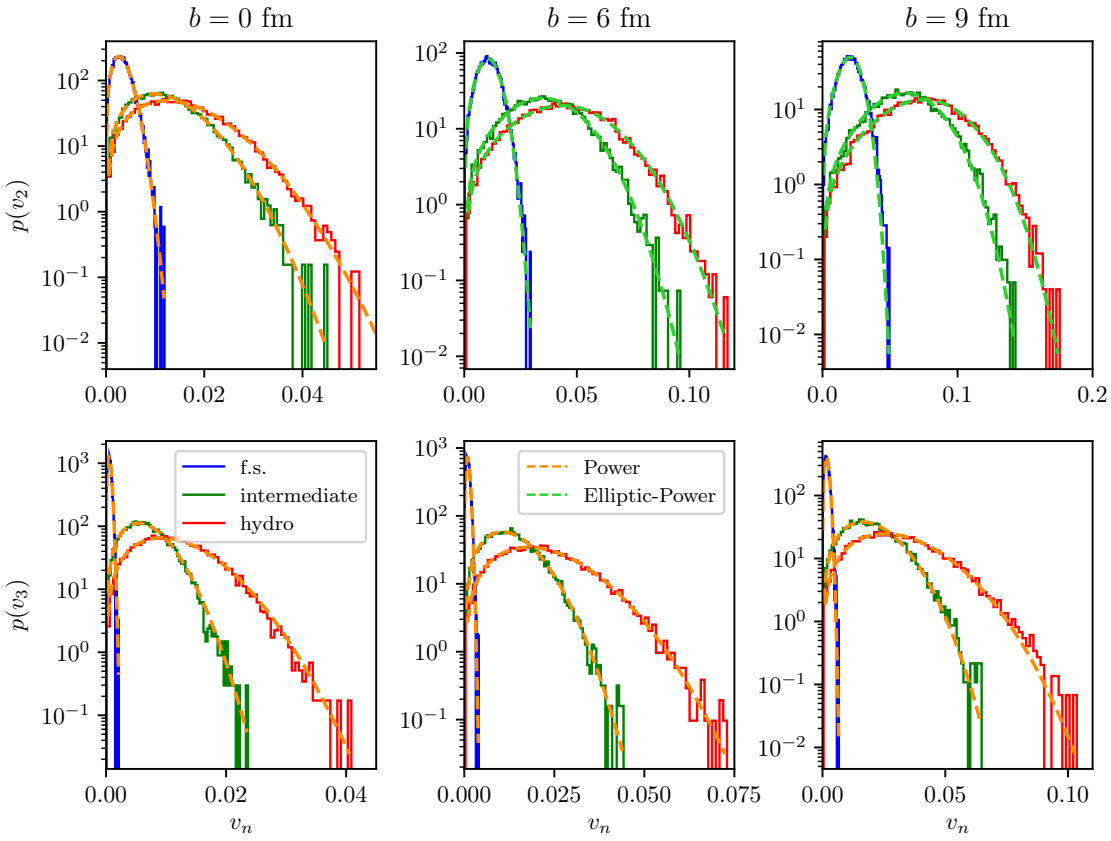

Figure 4.4: Probability distributions of final state flow coefficients v_2 (top), v_3 (bottom) for three different impact parameters $b = 0$ fm (left), $b = 6$ fm (center) and $b = 9$ fm (right) for three different inverse Knudsen numbers in the free-streaming limit, the intermediate regime and in the hydrodynamical limit. The fits are performed using an Elliptic-Power law Eq. (4.7) (green) or a Power law Eq. (4.8) (orange).

Turning now to the more quantitative description of the distributions in Fig. 4.4 using a fit with Eqs. (4.10) and (4.11) for the $v_n(\varepsilon_n)$ data, the response coefficients $\mathcal{K}_{n,n}$ are given in Tab. 4.2. There, we see that the α value from the (Elliptic-)Power law fit is essentially constant for a fixed impact parameter and that the information about the collisions is entirely encoded in the response coefficients, which increase with $\langle N_{\text{resc.}} \rangle$. Additionally, the values for α and ε_0 (if present) are similar to the ones from the initial state eccentricity distributions (see Tab. 4.1).

The relations for flow harmonics with $n \geq 4$ start to mix different eccentricities. In the case of quadrangular flow there is a linear scaling with ε_4 and a quadratic

Table 4.2: Fit parameters for the anisotropic flow coefficient distributions in Fig. 4.4. If ε_0 is not written Eq. (4.8) is used, otherwise Eq. (4.7). For the response coefficients $\mathcal{K}_{2,2}$ and $\mathcal{K}_{3,3}$ defined in Eqs. (4.10) and (4.11) were used respectively.

Elliptic-Power / Power	$b = 0$ fm	$b = 6$ fm	$b = 9$ fm
$p(v_2)$, $\langle N_{\text{resc.}} \rangle$ small	$\alpha = 155 \pm 2$ $\mathcal{K}_{2,2} = 0.04606 \pm 0.00008$	$\alpha = 60 \pm 2$ $\varepsilon_0 = 0.157 \pm 0.002$ $\mathcal{K}_{2,2} = 0.05873 \pm 0.00005$	$\alpha = 26.1 \pm 0.6$ $\varepsilon_0 = 0.262 \pm 0.002$ $\mathcal{K}_{2,2} = 0.06792 \pm 0.00005$
$p(v_2)$, $\langle N_{\text{resc.}} \rangle$ intermediate	$\alpha = 156 \pm 2$ $\mathcal{K}_{2,2} = 0.1722 \pm 0.0003$	$\alpha = 60 \pm 2$ $\varepsilon_0 = 0.157 \pm 0.002$ $\mathcal{K}_{2,2} = 0.1933 \pm 0.0002$	$\alpha = 26.1 \pm 0.7$ $\varepsilon_0 = 0.265 \pm 0.002$ $\mathcal{K}_{2,2} = 0.2034 \pm 0.0002$
$p(v_2)$, $\langle N_{\text{resc.}} \rangle$ large	$\alpha = 154 \pm 2$ $\mathcal{K}_{2,2} = 0.2165 \pm 0.0004$	$\alpha = 59 \pm 2$ $\varepsilon_0 = 0.158 \pm 0.002$ $\mathcal{K}_{2,2} = 0.2405 \pm 0.0003$	$\alpha = 25.9 \pm 0.6$ $\varepsilon_0 = 0.266 \pm 0.002$ $\mathcal{K}_{2,2} = 0.2477 \pm 0.0002$
$p(v_3)$, $\langle N_{\text{resc.}} \rangle$ small	$\alpha = 156 \pm 2$ $\mathcal{K}_{3,3} = 0.1722 \pm 0.0003$	$\alpha = 48.9 \pm 0.7$ $\mathcal{K}_{3,3} = 0.00835 \pm 0.00003$	$\alpha = 22.7 \pm 0.4$ $\mathcal{K}_{3,3} = 0.01005 \pm 0.00003$
$p(v_3)$, $\langle N_{\text{resc.}} \rangle$ intermediate	$\alpha = 148 \pm 2$ $\mathcal{K}_{3,3} = 0.0933 \pm 0.0002$	$\alpha = 52.2 \pm 0.7$ $\mathcal{K}_{3,3} = 0.1075 \pm 0.0002$	$\alpha = 23.4 \pm 0.4$ $\mathcal{K}_{3,3} = 0.1110 \pm 0.0002$
$p(v_3)$, $\langle N_{\text{resc.}} \rangle$ large	$\alpha = 141 \pm 2$ $\mathcal{K}_{3,3} = 0.1556 \pm 0.0005$	$\alpha = 51.5 \pm 0.6$ $\mathcal{K}_{3,3} = 0.1800 \pm 0.0004$	$\alpha = 23.3 \pm 0.3$ $\mathcal{K}_{3,3} = 0.1713 \pm 0.0004$

contribution of ε_2 [38, 65, 90–92]:

$$v_4 \simeq \mathcal{K}_{4,4}\varepsilon_4 + \mathcal{K}_{4,22}\varepsilon_2^2, \tag{4.13}$$

while for pentagonal flow v_5 there is a linear ε_5 contribution and a nonlinear contribution from the second and third harmonic [38, 91, 92]:

$$v_5 \simeq \mathcal{K}_{5,5}\varepsilon_5 + \mathcal{K}_{5,23}\varepsilon_2\varepsilon_3. \tag{4.14}$$

For v_4 and v_5 the linear part is only visible for the most central collisions [39]. Otherwise the nonlinear contribution dominates. In the latter two cases the simple rescaling law from Eq. (4.9) is not applicable, at least not if the nonlinear contributions dominate.

4.3 Conditional probabilities

To circumvent problems with non-linearities and mixtures of different eccentricities in the ansatz presented above, we will have a look at conditional probability distributions in the following.

4.3.1 Quantification of flow fluctuations

Within the theoretical description of a heavy-ion collision we have access to the symmetry plane orientation Φ_n in the initial state with respect to the impact parameter direction. For the final state we can also compute the anisotropic flow coefficients v_n, as well as their corresponding symmetry plane angles Ψ_n for each event. To make use of the inforamtion about the symmetry plane orientation, we look at the

cosine and sine parts of the flow coefficients separately:

$$v_{n,\mathrm{c}} \equiv \langle \cos(n\varphi) \rangle_{\mathbf{p}}, \tag{4.15}$$

$$v_{n,\mathrm{s}} \equiv \langle \sin(n\varphi) \rangle_{\mathbf{p}}, \tag{4.16}$$

where $\langle \dots \rangle_{\mathbf{p}}$ denotes a particle average. From the knowledge about $v_{n,\mathrm{c}}$ and $v_{n,\mathrm{s}}$ we can finally calculate Ψ_n.

For a self-consistent description we will also characterize the initial state by the cosine and sine part of the eccentricity:

$$\varepsilon_{n,\mathrm{c}} \equiv -\frac{\langle r^n \cos(n\theta) \rangle_{\mathbf{x}}}{\langle r^n \rangle_{\mathbf{x}}}, \tag{4.17}$$

$$\varepsilon_{n,\mathrm{s}} \equiv -\frac{\langle r^n \sin(n\theta) \rangle_{\mathbf{x}}}{\langle r^n \rangle_{\mathbf{x}}}, \tag{4.18}$$

where now $\langle \dots \rangle_{\mathbf{x}}$ denotes an average over the initial state energy density. In contrast to the eccentricities $\varepsilon_n^{\mathbf{x}}$ defined in Eq. (2.25), the values of $\varepsilon_{n,\mathrm{c}}$ and $\varepsilon_{n,\mathrm{s}}$ can become negative.

The reason why we investigate the cosine and sine parts of the flow coefficients separately is that their geometric origins are mainly uncorrelated. This is illustrated in Fig. 4.5 for $v_{2,\mathrm{s}}$ and $\varepsilon_{2,\mathrm{c}}$ for 10^4 events at $b = 6$ fm and the largest cross section used for our simulations. Our fluctuation analysis considers harmonics with $n = 2$

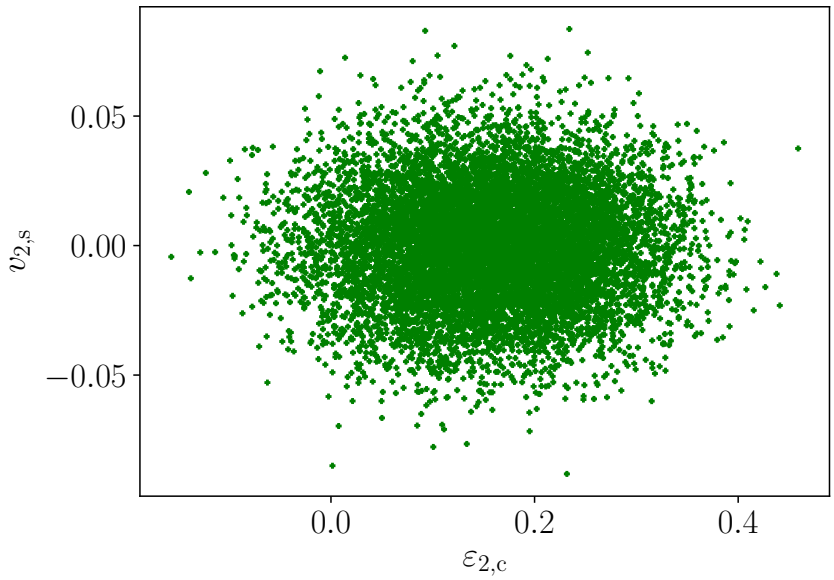

Figure 4.5: The scatter plot shows the final state $v_{2,\mathrm{s}}$ vs. initial state $\varepsilon_{2,\mathrm{c}}$ at impact parameter $b = 6$ fm with $\langle \mathrm{Kn} \rangle^{-1} = 13.74$ for 10^4 events.

and 3. This leads to four independent initial state quantities and the same amount of final state quantities which we can study as a function of $\langle \mathrm{Kn} \rangle^{-1}$. Notice, that the cosine and sine parts of the flow coefficients are not measured in experiments and experiments cannot select a fixed impact parameter. However, as our model lives in purely two dimensions, it is not possible to perform quantitative phenomenological studies.

For our studies we fix an impact parameter and initialize 10^4 initial energy density profiles, for which we compute the eccentricities $\varepsilon_{n,\mathrm{c/s}}$. From each energy density distribution we sample $N_{\mathrm{iter.}} = 10$ particle distributions which we evolve according to the transport algorithm described in Sec. 3.4.2. At the end of the time evolution we obtain the flow coefficients $v_{n,\mathrm{c/s}}$ averaged over the $N_{\mathrm{iter.}}$ realizations of the particlization and evolution in the transport algorithm. This gives us 10^4 events with four initial state and four final state quantities which we can correlate and investigate as a function of $\langle \mathrm{Kn} \rangle^{-1}$.

In our analysis we remove the 50 events with the smallest and 50 events with the largest eccentricities which we denote as outliers. The purpose of this is to obtain eccentricity bins which are not too wide, as we are interested in conditional probabilities at the end.[4] All other events are divided into five eccentricity bins with 2000 events each. Except for the first and last bins, wich contain 1950 events. In Fig. 4.6 we illustrate this procedure for $v_{2,\mathrm{c}}$ as a function of $\varepsilon_{2,\mathrm{c}}$ at $b = 6$ fm for two different values of $\langle \mathrm{Kn} \rangle^{-1}$ and indicate the bins by different colors. The outliers are indicated by the gray points. In the next step we use a linear or a linear + cubic

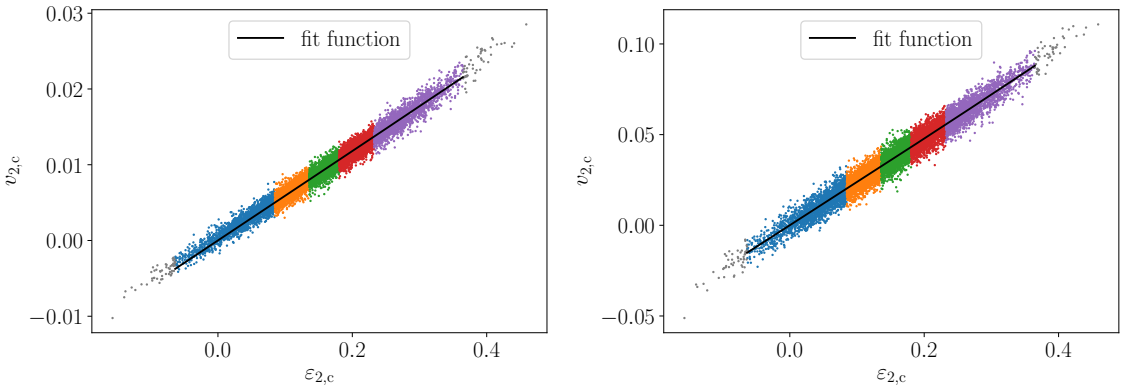

Figure 4.6: The scatter plot shows the final state $v_{2,\mathrm{c}}$ vs. initial state $\varepsilon_{2,\mathrm{c}}$ at impact parameter $b = 6$ fm with $\langle \mathrm{Kn} \rangle^{-1} = 0.34$ (left) and $\langle \mathrm{Kn} \rangle^{-1} = 13.74$ (right). The gray points indicate the removed events and the other colors indicate the five eccentricity bins. The black curves are fits with Eq. (4.12).

dependence to fit the events globally (Eqs. (4.10)-(4.12)). We denote the fit function by $\bar{v}_{n,\mathrm{c/s}}(\varepsilon_{n,\mathrm{c/s}})$. For the fit the use of Eq. (4.12) is only relevant for the simulations with impact parameter $b = 6$ and 9 fm. Looking at the width of the distributions in Fig. 4.6 we can already see that the distribution on the right, which is the one with more rescatterings, is broader. This observation is also true for the other flow harmonics. As we want to quantify this observation, we compute the moments of the distribution about the global fit. Denoting by $v_{n,\mathrm{c/s}}(\varepsilon_{n,\mathrm{c/s}})$ the $v_{n,\mathrm{c/s}}$ for a given $\varepsilon_{n,\mathrm{c/s}}$, we can compute powers of $v_{n,\mathrm{c/s}}(\varepsilon_{n,\mathrm{c/s}}) - \bar{v}_{n,\mathrm{c/s}}(\varepsilon_{n,\mathrm{c/s}})$. In the case of an infinite number of events this is equivalent to a computation of moments of the conditional probability distribution $p_{v|\varepsilon}(v_{n,\mathrm{c/s}}|\varepsilon_{n,\mathrm{c/s}})$ about the fit function. Due to the limited statistics, we can only approach the statistical behavior by introducing the bins with a finite width in $\varepsilon_{n,\mathrm{c/s}}$. If we would gather all points in a single bin this could in

[4] In our analysis we also checked that the removal of the outliers does not change our results.

principle lead to a situation where opposite behaviors are averaged out. This will become important later.

It is also not possible to estimate the conditional probability distribution directly via the right hand side of

$$p_{v|\varepsilon}(v_{n,\mathrm{c/s}}|\varepsilon_{n,\mathrm{c/s}}) = \frac{p_v(v_{n,\mathrm{c/s}})}{p_\varepsilon(\varepsilon_{n,\mathrm{c/s}})}, \tag{4.19}$$

as the individual probability distributions for $v_{n,\mathrm{c/s}}$ and $\varepsilon_{n,\mathrm{c/s}}$ have very small numbers at the tails. This can be seen also in Figs. 4.3 and 4.4, where the probability distributions of the absolute values of v_n and ε_n are shown.

We will now introduce the moments which we use for the characterization of the conditional probability distribution. For the sake of brevity we omit the indices c/s. The first moment about the fit function is given by

$$\mu = \frac{1}{N}\sum_{i=1}^{N}\left[v_{n,i}(\varepsilon_{n,i}) - \bar{v}_{n,i}(\varepsilon_{n,i})\right], \tag{4.20}$$

with i running over the N events in an eccentricity bin. In the following we will not mention the values of μ, which has always some small value of the order 10^{-5}, as the average over bins will vanish by construction of the fit function.

The second moment about the fit function is

$$\sigma_v^2 = \frac{1}{N}\sum_{i=1}^{N}\left[v_{n,i}(\varepsilon_{n,i}) - \bar{v}_{n,i}(\varepsilon_{n,i})\right]^2. \tag{4.21}$$

It almost coincides with the variance about the true average in a given bin and it has a dependence on the inverse mean Knudsen number. This dependence is due to the growth of the absolute value of v_n with $\langle \mathrm{Kn}\rangle^{-1}$. To compensate this growth we give the values σ_v^2 and divide them by the square of the linear coefficient in the fit function $\mathcal{K}_{2,2}^2$.

The third moment about the fit function is the skewness

$$\gamma_1 = \frac{1}{N}\sum_{i=1}^{N}\frac{\left[v_{n,i}(\varepsilon_{n,i}) - \bar{v}_{n,i}(\varepsilon_{n,i})\right]^3}{\sigma_v^3}. \tag{4.22}$$

γ_1 can be positive or negative. This is why we do not analyze the events in a single eccentricity bin.

The last moment about the fit function we consider is the (excess) kurtosis

$$\gamma_2 = \frac{1}{N}\sum_{i=1}^{N}\frac{\left[v_{n,i}(\varepsilon_{n,i}) - \bar{v}_{n,i}(\varepsilon_{n,i})\right]^4}{\sigma_v^4} - 3. \tag{4.23}$$

By studying up to the fourth moment we go beyond the study performed in Ref. [78] which assumed Gaussian fluctuations and only considered the variance of $p_{v|\varepsilon}(v_2|\varepsilon_2)$.

To obtain uncertainty estimates for our moments we calculate the variance $\sigma_{\mathcal{M}}^2$ of a given moment $\mathcal{M}$. For the computation of the variance we use a delete-d Jackknife algorithm with random sampling which is described in Appendix G.3. We deleted

ten percent of the bin data and calculated the variance of the moments for 3000 of these random samples.

Finally, we computed the average of the moments over the eccentricity bins. In the case of the skewness γ_1 we used its absolute value. For this average we used a weighted average to give less weight to the bins with larger uncertainties. We compute the weighted bin average $\langle \mathcal{M} \rangle$ and its corresponding variance $\sigma^2_{\mathcal{M}}$ by

$$\langle \mathcal{M} \rangle = \frac{\sum_j \mathcal{M}_j / \sigma^2_{\mathcal{M},j}}{\sum_j 1/\sigma^2_{\mathcal{M},j}}, \tag{4.24}$$

$$\sigma^2_{\mathcal{M}} = \frac{N_{\text{bins}}}{\sum_j 1/\sigma^2_{\mathcal{M},j}}, \tag{4.25}$$

where j runs over the N_{bins}, $\mathcal{M}_j$ is the moment in bin j and $\sigma^2_{\mathcal{M},j}$ the variance of the moment in the given bin.

4.3.2 Anisotropic flow in the initial state

In this subsection we want to investigate the anisotropic flow fluctuations in the initial state of the transport simulations. These are caused by the finite number of testparticles N_{p} in each event which causes some anisotropic flow. The fluctuations of $v_{n,\text{c/s}}$ about 0 can be estimated by $1/\sqrt{2N_{\text{p}}} = 10^{-3}$ [15] for $n > 1$ and $N_{\text{p}} = 5 \cdot 10^5$ testparticles in our simulations. The case $n = 1$ can not be estimated with the given relation, as we subtract the total momentum from each particle's momentum in the initial state. These fluctuations should be Gaussian and the event-plane angle Ψ_n should not be correlated to the participant-plane angle Φ_n.

We selected 5000 events of the 10^4 sampled initial conditions and computed $v_{n,\text{c/s}}$ in each event for $n = 2, 3$ to approximate the probability distributions of the initial state flow coefficients. Fig. 4.7 shows exemplary the probability distributions for impact parameters $b = 0$ fm. The results for the other impact parameters are presented in Appendix C.1. Similar to Sec. 4.3.1 we computed the moments of the

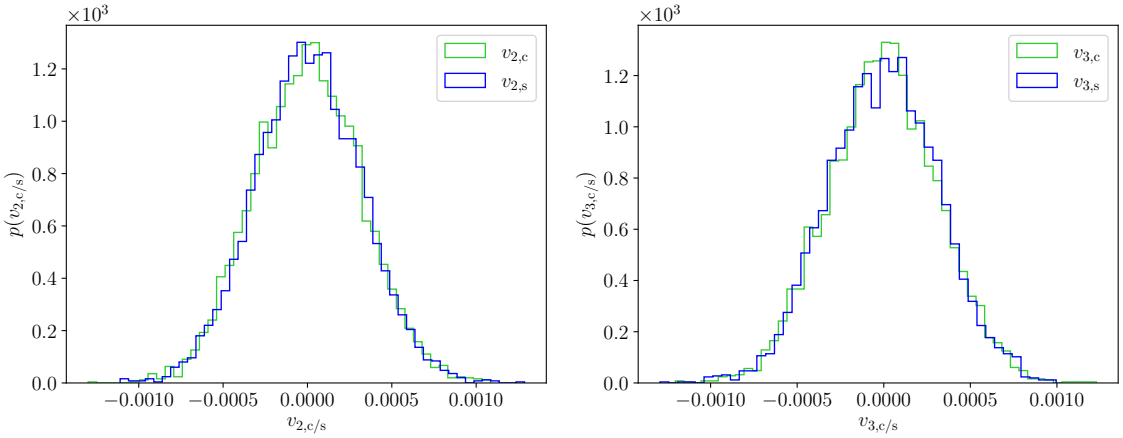

Figure 4.7: Initial state probability distributions of $v_{2,\text{c/s}}$ (left) and $v_{3,\text{c/s}}$ (right) including 5000 events at $b = 0$ fm.

distributions to characterize them and quantify their similarity mentioned above. In

contrast to the method described above, we used only one bin for all events here and we assume the averages to be zero, as they are of the order 10^{-5}, when we compute the moments. For the uncertainty estimation we use the Jackknife algorithm again and delete 500 events from each set repeating the computation 6000 times. We present the resulting values for the variance σ_v^2, absolute value of the skewness $|\gamma_1|$ and the excess kurtosis γ_2 in Table 4.3. Results for the moments of the distributions at the other impact parameters are again presented in Appendix C.1.

Table 4.3: Calculated moments from the probability distributions in Fig. 4.7 for $v_{n,\mathrm{c/s}}$ with $n = 2, 3$ at $b = 0, 6, 9$ fm including 5000 events. The variance σ_v^2 was divided by its rough estimate $1/(2N_\mathrm{p})$.

	$\sigma_v^2/(2N_\mathrm{p})^{-1}$	$\lvert\gamma_1\rvert$	γ_2
$b = 0$ fm			
$v_{2,\mathrm{c}}$	1.014 ± 0.020	0.041 ± 0.055	-0.030 ± 0.069
$v_{2,\mathrm{s}}$	0.990 ± 0.020	0.079 ± 0.057	0.063 ± 0.078
$v_{3,\mathrm{c}}$	0.996 ± 0.020	0.034 ± 0.057	0.013 ± 0.075
$v_{3,\mathrm{s}}$	0.996 ± 0.020	0.089 ± 0.055	-0.014 ± 0.073

4.3.3 Moments of the final state distribution

We will now discuss the flow harmonics in the final state and how the conditional probabilities depend on $\langle \mathrm{Kn} \rangle^{-1}$. As the global trends are similar for all impact parameters, we will only discuss the case $b = 6$ fm here and move the discussion of $b = 0, 9$ fm to Appendices C.4 and C.5. Tables 4.4-4.5 display the moments defined by Eqns. (4.20)-(4.23) for the harmonics $v_{2,\mathrm{c/s}}$ resp. $v_{3,\mathrm{c/s}}$ computed for three different cross sections, i.e. $\langle \mathrm{Kn} \rangle^{-1}$.

Table 4.4: Calculated moments of the probability distributions $p_{v|\varepsilon}(v_{2,\mathrm{c/s}}|\varepsilon_{2,\mathrm{c/s}})$ of the flow harmonics in the final state computed for 10^4 events at $b = 6$ fm. We divided the variance σ_v^2 by the linear coefficient from Eq. (4.12).

$\langle \mathrm{Kn} \rangle^{-1}$	$v_{2,\mathrm{c}}$			$v_{2,\mathrm{s}}$		
	$10^4\,\sigma_v^2/\mathcal{K}_{2,2}^2$	$\lvert\gamma_1\rvert$	γ_2	$10^4\,\sigma_v^2/\mathcal{K}_{2,2}^2$	$\lvert\gamma_1\rvert$	γ_2
0.34	1.754 ± 0.062	0.513 ± 0.091	0.317 ± 0.141	1.593 ± 0.055	0.249 ± 0.102	0.302 ± 0.165
3.43	1.313 ± 0.046	0.281 ± 0.105	0.481 ± 0.188	1.327 ± 0.046	0.257 ± 0.100	0.287 ± 0.158
13.73	3.185 ± 0.104	0.138 ± 0.093	0.080 ± 0.135	3.150 ± 0.104	0.155 ± 0.094	0.088 ± 0.132

Table 4.5: Calculated moments of the probability distributions $p_{v|\varepsilon}(v_{3,\mathrm{c/s}}|\varepsilon_{3,\mathrm{c/s}})$ of the flow harmonics in the final state computed for 10^4 events at $b = 6$ fm. We divided the variance σ_v^2 by the linear coefficient from Eq. (4.11).

$\langle \mathrm{Kn} \rangle^{-1}$	$v_{3,\mathrm{c}}$			$v_{3,\mathrm{s}}$		
	$10^3\,\sigma_v^2/\mathcal{K}_{3,3}^2$	$\lvert\gamma_1\rvert$	γ_2	$10^3\,\sigma_v^2/\mathcal{K}_{3,3}^2$	$\lvert\gamma_1\rvert$	γ_2
0.34	1.984 ± 0.063	0.282 ± 0.086	-0.026 ± 0.109	2.480 ± 0.079	1.077 ± 0.060	0.026 ± 0.113
3.43	0.294 ± 0.010	0.183 ± 0.103	0.305 ± 0.170	0.355 ± 0.012	0.576 ± 0.098	0.428 ± 0.173
13.73	0.697 ± 0.022	0.105 ± 0.088	-0.020 ± 0.106	0.775 ± 0.025	0.258 ± 0.085	-0.017 ± 0.097

Looking at the variance in Tables 4.4-4.5, which is divided by the square of the linear coefficient $\mathcal{K}_{n,n}^2$, we observe that it is largest for the cases where $\langle \mathrm{Kn} \rangle^{-1}$ is

large. For small $\langle \mathrm{Kn} \rangle^{-1}$ the values are close to the values in the initial state reported in Sec. 4.3.2. All in all, the spread of the flow coefficients about the fit function $\bar{v}_{n,\mathrm{c/s}}$ representing the average value increases with increasing average number of rescatterings $\langle \mathrm{Kn} \rangle^{-1}$. Additionally, this growth is stronger than that of $\bar{v}_{n,\mathrm{c/s}}$ itself, as the values are divided by $\mathcal{K}^2_{n,n}$. This result confirms the visual impression that the spread of the point cloud in the right panel of Fig. 4.6 is larger than that in the left panel.

The skewness which can have either positive or negative sign is reported as absolute values $|\gamma_1|$ in the tables, but there was a clear general trend observed before averaging over eccentricity bins. Bins with a positive $\varepsilon_{n,\mathrm{c/s}}$ mostly have positive values of $v_{n,\mathrm{c/s}}$ and a negative γ_1 corresponding to a distribution with a longer tail towards the left hand side of its positive average. This means that the distribution is skewed towards 0. Within hydrodynamics this negative skewness was observed for fluctuations of v_2 in Ref. [73], but as we will discuss later for a different reason. Bins with a negative $\varepsilon_{n,\mathrm{c/s}}$ mostly have positive values of γ_1, which causes again a skewness towards 0. The trend for the absolute value of the skewness $|\gamma_1|$ in most cases is a decrease with increasing $\langle \mathrm{Kn} \rangle^{-1}$. It seems that the absolute values of the skewness approach 0 for the largest cross section studied, which would lead to a Gaussian distribution in that case. In contrast to this, the simulation with the smallest number of rescatterings leads to $|\gamma_1|$ which is far from 0 and also larger than in the initial state. Unfortunately we did not simulate with even smaller number of rescatterings, as this hints at the fact that with a smaller number of rescatterings one could obtain a $v_{n,\mathrm{c/s}}$ distribution with a non-zero mean and large skewness towards zero, which will then decrease with more and more rescatterings.

Rather large error bars for the excess kurtosis make it more difficult to find general trends in the data. Nevertheless, we find two trends for γ_2. The first is that the γ_2 values are mostly positive and not compatible with zero. To be more concrete, the γ_2 values are always positive for v_2 and sometimes negative for v_3, while the negative values also agree with 0 within error bars. This finding coincides with the results in Ref. [74] which uses hydrodynamics to simulate the time evolution. The second trend we observe is a non-monotonic behavior with $\langle \mathrm{Kn} \rangle^{-1}$. We find that the maximum value is obtained at the intermediate value for the cross section we use. For this value the distribution is more peaked than a Gaussian, while for the smaller and larger value of the cross section the distribution is more Gaussian.

To summarize, we can say that for many rescatterings during the evolution the absolute value of the skewness and the kurtosis come close to the values of a Gaussian distribution. In that case the distribution comes back to the properties we found for the initial state distribution. For the final state the variance is larger than that of the initial-state flow harmonics. Compared to the hydrodynamic case a finite number of rescatterings results in a larger absolute skewness and kurtosis.

Let us also mention that we tried to compute the moments for the distribution $p_{v|\varepsilon}(v_{4,\mathrm{c/s}}|\varepsilon_{4,\mathrm{c/s}}, \varepsilon_{2,\mathrm{c/s}})$, as the quadrangular flow depends on the second and fourth eccentricity (Eq. (4.13)). In this case we need a binning in both eccentricities to compute the moments of the probability distribution for fixed eccentricity. However, when trying to draw conclusions from these moments we obtain rather indecisive results, as the statistics including our 10^4 events per impact parameter is not suffi-

cient in this case. This is the reason why we do not present results for $n \geq 4$ for the moments of the probability distributions $p_{v|\varepsilon}(v_{n,\mathrm{c/s}}|\varepsilon_{n,\mathrm{c/s}})$.

4.4 Event-plane angle distributions

We calculated the flow angles Ψ_n from $v_{n,\mathrm{c/s}}$, as well as the orientation Φ_n of the n-th symmetry plane from $\varepsilon_{n,\mathrm{c/s}}$. With these two angles at hand we can now study the probability distributions $p(n(\Psi_n - \Phi_n))$ for $n = 2$ and 3, which are shown in Fig. 4.8 for the different $\langle \mathrm{Kn} \rangle^{-1}$ at impact parameter $b = 6$ fm. Similar results for $b = 0$ fm and 9 fm are shown in Appendix C.5. We also show the probability distribution for the initial state labeled by $\langle \mathrm{Kn} \rangle^{-1} = 0$. For the initial state the distributions

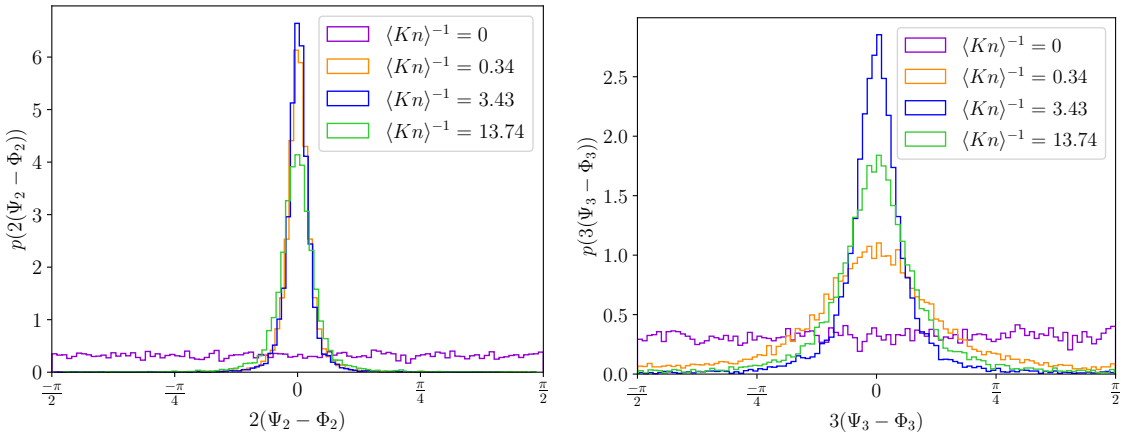

Figure 4.8: Probability distributions $p(2(\Psi_2 - \Phi_2))$ (left) and $p(3(\Psi_3 - \Phi_3))$ (right) for events at $b = 6$ fm for different $\langle \mathrm{Kn} \rangle^{-1}$. The initial state distribution is indicated by the label $\langle \mathrm{Kn} \rangle^{-1} = 0$.

are flat with small fluctuations. Thus, the initial flow which is caused by numerical noise is uncorrelated to the geometry of the initial state.

For the distributions with the flow angle Ψ_n computed at the end of the time evolution we find peaked distributions. Looking at $n = 3$, we find for the smallest value of $\langle \mathrm{Kn} \rangle^{-1} \approx 0.3 - 0.4$ that the distribution is broad with a maximum at $\Psi_3 - \Phi_3 = 0$ indicating that the initial anisotropy in position space is transferred into momentum space. Increasing the value of $\langle \mathrm{Kn} \rangle^{-1}$ by a factor of 10 leads to a sharply peaked distribution around $\Psi_3 - \Phi_3 = 0$. This implies that the flow angle and the symmetry plane of the initial state are almost aligned. Increasing the number of rescatterings further leads to a less peaked distribution which has again thicker tails for larger $|\Psi_3 - \Phi_3|$.

In the case of $n = 2$ we observe the same behavior as for $n = 2$ with the difference that for the smallest value of $\langle \mathrm{Kn} \rangle^{-1}$ the distribution is already very peaked around 0. This is true for all three considered impact parameters, although for $b = 0$ fm it can be observed to a lesser extent only. Again, with increasing $\langle \mathrm{Kn} \rangle^{-1}$ the peak bekomes sharper and then broadens for the largest number of rescatterings similar to the $n = 3$ case.

From Sec. 4.1 we know that the flow coefficient v_3 has a slower onset as v_2 with increasing $\langle \mathrm{Kn} \rangle^{-1}$ [83, 84]. This known behavior of the flow coefficients is also

transferred to the flow angles, as the $p(2(\Psi_2 - \Phi_2))$ distribution is always more peaked than the $p(3(\Psi_3 - \Phi_3))$ distribution for the same $\langle \mathrm{Kn} \rangle^{-1}$.

Comparing our results to other calculations from hydrodynamics [68] or hybrid [67] simulations, we find that for those distributions which have a clear peak, the width of the peak has the same magnitude.

We also tried to find a fit function for the $p(n(\Psi_n - \Phi_n))$ distributions but they cannot be fitted reasonably by a (truncated) Gaussian nor by a beta distribution.

4.4.1 Event-plane angle distributions with $n = 4$

It was mentioned before, that for the computation of the moments of the conditional probability distribution $p_{v|\varepsilon}(v_{4,\mathrm{c/s}}|\varepsilon_{4,\mathrm{c/s}}, \varepsilon_{2,\mathrm{c/s}})$ the statistics is not sufficient. For the event-plane angles this is not the case, here we have enough events for each impact parameter to see a clear trend. In general the interpretation is more complicated, as more angles play a role, i.e., Φ_2, Φ_4, Ψ_2 and Ψ_4.

First, we will have a look at the correlation between the symmetry planes of ε_2 and ε_4. The distributions for $b = 0$ and $b = 6$ fm are shown in Fig. 4.9, while the discussion for $b = 9$ fm is more complicated due to correlations of the initial-state symmetry planes and thus moved to Appendix C.6. For the afore mentioned

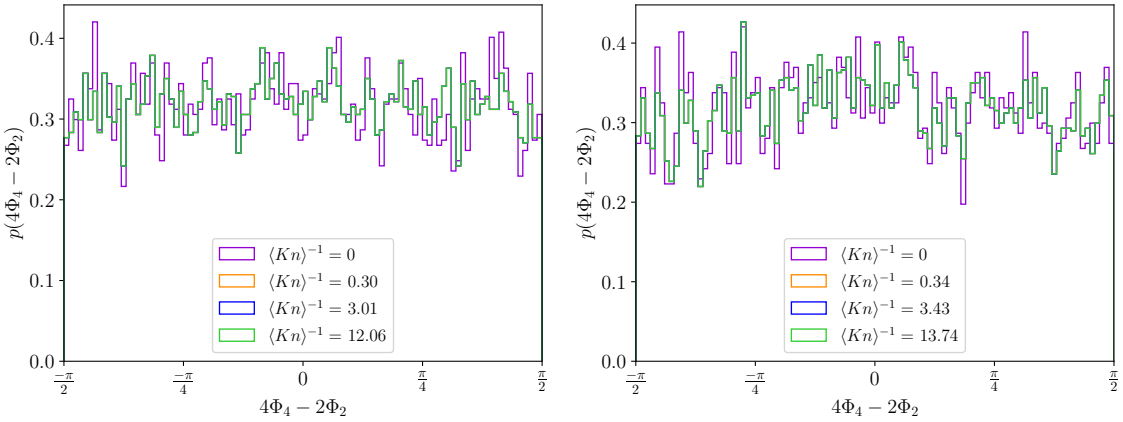

Figure 4.9: Probability distributions $p(4\Phi_4 - 2\Phi_2)$ for events at $b = 0$ fm (left) and $b = 6$ fm (right) for different $\langle \mathrm{Kn} \rangle^{-1}$. The initial state distribution is indicated by the label $\langle \mathrm{Kn} \rangle^{-1} = 0$.

impact parameters we find that the initial-state symmetry plane angles Φ_2 and Φ_4 are completely uncorrelated, as expected for central to medium-central collisions.[5] There the effect of the impact parameter is not strong enough to enforce a correlation between the orientation of the elliptic and the quadratic structures.

We will now go on and discuss the correlations between the final-state flow angle Ψ_4 and the initial-state symmetry planes Φ_4 resp. Φ_2 shown in Fig. 4.10 in the left resp. right panel. The final state distributions $p(4(\Psi_4 - \Phi_4))$ (left panel) show

[5] All curves collapse, as there is no time evolution needed for the computation of Φ_2 and Φ_4 and the initial state densities are always the same ones. Only the curve for $\langle Kn \rangle^{-1} = 0$ is different, since the curve results from the analysis in Sec. 4.3.2, where only half the amount of events was used.

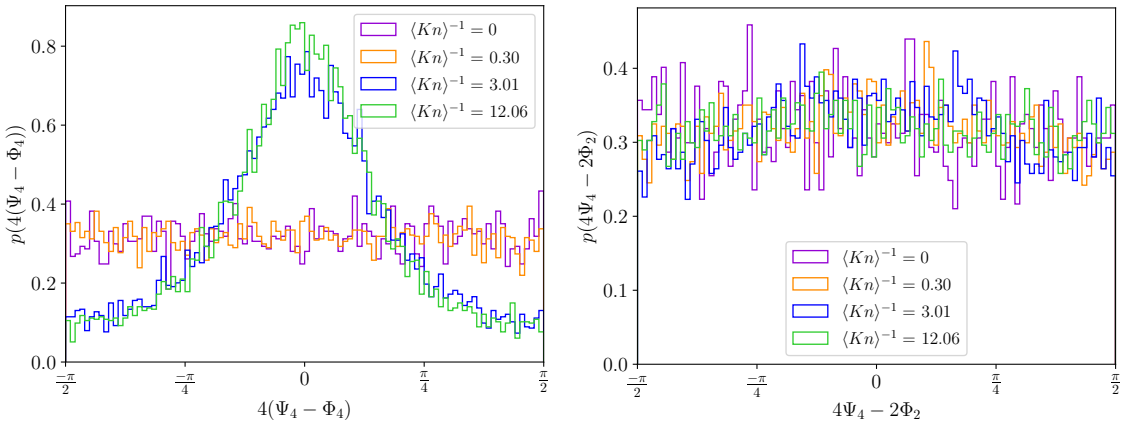

Figure 4.10: Probability distributions $p(4(\Psi_4-\Phi_4))$ (left) and $p(4\Psi_4-2\Phi_2)$ (right) for events at $b = 0$ fm for different $\langle \mathrm{Kn}\rangle^{-1}$. The initial state distribution is indicated by the label $\langle \mathrm{Kn}\rangle^{-1} = 0$.

no correlation in the initial state and for the smallest number of rescatterings. For the smallest number of rescatterings this behavior was to be expected, as also for the angle distributions shown in the last section we observed the broadening of the distribution with $n = 3$ with respect to the distribution with $n = 2$, as the onset of v_3 happens at smaller $\langle \mathrm{Kn}\rangle$ compared to v_3. The same is true for v_4, which has its onset for even smaller $\langle \mathrm{Kn}\rangle$. Increasing the number of rescatterings increases also the correlation of the flow angle Ψ_4 to the symmetry plane angle of ε_4. Thus, there is again a transfer of the initial state anisotropy from position space into momentum space, becoming more pronounced with more and more rescatterings. Looking at the right panel, we find no correlation between Ψ_4 and Φ_2 for all tested $\langle \mathrm{Kn}\rangle^{-1}$.

For impact parameter $b = 6$ fm (Fig. 4.11) we find the same trends as for $b = 0$ fm for the distribution $p(4(\Psi_4 - \Phi_4))$. One difference is that there is a small

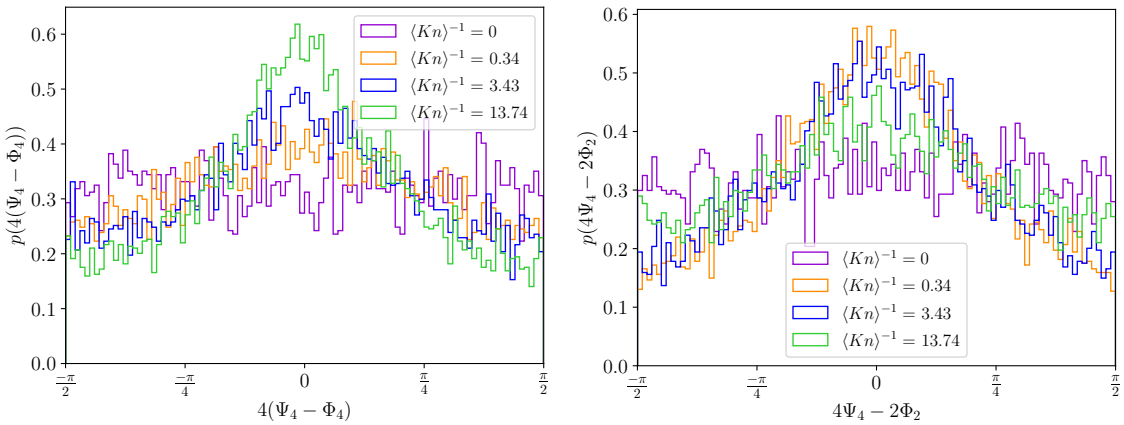

Figure 4.11: Probability distributions $p(4(\Psi_4-\Phi_4))$ (left) and $p(4\Psi_4-2\Phi_2)$ (right) for events at $b = 6$ fm for different $\langle \mathrm{Kn}\rangle^{-1}$. The initial state distribution is indicated by the label $\langle \mathrm{Kn}\rangle^{-1} = 0$.

correlation visible for the smallest number of rescatterings. Looking at the right panel we find the opposite behavior for $p(4\Psi_4 - 2\Phi_2)$. In the initial state there is no correlation, then there is the strongest correlation visible for the smallest number

of rescatterings, which decreases when going further into the hydrodynamical limit. So there is an opposite trend between the correlation of the fourth flow angle Ψ_4 to the angle Φ_4 resp. Φ_2 with increasing number of rescatterings during the time evolution.

4.5 Results for anisotropic flow fluctuations from the finite number of rescatterings

Gathering the results from the previous sections, we find that the $v_{n,\mathrm{c/s}}$ distributions about their mean value $\bar{v}_{n,\mathrm{c/s}}$ at a given eccentricity have the following quite robust behavior across different impact parameters:

- There is a decrease with $\langle \mathrm{Kn} \rangle^{-1}$ and then an increase in the values of the variance σ_v^2 of the fluctuations of $v_{n,\mathrm{c/s}}$ about the mean $\bar{v}_{n,\mathrm{c/s}}(\varepsilon_{n,\mathrm{c/s}})$.
- All $v_{n,\mathrm{c/s}}$ distributions are skewed towards 0. When there is an onset of anisotropic flow, the skewness takes a sizable value, e.g., the absolute value of the skewness has a value of order 0.5, which decreases then for an increasing number of rescatterings.
- The $v_{n,\mathrm{c/s}}$ distributions are predominantly more peaked than a Gaussian with the same variance, i.e. they have a positive excess kurtosis, which tends towards 0 when the number of rescatterings is increased.
- The event-plane angle distributions for $n = 2$ and 3 about their corresponding initial state participant-plane angle are peaked, with a broadening of the peak for the largest value of $\langle \mathrm{Kn} \rangle^{-1}$.
- The event-plane angle distributions for quadrangular flow have a more complex behavior due to possible correlations between the second and fourth symmetry planes.

It is important to emphasize that the fluctuations which are usually investigated are the ones from fluctuating eccentricities within a centrality bin. Here we investigated fluctuations at fixed eccentricity using the conditional probability distribution $p_{v|\varepsilon}(v_{n,\mathrm{c/s}}|\varepsilon_{n,\mathrm{c/s}})$ and then averaged the moments of this distribution over the eccentricity bins at a fixed impact parameter. This means that the fluctuations in the response function of anisotropic flow to the initial state eccentricity are investigated [60]. Their origin is the finite number of rescatterings in the system which transfer the initial geometrical anisotropy into a build up of anisotropic flow. Thus, the average value about which the flow coefficient fluctuates is the one obtained by solving the (fully deterministic) kinetic Boltzmann equation at the same Kn (or opacity) [81, 84].[6] The fluctuations which we have studied in the previous sections are not present in hydrodynamic simulations, at least if implementations of non-fluctuating hydrodynamics are considered.

[6] This assumes that the Boltzmann equation describes the single-particle phase-space distribution for the given system, which should hold true if the system is dilute.

One important finding from the conditional probability distributions and studying their moments is that the fluctuations are non-Gaussian. In this case the central-limit theorem does not apply due to the fact that there are not enough rescatterings in the system. It seems also quite intuitive that the skewness tends towards zero, as the initial flow is zero and has an upper bound in absolute value. Why the excess kurtosis is positive, i.e., the distribution is more peaked than a Gaussian with the same variance, is not clear. However, the decrease of the excess kurtosis for the highest number of rescatterings seems to be encoded in the $\Psi_n - \Phi_n$ distributions as well. This feature is not yet understood. One possibility could be that for large values of $\langle \mathrm{Kn} \rangle^{-1}$ there might be contaminations due to nonlinear mixing of eccentricities, e.g., a $\varepsilon_2 \varepsilon_4$ contribution to the fluctuations of v_2. These contaminations could occur in value as well as in the orientation. A study of these possible contaminations is beyond the scope of this work.

Chapter 5

Early time behavior of spatial and momentum anisotropies in kinetic theory across different Knudsen numbers

In this chapter we will investigate the early time behavior of anisotropies in position and momentum space. We will have a closer look at the non-universal behavior across different Knudsen numbers from the hydrodynamic to the quasi-collisionless regime at early times. Going to the quasi-collisionless limit it is possible to perform analytical calculations which can be compared to the numerical simulations. This section is based on Ref. [93]:

- *Early time behavior of spatial and momentum anisotropies in kinetic theory across different Knudsen numbers*
  N. Borghini, M. Borrell, H. Roch
  arXiv: 2201.13294 [nucl-th]

All analytical computations performed in this reference were performed by Nicolas Borghini and Marc Borrell. The numerical part of the work was done by the author.

The purpose of this paper is to investigate the early time dynamics of the fireball produced in relativistic heavy-ion collisions more closely. Especially the application

of hydrodynamics in small collision systems or peripheral collisions is still under debate [94, 95] and there are different approaches available to describe the early time dynamics.

In our approach we use kinetic transport theory which can model the fireball evolution along the whole range in the Knudsen number.[1]

5.1 Methods and setup

In this section the two approaches — numerical and analytical — are briefly presented and we will introduce the initial distribution which is needed for both computations.

5.1.1 Transport simulations

As the main characteristic quantities which we consider in this paper, namely anisotropic flow and spatial eccentricities – are mostly driven by the dynamics in the transverse plane, we will consider the system as purely two dimensional. The advantage of this simplified setup, which is even further simplified by using massless particles, is that the simulations become computationally cheaper and it is easier to overcome the statistical noise, especially in the few-collisions limit.

For the numerical simulations we use the test particle transport approach presented in Secs. 3.4.2-3.4.5. In contrast to the analytical calculation the transport code has the ability to perform simulations at basically all Knudsen numbers by varying the cross section σ. In all our simulations we assured that the dilution parameter D, defined in Eq. (3.23) is smaller than 0.1 to ensure covariance and locality.

In our simulations the number of test particles was typically $N_{\mathrm{p}} = 2 \times 10^5$ in the initial state of the simulation and we used of the order of $N_{\mathrm{iter.}} = \mathcal{O}(10^3)$ iterations to reduce statistical errors due to the finite particle number.

We also used the $2 \to 0$ transport code version introduced in Sec. 3.4.6 to have a better comparison to the analytical calculations, which only account for the loss term of the Boltzmann equation.

5.1.2 Analytical calculations

Using a single-particle phase space distribution function $f(t, \vec{x}, \vec{p})$ and the relativistic kinetic Boltzmann equation with a $2 \to 2$ collision kernel enables us to describe a dilute system which undergoes binary collisions. The fist assumption we make is that in the limit of large Knudsen numbers, i.e., the few-collisions limit, the distribution function will be close to the free-streaming distribution function. This approximation has been used in various (semi-)analytical studies for anisotropic flow in the few-collisions limit with different approximations for the collision kernel [80, 84, 89, 96–101].

[1] This is only true for the numerical simulation, as we will see later on.

In Ref. [102] it was pointed out that one can start irrespective of any approximation with a Taylor expansion of the distribution function

$$f(t,\vec{x},\vec{p}) = f^{(0)}(\vec{x},\vec{p}) + t\,\partial_t f(t,\vec{x},\vec{p})\Big|_0 + \frac{t^2}{2}\partial_t^2 f(t,\vec{x},\vec{p})\Big|_0 + \cdots, \tag{5.1}$$

with $f^{(0)}$ the initial distribution and all time derivatives evaluated at the initial time $t = 0$. Making now use of the Boltzmann equation

$$\partial_t f(t,\vec{x},\vec{p}) = -\frac{\vec{p}}{E}\cdot\vec{\nabla}_x f(t,\vec{x},\vec{p}) + \mathcal{C}[f], \tag{5.2}$$

the time derivatives in Eq. (5.1) can be replaced by spatial derivatives. If a form of the collision kernel is given then the evolution of the distribution function is described by its initial form and spatial derivatives thereof [102]:

$$\begin{aligned} f(t,\vec{x},\vec{p}) =& f_{\text{f.s.}}(t,\vec{x},\vec{p}) + t\,\mathcal{C}[f]\Big|_0 + \frac{t^2}{2}\left(-\frac{\vec{p}}{E}\cdot\vec{\nabla}_x\mathcal{C}[f] + \partial_t\mathcal{C}[f]\right)_0 \\ &+ \frac{t^3}{3!}\left(\frac{\left(\vec{p}\cdot\vec{\nabla}_x\right)^2}{E^2}\mathcal{C}[f] - \frac{\vec{p}}{E}\cdot\vec{\nabla}_x\partial_t\mathcal{C}[f] + \partial_t^2\mathcal{C}[f]\right)_0 + \mathcal{O}(t^4), \end{aligned} \tag{5.3}$$

with $f_{\text{f.s.}}$ grouping all terms without a collision kernel which is therefore the free-streaming distribution at $t = 0$. The re-expression of the time derivatives by the Boltzmann equation can be used again to obtain an expression which depends on $f^{(0)}$ and its spatial derivatives only. The cross section enters the calculation through the time derivatives of $\mathcal{C}[f]$ in increasing powers which characterize the rescatterings [102].[2] At this point it is also clear that any quantity at early times can be computed from this distribution function to an arbitrary precision if enough orders in t are considered.

Up to this point the analytical approach is not restricted to a particular system. However, to be able to compare with the numerical simulations we will now look at a two dimensional system with massless particles.

One minor drawback is that the analytical approach is not able to handle the full $2 \to 2$ collision kernel of the Boltzmann equation. The gain term, which does not contain the particle momentum on the left hand side of the Boltzmann equation makes the form of the differential cross section important. This problem can be cured by only looking at the loss term, i.e., a $2 \to 0$ kernel [89, 96]:

$$\mathcal{C}_{2\to 0}[f] = -\frac{E}{2}\int f(\mathbf{p}) f(\mathbf{p}_1) v_{\text{Møller}}\sigma\,\mathrm{d}^2\,\mathbf{p}_1, \tag{5.4}$$

where time and position arguments are neglected for brevity. It is obvious that this collision kernel violates particle number and energy conservation, but we are able to go to higher orders in the total cross section σ.

Comparing the analytical results to the $2 \to 0$ simulations it is important to keep in mind that the numerical simulations contain all orders in σ while the analytical result is truncated at some finite order in σ.

[2] We will illustrate this fact in the following parts.

5.1.3 Initial distribution function

The initial distribution function used in our work has been used in different studies before [84, 89, 96–101]. It provides us with a semi-realistic geometry for our computations. We assume that the initial distribution $f^{(0)}$ factorizes as

$$f^{(0)}(\mathbf{x}, \mathbf{p}_\mathrm{T}) = F(\mathbf{x})\, G(\mathbf{p}_\mathrm{T}, T(\mathbf{x})), \tag{5.5}$$

where the geometry is contained in the function F and the function G contains the momentum space dependence. Here we use a thermal distribution which depends on the position via the temperature:

$$G(\mathbf{p}_\mathrm{T}) = \frac{1}{2\pi T(\mathbf{x})^2} e^{-|\mathbf{p}_\mathrm{T}|/T(\mathbf{x})}. \tag{5.6}$$

The momentum distribution G is normalized to unity and thus $F(\mathbf{x})$ is the particle-number density. Via the equation of state for a massless gas of particles in two dimensions

$$T(\mathbf{x}) \propto \sqrt{F(\mathbf{x})}, \tag{5.7}$$

we can relate the temperature to the spatial distribution. This implies that the temperature in the central region is higher than in the outer regions.

Expressed in polar coordinates in the transverse plane we choose the position dependent part of the distribution function to be

$$F(r, \theta) = \frac{N_\mathrm{p}\, \mathrm{e}^{-\frac{r^2}{2R^2}}}{2\pi R^2} \left[1 - \sum_{k=2}^{3} \tilde{\varepsilon}_k \mathrm{e}^{-\frac{r^2}{2R^2}} \left(\frac{r}{R}\right)^k \cos(k\theta)\right], \tag{5.8}$$

with N_p the initial particle number and R the typical system size. This size sets a typical time scale for the system evolution. However, we will report our results in dimensionless time scales and thus it is not really relevant for our results. It is only relevant for a dimensionless quantity like the Knudsen number when combining it with the cross section and the number of particles in the system. The phase space distribution function is normalized to N_p, as G is normalized to unity and F to the particle number.

The real valued parameters $\tilde{\varepsilon}_2$ and $\tilde{\varepsilon}_3$ steer the spatial ellipticity or triangularity of the system. Matching the two coefficients to the eccentricities defined in Eq. (2.25) yields $\varepsilon_2^\mathbf{x} = \tilde{\varepsilon}_2/4$ and $\varepsilon_3^\mathbf{x} = \tilde{\varepsilon}_3/\sqrt{2\pi}$. For simplicity we have chosen $\Phi_2 = \Phi_3 = 0$ which has no influence on the results.[3] In the following we have chosen only one eccentricity to be non zero in a given simulation up to numerical fluctuations and we used the standard value of $\varepsilon_n^\mathbf{x} \simeq 0.15$.

It is important to notice that the momentum distribution is isotropic in the initial distribution (5.5) which is necessary for the analytical treatment and mostly fulfilled by the numerical simulations. Again we performed $N_\mathrm{iter.}$ iterations with the same positions of the test particles but different realizations in momentum space to get a

[3] Using complex valued $\tilde{\varepsilon}_n$ would result in the symmetry-plane angle Φ_n being the argument of the $\tilde{\varepsilon}_n$.

handle on the fluctuations of the observables due to finite test particle number N_p.[4] The different iterations are then averaged. In the following we shift all anisotropic flow curves to zero at $t = 0$ and indicate the statistical error $1/\sqrt{N_\mathrm{p} N_\mathrm{iter.}}$ by an error bar. The amount of rescatterings is characterized by the Knudsen number (3.24).

5.2 Onset of anisotropic flow from small to large Knudsen number

In this section we investigate the early time buildup of anisotropic flow across different Knudsen numbers while we keep the initial geometry of the system fixed.

It is a well known fact that the value of anisotropic flow v_n increases with the number of rescatterings when going from the few-collisions regime $\mathrm{Kn} \to \infty$ to the fluid-dynamical limit $\mathrm{Kn} \to 0$.[5] We will show this also for our specific initial condition below. In this work we are more interested in the onset of $v_n(t)$ which is only studied in the extreme limits of the Knudsen number mentioned above. Fluid dynamical simulations [37, 103–105] or general scaling arguments [106] have shown that $v_2(t) \propto t^2$ or more general $v_n(t) \propto t^n$ at early times. Transport simulations [56, 83] and analytical calculations [89, 96] in the large Kn regime yield a slower growth with $v_n(t) \propto t^{n+1}$.

In our study we want to bridge the gap between these two limiting regimes and map out the early time behavior of v_2 and v_3. To do this we use the full $2 \to 2$ collision kernel in the simulations.

We show the values of $v_2(t)$ for $t/R \leq 0.7$ and $v_3(t)$ for $t/R \leq 0.9$ for a variety of different Knudsen numbers in the range $\mathrm{Kn} = 0.02$ to $\mathrm{Kn} \approx 10$ in Fig. 5.1. Within

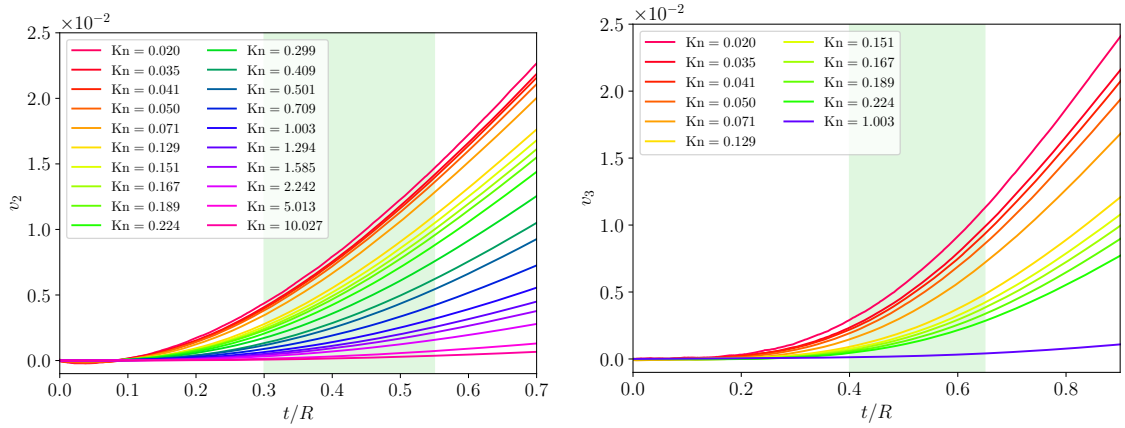

Figure 5.1: Examples for v_2 (left) and v_3 (right) as function of t/R for different Knudsen numbers. The green shaded region marks the interval for the end points of the fits.

this range the number of rescatterings per particle varies from about 25 to less than 0.1 on average. In the few collisions limit the spatial deformation in the initial state

[4] The initial v_1 signal is completely removed by subtracting the mean momentum from every particle in the initial state.

[5] In the limit $\mathrm{Kn} \to \infty$ no anisotropic flow develops.

is less efficiently converted into a flow signal and additionally we observe that at a given time and Kn the value of v_3 is significantly smaller than the v_2 value. This is the reason why we have a narrower interval of Knudsen numbers for v_3.

Similar to the scalings reported from literature above, we fit the flow onset using a power-law ansatz

$$v_n\left(\frac{t}{R}\right) = \beta_n\left(\frac{t}{R}\right)^{\gamma_n}. \tag{5.9}$$

As due to the finite particle number there are initial state flow fluctuations present for all the curves, we shift them to zero at the initial time to spare an additional offset parameter in the fit. This is a valid procedure as we are only interested in the flow scaling behavior. For the values of β_n we find that they increase when going into the hydrodynamical limit.

One issue with the performed fits is that the interval in t/R is not a well defined quantity, i.e., what is early time? To circumvent this problem, we use $t = 0$ as a starting point for the fits and the end point is determined randomly within the green shaded bands in Fig. 5.1. The problem with the end point of the fit is that if its too small, the fit is contaminated by numerical noise and if its too large, then higher powers in time might start to play a significant role for the scaling. We perform 500 fits with a randomly chosen end point using expression (5.9) for all Knudsen number values. The results for the scaling exponents γ_n with $n = 2, 3$ of each fit with a random end point are displayed in Fig. 5.2 by the gray lines for each Knudsen number. We also performed a weighted average for the scaling exponents over all

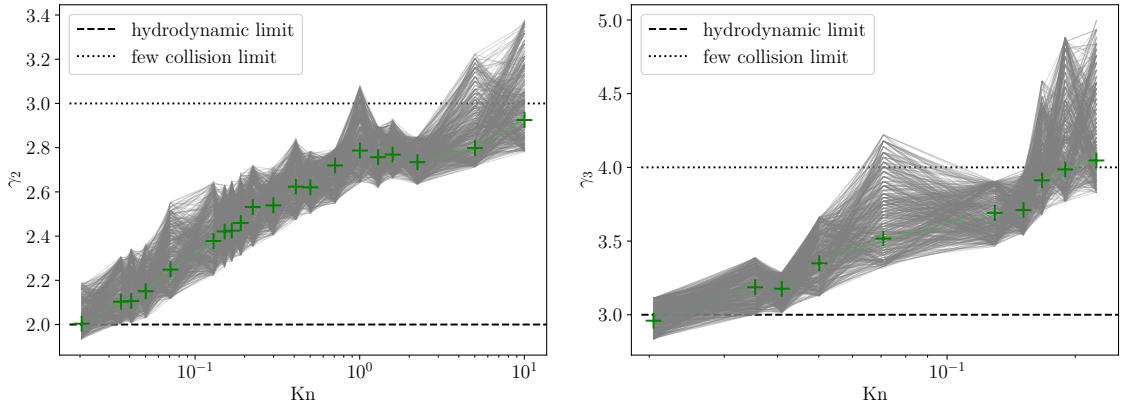

Figure 5.2: Scaling exponent γ_2 (left) or γ_3 (right) as a function of the Knudsen number. The gray lines indicate the 500 realizations of the fit over different time intervals, while the green points correspond to the weighted average (5.10).

500 fit lines at each Kn such that the fits with larger uncertainties have less weight using

$$\bar{\gamma}_n = \frac{\sum_j \gamma_{n,j}/\sigma^2_{\gamma_{n,j}}}{\sum_j 1/\sigma^2_{\gamma_{n,j}}}, \tag{5.10}$$

with $\sigma^2_{\gamma_{n,j}}$ the squared fit uncertainty on $\gamma_{n,j}$ for the j-th fit. The index j runs over all 500 fits and thus the gray lines in Fig. 5.2 provide us with a very conservative (non-symmetric) error band to the average scaling exponents $\bar{\gamma}_n$ shown in green.

The scalings show a clear trend, even if the uncertainty bands are quite large, for the scaling exponents γ_2 and γ_3. We can see a crossover from the hydrodynamic limit, where $\gamma_n = n$, to the few-collisions regime, where $\gamma_n = n + 1$, over the range of Knudsen numbers. A direct comparison between γ_2 and γ_3 shows that for v_3 this crossover happens on a much smaller range in Knudsen numbers, which is actually in the regime, where v_2 is already close to its hydrodynamical scaling.

We will now put our findings into the context of the already known behavior of v_2 and v_3 at late times, where the anisotropic flow has reached its final value in the time evolution of the system. If we go from the free-streaming limit into the direction of smaller Kn, the v_2 signal rises before the v_3 signal [77, 83], which is also displayed in Fig. 5.3 for our initial condition. For the fits to the individual

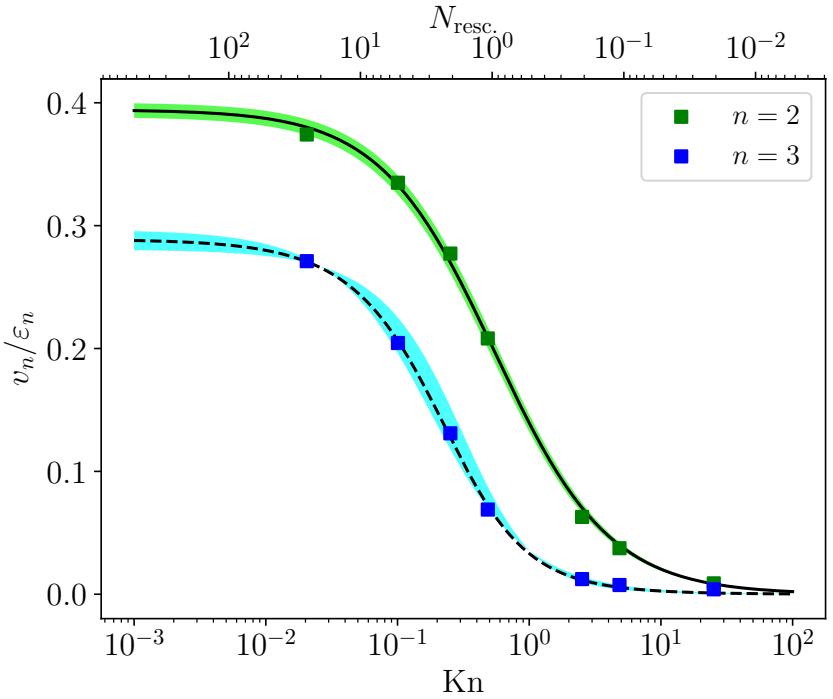

Figure 5.3: v_n/ε_n as a function of the Knudsen number and the mean number of rescatterings $N_{\text{resc.}}$ per particle, where v_n and $N_{\text{resc.}}$ are estimated at time $t = 100R$. The fits were performed with Eqs. (4.4)–(4.5). The colored bands show the 1σ fit error.

simulations Eqs. (4.4) and (4.5) were used.

It is important to note that with the extraction of $\gamma_3 \approx 4$ in the few-collisions limit of v_3 we reached a limit of what we can do to obtain reasonable uncertainties. This is the reason why we did not try to extract the scaling behavior of v_4, which is expected to change its scaling from t^4 to t^5 with increasing Knudsen number.

5.3 Number of rescatterings

Now we want to compare the results of the analytical calculations described in Sec. 5.1.2 to the numerical simulations using the expansion 5.3. Therefore, we use

different orders in the cross section included in the analytical results, as we have already seen that the scaling of the flow coefficients $v_n(t)$ does not have an integer value at "intermediate" Knudsen numbers. Within our framework we are able to sum different contributions from the Taylor series to compare the resulting effective behavior to the full transport simulations.

We start with the most basic observable one can think of, the number of rescatterings in the system, which is rescaled by twice the number of particles N_p. The factor 2 accounts for the two particles interacting in one collision. From the analytical side $N_\mathrm{resc.}$ is one half times the integral of the collision rate. This gives us the simple possibility to compute it from the collision integral of the $2 \to 0$ collision kernel over the whole phase space:[6]

$$N_\mathrm{resc.}(t) = \frac{1}{2N_\mathrm{p}} \int_0^t \Gamma(t')\, \mathrm{d}t' \tag{5.11}$$

$$= \frac{1}{N_\mathrm{p}} \int_0^t \int -\mathcal{C}_{2\to 0}[f(t', \mathbf{x}, \mathbf{p})]\, \frac{\mathrm{d}^2\mathbf{x}\mathrm{d}^2\mathbf{p}}{E} \mathrm{d}t'. \tag{5.12}$$

In the analytical treatment we are only able to compute $f(t, \mathbf{x}, \mathbf{p})$ at early times in the $2 \to 0$ scenario. For this reason we will also consider the numerical $2 \to 0$ simulations. Remember, that this is the model where the particle number is not a conserved quantity. The analytical results for $N_\mathrm{resc.}$ are computed up to order t^{11} in time and up to order σ^5 in the cross section.[7]

In Fig. 5.4 we show the transport simulation results in green for two different Knudsen numbers, $\mathrm{Kn} \approx 25$ (full line) and $\mathrm{Kn} \approx 5$ (dashed line), where we rescaled the latter Knudsen number results by a factor 1/5 such that a proportionality to σ would be directly visible. We find that this proportionality is not present, as the two curves do not coincide. This tells us that going to higher orders in the cross section is important to describe $N_\mathrm{resc.}(t)$.

Comparing the analytical result at order σ (blue) we find that the curves coincide, as they should by construction. Additionally they are close to the numerical results at $\mathrm{Kn} \approx 25$ up to $t/R \approx 0.3$. Going beyond order σ, namely to σ^5 (orange), shows that the agreement with the simulations can be improved for both Knudsen numbers considered here.

We were able to show that $N_\mathrm{resc.}(t)$ is well described in the analytical calculation, which is a necessary prerequisite for other observables like anisotropic flow coefficients which depend on this quantity. It is also worth noting that in the case $\mathrm{Kn} \approx 5$ about 16% of the particles disappear during the time evolution of the system, where most of the particles are lost in the dense state during the initial state. This is also the reason why the simulation results of the $2 \to 2$ and $2 \to 0$ collision kernel show significant differences during this early stage and makes it important to compare the $2 \to 0$ kernel with the analytical results.

[6] This integral over the loss term of the collision kernel gives the number of rescatterings for any type of binary collisions for two identical particles. It is not restricted to our modified collision kernel, as the notation might suggest.

[7] It is important to note that at $\mathcal{O}(t^{11})$ there are terms up to σ^{10}, that is why our results for $N_\mathrm{resc.}(t)$ at order t^{11} are not complete. We are slightly inconsistent here, as the number of terms to compute grows significantly with increasing order in the cross section.

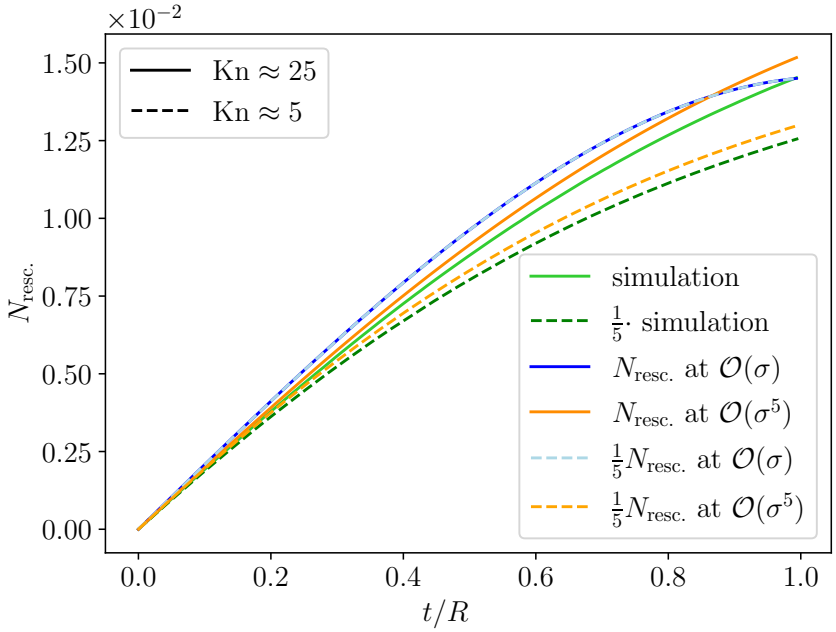

Figure 5.4: Number of rescatterings per particle for Kn ≈ 25 (full) and Kn ≈ 5 (dashed) for the $2 \to 0$ collision kernel simulation (green). The analytical results — computed up to $\mathcal{O}(t^{11})$ — are shown at $\mathcal{O}(\sigma)$ (blue) and $\mathcal{O}(\sigma^5)$ (orange) for the corresponding Knudsen numbers.

5.4 Anisotropic flow coefficients

Now that we have discussed the time dependence of $N_{\text{resc.}}$ we can go back to the anisotropic flow coefficients v_n at early times. In this case we assume that there is no "preflow" in the system, that means that $v_n(t = 0) = 0$. As we want to compare to the analytical calculations similar to the ones in [89, 96], we will use the $2 \to 0$ scenario for the simulations. However, we found that in the limit of large Knudsen numbers both collision kernels yield similar simulation results for $v_2(t)$ with $t \lesssim R$.[8] As in the case of Kn ≈ 1 about $60 - 80\%$ of the particles are vanishing in the $2 \to 0$ setup, it is only possible to study the dependence of v_n for "large" Knudsen numbers.

Results for $v_2(t)$ at two different Knudsen numbers are given in Fig. 5.5. The simulation results are again shown in green and the statistical error in the initial state caused by the finite number of particles (see Eq. (4.2)) is indicated by an error bar at $t = 0$. Results for $v_2(t)$ from the analytical approach are shown in blue resp. orange by keeping terms up to order t^{15} but only terms up to order σ resp. σ^3. Ref. [93] has shown that possible contributions at $\mathcal{O}(\sigma)$ start from t^3 and show up at odd orders in time, while those at $\mathcal{O}(\sigma^2)$ start from t^4 and show up at even orders in time. Similarly to $\mathcal{O}(\sigma)$ the terms of order $\mathcal{O}(\sigma^3)$ are again showing up at odd orders in time, but only from t^5 on.

Focusing now on Fig. 5.5 we observe a nice agreement for Kn ≈ 25 (left panel) between numerical and analytical results at first order in the cross section up to

[8] We find that the $2 \to 0$ kernel yields slightly smaller $v_2(t)$ values and that the deviation between the kernels increases with decreasing Kn. This is caused due to the faster dilution in the $2 \to 0$ system. More detailed results are provided in Ch. 6 (Ref. [107]).

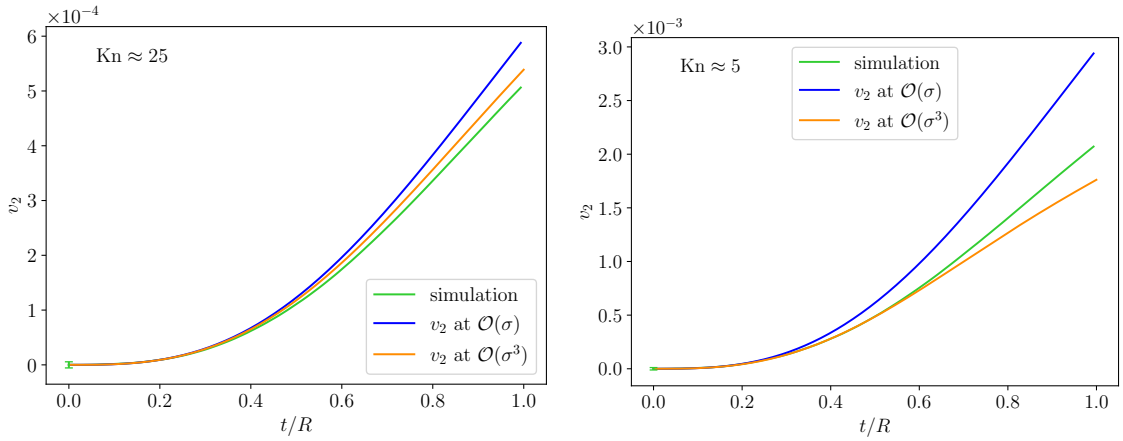

Figure 5.5: Elliptic flow v_2 as a function of t/R for Kn ≈ 25 (left) and Kn ≈ 5 (right). Results from the numerical $2 \to 0$ simulations are shown in green and the analytical results are shown to $\mathcal{O}(\sigma)$ (blue) and $\mathcal{O}(\sigma^3)$ (orange). Both analytical curves include terms up to $\mathcal{O}(t^{15})$.

$t/R \approx 0.4$, while going to order σ^3 again improves the agreement in such a way that the growth of $v_2(t)$ is slown down. This is not a trivial result keeping in mind that the analytical approach is a Taylor series in t/R and that the result at $t/R = 1$ differs by less than 10% from the simulation.

As expected, the inclusion of higher orders in σ is even more important at the five times smaller Knudsen number shown in the left panel. For the results at $\mathcal{O}(\sigma^3)$ we obtain a good agreement between the two approaches up to $t/R \approx 0.6$.

We can conclude that the higher order terms in the cross section are important for the comparison to the numerical results. If we would consider enough powers in t and σ it should be possible to reproduce the scaling behavior of the flow reported as γ_2 in Sec. 5.2. However, including more powers in time will improve the late time behavior of the curves but it will not signifficantly affect the early time behavior. Increasing the order of the cross section would improve the results for smaller Knudsen numbers by the cost that the computations become much more expensive.

Investigating now the triangular flow $v_3(t)$, one of the first things to notice is that the $2 \to 0$ kernel yields much more different results than the $2 \to 2$ kernel, especially at times $t \gtrsim R$. This will be described in further detail in Ch. 6. Comparing the v_3 signals at Kn ≈ 5 or 25 in Fig. 5.3 shows that they are already very small at the end of the time evolution in the $2 \to 2$ scenario, which will be intensified in the $2 \to 0$ case and by simulating only up to $t/R \approx 1$. This implies a new problem, in particular that there is a non vanishing initial v_3 in the initial state, which can lead to a (small) linear rise of $v_3(t)$ at early times [102]. We can observe this rise at both Knudsen numbers shown in Fig. 5.6.

A second problem arising in the analytical calculations with the $2 \to 0$ kernel is that the $v_3(t)$ signal at $\mathcal{O}(\sigma)$ vanishes at all times.[9] Therefore, we have to go to higher orders in the cross section to find a $v_3(t)$ signal within the Taylor series approach.

Figure 5.6 shows the triangular flow for the same Kn values that we have used

[9] Actually, all odd flow harmonics vanish at order σ.

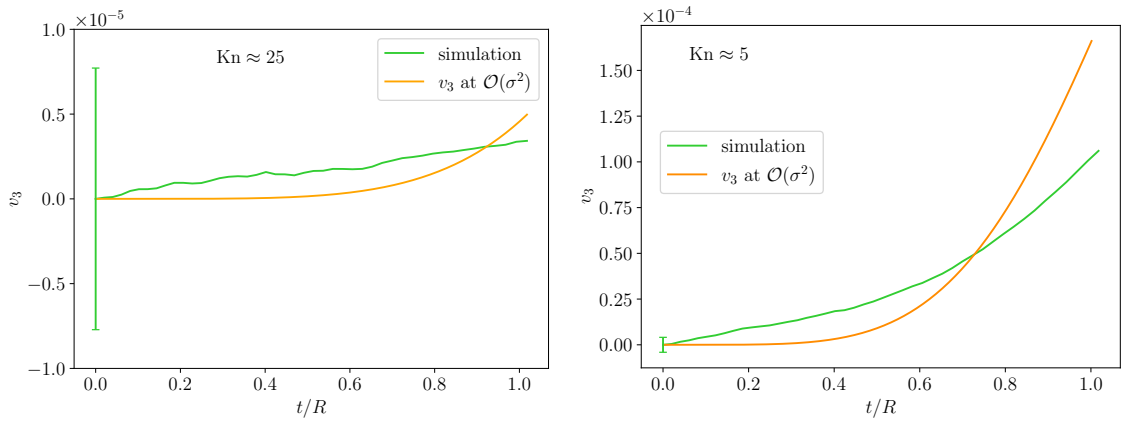

Figure 5.6: Triangular flow v_3 as a function of t/R for Kn ≈ 25 (left) and Kn ≈ 5 (right). Results from the $2 \to 0$ collision kernel are shown in green and the analytical results are shown to $\mathcal{O}(\sigma^2)$ (orange).

for $N_{\text{resc.}}$ and v_2. We include terms up to t^{11} and $\mathcal{O}(\sigma^2)$, resulting in a leading term $v_3(t) \propto \sigma^2 (t/R)^5$ which grows slowly in time compared to $v_2(t)$.

As the shapes of the curves are different for the two approaches — which can be explained by the fact that the analytical calculation does not include any preflow and thus has no linear rise — we can just say that the results are of the same magnitude. This is to some extent a surprise, as the $2 \to 0$ scenario has a v_3 which is proportional to σ^2 and not to σ and on the other hand one can fit the v_3 points in Fig. 5.3 using Eq. (4.5) with $v_3 \propto \text{Kn}^{-1}$ for large Kn. However, these are the results for $v_3(t)$ which come together with the successful description of the numerical results. In Sec. 5.6 we will see that there are also alternative measures of triangular flow, where an energy weight is used and which lead to different results.

5.5 Spatial characteristics

Here we will discuss the anisotropies in position space, i.e., spatial eccentricities $\varepsilon_n^{\mathbf{x}}$ and related quantities. In contrast to anisotropic flow many of these quantities do already have a non trivial time dependence in the free-streaming case. In Ref. [102] it was even pointed out that the change in these geometrical quantities due to rescatterings of particles is subleading in time with respect to the free-streaming evolution. This is why we will first look at collisionless systems taking into account only $f_{\text{f.s.}}$ in Eq. (5.3) and we will consider the $2 \to 2$ kernel in this section. For the free-streaming system this does not make a difference, but if we include rescatterings later on this is crucial.

In this section we will consider particle-number weighted as well as energy-weighted eccentricities $\varepsilon_n^{\mathbf{x}}(t)$ (Eq. (2.25)) resp. $\varepsilon_n^{\mathbf{x},E}(t)$. The definition of the energy-weighted eccentricities is the same with an additional factor $E \equiv |\mathbf{p}|$, being the energy of a particle with momentum $\mathbf{p}$, in the integrals in Eq. (2.25). The time behavior in the free-streaming case is given by [102]:

$$\varepsilon_n(t) \simeq \frac{\varepsilon_n(0)}{1 + a_n (t/R)^2}, \tag{5.13}$$

where in the case $n = 2$ the equality is exact, while for $n > 2$ it holds up to terms of order $(t/R)^4$ or even higher if $n > 3$. The initial condition introduced in Sec. 5.1.3 yields $a_2 = 1/2$ for a particle number weight for $\varepsilon_2^{\mathbf{x}}$, while we obtain $a_2 = 3/4$ for an energy weight for $\varepsilon_2^{\mathbf{x},E}$. For the third harmonic we obtain $a_3 = 3/4$ and $9/8$ for particle resp. energy weight for $\varepsilon_3^{\mathbf{x}}$ resp. $\varepsilon_3^{\mathbf{x},E}$.[10]

The standard scenario we will consider in this section is an initial eccentricity of $\varepsilon_n^{\mathbf{x}} = 0.15$. Again, we can only use a finite number of particles, $N_{\mathrm{p}} = 2 \times 10^5$ in this case, such that the value is not exactly reached. However, the fluctuations in the simulations can be decreased by fixing the initial positions of the particles for $N_{\mathrm{iter.}} = 3.2 \times 10^4$ iterations and resample the momentum distribution only. Additionally, the momentum distribution depends on the positions of the test particles via the temperature, such that the energy-weighted eccentricities $\varepsilon_2^{\mathbf{x},E}$ and $\varepsilon_3^{\mathbf{x},E}$ can differ from each other. In Fig. 5.7 the free-streaming eccentricities are shown for the different weights. The full curves can be nicely fitted using Eq. (5.13) giving us

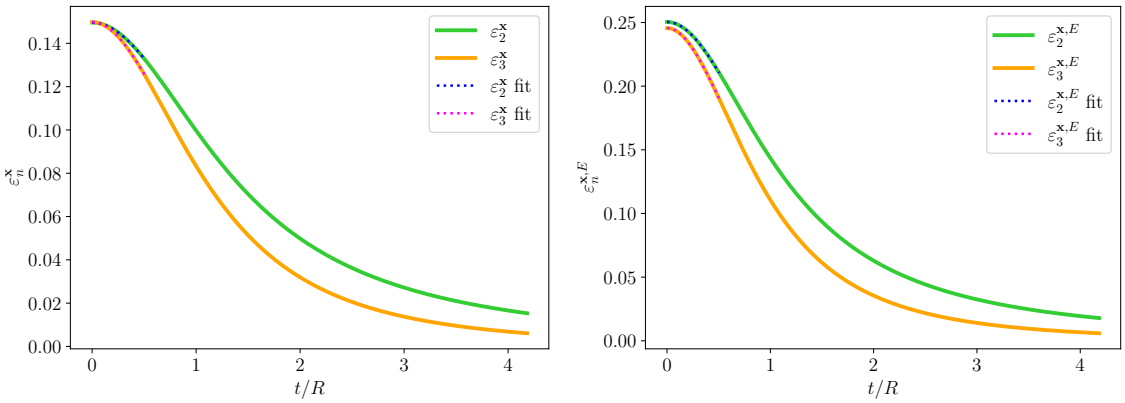

Figure 5.7: Time evolution of the spatial eccentricities in a collisionless system. The left panel shows particle-number weighted eccentricities $\varepsilon_2^{\mathbf{x}}$, $\varepsilon_3^{\mathbf{x}}$, the right panel eccentricities $\varepsilon_2^{\mathbf{x},E}$, $\varepsilon_3^{\mathbf{x},E}$ with energy weighting. The dotted curves are fits with Eq. (5.13) and the parameters given in Table 5.1.

the fit parameters presented in Tab. 5.1, where we fitted the numerical results with Eq. (5.13) up to $t/R = 0.5$. In all cases the fitted $\varepsilon_n(0)$ coincides with the values

Table 5.1: Parameters of the fit function Eq. (5.13) for ε_n with particle-number and energy weight.

weight	$\varepsilon_2(0)$	a_2
particle number	0.1496	0.5005
energy	0.250	0.745
weight	$\varepsilon_3(0)$	a_3
particle number	0.1499	0.7626
energy	0.246	1.141

computed in the initial state of the simulations. Then all extracted a_n values from

[10] These specific values are only valid for the initial condition given in Sec. 5.1.3, while Eq. (5.13) is true for any free-streaming distribution.

the fit are in good agreement with the analytically predicted values, where we see a better agreement for $n = 2$, where Eq. (5.13) is exact, than for $n = 3$, where the equation is only correct up to terms of order $(t/R)^4$. Note, that the energy-weighted eccentricities decrease faster than the particle-number weighted ones. This behavior is also encoded in the larger values of a_n.

If there are no collisions present in the system evolution there is no possibility to transfer a spatial anisotropy into a momentum anisotropy, i.e., to generate anisotropic flow. For this reason the eccentricities fall off most slowly in the free-streaming case, while any number of rescatterings can only lead to a faster decrease. When the number of collisions is sufficiently large, there is also the possibility that the eccentricities can change sign, which was also observed in hydrodynamical simulations [105]. The change due to collisions at relatively large Knudsen numbers (Kn $\approx$ 25 or 5) is not really visible, as displayed in Fig. 5.8. Just to show the sign

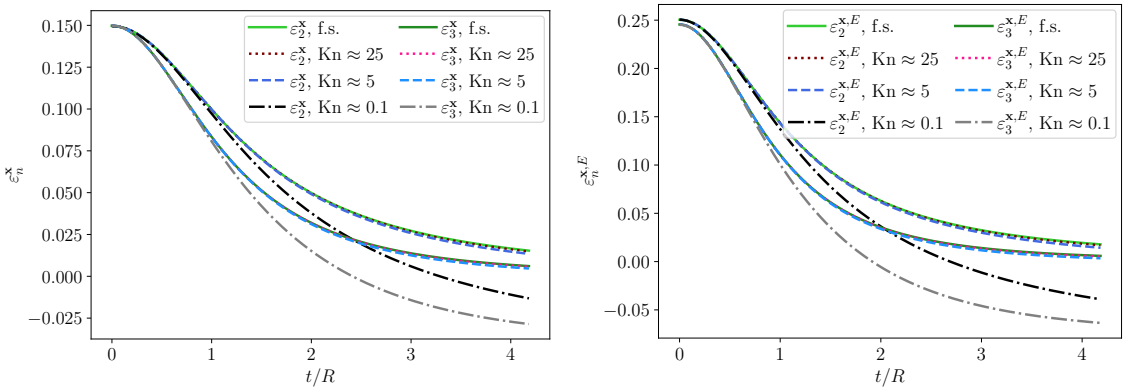

Figure 5.8: Time evolution of the spatial eccentricities in a collisionless (full lines) and in an interacting system with few rescatterings (dotted and dashed lines). The left panel shows particle-number weighted eccentricities $\varepsilon_2^{\mathbf{x}}$, $\varepsilon_3^{\mathbf{x}}$, the right panel eccentricities $\varepsilon_2^{\mathbf{x},E}$, $\varepsilon_3^{\mathbf{x},E}$ with energy weighting. For comparison, we also show the behavior in a system in the fluid-dynamical regime (dotted-dashed lines).

change in the eccentricities there is also a curve at Kn $\approx$ 0.1 in the almost fluid-dynamical regime. These curves deviate strongly from the (almost) free-streaming behavior for $t/R \gtrsim 1$, as the anisotropic flow which is generated needs time to develop and have some effect on the systems' geometry.

If we want to investigate the influence of rescatterings on the geometric quantities in more detail, we might have a look at the numerator and the denominator of the eccentricities separately. For simplicity we will only look at the numerators and denominators of $\varepsilon_2^{\mathbf{x}}$ and $\varepsilon_2^{\mathbf{x},E}$ here and present the results for the third harmonic in Appendix D.2, as the results are similar. To see the influence of the collisions directly, we subtract the free-streaming result from all curves.

We begin with the numerator of the eccentricity and subtract the free-streaming result. For the $r^2\cos(2\theta)$ we can again look at a particle-weighted or energy-weighted average. In the free-streaming case with no initial anisotropic flow this quantity is supposed to be a constant in time. A departure from this free-streaming case is shown in Fig. 5.9 for Kn $\approx$ 25 (left panel) and 5 (right panel). To make the quantities dimensionless, we have scaled the values by the initial value of the average

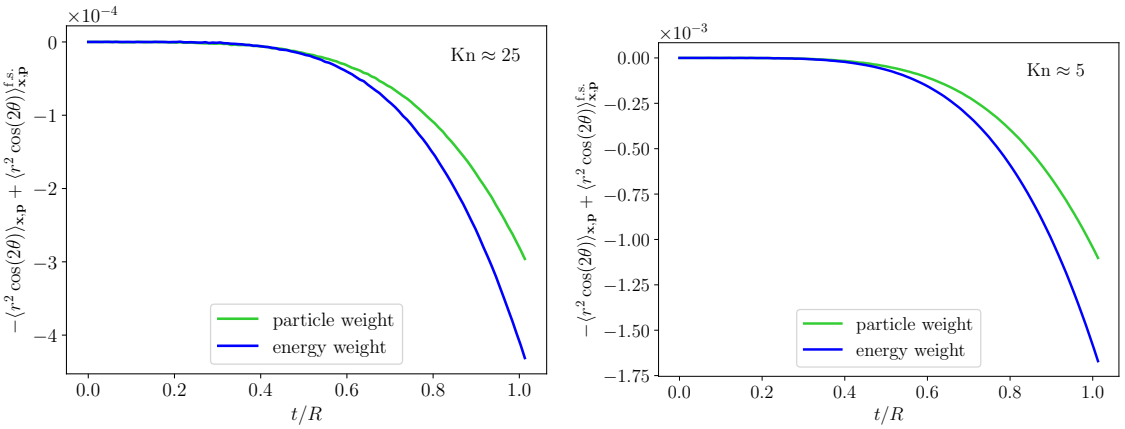

Figure 5.9: Time evolution of the departure of $-\langle r^2\cos(2\theta)\rangle_{\mathbf{x},\mathbf{p}}$ with particle-number (green) and energy (blue) weighting from its free streaming value, for simulations with Kn ≈ 25 (left panel) or Kn ≈ 5 (right panel).

of $r^2\cos(2\theta)$, such that the curves show the relative change of the averaged value caused by rescatterings in the system. First, we notice that the relative change is of the order 10^{-4} in the simulations with Kn ≈ 25 and 10^{-3} at Kn ≈ 5. The signal in the Kn ≈ 5 case is approximately five times larger than at Kn ≈ 25, i.e., it seems to have a scaling proportional to Kn^{-1} or σ or $N_{\mathrm{resc.}}$.

For a further quantification of this behavior we tried to fit the curves in Fig. 5.9 with a power-law ansatz

$$-\left\langle r^2\cos(2\theta)\right\rangle_{\mathbf{x},\mathbf{p}}(t)+\left\langle r^2\cos(2\theta)\right\rangle^{\mathrm{f.s.}}_{\mathbf{x},\mathbf{p}}\propto\left(\frac{t}{R}\right)^{\chi}. \tag{5.14}$$

Similar to the procedure in Sec. 5.2 we perform several fits starting at $t = 0$ and ending at t/R in a range from 0.35-0.7. These fits with different end points result in exponents which are in the range $\chi = 3.5$-5.5 indicating a rather slow growth in time. Again we can use knowledge from Sec. 5.2 and the fits for the $v_3(t)$ behavior we know that this might hint to an exponent which is $\chi \geq 4$, but it is hard to make a strong statement here. The signal in Fig. 5.9 is one or two orders of magnitude smaller than the $v_3(t)$ signals which were already in the regime where the interpretation of the results become difficult due to the fluctuations.

From the analytical point of view one can say that using particle-number or energy conservation, depending on the weight used for the average, leads to vanishing contributions at order t^2 or below, such that the scaling has to obey $\chi \geq 3$ [102]. Additionally one can show that contributions from the loss term in the $2 \to 2$ kernel vanish at all orders due to parity arguments in momentum space. As we are not able to compute the gain term contributions, we can only say that $\chi \geq 3$ has to be fulfilled, which is in agreement with the numerical findings.

Now we investigate the denominator of $\varepsilon_2^{\mathbf{x}}$, which is the definition of the mean square radius of the system. This quantity is obviously changing in time even without collisions, as the system expands. In free-streaming the quantity obeys

$$\left\langle r^2\right\rangle^{\mathrm{f.s.}}_{\mathbf{x},\mathbf{p}}(t)=\left\langle r^2\right\rangle_{\mathbf{x},\mathbf{p}}(0)+\left\langle v^2\right\rangle_{\mathbf{x},\mathbf{p}}(0)t^2, \tag{5.15}$$

with v^2 the squared transverse velocity of the particles. In our case, since the particles are massless, it is the squared velocity of light.

Figure 5.10 shows the departure $\langle r^2 \rangle_{\mathbf{x},\mathbf{p}}(t) - \langle r^2 \rangle^{\text{f.s.}}_{\mathbf{x},\mathbf{p}}(t)$ of the mean square radius from a system without collisions, again scaled by the initial value of $\langle r^2 \rangle_{\mathbf{x},\mathbf{p}}$. The

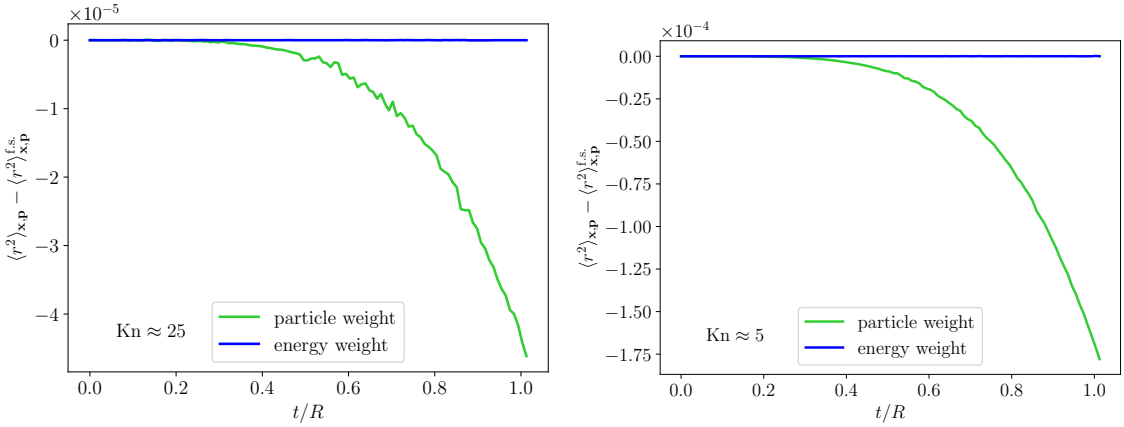

Figure 5.10: Time evolution of the departure of $\langle r^2 \rangle_{\mathbf{x},\mathbf{p}}$ with particle-number (green) or energy (blue) weighting from its free streaming behavior, for simulations with Kn ≈ 25 (left panel) or Kn ≈ 5 (right panel).

negative signal tells us that the expansion of the system is slowed down by the collisions, which seems quite intuitive: an acceleration of the outgoing particles is not possible, as the particles are already moving at the speed of light. Again, we can find a factor five going from Kn ≈ 25 to 5 and therefore the scaling seems to be linear in the Knudsen number. As for the numerator of the eccentricity we performed a power-law fit with

$$\left\langle r^2 \right\rangle_{\mathbf{x},\mathbf{p}} - \left\langle r^2 \right\rangle^{\text{f.s.}}_{\mathbf{x},\mathbf{p}} \propto \left(\frac{t}{R} \right)^{\chi'} \tag{5.16}$$

finding exponents in the range $\chi' = 4.1\text{-}4.5$ for the different end points of the fit. Analytically we find $\chi' \geq 3$ [102], which is again consistent with the findings from the fit.

For the mean square radius there is an important difference between the particle-weighted and energy-weighted average. In the case of the energy-weighted average we find in Fig. 5.10 that the quantity is a constant in time. An analytical proof for this is shown in Appendix D.1. It is important to note that this holds only in the case of two dimensions and massless particles. Additionally for $\langle r^3 \rangle_{\mathbf{x},\mathbf{p}}$ there is a time dependence, as is shown in Appendix D.2. The study of $\langle r^2 \rangle_{\mathbf{x},\mathbf{p}}$ and $\langle r^3 \rangle_{\mathbf{x},\mathbf{p}}$ for the different weights in the average shows that the transport of energy density and particle density is not connected via a one-to-one relationship.

5.6 Alternative measures of anisotropic flow

As mentioned before, there are several alternative possibilities how to quantify anisotropic collective flow. Now we want to compute the anisotropic flow differently and compare the early time behavior to the results from Secs. 5.2 and 5.4.

The first possibility we want to look at is the Fourier harmonics of the transverse energy distribution, which was also investigated in a number of recent kinetic theory studies [84, 98–101]. These "energy weighted flow coefficients" are defined by

$$v_n^E(t) \equiv \frac{\int E f(t,\mathbf{x},\mathbf{p}) \cos\left[n\left(\phi_\mathbf{p} - \Psi_n^E\right)\right] \, \mathrm{d}^2\mathbf{x}\mathrm{d}^2\mathbf{p}}{\int E f(t,\mathbf{x},\mathbf{p}) \, \mathrm{d}^2\mathbf{x}\mathrm{d}^2\mathbf{p}} \tag{5.17}$$

with the n-th harmonic event plane Ψ_n^E. The factor E in the integrals is the only difference to the "particle weighted flow harmonics" used in the sections before. Here, we have $\Psi_n^E = 0$, as we consider the initial-state symmetry plane to be oriented with $\Phi_n = 0$.

In our considered case (massless particles) and with $p_z = 0$, the energy-weighted elliptic flow v_2^E coincides with the definition in fluid-dynamical simulations [88,108][11] and reads

$$\varepsilon_2^\mathbf{p} \equiv \frac{\int \left[T^{xx}(\mathbf{x}) - T^{yy}(\mathbf{x})\right] \, \mathrm{d}^2\mathbf{x}}{\int \left[T^{xx}(\mathbf{x}) + T^{yy}(\mathbf{x})\right] \, \mathrm{d}^2\mathbf{x}} \tag{5.18}$$

for our two-dimensional setup. The two diagonal components of the energy momentum tensor T^{xx} and T^{yy} can be computed from

$$T^{\mu\nu}(\mathbf{x}) \equiv \int p^\mu p^\nu f(t,\mathbf{x},\mathbf{p}) \, \frac{\mathrm{d}^2\mathbf{p}}{E}. \tag{5.19}$$

In contrast to the other definitions of anisotropic flow the form in Eq. (5.18) can be used on the level of an energy momentum tensor and makes a "particlization" procedure with a Cooper-Frye approach redundant.

Similar to Sec. 5.2 we want to find out how $\varepsilon_2^\mathbf{p}$ scales at early times for different Knudsen numbers. So we have again a look at the $2 \to 2$ collision kernel and at Knudsen numbers ranging from 0.02 up to 25 for the onset of $\varepsilon_2^\mathbf{p}(t) = v_2^E(t)$ shown in Fig. 5.11. We use again a power-law ansatz

$$\varepsilon_2^\mathbf{p}\left(\frac{t}{R}\right) = \beta_2'\left(\frac{t}{R}\right)^{\gamma_2'} \tag{5.20}$$

to perform 500 fits with different time intervals to map out the whole range of possible values for γ_2' displayed in the right panel of Fig. 5.11. We find that the behavior of γ_2' for varying Kn is similar to the one for γ_2 (Fig. 5.2). There is a change from $\gamma_2' \approx 2$ in the hydrodynamical regime to $\gamma_2' \approx 3$ in the few collisions limit. The statement here is that $\varepsilon_2^\mathbf{p}(t)$ behaves as $v_2(t)$ for early times.

With arguments from Sec. IV.1 in Ref. [102] one finds in the absence of initial flow that the leading contribution is

$$\varepsilon_2^\mathbf{p}(t) \propto \sigma t^3 + \mathcal{O}(t^4), \tag{5.21}$$

[11] Note the misprint in the definition of $\varepsilon_2^\mathbf{p}$ in Eq.(3.2) of Ref. [108], as mentioned in Ref. [109].

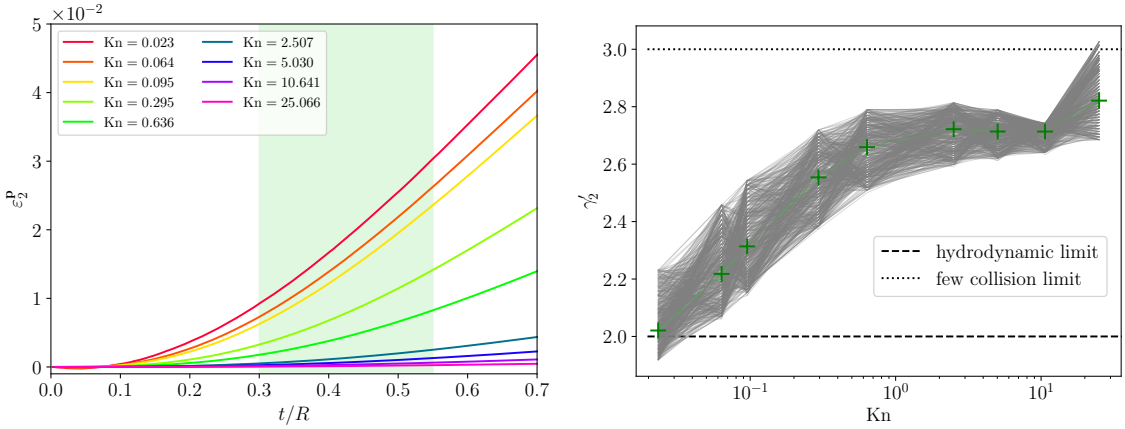

Figure 5.11: Left panel: Early time dependence of $\varepsilon_2^{\mathbf{P}} = v_2^E$ for various Knudsen numbers. Right panel: Dependence of the scaling exponent γ_2' [Eq. (5.20)] on the Knudsen number, using the same color code as in Fig. 5.2.

with the $\mathcal{O}(t^4)$ term contributing already at order σ^2. Again, this coincides with the $v_2(t)$ behavior and it is shown in Fig. 5.11 (right panel) by a dotted line.

In the next step we computed the Taylor series approach up to $\mathcal{O}(t^9)$ at order σ with the $2 \to 0$ collision kernel and compare it to the simulations including the same kernel in Fig. 5.12. There is a nice agreement between both approaches until

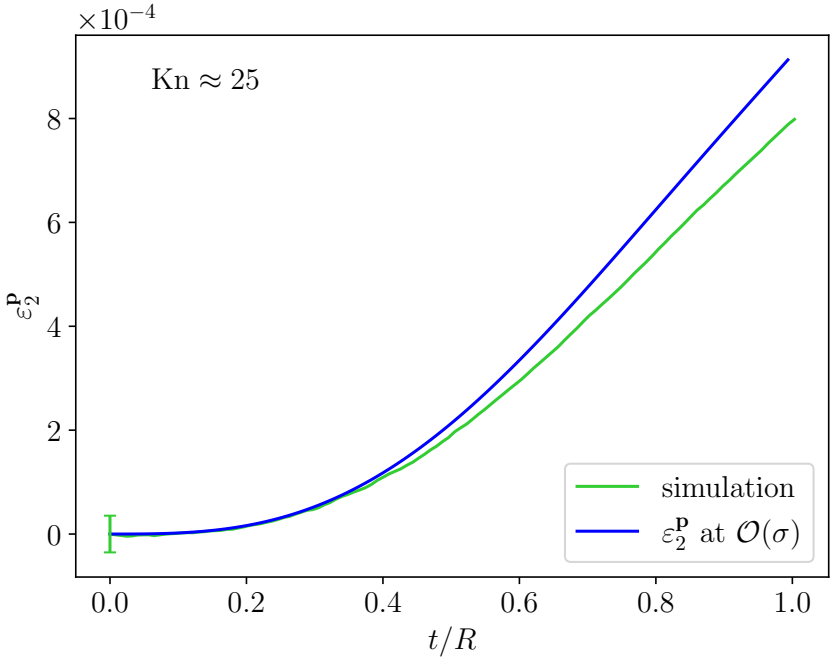

Figure 5.12: Early time evolution of $\varepsilon_2^{\mathbf{P}} = v_2^E$ at Kn ≈ 25. The results of the $2 \to 0$ simulation are shown in green, the analytical calculation at $\mathcal{O}(\sigma)$ in blue.

$t/R \simeq 0.4$ which could be improved, in a similar way as for $v_2(t)$, by including more powers in σ and t. As the analytical computations are already quite extensive, we do not perform these calculations any more.

Going now to $n = 3$ we can discuss the energy-weighted triangular flow $v_3^E(t)$ shown in Fig. 5.13 for the $2 \to 0$ kernel simulations (green) at Kn ≈ 25 (left panel)

and Kn ≈ 5 (right panel). The energy-weighted triangular flow is significantly larger

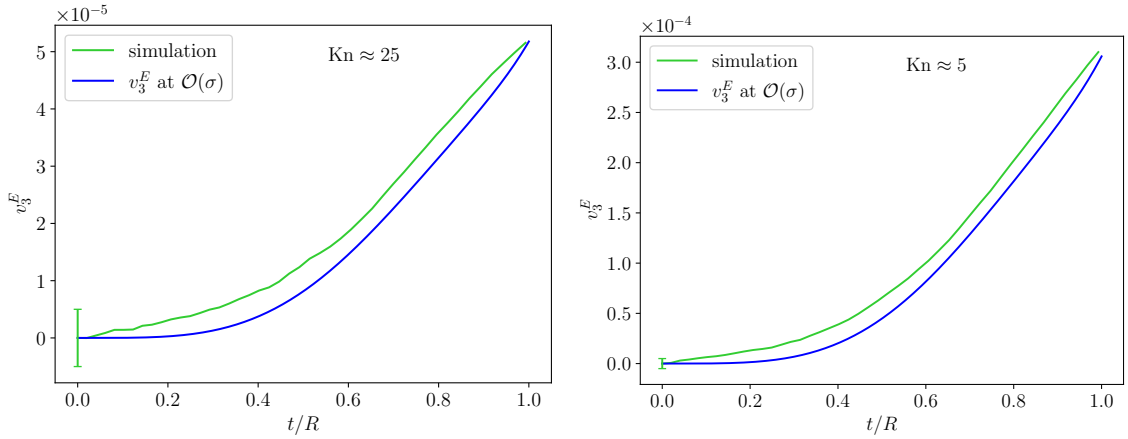

Figure 5.13: Early time development of energy-weighted triangular flow v_3^E for Kn ≈ 25 (left panel) and Kn ≈ 5 (right panel) from numerical simulations with the $2 \to 0$ collision kernel (green) and analytical calculations at $\mathcal{O}(\sigma)$ (blue).

than the particle-number weighted triangular flow (Fig. 5.6) and also less sensitive to initial-state fluctuations of the flow signal. The blue curves in Fig. 5.13 show the analytical results at linear order in the cross section and including terms up to order t^{10}. In contrast to the $v_3(t)$, which scales as $\mathcal{O}(\sigma^2)$, the $v_3^E(t)$ is already present at order σ. We find a good agreement between analytical and numerical results for both Knudsen numbers while taking into account the initial-state fluctuations of the simulation results, which lead to a linear growth at small t/R. Using more powers in t and σ in the analytical calculations could also improve the fact that the curvature around $t/R \approx 1$ is different, but this is not our goal.

Above it was discussed that the particle based description of anisotropic flow has the need for a particlization process if hydrodynamical models are used and thus a description using Eq. (5.18) is more natural on the level of an energy momentum tensor. However, the generalization of $\varepsilon_2^{\mathrm{P}}$ to higher harmonics is not straightforward. This was the reason why in Ref. [37] a definition was introduced on the "macroscopical" level for fluid-dynamical descriptions, which is generalizable to higher harmonics. Indeed, this generalized flow measure can be used in any microscopical model as well. Adapted to our two-dimensional setup the measure for elliptic flow from Ref. [37] is given by

$$\alpha_2^{\mathrm{P}} \equiv \frac{\int \left[T^{0x}(\mathbf{x})u_x(\mathbf{x}) - T^{0y}(\mathbf{x})u_y(\mathbf{x})\right] \mathrm{d}^2\mathbf{x}}{\int T^{00}(\mathbf{x})u_0(\mathbf{x})\, \mathrm{d}^2\mathbf{x}}, \tag{5.22}$$

with the flow velocity $u^\mu(\mathbf{x})$. Considering only a single particle species the natural choice for it is

$$u^\mu(\mathbf{x}) = \frac{N^\mu(\mathbf{x})}{\sqrt{N^\mu(\mathbf{x})N_\mu(\mathbf{x})}}, \tag{5.23}$$

with

$$N^\mu(\mathbf{x}) \equiv \int p^\mu f(t,\mathbf{x},\mathbf{p})\,\frac{\mathrm{d}^2\mathbf{p}}{E}. \tag{5.24}$$

From the analytical point of view the implementation of $\alpha_2^{\mathbf{p}}$ is straightforward, as $f(t,\mathbf{x},\mathbf{p})$ is known. Implementing the observable in the transport simulations is more challenging, as the energy momentum tensor is not computed at each point in space and time. This is why we have to divide the system into $N_{\text{cells}} = 40^2$ cells on a rectangular grid. Here, we have checked that the results do not depend on the number of cells by varying the number from $N_{\text{cells}} = 20^2$ to $N_{\text{cells}} = 120^2$ using $N_{\text{p}} = 5 \times 10^5$ particles. When using more than $N_{\text{cells}} = 60^2$ cells the signal starts to fluctuate, as there are too few particles inside the cells. This could be solved by using even more particles. For each cell the sum of the momentum components p_x and p_y are computed, which are denoted by P_x resp. P_y. We also need the total energy $E_{\text{tot.}}$ in each cell, the number of particles and the mean velocity per particle $\bar{\mathsf{v}}_x \equiv \mathsf{P}_x/E_{\text{tot.}}$ and $\bar{\mathsf{v}}_y \equiv \mathsf{P}_y/E_{\text{tot.}}$. Using these definitions we can approximate the numerator of Eq. (5.22) by

$$\left\langle T^{0x}u_x - T^{0y}u_y \right\rangle_{\mathbf{x}} \approx \frac{1}{N_{\text{cells}}} \sum_{i=1}^{N_{\text{cells}}} \frac{\mathsf{P}_{x,i}\bar{\mathsf{v}}_{x,i} - \mathsf{P}_{y,i}\bar{\mathsf{v}}_{y,i}}{\sqrt{1-\bar{\mathsf{v}}_{x,i}^2 - \bar{\mathsf{v}}_{y,i}^2}} \tag{5.25}$$

and the denominator by

$$\left\langle T^{00}u_0 \right\rangle_{\mathbf{x}} \approx \frac{1}{N_{\text{cells}}} \sum_{i=1}^{N_{\text{cells}}} \frac{E_{\text{tot.},i}}{\sqrt{1-\bar{\mathsf{v}}_{x,i}^2 - \bar{\mathsf{v}}_{y,i}^2}}. \tag{5.26}$$

The denominator in the latter expressions is due to the normalization of the velocity.

For the analytical setup it is important to compute the free-streaming case, which is for $\alpha_2^{\mathbf{p}}$ not a constant but has a quadratic time dependence:

$$\alpha_2^{\mathbf{p}}(t) \propto t^2 + \mathcal{O}(t^3). \tag{5.27}$$

The proportionality factor of the t^2 term actually includes the spatial eccentricity $\varepsilon_2^{\mathbf{x}}$, which means that elliptic flow can develop even if there are no collisions in the system.

Introducing collisions in the system modifies the t^3 order, which is consistent with the onset of $v_2(t)$ or $\varepsilon_2^{\mathbf{p}}(t)$ but subleading to the free-streaming behavior.

Figure 5.14 shows the early time $\alpha_2^{\mathbf{p}}(t)$ for the case of a $2 \to 2$ collision kernel with intermediate number of rescatterings (orange line), in free-streaming (green line) and for the analytical case with free-streaming (dotted blue). As stated above, the collisions lead to a departure from the free-streaming case starting from $t/R \approx 0.8$ only and have a subleading effect at early times.

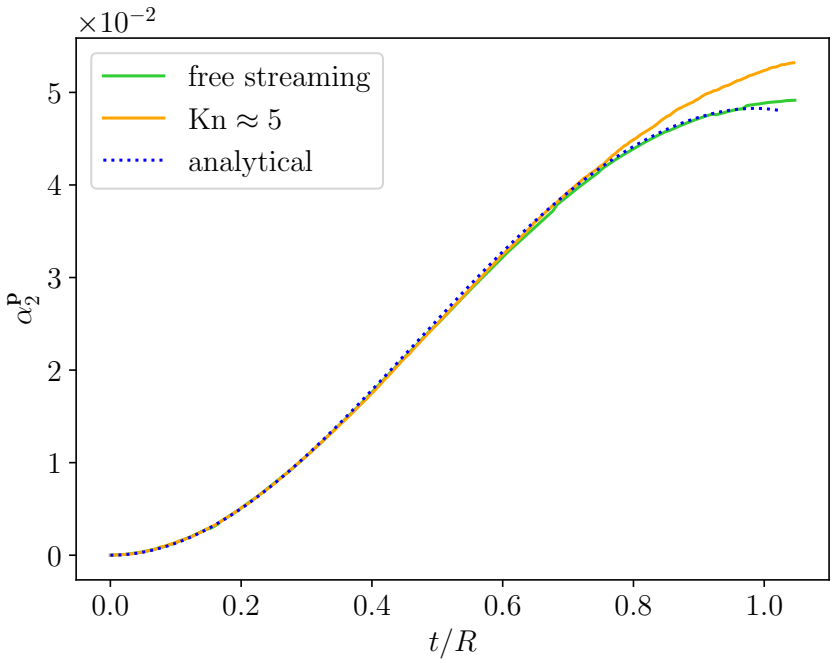

Figure 5.14: Time dependence of α_2^{P} for simulations (full lines) in a collisionless (green) system or in the few collisions regime (orange), together with the analytical result in the free streaming case (dotted blue line).

Chapter 6

Different origins of even and odd anisotropic flow harmonics at large Knudsen numbers

This chapter is based on Ref. [107]:

- *Even anisotropic-flow harmonics are from Venus, odd ones are from Mars*
  B. Bachmann, N. Borghini, N. Feld, H. Roch
  arXiv: 2203.13306 [nucl-th]

In this work we tested how efficient the "escape mechanism" translates initial spatial anisotropies into anisotropic flow. By comparison of three different setups we find that the even anisotropic flow harmonics behave similar in all approaches, while the odd flow harmonics behave different.

The analytical computations in this work were performed by Nicolas Borghini and Nina Feld. One of the simulation setups, i.e., the $2 \to 0$ collision kernel (Sec. 3.4.6), was implemented in the code by Benedikt Bachmann. All numerical calculations in this work were performed by the author.

As mentioned above we have three different setups to investigate the production of the anisotropic flow by the "escape mechanism". Two of these scenarios are numerical simulations with the transport code, one with the $2 \to 2$ collision kernel (Sec. 3.4.3-3.4.5) and another one with the $2 \to 0$ collision kernel (Sec. 3.4.6). The $2 \to 0$ simulations give the flow of the particles which did not undergo a collision during the time evolution of the system, i.e., which "escaped". The analytical setup

uses kinetic theory including the loss term of the Boltzmann equation only and including the first order in the cross section, which gives an approximation of the $2 \to 0$ scenario.

6.1 Analytical approach

We start by introducing the analytical approach which uses the classical on-shell phase space distribution f obeying the relativistic Boltzmann equation

$$p^\mu \partial_\mu f(t, \mathbf{x}, \mathbf{p}) = \mathcal{C}[f(t, \mathbf{x}, \mathbf{p})]. \tag{6.1}$$

As mentioned above, we use the loss term of the collision kernel for binary scatterings

$$\mathcal{C}_{\text{loss}}[f(t, \mathbf{x}, \mathbf{p})] = -\frac{E_\mathbf{p}}{2} \int f(t, \mathbf{x}, \mathbf{p}) f(t, \mathbf{x}, \mathbf{p}_1) v_{\text{Møller}} \sigma \, \mathrm{d}^2\mathbf{p}_1 \tag{6.2}$$

with E_p the energy of a particle with momentum $\mathbf{p}$, the Møller velocity $v_{\text{Møller}}$ and the total cross section σ. Let us emphasize again, that this collision kernel does not conserve particle number during the time evolution. The Møller velocity for massless particles in two dimensions can be expressed by $v_{\text{Møller}} = 1 - \cos(\varphi_\mathbf{p} - \varphi_1)$ where $\varphi_\mathbf{p}$ and φ_1 are the azimuths of the particle momenta $\mathbf{p}$ resp. $\mathbf{p}_1$.

Our main characteristic quantity is anisotropic flow, which is given by the Fourier coefficients of the particle distribution [15]. The flow coefficients were defined in Eq. (1.6). Note, that we use the distribution function $f(t, \mathbf{x}, \mathbf{p})$ here such that in Eq. (1.6) one has to integrate over the position space as well. Additionally the distribution function is oriented such that only the cos-part is different from zero.[1] We can write the flow coefficients in our setup as

$$v_n(t) = \frac{\int f(t, \mathbf{x}, \mathbf{p}) \cos(n\varphi_\mathbf{p}) \, \mathrm{d}^2\mathbf{x}\mathrm{d}^2\mathbf{p}}{\int f(t, \mathbf{x}, \mathbf{p}) \, \mathrm{d}^2\mathbf{x}\mathrm{d}^2\mathbf{p}}, \tag{6.3}$$

where the denominator is the particle number $N(t)$ at a given time t. Computing the time derivative gives two contributions:

$$\partial_t v_n(t) = \frac{1}{N(t)} \int \partial_t f(t, \mathbf{x}, \mathbf{p}) \cos(n\varphi_\mathbf{p}) \, \mathrm{d}^2\mathbf{x}\mathrm{d}^2\mathbf{p} - \frac{\partial_t N(t)}{N(t)} v_n(t). \tag{6.4}$$

Then the time derivative of the distribution function $\partial_t f$ can be replaced by the Boltzmann equation. The part including the spatial gradient of f vanishes when integrating over the position space variable $\mathbf{x}$, such that the only remaining contribution is due to the collision term of the Boltzmann equation. This term is at leading order linear in the cross section σ. Restricting ourselves to this order of the cross section we may neglect the change in the particle number due to only considering the loss term which does not conserve the particle number. We can approximate the denominator in the first term in Eq. (6.4) by $N(t) \simeq N(0)$, which we will denote

[1] For the simulations this is only true up to numerical fluctuations due to the finite number of particles.

by N in the following. A second approximation is that we neglect the evolution of the phase-space density due to rescatterings in the numerator as well, which means that we replace $f(t, \mathbf{x}, \mathbf{p})$ by the free-streaming distribution $f_{\text{f.s.}}(t, \mathbf{x}, \mathbf{p})$ coinciding with f initially [10, 96, 97]:

$$f_{\text{f.s.}}(t, \mathbf{x}, \mathbf{p}) = f^{(0)}(\mathbf{x} - \mathbf{v}t, \mathbf{p}). \tag{6.5}$$

Here $\mathbf{v} \equiv \mathbf{p}/|\mathbf{p}|$ and the distribution function at $t = 0$ is denoted by $f^{(0)}(\mathbf{x} - \mathbf{v}t, \mathbf{p})$.

Going to the second term of Eq. (6.4), the derivative $\partial_t N(t)$ is (at least) of order $\mathcal{O}(\sigma)$. If there is no "preflow" in the system then the $v_n(t)$ is also of order $\mathcal{O}(\sigma)$, such that in total the term is at least of order $\mathcal{O}(\sigma^2)$ and will be neglected from now on. It is important to note that the term contributes at linear order in the cross section and if the flow is initially not vanishing it may not be dropped.

Considering the previous discussion the evolution equation (6.4) is replaced by

$$\partial_t v_n(t) = \frac{1}{N} \int \frac{\mathcal{C}[f_{\text{f.s.}}(t, \mathbf{x}, \mathbf{p})]}{E_{\mathbf{p}}} \cos(n\varphi_{\mathbf{p}}) \, \mathrm{d}^2\mathbf{x}\mathrm{d}^2\mathbf{p}, \tag{6.6}$$

which is valid at order $\mathcal{O}(\sigma)$ for all collision terms which are of the same order in the cross section. When inserting the loss term (6.2) for the collision kernel and performing the time integral, we are left with

$$\begin{aligned} v_n(t) &= -\frac{\sigma}{2N} \int_0^t \int f_{\text{f.s.}}(t', \mathbf{x}, \mathbf{p}) f_{\text{f.s.}}(t', \mathbf{x}, \mathbf{p}_1)[1 - \cos(\varphi_{\mathbf{p}} - \varphi_1)] \cos(n\varphi_{\mathbf{p}}) \, \mathrm{d}^2\mathbf{x}\mathrm{d}^2\mathbf{p}\mathrm{d}^2\mathbf{p}_1\mathrm{d}t' + \mathcal{O}(\sigma^2) \\ &= \int_0^t \int_0^\infty D_n(t', r) r \, \mathrm{d}r\mathrm{d}t' + \mathcal{O}(\sigma^2). \end{aligned} \tag{6.7}$$

The second line is the definition of the angle-averaged local v_n production rate [100] discussed in Sec. 6.7. These expressions assume that $v_n(t = 0) = 0$.

Within the analytical approach the anisotropic flow coefficients are directly related to the initial state phase distribution $f^{(0)}$ via Eq. (6.5), which will be discussed now. A first assumption we make is that $f^{(0)}$ factorizes into the particle number density, giving the geometry of the system, and a momentum distribution:

$$f^{(0)}(\mathbf{x}, \mathbf{p}) = F(\mathbf{x})G(\mathbf{p}), \tag{6.8}$$

where the function G is normalized to unity, when integrating over momentum space. The reason for this factorization assumption is that otherwise the analytical calculations are not tractable, which give us analytical expressions for the flow coefficients when assuming the spatial distribution (6.9). However, this assumption is not harmless, especially when considering the odd flow harmonics later on. G is chosen isotropic in momentum space to have no anisotropic flow in the initial state. If initial flow should be considered it is possible to include it via a Fourier expansion of $G(\mathbf{p})$ [110].[2]

[2]The inclusion of preflow leads to rather lengthy expressions and the evolution at leading order in σ is no longer guaranteed due to the second term in Eq. (6.4) discussed above.

Our position space distribution is a distorted Gaussian

$$F(r,\theta) = \frac{Ne^{-r^2/2R^2}}{2\pi R^2}\left[1 - \sum_{j=2}^{6} \tilde{\varepsilon}_j e^{-r^2/2R^2} \left(\frac{r}{R}\right)^j \cos(j\theta)\right], \tag{6.9}$$

with particle number N and the typical system size R which is used to make lengths and time dimensionless in the following. Recent studies [80, 81, 84, 99–101] have used the same distribution functions quite extensively, as it gives the possibility to implement eccentricities (2.25) for the initial state which are independent of each other.[3] To cross check our results we computed the flow harmonics also using a different distribution function in position space in Appendix E.3. The $\tilde{\varepsilon}_n$ coefficients in Eq. (6.9) are related to the eccentricities defined in Eq. (2.25) by

$$\varepsilon_n = \frac{(n-1)!}{2^{\frac{2+n}{2}}\Gamma\left(\frac{n}{2}\right)}\tilde{\varepsilon}_n, \tag{6.10}$$

which is $\varepsilon_2 = \tilde{\varepsilon}_2/4$, $\varepsilon_3 = \tilde{\varepsilon}_3/\sqrt{2\pi}$, $\varepsilon_4 = 3\tilde{\varepsilon}_4/4$, and so on.[4] To ensure the positivity of the distribution function the values of $\tilde{\varepsilon}_n$ should not be too large. In typical cases with only a single eccentricity the maximum $\tilde{\varepsilon}_n$ should be chosen such that $\varepsilon_n < \varepsilon_{n,\max} \simeq 0.35$, which is the case in all our calculations. The typical value we used is $\tilde{\varepsilon}_n$ such that $\varepsilon_n = 0.15$ or even zero in Sec. 6.2 when computing the number of rescatterings.

6.2 Numerical simulations

The numerical setup for this work was extensively described in Sec. 3.4.3-3.4.5 for the $2 \to 2$ collision kernel and in Sec. 3.4.6 for the $2 \to 0$ collision kernel. So here we will just recall the most basic ingredients of the simulation setup. We use N massless particles modeled by N_p test particles with radius $(N/N_\mathrm{p})\sigma/2$. σ is the total cross section of the "physical" particles.

Let us also discuss the most important difference between the $2 \to 0$ simulation and the analytical results. In the simulation the phase-space distribution is changed by rescatterings, which is not the case in the analytical calculation, thus the simulation contains all orders in the cross section and we may depart from the few-collision regime to see how the flow signal behaves when most of the particles disappear from the system.

Ref. [111] introduced a similar approach with $2 \to 2$ and $2 \to 0$ collision kernels, with the difference that their $2 \to 0$ kernel still treats particles as "active" after a collision, but randomizes their momentum azimuths. In that case the particles still contribute to the generation of anisotropic flow in this AMPT version.

The initial state of the simulations is sampled from the distribution function (6.9), while momenta are chosen to be Boltzmann distributed with a position-independent

[3] The distribution function (6.9) directly implies $\Phi_n = 0$ in Eq. (2.25), which we assume here without loss of generality by considering only a single $\varepsilon_n \neq 0$ at a time.

[4] Note, that we will drop the exponent $\mathbf{x}$ for the spatial eccentricities from now on, as from now on there can not be any confusion with the energy-weighted elliptic flow defined in Eq. (5.18) and which is not considered in the following.

temperature. This is different to the setup used in Ch. 5. In this work we used N_p ranging from 2×10^5 to 2×10^6 test particles, which still leads to anisotropies in momentum space and non uniform parts of the momentum distribution across the whole geometry. Fixing the initial particle positions and resampling the momenta for multiple iterations $N_\mathrm{iter.}$ improves the situation. Presented results are averaged over the $N_\mathrm{iter.}$ iterations. We assured that the product $N_\mathrm{p} N_\mathrm{iter.}$ is always larger than 10^9 for the simulations.

When considering Eq. (6.9), the average particle number density in two dimensions is $N/4\pi R^2$. Together with the definition of the Knudsen number (Eq. (3.24)) we obtain

$$\mathrm{Kn} = \frac{4\pi R}{N\sigma}. \tag{6.11}$$

This dimensionless number is used to quantify the number of rescatterings in the system. The average number of rescatterings per particle $N_\mathrm{resc.}$ computed for the whole time evolution scales linearly with Kn^{-1} as shown in Fig. 6.1 for the $2 \to 2$ simulations. In practice we compute this number at $t/R = 30$. For the $2 \to 0$

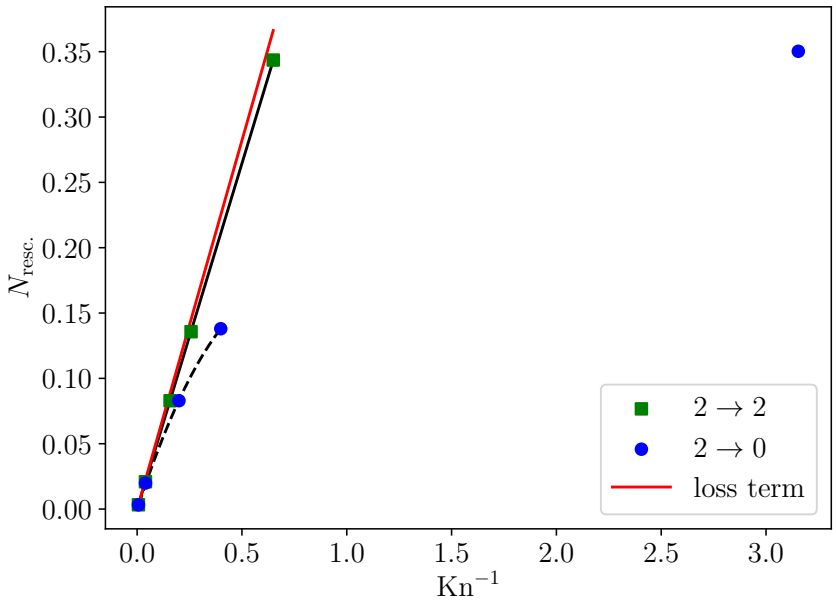

Figure 6.1: Mean number of rescatterings per particle over the system evolution as a function of the inverse Knudsen number estimated in the initial state, Eq. (6.11), for the $2 \to 2$ (green squares, fit with $N_\mathrm{resc.} \approx 0.529\,\mathrm{Kn}^{-1}$) and $2 \to 0$ (blue circles, fitted with a quadratic ansatz: dashed line) scenarios. The red line $N_\mathrm{resc.} = \mathrm{Kn}^{-1}/\sqrt{\pi}$ is the prediction of the analytical approach.

scenario a given value of $N_\mathrm{resc.}$ needs a larger Kn^{-1}, i.e., cross section due to the faster dilution of the system caused by the fact that particles can only scatter once. The following results are mostly in the few-rescatterings regime $N_\mathrm{resc.} \approx 0.02$ and in a regime with more rescatterings ($N_\mathrm{resc.} \approx 0.14$), where the approximations are not that well justified. In Appendix E.2 we show some results for $N_\mathrm{resc.} \approx 0.35$ which clearly violates the assumption that the distribution function is to a good extent approximated by the free-streaming distribution at all times.

6.3 Elliptic flow

We start our discussion of the flow harmonics with elliptic flow [16] using the initial spatial profile (6.9) with only $\tilde{\varepsilon}_2$ such that $\varepsilon_2 = 0.15$.[5] Figure 6.2 shows the time dependence of v_2 for $N_{\text{resc.}} \approx 0.02$ (left panel) and $N_{\text{resc.}} \approx 0.14$ (right panel) using the $2 \to 2$ (green) and $2 \to 0$ (blue) transport codes.[6] The error bar at $t = 0$

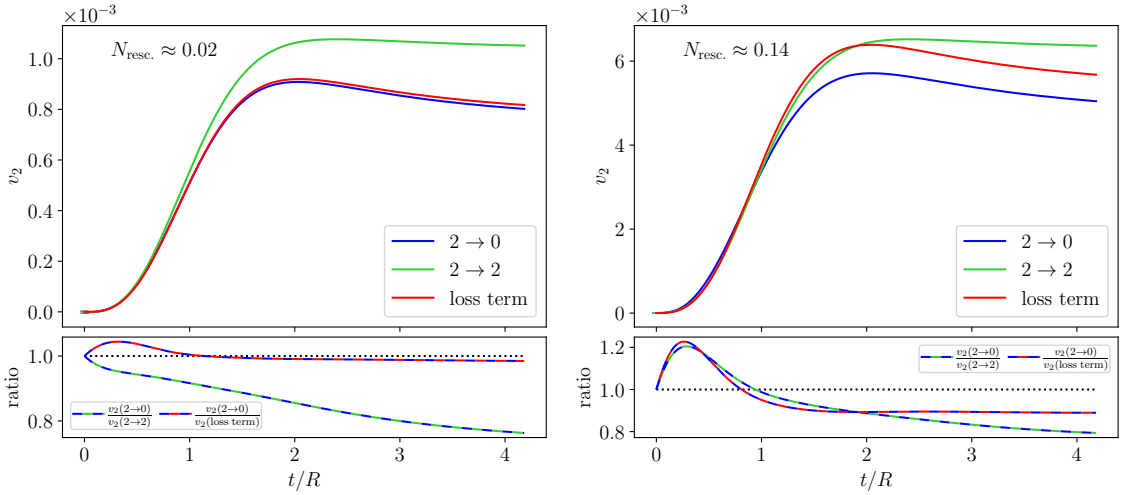

Figure 6.2: Left: Time dependence of elliptic flow v_2 in systems with initially $\varepsilon_2 = 0.15$ and on average $N_{\text{resc.}} \approx 0.02$ (left) or 0.14 (right) rescatterings per particle. The green curves are for systems with elastic binary scatterings, the blue lines for the $2 \to 0$ scenario and the red ones show the analytical result (6.12). The bottom panels show ratios of the curves from the upper panels.

indicates the statistical error $1/\sqrt{2N_{\text{iter.}}N_{\text{p}}}$ of the flow signal in the initial state. Analytical results for v_2

$$v_2(t) = \frac{8}{27}\text{Kn}^{-1}\,\varepsilon_2\,\mathrm{e}^{-2t^2/3R^2}\left[\left(\frac{3R}{t}+\frac{2t}{R}\right)I_1\left(\frac{2t^2}{3R^2}\right)-\frac{t}{R}I_0\left(\frac{2t^2}{3R^2}\right)\right] \tag{6.12}$$

using modified Bessel functions of first kind I_0 and I_1 are shown in red. The inverse Knudsen number for the analytical curve is chosen such that it matches the $N_{\text{resc.}}$ of the simulations. Expanding Eq. (6.12) in time yields $v_2(t) \propto t^3$ for $t \ll R$, which matches the results of previous studies [10, 56, 83, 102].

For a more sophisticated quantification of the deviation between the three different scenarios we fitted the simulation results by Padé approximants

$$v_2(t) \sim \frac{\sum_{k=3}^{5} a_k (t/R)^k}{1+\sum_{k=1}^{5} b_k (t/R)^k} \tag{6.13}$$

after shifting the curves to $v_2(t=0) = 0$. This procedure washes out the numerical fluctuations which are present, especially at early times. One disadvantage is the

[5] In the numerical simulations this value is only reached up to fluctuations due to the finite number of particles.

[6] We show results with $N_{\text{resc.}} \approx 0.35$ in Fig. E.1.

domination of the fit by the values at $t/R \gtrsim 1$ such that the early time behavior is not captured very accurately. With the fits we computed the ratios of the curves in the upper panels of Fig. 6.2, which are shown in the narrower lower panels of the same figure.

We find that the curves are very similar in all three approaches. They have a slow onset, which is followed by an almost linear rise saturating eventually. A maximum v_2 is reached around $t/R \approx 2$ with a small decrease afterwards, which is barely visible in the $2 \to 2$ result. One remarkable finding is that the shape of the curves is quite similar to curves in the fluid-dynamical limit, as presented in Ref. [83] (Fig.3 with a slightly different initial distribution).

What is important for our purposes is that the elliptic flow signal in the $2 \to 0$ scenario differs at most by 20% from the "full" $2 \to 2$ case and the analytical result is extremely well reproduced by the $2 \to 0$ scenario for $N_{\text{resc.}} \approx 0.02$. For $N_{\text{resc.}} \approx 0.14$ the agreement is still reasonable but less impressive due to the higher orders in σ or Kn^{-1} which become important and which are not included in the analytical setup. In Ch. 5 we have shown that one can improve the agreement between the $2 \to 0$ collision kernel and the analytical result by going to higher orders in the cross section, but at the cost that these results are only for early times.

The results in Fig. 6.2 show that in the few-rescatterings regime the v_2 signal is dominated by the processes modeled by the loss term of the Boltzmann equation. This means that the v_2 arises to a large extent from the anisotropic survival probability of particles when propagating through the system [10, 96]. This process is usually called "escape mechanism" picture [111].

6.4 Triangular flow

Turning now to triangular flow v_3 [36] using Eq. (6.9) with only $\tilde{\varepsilon}_3$ such that $\varepsilon_3 = 0.15$, we present simulation results in Fig. 6.3 with $N_{\text{resc.}} \approx 0.02$ (top left), $N_{\text{resc.}} \approx 0.08$ (top right) and $N_{\text{resc.}} \approx 0.14$ (bottom). One of the most obvious results is that the v_3 signal vanishes identically within the analytical approach, if there is no initial flow. A proof of this result involving the cancellation of different spatial regions in our special setup is given in Appendix E.1. An additional discussion is presented in Sec. 6.7 later on. More generally the proof shows that the odd flow harmonics vanish at leading order in σ but it can be non-zero at higher orders [93].

Looking at the numerical results, we see that there are some differences comparing with the elliptic flow. The first difference is the absolute size of the signal, which is an order of magnitude smaller than v_2, such that the numerical noise has a larger impact on the curves and especially on the initial state.[7] A second thing to notice is that the $2 \to 0$ scenario gives a non-zero result, which hints at the fact that this scenario includes all orders in σ and that v_3 arises only at higher order in the cross section.

The third observation is that the $2 \to 0$ results do not match with the $2 \to 2$ scenario. At $N_{\text{resc.}} \approx 0.02$ the $2 \to 0$ result is about a factor 1.5 below, while it is

[7] Considering an analytical calculation with an initial v_3 leads to a slightly evolving signal, which is compared with the transport simulation signals negligible and therefore not shown in Fig. 6.3.

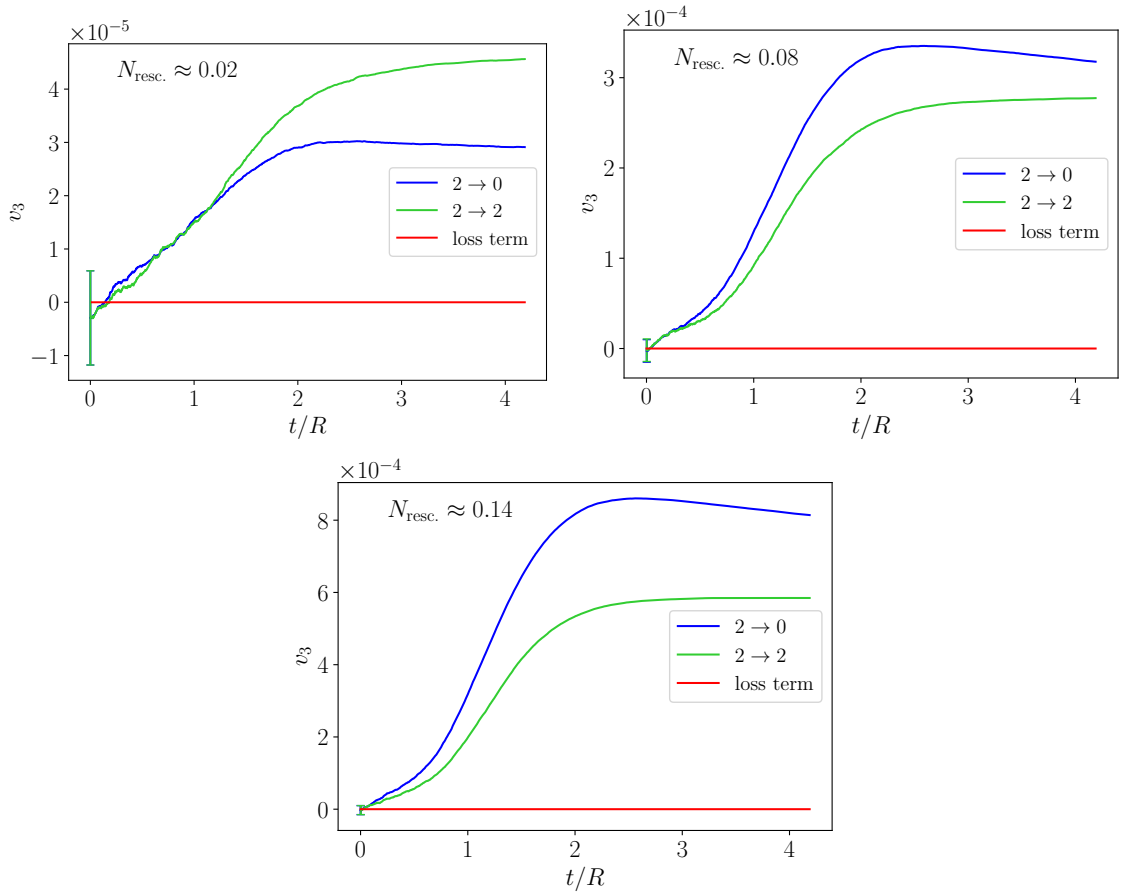

Figure 6.3: Time dependence of triangular flow v_3 in systems with initially $\varepsilon_3 = 0.15$ and on average $N_{\text{resc.}} \approx 0.02$ (top left), 0.08 (top right) or 0.14 (bottom) rescatterings per particle. The green curves are for systems with elastic binary scatterings, the blue lines for the $2 \to 0$ collision kernel. The constant red line $v_3 = 0$ is the output of the analytical approach.

larger at the two larger values of $N_{\text{resc.}}$. In the $2 \to 2$ simulations we find that v_3 scales approximately with $N_{\text{resc.}}$, while in the $2 \to 0$ case it scales rather with $N^2_{\text{resc.}}$.

Instead of particle-number weighted anisotropic flow coefficients in some recent studies "energy weighted triangular flow" v_3^E, i.e., the third Fourier coefficient of the transverse energy distribution, was considered [84, 100, 101]. To compare with the literature, we show v_3^E in Fig. 6.4 for the same systems as in Fig. 6.3. We find again significant differences between the $2 \to 2$ and $2 \to 0$ collision kernels, especially for $t \gtrsim R$. For earlier times the results are closer to each other, which might be a coincidence due to the fluctuations driving the early time behavior. These fluctuations are caused by the finite amount of particles which make it impossible to have an exactly isotropic momentum distribution which is identical everywhere in the transverse plane, such that the numerical setup differs from the idealized scenario.

The v_3 behavior shows a clear difference between the $2 \to 0$ and $2 \to 2$ scenario, which contrasts the findings for v_2 in Sec. 6.3. Additionally we find the difference between the analytical leading order cross section calculation with the numerical results. This is hinting at the gain term describing the final state of the particle

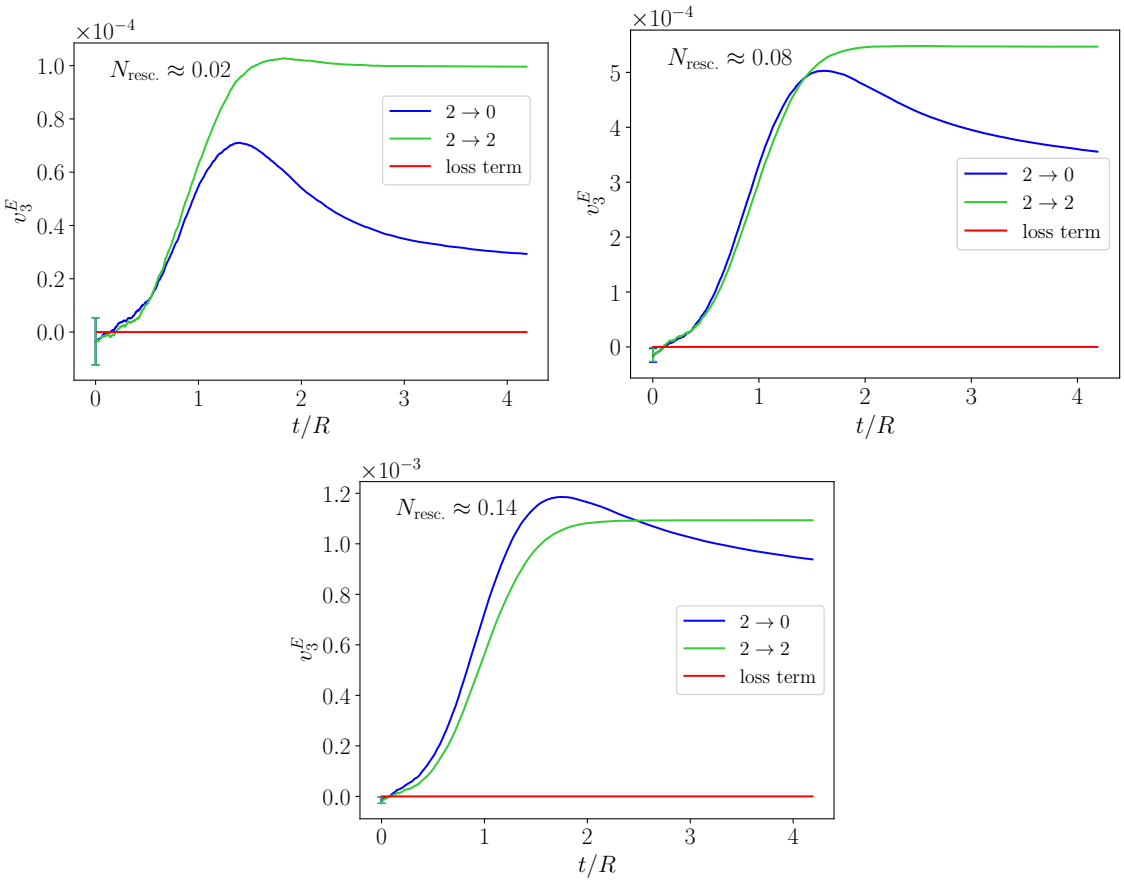

Figure 6.4: Time dependence of energy-weighted triangular flow v_3^E in systems with initially $\varepsilon_3 = 0.15$ and on average $N_{\text{resc.}} \approx 0.02$ (top left), 0.08 (top right) or 0.14 (bottom) rescatterings per particle. The green curves are for systems with elastic binary scatterings, the blue lines for the $2 \to 0$ collision kernel. The constant red line $v_3^E = 0$ is the output of the analytical approach.

rescatterings which seems to have an important role: The v_3 signal is not dominated by particles which underwent no rescatterings and escaped anisotropically from the system.

6.5 Quadrangular flow

For v_4 we find similar results as for the elliptic flow v_2: the numerical $2 \to 2$ and $2 \to 0$ scenario and the analytical result have a good agreement if the number of rescatterings is small. This is again a hint at the escape mechanism playing the dominant role for the v_4 generation in this regime.

For v_n with $n \geq 4$ there exists an additional possibility to generate a signal by nonlinear mixing with other eccentricities. To the present knowledge the flow harmonics with $n \leq 3$ are less affected by nonlinear effects with eccentricities ε_k with $k \neq n$. The v_4 signal might not be caused by the ε_4 only, but also by the ε_2 in the initial state [38, 65, 80, 90, 91].

Assuming only a non-vanishing $\tilde{\varepsilon}_4$ in the initial state the analytical calculation

yields

$$v_4(t) = \frac{16}{1215}\mathrm{Kn}^{-1}\varepsilon_4 \mathrm{e}^{-2t^2/3R^2}\left[\left(\frac{162R^3}{t^3}+\frac{63R}{t}+\frac{24t}{R}+\frac{5t^3}{R^3}\right)I_1\left(\frac{2t^2}{3R^2}\right) - \left(\frac{54R}{t}+\frac{21t}{R}+\frac{5t^3}{R^3}\right)I_0\left(\frac{2t^2}{3R^2}\right)\right], \tag{6.14}$$

while we obtain

$$v_4(t) = -\frac{1}{10}\mathrm{Kn}^{-1}\varepsilon_2^2 \mathrm{e}^{-t^2/R^2}\left[\left(\frac{48R^3}{t^3}+\frac{28R}{t}+\frac{16t}{R}+\frac{5t^3}{R^3}\right)I_1\left(\frac{t^2}{R^2}\right) - \left(\frac{24R}{t}+\frac{14t}{R}+\frac{5t^3}{R^3}\right)I_0\left(\frac{t^2}{R^2}\right)\right] \tag{6.15}$$

assuming that only an $\tilde{\varepsilon}_2$ is present. If there both, a non-vanishing $\tilde{\varepsilon}_2$ and a non-vanishing $\tilde{\varepsilon}_4$ in the initial state, the two terms on the right hand side add up. In Fig. 6.5 we show these analytical results together with the $2 \to 2$ (green) and $2 \to 0$ (blue) results. The upper panels show results with $\tilde{\varepsilon}_4 \neq 0$ leading to $\varepsilon_4 = 0.15$ and the lower panels show results with $\tilde{\varepsilon}_2 \neq 0$ leading to $\varepsilon_2 = 0.15$. All other $\tilde{\varepsilon}_k$ are chosen to be zero in the two cases. The left panels show the v_4 evolution with $N_{\text{resc.}} \approx 0.02$ and the right ones with $N_{\text{resc.}} \approx 0.14$. Again, we present results for $N_{\text{resc.}} \approx 0.35$ in Appendix E.2 in Fig. E.2.

Fig. 6.5 shows that for both initial eccentricities the $2 \to 2$ collision kernel is well approximated by the $2 \to 0$ collision kernel if $N_{\text{resc.}}$ is small. This is supported by the nice agreement with the analytical curves which also shows that $v_4 \propto \sigma$ in the small $N_{\text{resc.}}$ regime. There is a less good agreement for $N_{\text{resc.}} \approx 0.14$ between analytical result and $2 \to 0$ scenario, which can be attributed to the analytical calculation being only at order σ.

From the results in Fig. 6.5 one could deduce that v_4 is — similar to the elliptic flow v_2 — mainly driven by the particles which escaped the system without undergoing a collision in the small $N_{\text{resc.}}$ regime. Nevertheless, there are some important differences between v_2 and v_4. Namely, the v_4 signal changes sign during the time evolution, which does not happen for v_2. Additionally, the shape of the $v_2(t)$ curves is basically the same for all simulations along the Kn^{-1} axis, which is not true for $v_4(t)$. We find that for $N_{\text{resc.}} \gtrsim 5$ in the $2 \to 2$ scenario the v_4 signal from $\varepsilon_4 > 0$ is positive at late times, similar to the results in Ref. [83, 84], but different from the results in Fig. 6.5.[8,9] From this we can deduce that the linear scaling of the large time v_4 in $N_{\text{resc.}}$ breaks at larger cross sections. In Ref. [101] a negative v_4^E was found for a positive initial ε_4 in the few-rescatterings regime, although they used a collision kernel based on the relaxation time approximation. The difference in the collision kernel may be the reason why our results are different at early times (negative v_4) in a scenario with $\varepsilon_2 \neq 0$ and $\varepsilon_4 = 0$ in the initial state.

[8] In this regime the $2 \to 0$ scenario makes no sense, since all the particles would be "inactive" in that case.

[9] The results in Ref. [83] used a different initial profile (Eq. (E.7)). On the other hand the results in Ref. [84] are for energy-weighted flow coefficients v_4^E. We have checked that the energy-weighted flow behaves similar to our setup and it seems that the small $N_{\text{resc.}}$ value in our setup is even smaller than the low-opacity region studied in Ref. [84].

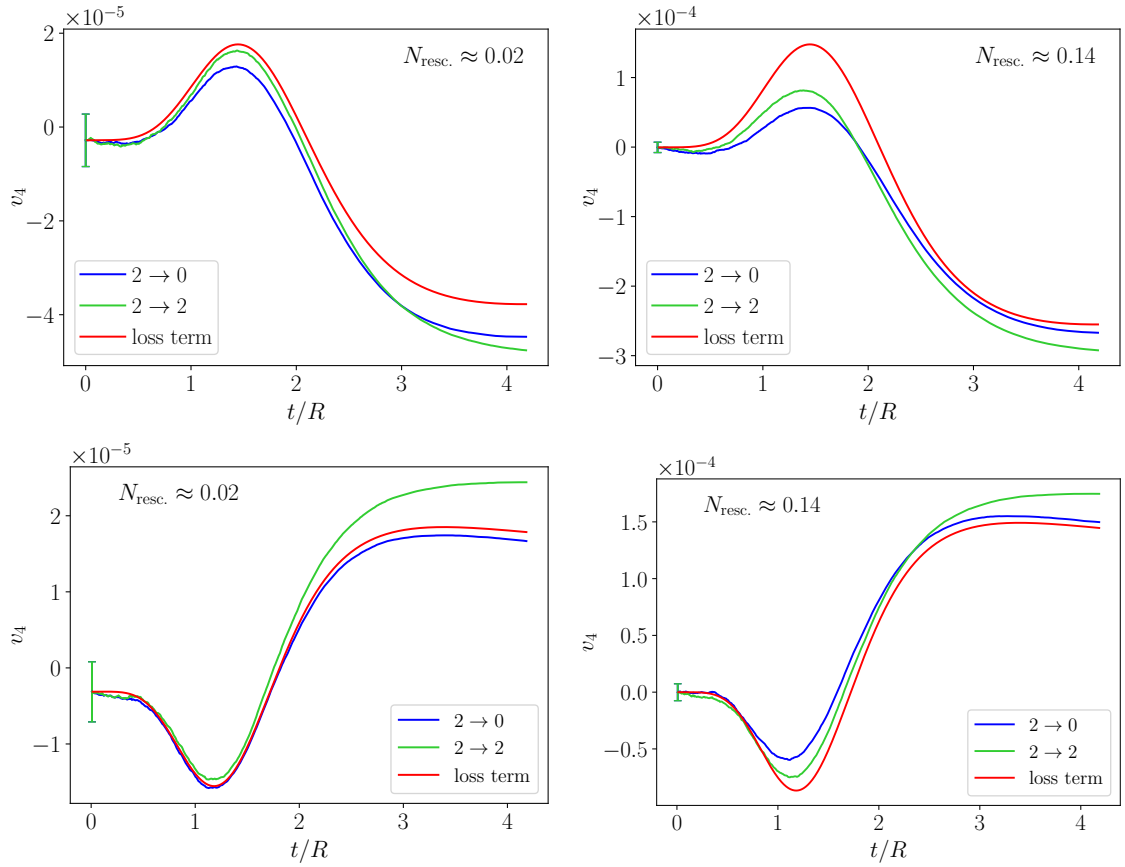

Figure 6.5: Time dependence of quadrangular flow v_4 in systems with on average $N_{\text{resc.}} \approx 0.02$ (left) or 0.14 (right) rescatterings per particle. The top panels are for a system with an initial quadrangularity $\varepsilon_4 \approx 0.15$ and $\varepsilon_2 = 0$; the bottom panels for an initial state with $\varepsilon_2 = 0.15$ and $\varepsilon_4 = 0$. The green curves are for systems with elastic binary scatterings, the blue lines for the $2 \to 0$ scenario and the red ones show the analytical results Eq. (6.14) (top) or Eq. (6.15) (bottom).

In total we find that there is a quite similar behavior of v_4 resulting either linearly from ε_4 or nonlinearly from ε_2 compared to v_2, when considering that the production mechanism is dominantly the anisotropic escape of particles. It is interesting to see that the ε_4 and ε_2 contributions are of the same order but with opposite signs in the small $N_{\text{resc.}}$ regime. This could lead to a cancellation and thus to a v_4 signal which can lie in a wide range of values at late times and can even be negative.

The next flow harmonic would be v_5. We will not discuss it since the analytical result is the same as for v_3: as an odd harmonic it will vanish identically in our scenario at leading order in σ. This implies that the v_5 signal in the $2 \to 0$ simulation would arise at order $N_{\text{resc.}}^2$ and at order $N_{\text{resc.}}$ in the $2 \to 2$ collision kernel. It would again lead to differences in the results of the two transport simulations, which we did not try to perform, as the simulations would be computationally expensive.

6.6 Hexagonal flow

In Fig. 6.6 we show our results for the hexagonal flow v_6. Due to the small signals it is

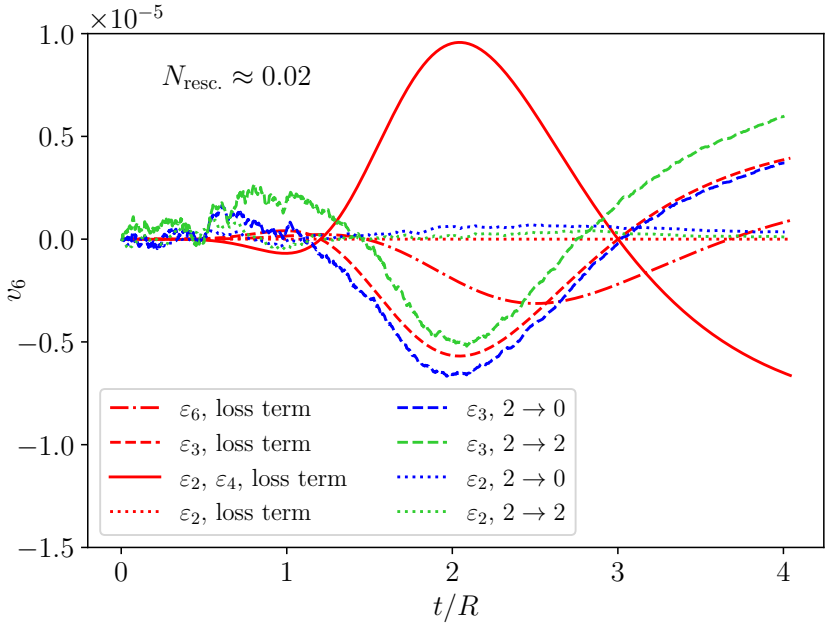

Figure 6.6: Time dependence of hexagonal flow v_6 in systems with on average $N_{\text{resc.}} \approx 0.02$ per particle and with different initial geometrical profiles, as described in the text.

the limit of what we can achieve numerically with a reasonable control of the signal at $N_{\text{resc.}} \approx 0.02$. Here we can reuse simulations which were already performed for v_2 and v_3, as the v_6 signal can result from a variety of different initial geometries [112–114]. Possible geometrical sources are $v_6 \propto \varepsilon_6$ (linear response, dot-dashed line), $v_6 \propto \varepsilon_3^2$ (quadratic response, dashed lines), $v_6 \propto \varepsilon_2^3$ (cubic response, dotted lines) or $v_6 \propto \varepsilon_2 \varepsilon_4$ (mixed quadratic response, full line). We have always chosen $\varepsilon_n = 0.15$ for the non-vanishing eccentricities and the numerical results including ε_2 and ε_3 stem from the same simulations as in Sec. 6.3 and 6.4. For the sake of computational costs we did not perform simulations with an initial ε_6 or non-zero ε_2 and ε_4.[10]

The v_6 results with an initial ε_3 are in good agreement between the different approaches of this paper for $N_{\text{resc.}} \approx 0.02$. This agreement contrasted with the very different result for v_3 in Sec. 6.4 reinforces the main conclusion that there are different mechanisms producing even and odd flow harmonics.

We find for v_6 produced by an initial ε_2 that the signals are very small but still consistent between the $2 \to 2$ and $2 \to 0$ scenarios. For the analytical case the result is zero, which is consistent with Ref. [80], where it was pointed out that in a model without quantum effects and only binary collisions a ε_2^3 contribution to v_6 (and also v_2) cannot occur at leading order in the cross section.

Considering the analytical results for either $\varepsilon_6 = 0.15$ or $\varepsilon_2 = \varepsilon_4 = 0.15$ we find that they are of the same order of magnitude as the results for $\varepsilon_3 = 0.15$ and similar to the v_4 behavior a sign change occurs (twice in this case) during the evolution.

[10] Let us note that in the analytical calculation the symmetry planes Ψ_2 and Ψ_4 are aligned.

6.7 Local production rate of anisotropic flow

To get a better feeling of the temporal and spatial origin of the anisotropic flow signals we will now have a look at their production rate as a function of time and position [100, 101]. We have defined the production rate $D_n(t, r)$, which is averaged over the polar angle of the production point, in Eq. (6.7). Figure 6.7 shows the results for $D_n(t, r)$ from the analytical approach for $n \in \{2, 3, 4\}$ for the setups from Secs. 6.3-6.5 and with $N_{\text{resc.}} \approx 0.02$. In the figure we show all production rates

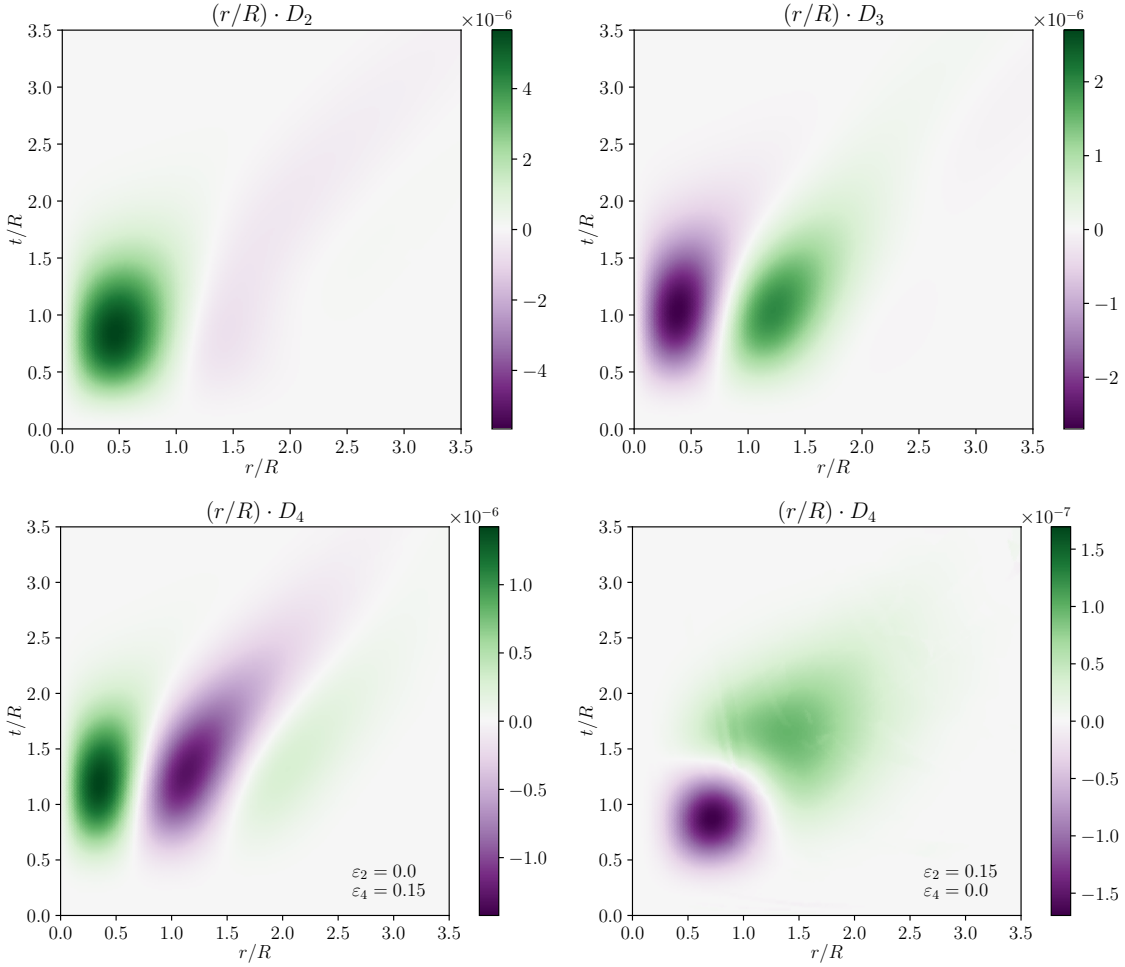

Figure 6.7: Angle-averaged local production rates D_2 (upper left), D_3 (upper right), and D_4 for an initial state with $\varepsilon_2 = 0$ and $\varepsilon_4 = 0.15$ (bottom left) or with $\varepsilon_2 = 0.15$ and $\varepsilon_4 = 0$ (bottom right).

multiplied by r such that the production rate $\partial_t v_n(t)$ of the anisotropic flow $v_n(t)$ is given by the integral over the r coordinate.

The upper row shows D_2, D_3 and the lower left is displaying D_4 resulting from a linear response of the flow signal to the corresponding ε_n. All three plots show similar qualitative features in their structure. For the innermost region, extending up to $r \simeq R$ for D_2 and up to $r \simeq 0.7R$ for D_3 and D_4, we find that the contribution has the same sign for the whole evolution. In the case $n = 2$ and 4 it is positive and for $n = 3$ negative. Then there is a region further outside which has opposite sign,

which is more pronounced in the case $n = 3$ and 4 than for $n = 2$. Going to later times these regions extend to larger r values but become fainter and are actually less pronounced than in a similar study with energy-weighted flow [101].

As the space and time dependent production rate D_n reflects the time dependence of the corresponding anisotropic flow coefficients v_n as well, the sign change in $v_4(t)$ from positive to negative in the upper left panel of Fig. 6.5 is also reflected there. The v_4 signal has a derivative which turns negative around $t/R \simeq 1.5$. This is represented in the production rate D_4 in the lower left panel of Fig. 6.7 by the progressive dominance of the region at intermediate values of r. Analogously the small decrease of the $v_2(t)$ signal for $t/R \gtrsim 2$ is reflected by the negative outer region in $D_2(t, r)$. The contributions for $n = 3$ from the regions with opposite sign in the upper right panel in Fig. 6.7 cancel each other at all t such that $\partial_t v_3(t) = 0$. In Ref. [100] they found an "almost nearly perfect cancellation" with a very small negative v_3^E value.

One other feature we can observe in the $D_n(t, r)$ plots is that the buildup of the linear D_n is slower for increasing n, which reflects the scaling behavior $v_n \propto t^{n+1}$ in the few collisions regime [102].

In the lower right panel of Fig. 6.7 we show the non-linear response of v_4 to an initial ellipticity ε_2, which shows a completely different behavior with a clear negative contribution at early times and $r \lesssim 1.3R$. This negative contribution is followed by a positive contribution at later times and for all r values. From the analytical point of view it is possible to show that if there is only an initial ellipticity $\varepsilon_2 \neq 0$ then the loss term creates a negative $v_4 \propto -\varepsilon_2^2$ irrespective of the sign of the eccentricity.[11] During the time evolution the ellipticity decreases due to a generation of a v_2 signal. On the other hand due to the buildup of a negative v_4 there is also a positive quadrangularity ε_4 produced giving then rise to the positive contributions to v_4 at later times, as it is visible in the bottom panels of Fig. 6.5.

[11] Remember, that the sign of the eccentricity controls its orientation. If the sign is positive then the short axis is along the x-direction, otherwise along the y-direction.

Chapter 7

Statistical analysis of initial state and final state response in heavy-ion collisions

Over the last years experiments with heavy-ion collisions have shown that they are a tool to study QCD matter dynamically evolving in an out-of-equilibrium state. The bulk dynamics of the fireball can be described using relativistic dissipative fluid dynamics [5, 109, 115]. It was also shown in the last years that the pre-equilibrium stage — bringing the system closer to a local thermal equilibrium to make hydrodynamics applicable — is a crucial step in the time evolution of the system and has an impact on final state observables [11, 116].

To describe a system with relativistic hydrodynamics one needs two ingredients. As the equations of motion are a set of partial differential equations which is not closed, an equation of state is needed to close the system. Additionally one needs an initial condition for the fluid dynamical fields. The problem is now that this initial condition is not directly accessible via the experimental results and the non-linear time evolution of the medium showed that the fluctuations in the initial state can be either intensified or washed out [75, 117]. The situation is even more complex, as the observables are highly influenced by the geometry of the colliding system, which means that there is no direct measurement of the impact parameter possible, but only a certain region in centrality is accessible.

When generating a set of initial state configurations there are two possibilities how to proceed. The first most intuitive, but computationally expensive, way is, to evolve each configuration on its own in time. This approach is called "event-by-event" method. A second possibility is to split the configurations into a background and fluctuating components about it. Fluctuations are then evolved with response functions and they can be expanded in a basis of modes. With this at hand it is sufficient to evolve — just once for a given initial state model — the background and the response functions for the fluctuations, which is computationally much cheaper than the event-by-event approach [118–124].

In this chapter we will extend the framework of the mode-by-mode evolution via the introduction of a density matrix formalism, where the background is subtracted from the density matrix such that it incorporates the fluctuations only. By diagonalizing this matrix we obtain an orthonormal basis of uncorrelated fluctuation modes capturing the event-by-event initial state fluctuations. To study this approach we will use two different initial state models — a Glauber model and a Saturation model — which gives us the possibility to study the differences between these two models within this new framework. Additionally we will evolve the initial states within a dynamical model — KøMPøST and MUSIC — to investigate the impact of the mode-by-mode linear response on the final state observables. We also perform event-by-event simulations to compare to the commonly used approach.

This chapter is based on:[1]

- *Statistical analysis of the initial state and final state response in heavy-ion collisions*
  N. Borghini, M. Borrell, N. Feld, H. Roch, S. Schlichting, C. Werthmann

This chapter will first introduce the theoretical framework for the density matrix formalism in Sec. 7.1 followed by a statistical characterization of the background and the fluctuation modes using different characterization schemes. Section 7.2 will then introduce the (non-)linear response theory for the fluctuation modes, the setup of the dynamical system evolution and the linear and quadratic response of the individual modes. The dynamical response of the flow coefficients to the initial state eccentricities is computed on a mode-by-mode basis and we will also discuss the statistics and correlations of the different observables. Additionally we will

[1] The paper is currently in preparation.

present the results of a Gaussian statistics ansatz using the linear response theory and compare to the event-by-event ansatz.

7.1 Statistical characterization of the initial state

We will start in this section with the derivation of the statistical initial state characterization for the different initial state models, where we define the average state and the orthonormal basis of uncorrelated fluctuation modes in Sec. 7.1.1. The models are briefly introduced in Sec. 7.1.2 and we present the results for the average states and the modes — mainly for the impact parameters $b = 0$ and 9 fm — in Sec. 7.1.3 and their characterization in Sec. 7.1.4.

7.1.1 Mode decomposition of the initial state

Our aim is to show that one can write a set of N_{ev} initial state model configurations $\{\Phi^{(i)}\}$ with event-by-event fluctuations as an average configuration $\bar{\Psi}$ and fluctuation modes $\{\Psi_l\}$ such that one can express every configuration $\Phi^{(i)}$ by the sum of the average state $\bar{\Psi}$ and a combination of modes

$$\Phi^{(i)}(\mathbf{x}) = \bar{\Psi}(\mathbf{x}) + \sum_l c_l^{(i)} \Psi_l(\mathbf{x}). \tag{7.1}$$

These configurations $\Phi^{(i)}$ which are functions of the position can be energy or entropy density profiles at fixed impact parameter or also in a centrality class. The expansion coefficients $\{c_l^{(i)}\}$ are centered and uncorrelated random variables with unit variance:

$$\langle c_l \rangle = 0, \tag{7.2}$$

$$\langle c_l c_{l'} \rangle = \delta_{ll'}. \tag{7.3}$$

We denote the average over events by $\langle \ldots \rangle$ and for brevity we neglect the position dependence of the states in the following equations. As the thermodynamic quantities which we want to decompose are real-valued, the states $\Phi^{(i)}$ are real-valued as well.

The average state or event computed from N_{ev} events is defined by

$$\bar{\Psi} \equiv \frac{1}{N_{\mathrm{ev}}} \sum_{i=1}^{N_{\mathrm{ev}}} \Phi^{(i)}. \tag{7.4}$$

In the next step we propose an orthonormal set of functions $\{\tilde{\chi}_l\}$ giving a basis on the Hilbert space spanned by the configurations $\{\Phi^{(i)}\}$. As usual the inner product on this space is the one for square-integrable functions, which is an overlap integral over the whole space. All deviations from the average state can be decomposed over this basis

$$\Phi^{(i)} = \bar{\Psi} + \sum_l \tilde{c}_l^{(i)} \tilde{\chi}_l. \tag{7.5}$$

From this expression it is obvious that the expansion coefficients obey the relation

$$\frac{1}{N_{\mathrm{ev}}}\sum_{i=1}^{N_{\mathrm{ev}}}\tilde{c}_l^{(i)}=0. \tag{7.6}$$

Assuming now that each event in the sample has the same probability to occur, then for each basis vector $\tilde{\chi}_l$ the corresponding coefficients $\{\tilde{c}_l^{(i)}\}$ is the realization of a random variable $\tilde{c}_l$ with $\langle c_l\rangle = 0$ according to Eq. (7.6). As in quantum mechanics, we can now assign a density matrix to these equiprobable states given by

$$\frac{1}{N_{\mathrm{ev}}}\sum_i \Phi^{(i)}\Phi^{(i)\mathsf{T}}, \tag{7.7}$$

which equals

$$\frac{1}{N_{\mathrm{ev}}}\sum_i \Phi^{(i)}\Phi^{(i)\mathsf{T}} = \bar{\Psi}\bar{\Psi}^{\mathsf{T}} + \sum_{l,l'}\langle\tilde{c}_l\tilde{c}_{l'}\rangle\,\tilde{\chi}_l\tilde{\chi}_{l'}^{\mathsf{T}}, \tag{7.8}$$

as follows from Eqs. (7.5)-(7.6). The next step is to write a density matrix as

$$\rho \equiv \frac{1}{N_{\mathrm{ev}}}\sum_i \Phi^{(i)}\Phi^{(i)\mathsf{T}} - \bar{\Psi}\bar{\Psi}^{\mathsf{T}} = \sum_{l,l'}\langle\tilde{c}_l\tilde{c}_{l'}\rangle\,\tilde{\chi}_l\tilde{\chi}_{l'}^{\mathsf{T}}, \tag{7.9}$$

which contains the fluctuations about the average state.

This density matrix is then diagonalized

$$\rho\tilde{\Psi}_l = \lambda_l\tilde{\Psi}_l \tag{7.10}$$

and the orthonormal eigenvectors $\{\tilde{\Psi}_l\}$ are sorted according to their corresponding eigenvalue λ_l. The eigenvalue quantifies the relative importance of the $\tilde{\Psi}_l$ contribution to the set of the N_{ev} random sampled events. We can also write the density matrix in its spectral form as

$$\rho = \sum_l \lambda_l\tilde{\Psi}_l\tilde{\Psi}_l^{\mathsf{T}}, \tag{7.11}$$

while comparing it to Eqs. (7.9) and (7.11) reveals that we might choose the eigenvector basis $\{\tilde{\Psi}_l\}$ of ρ as the arbitrary basis $\{\tilde{\chi}_l\}$ in Eq. (7.5). For all combinations of l, l' the expansion coefficients obey

$$\langle\tilde{c}_l\tilde{c}_{l'}\rangle = \lambda_l\delta_{ll'} \tag{7.12}$$

together with $\langle\tilde{c}_l\rangle = 0$.

In the last step all the eigenvectors of ρ are rescaled as

$$\Psi_l \equiv \sqrt{\lambda_l}\tilde{\Psi}_l. \tag{7.13}$$

This leads to the set $\{\Psi_l\}$ being an orthogonal basis, with basis vectors not normalized to unity. With this rescaling the modes represent the fluctuations about

the average state and the $\sqrt{\lambda_l}$ encodes the contribution of $\tilde{\Psi}_l$ to a configuration. Additionally, we redefine the expansion coefficients as

$$c_l \equiv \frac{\tilde{c}_l}{\sqrt{\lambda_l}}. \tag{7.14}$$

Then the decomposition of a given event over the basis Eq. (7.5) has the form of Eq. (7.1), while $\langle \tilde{c}_l \rangle = 0$ immediately becomes Eq. (7.2) and Eq. (7.12) transforms into Eq. (7.3). We have now reached our goal defined at the beginning of this subsection.

For a real calculation of the basis it is inconvenient to store a large set of initial density profiles from a given initial state model, which are in the following energy density profiles, as this would require a large amount of disc space. It is easier to directly compute the average state (7.4) and the density matrix involving Eq. (7.9), where the latter is then diagonalized to compute the modes $\{\Psi_l\}$ and their eigenvalues λ_l. One important remark about the basis is that the average state is not part of the basis, as its projector is subtracted from the density matrix in Eq. (7.9), meaning that the average state could be decomposed over the basis.

7.1.2 Models

In this chapter we will use two different initial state models to illustrate the mode decomposition for Pb-Pb collisions at $\sqrt{s_{\mathrm{NN}}} = 5.02$ TeV. Both of these models are described in Ch. 2, namely the MC Glauber model (Secs. 2.1.2+2.2) and a Saturation model (Sec. 2.3).

Let us only briefly repeat that both models are based on a MC Glauber sampling of the Pb nuclei, where for the Woods-Saxon distribution (2.1) $R = 6.62$ and $a = 0.546$ fm was used here. In the Glauber model the minimum nucleon separation representing the Fermi repulsion was set to 0.4 fm and the inelastic nucleon-nucleon cross section is $\sigma_{\mathrm{NN}}^{\mathrm{inel}} = 67.6$ mb for the investigated collision energy. For our study we fix the impact parameters, mostly $b = 0$ or $b = 9$ fm, along the x-axis and then produce initial energy density profiles according to the methods given in the above referenced sections.

7.1.3 Mode decomposition for the Glauber and Saturation model

Now we want to apply the framework introduced in Sec. 7.1.1 to the initial state energy density profiles of the models mentioned in Sec. 7.1.2, where we generated for each model and impact parameter $N_{\mathrm{ev}} = 2^{21}$ profiles. By this large number of profiles we ensure the reduction of statistical uncertainties and it lifts degeneracies for modes with eigenvalues which lie close to each other.

Using Eqs. (7.4) and (7.9) for the average state $\bar{\Psi}$ and the density matrix ρ respectively, we compute the two quantities for each set of random events. As a finite basis for the decomposition of the latter two quantities we use an orthogonal grid with $N_s = 128$ sites in one direction and a spacing of 0.19 resp. 0.21 fm for the Glauber resp. Saturation model. Then the ρ matrix is computed within the

orthonormal basis where each of the N_s^2 elements of the grid has a unit weight at the specific grid site and vanishes everywhere else. The diagonalization process of this $N_s^2 \times N_s^2$-dimensional representation of the density matrix is the most time consuming step to generate the set of modes $\{\Psi_l\}$ and their corresponding eigenvalues $\{\lambda_l\}$.

Figure 7.1 shows the energy density profiles of the average state $\bar{\Psi}$ at four different impact parameters — always oriented along the x-axis — computed for both initial state models. The average events for both models are azimuthally symmetric at

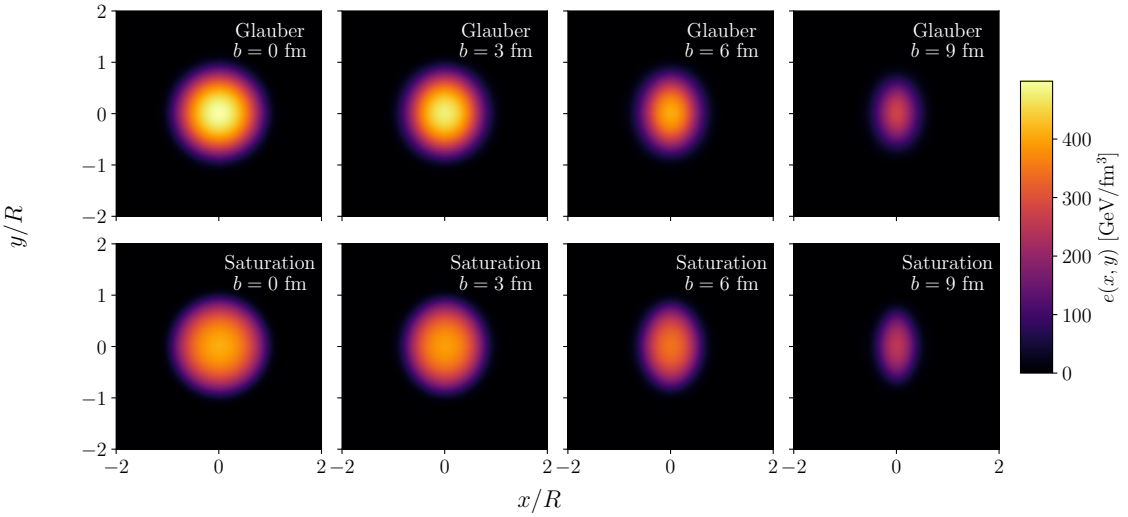

Figure 7.1: Energy density profiles of the average event $\bar{\Psi}$ for different impact parameters (from left to right: $b = 0$, 3, 6, 9 fm) in the Glauber (top) and Saturation (bottom) models.

$b = 0$ and become more and more elliptic with increasing impact parameter. It seems that one can already by eye see that the average events for the larger impact parameters are more elliptic in the Saturation model than in the Glauber model. This will be quantified later on. In contrast the energy density values in the center computed from the Glauber model are larger, although both models are calibrated in such a way that they reproduce the same charged hadron multiplicity for the most central LHC events.

For the average state of the Glauber model a natural question which arises is whether the density profile coincides with a profile generated in an optical Glauber model. In fact, we checked that $\bar{\Psi}$ is similar to an optical Glauber profile generated with the same scaling with N_{part} and N_{coll} and the same input parameters. We made a qualitative comparison of the two profiles by plotting them on top of each other, which revealed that there are only small differences in the outer regions. A more quantitative comparison was performed by a decomposition of the two profiles in a Bessel-Fourier series expansion of the two density profiles (Sec. 2.4.2).

Before describing the modes in further detail let us have a look at the expansion coefficients $\{c_l\}$. Using Eq. (7.1) we decomposed 8192 events of the N_{ev} events in the full sample used to compute the average state and the fluctuation modes. We introduce the number l to label the individual modes, where $l = 0$ is the most probable mode and the subsequent modes are labeled in the order of decreasing occurrence probability. For each l we thus obtain 8192 values for the coefficients c_l.

These are shown in Fig. 7.2 for the 15 most probable modes ($0 \leq l \leq 14$) and some higher modes ($l \in \{200, 201, 202\}$) in the Glauber model at impact parameters $b = 0$ and $b = 9$ fm.[2] For comparison a Gaussian distribution with unit variance is shown.

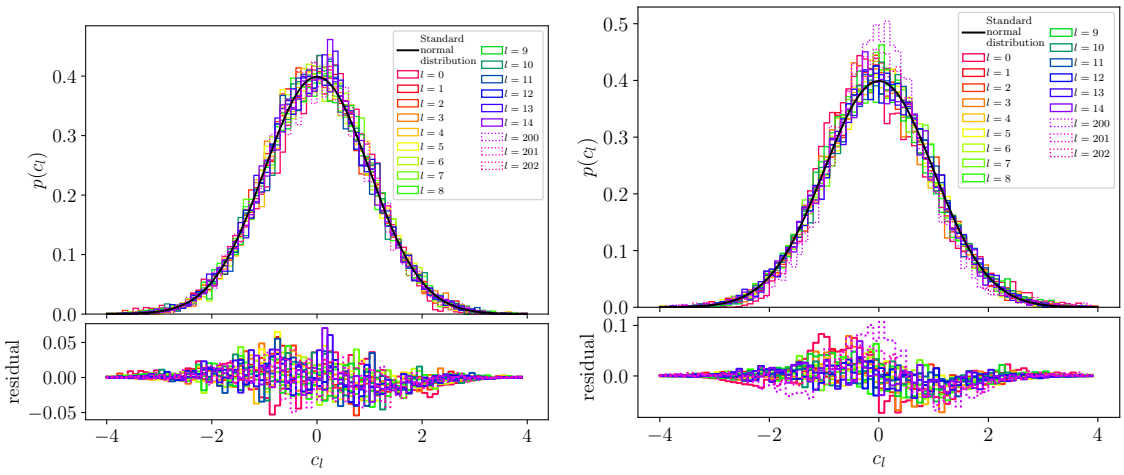

Figure 7.2: Relative frequency of the expansion coefficients c_l (histograms) computed from 8192 events in the Glauber model at $b = 0$ (left) and $b = 9$ fm (right), compared with a standard Gaussian distribution (full black line).

Looking at the left panel of Fig. 7.2 we see that at vanishing impact parameter the distributions are very close to the Gaussian curve for all values of l. The residual difference between the individual curves and the Gaussian curve is at most of the order 0.05 in absolute value. Going to the right panel we find that the distributions are still close to the Gaussian curve, but there are larger differences compared to the values for $b = 0$ up to 0.1 in absolute value for the displayed values of l. We can also observe that there are some distributions, e.g., $p(c_0)$, which are skewed even if l is small. Additionally, the tails for the modes with large values of l are thinner compared to the Gaussian curve, which hints at a positive excess kurtosis.

To quantify this visual impression further, we computed the first four moments of the $p(c_l)$ distributions computed from the 8192 events for both initial state models. The moments or related quantities thereof are presented in Appendix F.1.

Now we want to quantify the relative importance of the fluctuation modes $\{\Psi_l\}$ to the full set of N_{ev} random events. As the average state $\bar{\Psi}$ is not part of the basis, i.e., not an eigenvector of ρ, we define the quantities

$$w_l \equiv \frac{||\Psi_l||}{\sum_l ||\Psi_l|| + ||\bar{\Psi}||} = \frac{\sqrt{\lambda_l}}{\sum_l \sqrt{\lambda_l} + ||\bar{\Psi}||} \tag{7.15}$$

and

$$\bar{w}_l \equiv \frac{||\bar{\Psi}||}{\sum_l ||\Psi_l|| + ||\bar{\Psi}||} = \frac{||\bar{\Psi}||}{\sum_l \sqrt{\lambda_l} + ||\bar{\Psi}||}, \tag{7.16}$$

[2]The results for the Saturation model are not shown, as they are similar to the ones in the Glauber model.

where the denominator is the sum of the norms of all modes and of the average state. In practice we sum over all 16384 eigenvalues, such that the weights $\{w_l\}$ and $\bar{w}$ sum up to 1.

Figure 7.3 shows the first 64 relative weights w_l and the one of the average state $\bar{w}_l$ for both models at impact parameter $b = 0$ (left) and $b = 9$ fm (right).[3] For

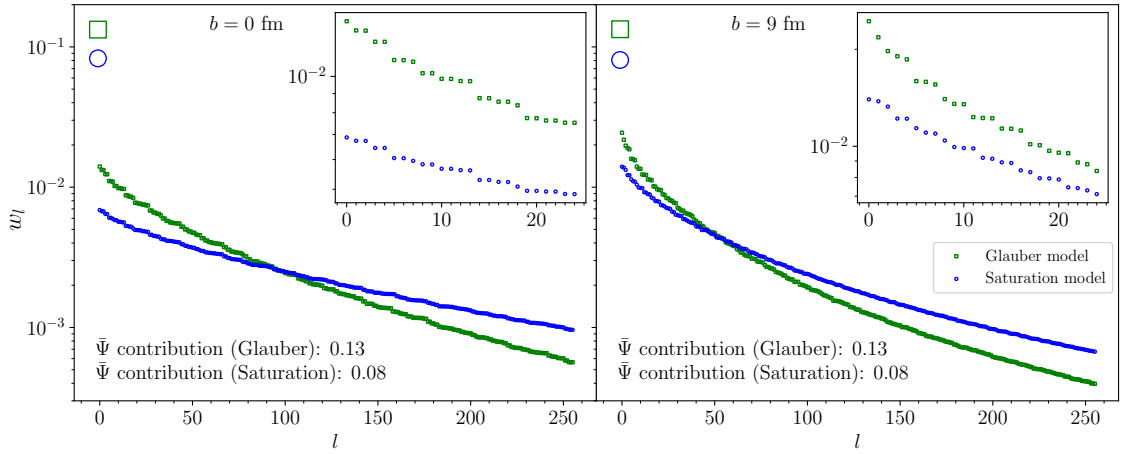

Figure 7.3: Relative weights of the first 64 fluctuation modes w_l (Eq. (7.15)) and the average state $\bar{w}_l$ (Eq. (7.16), large symbols at $l = -1$) at impact parameter $b = 0$ (left) and $b = 9$ fm (right) in the Glauber (squares) and the Saturation model (circles).

both impact parameters the contribution of $\bar{\Psi}$ is $\bar{w} = 13\%$ in the Glauber model, $\bar{w} = 8\%$ in the Saturation model, while the fluctuation modes have a relative weight of less than 1% resp. $2 - 3\%$ at $b = 0$ fm resp. $b = 9$ fm decreasing with increasing mode number l. The contribution of the first modes at $b = 9$ fm is slightly larger with a steeper falloff for increasing l. We can see here that events at larger impact parameter have larger density fluctuations compared to the average event.

If we now compare both models, we find that the relative weights w_l have a steeper falloff within the Glauber model and its average event has also a larger contribution than in the Saturation model. This can be explained by the fact that the energy density in the Saturation model has finer structures, which leads to a higher probability for high-order perturbations in the energy density profile. The effects of the smearing radius in the Glauber model or even the introduction of a Glauber model on the level of valence-quarks is not further investigated here.

Looking at the inset plots in Fig. 7.3 one can see that at $b = 0$ fm there are degenerate modes with the same eigenvalues, for instance $(1, 2)$, $(3, 4)$, $(5, 6)$, and so on. Going to $b = 9$ fm this degeneracy is partly lifted, which will be discussed in further detail in Sec. 7.1.4.

As we have rescaled the modes by the square-root of their corresponding eigenvalue, the modes represent the event-by-event fluctuations of the initial state energy density about the average state $\bar{\Psi}$. They represent which fluctuations are more or less likely to occur in the density profile. Figure 7.4 shows the three mode examples

[3] There is a decrease of the wights with increasing l, which is introduced by the sorting of the eigenvalues after the diagonalization of ρ.

($l = 0, 1, 3$) obtained from the Glauber model (top row) and the Saturation model (bottom row) at $b = 0$ fm. These modes are chosen, as they show typical symme-

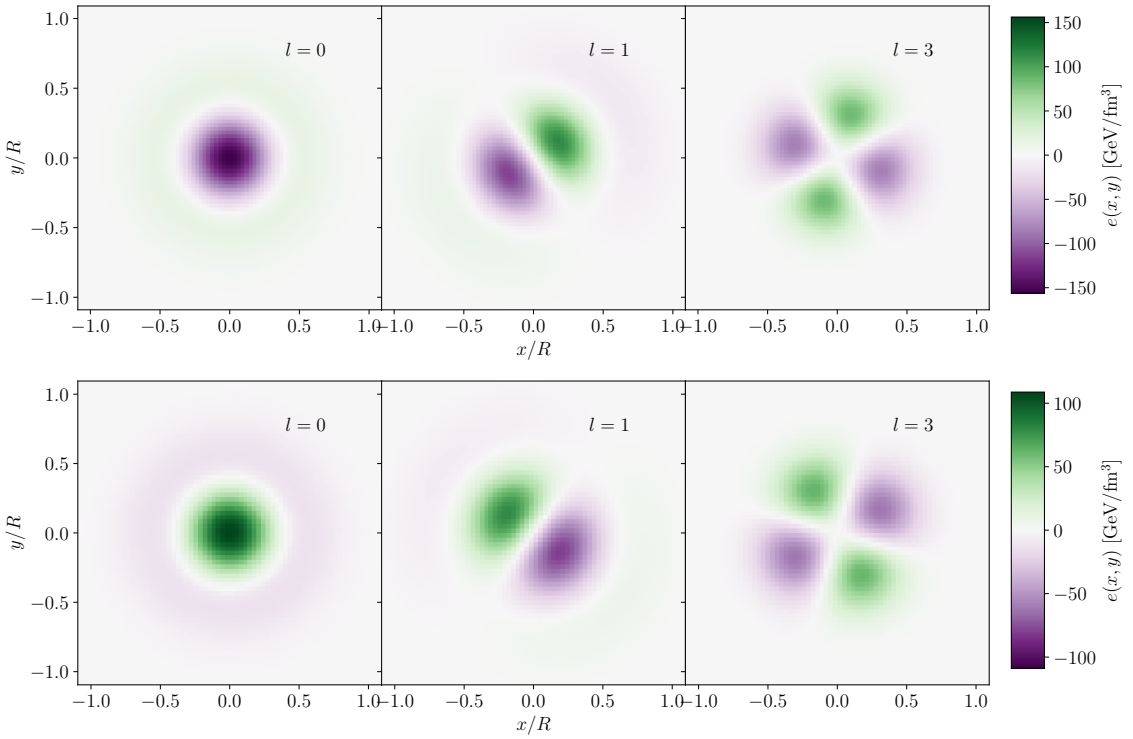

Figure 7.4: Exemplary modes $l = 0, 1, 3$ at impact parameter $b = 0$ fm in the Glauber (top) and Saturation (bottom) models. The overall sign of the modes are arbitrary.

tries, $l = 0$ has a radial symmetry, $l = 1$ has a dipole structure and $l = 3$ has a quadrupole structure.

As the modes have positive and negative parts one could think that the negative parts are problematic. However, the modes do always come on top of an average state, which exhibits significantly larger values, such that the sum of $\bar{\Psi}$ and c_l times Ψ_l is positive definite everywhere as long as c_l is not much larger than 1. With this it becomes clear that the modes in the Saturation model take smaller values than in the Glauber model, as the same holds true for the average state in the two models respectively.

Additionally it is important to note that the overall sign of a mode has no physical meaning, since $-\Psi_l$ is also an eigenvector of the density matrix ρ with the same eigenvalue (and norm) as Ψ_l. This is why there is no important physical implication for the difference between $l = 0$ mode of the two models in Fig. 7.4 which have opposite sign.

In the following Section the modes and their shapes are further discussed and characterized.

7.1.4 Characterization of the average state and the modes for the Glauber and Saturation model

We present the first 60 eigenvectors of the density matrix ρ in Appendix F.2 for both initial state models and both considered impact parameters (Glauber: Figs. F.5-F.6; Saturation: Figs. F.7-F.8). For a better comparison between the eigenvectors the set $\{\tilde{\Psi}_l\}$ is shown, i.e., they all have the same norm.

For the $b = 0$ fm modes one can easily identify those with a radial symmetry, e.g., $l = 0, 7, 18, 33$ in the Glauber model, where the number of zero crossings with increasing distance from the center is increasing with l. There are also eigenvectors which are similar in the sense that one can transform one into the other by a rotation with an integer fraction of 180°. The modes $l = 1$ and 2 have to be rotated by $\pi/2$, $l = 3, 4$ by $\pi/4$, $l = 5, 6$ by $\pi/6$ and so on. These pairs are the same modes that have the degeneracy in their eigenvalues (see Fig. 7.3) spanning a two-dimensional space of eigenvectors with arbitrary orientation in the transverse plane. There are also eigenvectors which show a more complicated profile, e.g., $l = 40$ in the Glauber or $l = 33$ in the Saturation model, where more then two eigenvectors are (almost) degenerate. As an example let us look at $l = 33$ in the Saturation model. This mode has a radial structure with a small admixture of eigenvectors which show an invariance under $\pi/4$ rotations, e.g., $l = 34, 35$.

For a finite impact parameter there is a broken radial symmetry and thus there are no radially symmetric eigenvectors. In this case one can even see that most of the eigenvectors now have an orientation along the x- and y-axes as reflection-symmetry or anti-symmetry axes. We also see that the degeneracy in the eigenvalues is partially lifted and that the eigenvectors have more complicated structures than at $b = 0$ fm. This is the reason why we will now introduce several quantities to quantify the characteristics of the eigenvectors, as well as the average state.

7.1.4.1 Azimuthal and radial dependence

To obtain a more sophisticated and quantitative characterization of the obtained eigenmodes of the density matrix ρ, we will now introduce several new quantities.

The first new quantity is the total energy of a mode $\Psi_l(r, \theta)$ which is given by

$$\mathcal{E}_l = \int \Psi_l(r, \theta)\, r \mathrm{d}r \mathrm{d}\theta. \tag{7.17}$$

As we have constructed the modes in such a way that they represent the fluctuations about the average event, the energies of the modes themselves should be relatively small compared to the average event. This is also required to maintain the positivity of the energy density.

In addition to the energy of the modes we can also characterize their azimuthal shape by eccentricities. Here we have to use a different definition of the eccentricities then the one introduced in Eq. (2.25), as the integral in the denominator would be (almost) vanishing if we consider an individual mode. Therefore, we redefine the

complex eccentricities as

$$\tilde{\varepsilon}_1 \equiv -\frac{\int r^3 e^{\mathrm{i}\theta} \Psi_l(r,\theta)\, r\mathrm{d}r\mathrm{d}\theta}{\int r^3 \bar{\Psi}(r,\theta)\, r\mathrm{d}r\mathrm{d}\theta} \quad \text{for } n=1, \tag{7.18}$$

$$\tilde{\varepsilon}_n \equiv -\frac{\int r^n e^{\mathrm{i}n\theta} \Psi_l(r,\theta)\, r\mathrm{d}r\mathrm{d}\theta}{\int r^n \bar{\Psi}(r,\theta)\, r\mathrm{d}r\mathrm{d}\theta} \quad \text{for } n \geq 2, \tag{7.19}$$

where we use the average event $\bar{\Psi}$ in the denominator and denote the modulus of the eccentricity for a given mode Ψ_l by $|\tilde{\varepsilon}_n|_l$. With this definition of the eccentricity (Eq. (7.19)) we can also quantify the energy of the modes divided by the energy of the average event when using $n = 0$, leading to $|\tilde{\varepsilon}_0|_l = \mathcal{E}_l/\bar{\mathcal{E}}$.

In Tab. 7.1 we give the eccentricity values for the average states of the two models at $b = 0$ and 9 fm using Eqs. (7.18)-(7.19) with $\bar{\Psi}$ instead Ψ_l in the numerator. As

Table 7.1: Eccentricities of the average states in both models at $b = 0$ fm and $b = 9$ fm.

$\lvert\varepsilon_1\rvert$	$\lvert\varepsilon_2\rvert$	$\lvert\varepsilon_3\rvert$	$\lvert\varepsilon_4\rvert$	$\lvert\varepsilon_5\rvert$
Glauber	$b = 0$ fm			
3.0×10^{-5}	3.9×10^{-5}	1.1×10^{-4}	3.3×10^{-5}	4.5×10^{-5}
Saturation	$b = 0$ fm			
6.0×10^{-5}	9.3×10^{-5}	5.5×10^{-5}	4.7×10^{-5}	3.9×10^{-5}
Glauber	$b = 9$ fm			
5.7×10^{-5}	2.9×10^{-1}	2.6×10^{-4}	9.4×10^{-2}	9.0×10^{-5}
Saturation	$b = 9$ fm			
1.7×10^{-4}	4.0×10^{-1}	7.4×10^{-5}	2.0×10^{-1}	1.7×10^{-4}

expected, the rotational symmetry at vanishing impact parameter gives us vanishing eccentricities. An exact zero can not be obtained due to the finite mode resolution and therefore a limited precision in the integrations, as well as the finite number of events leading to values of the order 10^{-4} or smaller.

The average state at $b = 9$ fm has spatial anisotropies with even n, i.e., ε_2 and ε_4 in both models which are of the order of 0.1. For the other eccentricities we find again values of the order of the fluctuations in the $b = 0$ fm case, again due to numerical fluctuations. In this case the Saturation model has a $\approx 40\%$ larger ε_2 and ε_4 is more than twice as large compared to the Glauber model. This fact has been observed before, as the Saturation model has sharper edges of the density distribution [40].

Displaying the eccentricities in Fig. 7.5, we use the first five eccentricities $|\tilde{\varepsilon}_n|_l$ (Eqs. (7.18)-(7.19)) and the energy content of the modes compared to that of the average state $|\tilde{\varepsilon}_0|_l$.

If we consider collisions at $b = 0$ fm then the modes with a clearly non-vanishing energy exhibit around 1% of the average state energy. These few exceptional modes with roughly hundred times more energy compared to the other modes with $|\tilde{\varepsilon}_0|_l \lesssim 10^{-4}$ are the ones we have already identified as "radial" (see Fig. 7.4 left panels).

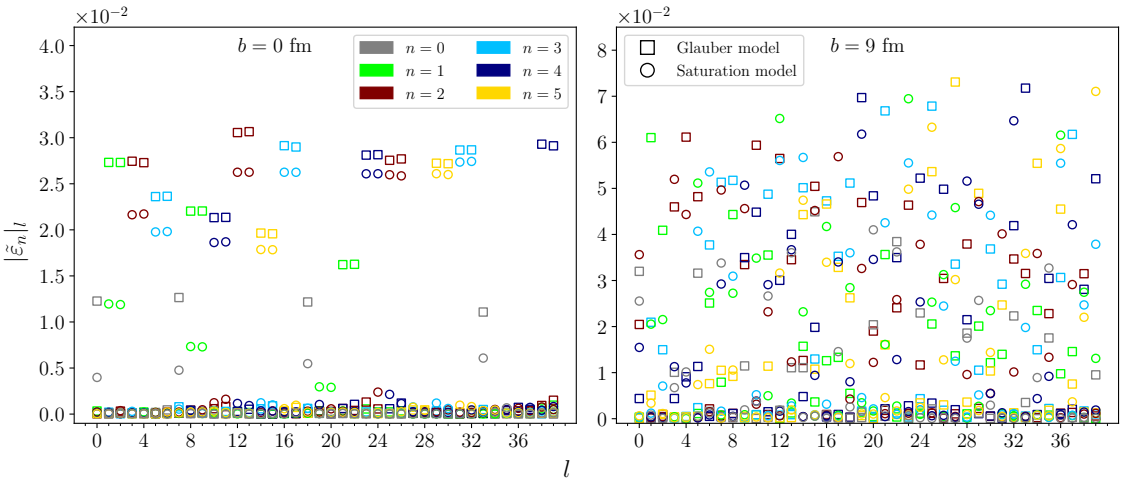

Figure 7.5: Eccentricities of the individual modes and their relative energies (normalized by the average state energy) defined in Eqs. (7.18)-(7.19) for impact parameter $b = 0$ fm (left) and $b = 9$ fm (right) in the Glauber model (squares) and the Saturation model (circles).

The radial modes have up to numerical fluctuations of the order $|\tilde{\varepsilon}_n|_l \lesssim 10^{-3}$ for $n \geq 1$ no eccentricities. A small amount of remaining energy within the non-radial modes is most probably due to grid artifacts, which make it impossible to resolve the modes exactly.

For the eccentricities we find at $b = 0$ fm that the modes with a given ε_n occur in pairs, with the exception that the radial modes come as a singlet. For example, the modes $l = 1, 2$ have a sizable $\tilde{\varepsilon}_1$ followed by the modes $l = 3, 4$ which have a sizable $\tilde{\varepsilon}_2$ and so on. This is enforced by the rotational symmetry at vanishing impact parameter which does not imply a preferred direction such that the modes with closely lying eigenvalues, which are almost degenerate, are similar up to a rotation. Small differences in the eccentricities of a mode pair can be assigned to the numerical fluctuations. Another thing to notice in the left panel of Fig. 7.5 is that in both models the modes $l = 20$ and 28 do not show any eccentricity nor energy. We can explain this by looking at the eigenvectors of the two models in Figs. F.5 and F.7, where we can see that these modes have a $\tilde{\varepsilon}_7$ symmetry which we do not show. Comparing both models it becomes evident that the eccentricities of the modes from the Glauber model are in general larger compared to those from the Saturation model but the structure of the modes is the same in both models.

Now we turn to the right panel of Fig. 7.5 which shows the $b = 9$ fm eccentricities. For the broken rotational symmetry we find now that the modes do no longer occur in pairs with regards to the eccentricities $|\tilde{\varepsilon}_n|_l$ for $n \geq 1$. Recall, that the same is also true for w_l, where the degeneracy of the modes was lifted. The lack of rotational symmetry leads to the absence of purely radial modes, which is also visible in the eigenvector plots in Figs. F.6 and F.8. There one can see that the eigenvectors at $b = 9$ fm are elongated along the x- or y-axis leading to more modes with sizable $\tilde{\varepsilon}_2$. In general the modes do not seem to have a single eccentricity as it is the case for vanishing impact parameter but rather a contribution to either all odd or all even eccentricities. However, there are exceptions to this behavior, e.g., mode $l = 15$ in

the Glauber model, where we can see a mixture of even and odd eccentricities. This can be caused by the degeneracy of the eigenvalues between two modes which is visible in Fig. 7.3 and leads to a mode mixing. For impact parameter $b = 9$ fm there are more modes with up to a few percent of the average state energy. When we compare the order of the modes between the two initial state models we find that it is no longer the same as it was in the rotationally symmetric case at $b = 0$ fm.

For a further characterization of the modes and the average states we perform a rotation of each mode such that the largest $|\tilde{\varepsilon}_n|$ obtained from Eqs. (7.18)-(7.19) is oriented along the x-axis. This is maximizing the real part of $\tilde{\varepsilon}_n$ and up to numerical fluctuations the imaginary part vanishes. We define the two quantities $\mathcal{C}_l(r)$ and $\mathcal{S}_l(r)$ for the rotated modes by

$$\mathcal{C}_l(r) \equiv \int \mathrm{d}\theta \; \Psi_l(r,\theta)\cos(n\theta), \tag{7.20}$$

$$\mathcal{S}_l(r) \equiv \int \mathrm{d}\theta \; \Psi_l(r,\theta)\sin(n\theta). \tag{7.21}$$

If one considers these quantities for the average state, then the angle θ is measured from the x-axis. As we want to make the two quantities comparable between the two initial state models, we normalize them by the corresponding average state energy:

$$\mathcal{A}_l(r) \equiv -\frac{\mathcal{C}_l(r)}{\bar{\mathcal{E}}}, \tag{7.22}$$

$$\mathcal{B}_l(r) \equiv -\frac{\mathcal{S}_l(r)}{\bar{\mathcal{E}}}, \tag{7.23}$$

where we denote by $l = \bar{\Psi}$ the functions for the average state. The latter two quantities are similar to the definition of the mode eccentricities $\tilde{\varepsilon}_n$, with the difference that there is no r^n weight in the numerator and no integration over r in the numerator and denominator.

In Fig. 7.6 we present the quantity $\mathcal{A}_{\bar{\Psi}}(r)$ for the average states of the Glauber (full lines) and the Saturation model (dotted lines) at the two different impact parameters. The horizontal axis is rescaled by the typical system radius R, which is the radius of the lead nucleus used for the sampling of the nucleons in the MC Glauber model, i.e., $R_{\mathrm{Pb}} = 6.62$ fm. As expected, the density profiles are positive. Comparing the two models we find that their average events both have a similar extent in the radial direction for both impact parameters. For $b = 0$ fm the Glauber model has more energy in the center, what we have also seen in Fig. 7.1, but it drops faster in the outer regions compared to the Saturation model result. At non-vanishing impact parameter the opposite behavior is found.

For the modes there have to be sign changes in the transverse profiles $\mathcal{A}_l(r)$, as the modes with the same rotational symmetry are orthogonal to each other. We denote the "k-th excitation" (of a given rotational symmetry) the modes with $k-1$ sign changes in $\mathcal{A}_l(r)$.

In Fig. 7.7 we show the transverse profiles for the first five radial modes in the two initial state models at $b = 0$ fm. To have a better overview, we multiplied the modes by -1 which have a negative value at $r = 0$ in Figs. F.5 and F.7. All the radial modes have in common that they start at a finite value at $r = 0$ and have

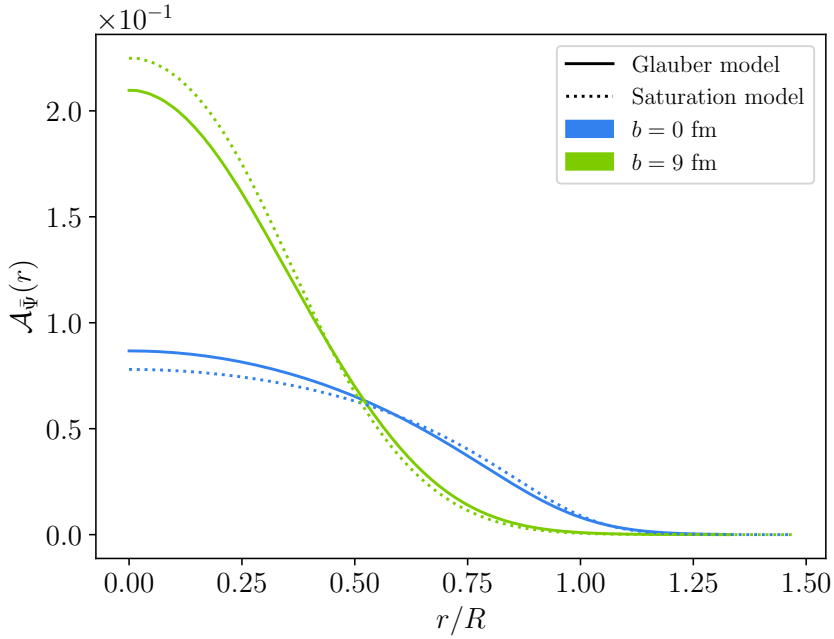

Figure 7.6: $\mathcal{A}_{\bar{\Psi}}(r)$ (Eq. (7.22)) for the average states in the Glauber (full lines) and Saturation (dotted lines) model at $b = 0, 9$ fm.

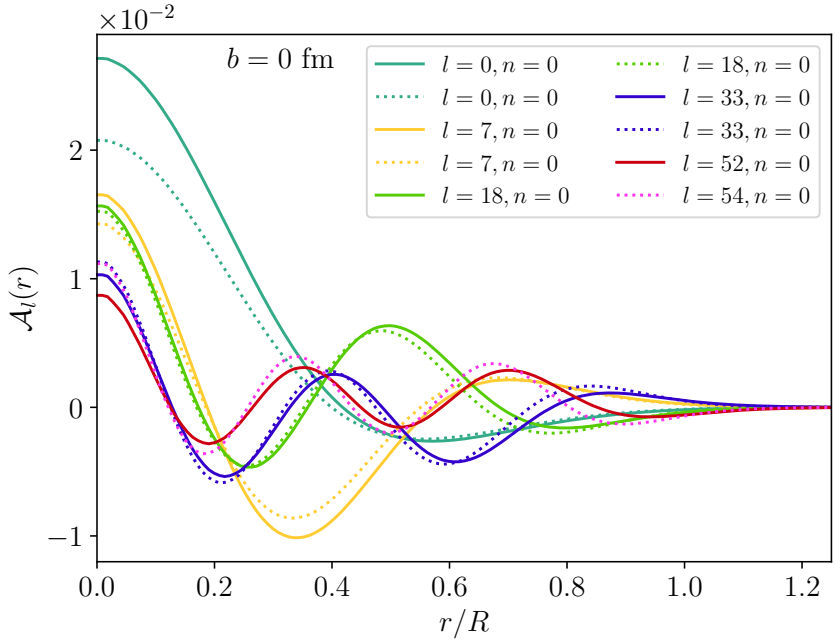

Figure 7.7: $\mathcal{A}_{\bar{\Psi}}(r)$ for the radial modes in the Glauber (full lines) and Saturation (dotted lines) models at $b = 0$ fm.

at least one sign change. The decrease of the amplitude at $r = 0$ for a given model with increasing l is due to the decreasing norm $||\Psi_l|| = \sqrt{\lambda_l}$ of the modes.

We present the first excitation, i.e., a constant sign, modes with a $\tilde{\varepsilon}_n$ in Fig. 7.8 for $n \in \{1, \ldots, 5\}$.

At $b = 0$ fm the two models show the same combination of modes l and spatial anisotropies $n \in \{2, \ldots, 5\}$ (see also Fig. 7.5). We did not find a mode with $n = 1$

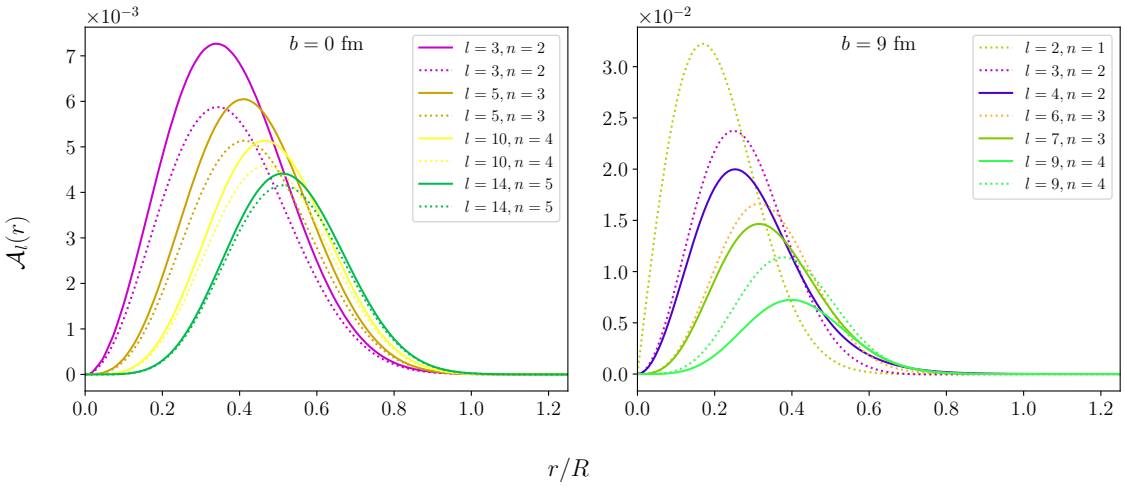

Figure 7.8: $\mathcal{A}_l(r)$ (Eq. (7.22)) for the "first excitation" modes for each harmonic n, corresponding to the maximal $\tilde{\varepsilon}_n$, at $b = 0$ fm (left) and $b = 9$ fm (right). Full resp. dotted lines show the results for the Glauber resp. Saturation models.

without a sign change along r in both models. Such a mode is only found for the Saturation model at $b = 9$ fm (right panel Fig. 7.8). Additionally there is no mode with a $n = 5$ and no sign change in $\mathcal{A}_l(r)$. Another observation is that for increasing l and n the maxima of the quantity $\mathcal{A}_l(r)$ are at larger radii and they decrease in amplitude.

The second excitations are given in Fig. 7.9, where we find the same trend for the maxima as for the first excitations for the modes with $n \in \{2, \ldots, 5\}$. We find

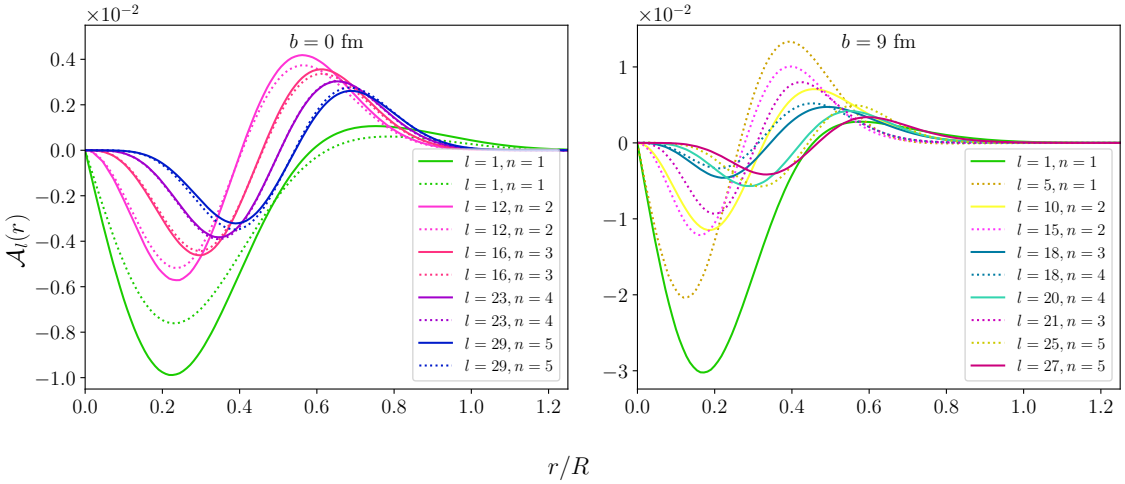

Figure 7.9: $\mathcal{A}_l(r)$ (Eq. (7.22)) for the "second excitation" modes for each harmonic n, corresponding to the maximal $\tilde{\varepsilon}_n$, at $b = 0$ fm (left) and $b = 9$ fm (right). Full resp. dotted lines show the results for the Glauber resp. Saturation models.

again that the $\tilde{\varepsilon}_1$ modes are special, as they have a first extremum which is quite large in amplitude compared to the amplitude of the following extremum at larger r. All other harmonics show minima and maxima which are of similar magnitude.

For the quantity $\mathcal{B}_l(r)$ we find values which are one or more orders of magnitude smaller than the values of $\mathcal{A}_l(r)$ at both impact parameters. Thus, they are more

affected by a finite grid spacing and numerical integration errors. We will not discuss them further, as they are expected to vanish anyhow.

7.1.4.2 Comparison to Bessel-Fourier decomposition

An alternative way of characterizing the average state $\bar{\Psi}$ and the fluctuation modes $\{\Psi_l\}$ we have discussed previously is to us a different choice of basis which is not "optimized" in the sense that one uses the modes directly.

One basis one can use for the two-dimensional density profiles from our two initial state models is the one used for a Bessel-Fourier decomposition, which has been used before to characterize initial state densities [41,117,119,122]. The biggest advantage of this basis decomposition is the data reduction, where we will see that one can store a single mode to a very good approximation with $\mathcal{O}(10)$ expansion coefficients, while our orthogonal grid basis uses $\mathcal{O}(10^4)$ values to store a single mode. This basis gives also the opportunity to perform (semi-)analytical calculations in a mode-by-mode approach, which is not possible with the "trivial" grid basis.

The Bessel-Fourier decomposition has been defined in Sec. 2.4.2 such that we can directly present the results for the coefficients $|A_{n,k}|$ for the average event and the modes from the Glauber model. As the Saturation model leads to similar results in the Bessel-Fourier expansion we will only stick to the Glauber model results to keep the discussion short.

In Fig. 7.10 we show the absolute values of the Bessel-Fourier coefficients for the average states at $b = 0$ and 9 fm presented in the upper panel of Fig. 7.1. For vanishing impact parameter the only non-vanishing components are $A_{0,k}$, which

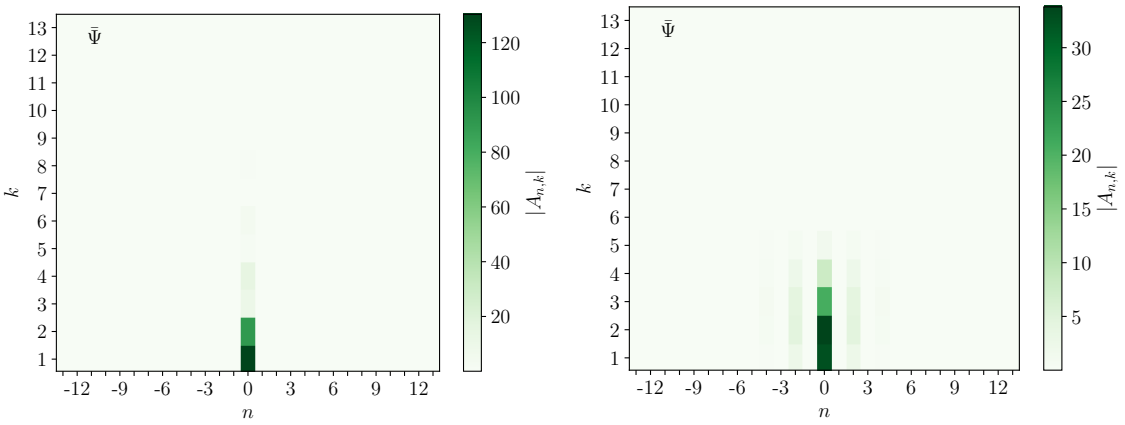

Figure 7.10: Absolute values of the expansion coefficients $|A_{n,k}|$ for the average states at $b = 0$ fm (left) and $b = 9$ fm (right) in the Glauber model.

was to be expected, since the average state is radially symmetric. These radially symmetric coefficients decrease rapidly for increasing values of k. When we look at the case $b = 9$ fm we can see directly that more coefficients are needed for the description of the average state. Similar to $b = 0$ fm we find a large contribution at $n = 0$, with the difference that the coefficient $A_{0,2}$ is now larger than $A_{0,1}$. In addition we obtain smaller coefficients with $n = 2$ and 4, which correspond to the reported ε_2 and ε_4 shape reported in Tab. 7.1 for $b = 9$ fm.

Figures 7.11-7.12 display the absolute values $|A_{n,k}|$ for some selected modes at $b = 0$ and $b = 9$ fm respectively. In the case where the impact parameter is

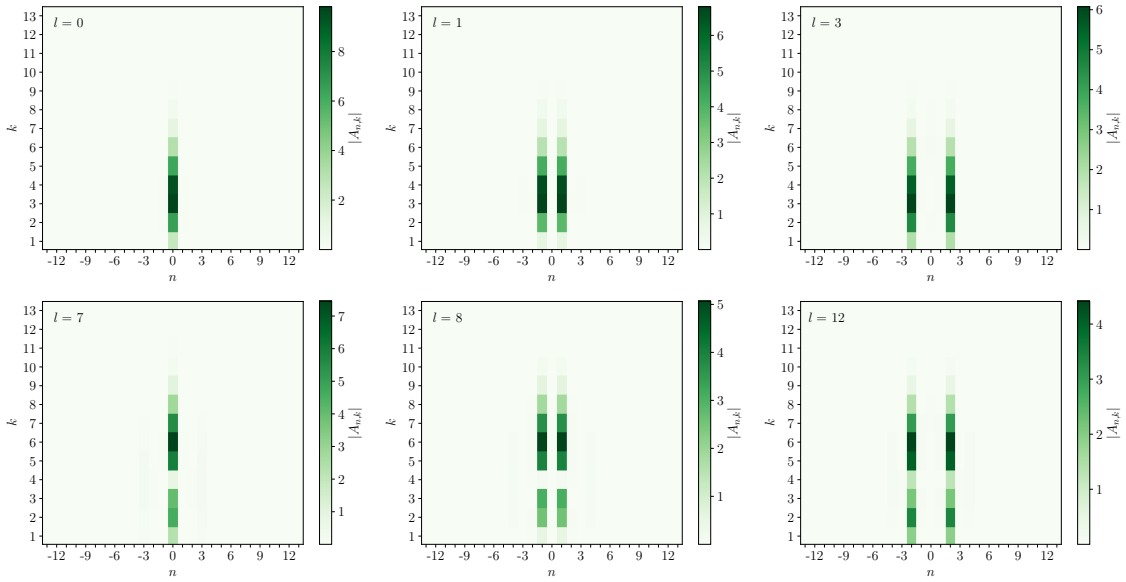

Figure 7.11: Absolute values of the expansion coefficients $|A_{n,k}|$ for radial modes (left), ε_1 modes (center) and ε_2 modes (right) at $b = 0$ fm in the Glauber model. The upper panel shows the first modes of the corresponding harmonic and the lower panel the next higher excitation of the harmonics.

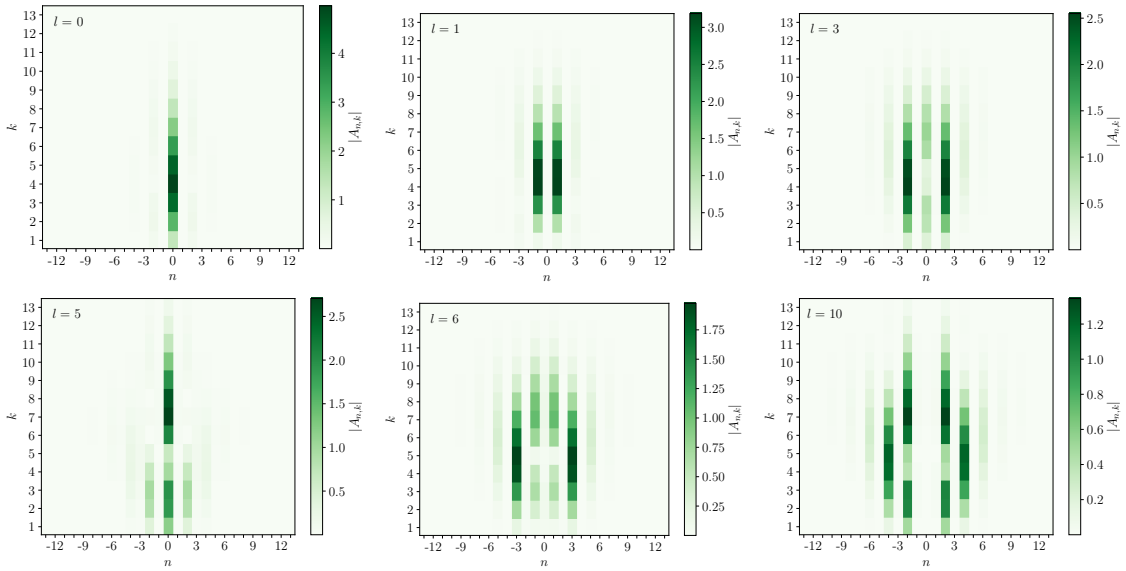

Figure 7.12: Absolute values of the expansion coefficients $|A_{n,k}|$ for radial modes (left), ε_1 modes (center) and ε_2 modes (right) at $b = 9$ fm in the Glauber model. The upper panel shows the first modes of the corresponding harmonic and the lower panel the next higher excitation of the harmonics.

vanishing we have already found that there are modes which are radial or have a single eccentricity $\tilde{\varepsilon}_n$. The left panel of Fig. 7.11 shows the radial modes with $l = 0$ resp. $l = 7$ at the top resp. bottom. As for the average state we see that only

coefficients with $n = 0$ contribute and we find that the largest coefficient has a larger k compared to the average state. Comparing the two modes, which we have characterized as first and second radial excitation before, we see that the second excitation ($l = 7$) changes sign twice in the radial direction, while the first excitation ($l = 0$) has only one sign change. This implies that the higher the excitation the more sign changes are there in radial direction, such that the structure is on smaller length scales. Thus, there is more weight of the $|A_{n,k}|$ at higher k-values. We find this also when looking at the $\tilde{\varepsilon}_1$ (middle panels in Fig. 7.11) or for $\tilde{\varepsilon}_2$ modes (right panels). As expected, these modes have only sizable contributions at $A_{\pm 1,k}$ or $A_{\pm 2,k}$ respectively. Similar to the radial case we find again that the higher excitations (lower panels) show two maxima with increasing k in the $|A_{n,k}|$ values.

For impact parameter $b = 9$ fm we know from Fig. 7.5 that the modes show in general multiple non-vanishing $\tilde{\varepsilon}_n$. In the Bessel-Fourier expansion we can see this fact in Fig. 7.12, where there are multiple sizable $A_{n,k}$ values for different n. To have an easier denomination of the modes we will call a mode "mostly-ε_n" for n which shows the largest eccentricity. We show a mostly-ε_1 (middle upper panel), two mostly-ε_2 modes (right panels) and a mostly-ε_3 mode (middle lower panel). In the left panels we show the Bessel-Fourier coefficients for "quasi-radial" modes. These have their maximum coefficients at $n = 0$. Compared to the vanishing impact parameter case we need significantly more coefficients, even for low-lying modes with $l \leq 10$, in both azimuthal (n) and radial (k) direction. This shows again that there is more structure at the smaller length scales.

7.2 Mode-by-mode response

In Sec. 7.2.1 we will introduce the theoretical framework for a (non-)linear mode-by-mode response for different characteristics of the system introduced in Sec. 7.2.2. Section 7.2.3 will then shortly introduce the dynamical framework including KøMPøST and MUSIC, which we will use to evolve the initial energy densities in time. Afterwards we present the results on the response of observables in the Glauber model (Sec. 7.2.4) and we investigate the linear and non-linear hydrodynamic response coefficients to the initial-state geometry for single modes in Sec. 7.2.5.

7.2.1 Theory

Given a set of observables $\{O_\alpha\}$, where the index α is labeling the type of characteristics, and a random event Φ characterized by an average state $\bar{\Psi}$ and modes Ψ_l corresponding to the rescaled eigenvectors of the density matrix ρ, we can write the decomposition[4]

$$\Phi = \bar{\Psi} + \sum_l c_l \Psi_l. \tag{7.24}$$

[4]In this context we will use the word "observable" also for the initial state quantities which are not measurable in experiments.

Then the observables O_α can be expanded in a Taylor series as

$$\begin{aligned} O_\alpha(\Phi) &= O_\alpha\left(\bar{\Phi}\right) + \sum_l \left.\frac{\partial O_\alpha}{\partial c_l}\right|_{\bar{\Psi}} c_l + \frac{1}{2}\sum_{l,l'} \left.\frac{\partial^2 O_\alpha}{\partial c_l \partial c_{l'}}\right|_{\bar{\Psi}} c_l c_{l'} + \mathcal{O}\left(c_l^3\right) \\ &\equiv \bar{O}_\alpha + \sum_l L_{\alpha,l} c_l + \frac{1}{2}\sum_{l,l'} Q_{\alpha,ll'} c_l c_{l'} + \mathcal{O}\left(c_l^3\right). \end{aligned} \tag{7.25}$$

By $\bar{O}_\alpha$ we denote the value of the observable of the average state $\bar{\Psi}$ and $L_{\alpha,l}$ resp. $Q_{\alpha,ll'}$ is the linear resp. quadratic response of the observable α to the mode with index l resp. l and l'.

Performing then an average over a given observable O_α yields

$$\begin{aligned} \langle O_\alpha \rangle &\simeq \left\langle \bar{O}_\alpha + \sum_l L_{\alpha,l} c_l + \frac{1}{2}\sum_{l,l'} Q_{\alpha,ll'} c_l c_{l'} \right\rangle \\ &= \bar{O}_\alpha + \frac{1}{2}\sum_l Q_{\alpha,ll}, \end{aligned} \tag{7.26}$$

where we used $\left\langle \bar{O}_\alpha \right\rangle = \bar{O}_\alpha$ as well as the properties from Eqs. (7.2)-(7.3) for the statistics of the expansion coefficients c_l. We find that for this average there is no contribution from the linear response coefficients as well as the quadratic response with $l \neq l'$.

Additionally we can compute the covariance of an observable following naturally from Eq. (7.25) in combination with Eq. (7.26) leaving us with

$$\left\langle \left(O_\alpha - \bar{O}_\alpha\right)\left(O_\beta - \bar{O}_\beta\right) \right\rangle = \sum_l L_{\alpha,l} L_{\beta,l}, \tag{7.27}$$

where the case $\alpha = \beta$ yields the variance of O_α.

To actually calculate the response coefficients, we define two new states Ψ_l^+ and Ψ_l^- as

$$\Psi_l^+ \equiv \bar{\Psi} + \delta\Psi_l, \tag{7.28}$$

$$\Psi_l^- \equiv \bar{\Psi} - \delta\Psi_l, \tag{7.29}$$

where we introduce the small parameter δ to compute the derivatives in Eq. (7.25) numerically. By using these new perturbed states we can compute observables with them, as their densities are positive everywhere such that they can be evolved in time. The observables of these states are denoted as $O_{\alpha,l}^{\pm}\left(\Psi_l^{\pm}\right)$ such that we can write first-order and second-order centered derivatives as

$$L_{\alpha,l} = \frac{O_{\alpha,l}^+ - O_{\alpha,l}^-}{2\delta}, \tag{7.30}$$

$$Q_{\alpha,ll} = \frac{O_{\alpha,l}^+ + O_{\alpha,l}^- - 2\bar{O}_\alpha}{\delta^2}. \tag{7.31}$$

The expansion of the observables and their first moments (Eqs. (7.25)-(7.27)) can be extended to higher orders in $\{c_l\}$ and as they are by construction of order

1 the effects of higher orders should be tested in the future. In the following we will see that cutting the expansion at order c_l^2 can give a sufficient approximation for numerous observables. If we would extend the expansion to the next higher order in c_l then n-point averages with $n \geq 3$ for $\{c_l\}$ would appear. These higher n-point functions are not fixed within the construction of the basis as the one- and two-point functions (Eqs. (7.2)-(7.3)) such that they have to be determined from the event sample.

7.2.2 Characteristics

As we want to include several observables in our linear response framework, let us now introduce them.

We start with the computation of characteristic quantities of the initial state from the centered initial state energy density. The latter is either computed for the states $\bar{\Psi}$, Ψ_l^+ or Ψ_l^- defined in Eqs. (7.4), (7.28)-(7.29) for the first 256 modes and different values of δ specified in Sec. 7.2.4.1 or for randomly sampled events in one of the two initial state models considered. From the states $\bar{\Psi}$ and $\Psi_l^\pm$ we can then compute the linear and quadratic response coefficients given in Eqs. (7.30)-(7.31).

The total energy per unit rapidity $\mathrm{d}E/\mathrm{d}y$ is given by the integral over the energy density in the whole transverse plane

$$\frac{\mathrm{d}E}{\mathrm{d}y} \equiv \int e(r,\theta)\, r\mathrm{d}r\mathrm{d}\theta, \tag{7.32}$$

anticipating the fact that our system is longitudinally boost-invariant. A second observable is the average square radius $\{r^2\}$, where $\{\dots\}$ denotes an average over the centered density:

$$\{r^2\} = \frac{\int r^2 e(r,\theta)\, r\mathrm{d}r\mathrm{d}\theta}{\int e(r,\theta)\, r\mathrm{d}r\mathrm{d}\theta}. \tag{7.33}$$

In addition we compute the cosine and sine parts of the spatial eccentricities $\varepsilon_{n,\mathrm{c}}$ and $\varepsilon_{n,\mathrm{s}}$, defined by taking the real resp. imaginary part of the definitions in Eq. (2.25), for the first five harmonics to characterize the spatial anisotropies of the energy density. Notice, that in contrast to the afore defined "mode eccentricities" $\tilde{\varepsilon}_n$ in Sec. 7.1.4 this definition has the same density in the numerator and denominator.

Now we will turn to the final state observables after evolving the system in time, which is described in Sec. 7.2.3, consisting of hadrons. We compute the final-state observables at midrapidity from the charged hadron distribution $\mathrm{d}N_{\mathrm{ch}}/p_{\mathrm{T}}\mathrm{d}p_{\mathrm{T}}\mathrm{d}\varphi_{\mathrm{p}}\mathrm{d}\eta$ obtained from each event.[5] The number of charged hadrons per unit rapidity $\mathrm{d}N_{\mathrm{ch}}/\mathrm{d}\eta$ is given by

$$\frac{\mathrm{d}N_{\mathrm{ch}}}{\mathrm{d}\eta} \equiv \int \frac{\mathrm{d}N_{\mathrm{ch}}}{\mathrm{d}\eta p_{\mathrm{T}}\mathrm{d}p_{\mathrm{T}}\mathrm{d}\phi_{\mathrm{p}}}\, p_{\mathrm{T}}\mathrm{d}p_{\mathrm{T}}\mathrm{d}\phi_{\mathrm{p}}, \tag{7.34}$$

[5] Midrapidity means the pseudorapidity in the range $|\eta| \leq 0.5$.

where ϕ_{p} is the azimuth of the particle in momentum space. The integral over the transverse momentum p_{T} is performed in the range 0.01-3 GeV/c for all our observables.

Next we define the event-by-event transverse momentum $[p_{\mathrm{T}}]$

$$[p_{\mathrm{T}}] \equiv \frac{\int p_{\mathrm{T}} \frac{\mathrm{d}N_{\mathrm{ch}}}{\mathrm{d}\eta p_{\mathrm{T}} \mathrm{d}p_{\mathrm{T}} \mathrm{d}\phi_{\mathrm{p}}} \, p_{\mathrm{T}} \mathrm{d}p_{\mathrm{T}} \mathrm{d}\phi_{\mathrm{p}}}{\int \frac{\mathrm{d}N_{\mathrm{ch}}}{\mathrm{d}\eta p_{\mathrm{T}} \mathrm{d}p_{\mathrm{T}} \mathrm{d}\phi_{\mathrm{p}}} \, p_{\mathrm{T}} \mathrm{d}p_{\mathrm{T}} \mathrm{d}\phi_{\mathrm{p}}}. \tag{7.35}$$

The last type of final-state observables considered are the integrated anisotropic flow coefficients v_n already defined in Eq. (1.6). To be consistent with the initial state observables, we will also look at the cosine and sine parts of the flow coefficients, i.e. $v_{n,\mathrm{c}}$ and $v_{n,\mathrm{s}}$. Considering the real and imaginary parts of the eccentricities and the flow coefficients separately has the advantage that the observables are more smooth around $\delta = 0$ being able to take positive and negative values. In contrast the absolute values $\varepsilon_n = \sqrt{(\varepsilon_{n,\mathrm{c}})^2 + (\varepsilon_{n,\mathrm{s}})^2}$ or v_n are never negative, such that the first derivative of these observables with respect to some of the expansion coefficients c_l at $\delta = 0$ may be undefined.

7.2.3 Time evolution

For the time evolution we employ two well established numerical frameworks. The pre-equilibrium evolution is described by the effective kinetic theory description KøMPøST [125] and the relativistic dissipative hydrodynamics stage is using MUSIC [126–128].

Using the energy density profiles from the Glauber and Saturation models we initialize an energy-momentum tensor

$$T^{\mu\nu}(\tau_0, x, y) = \mathrm{diag}(e(x,y), e(x,y)/2, e(x,y)/2, 0) \tag{7.36}$$

similar to Ref. [125] assuming longitudinal boost invariance. The initial state energy densities provided by the two initial state models are stored on a grid with spacings 0.19 resp. 0.21 fm for the Glauber resp. Saturation model. As these grids are too coarse for the subsequent evolution, we used a bilinear interpolation (Appendix G.2) of the energy density to obtain a grid spacing of 0.1 fm for both models. The pre-equilibrium stage is initialized at $\tau_0 = 0.2$ fm/c and we let the system evolve with an effective shear viscosity to entropy density ratio $\eta/s = 0.16$ until $\tau_{\mathrm{hydro}} = 1.1$ fm/c.

After the pre-equilibrium stage the energy momentum tensor is further evolved within MUSIC in the boost-invariant mode, i.e. 2+1 dimensional. The equation of state we use is a lattice QCD result by the hotQCD collaboration [129]. First order transport coefficients are chosen to be a constant $\eta/s = 0.16$ and a vanishing bulk viscosity. At $T_{\mathrm{fo}} = 155$ MeV a Cooper-Frye freeze-out is performed using the Cornelius algorithm [130] to find the hyper-surface including δf corrections. In the freeze-out process we include 320 particle species whose momentum distributions are computed. Afterwards decays are performed without including any further hadronic rescatterings. Finally the observables are computed from the resulting charged-hadron single-particle distributions using the equations presented in Sec. 7.2.2.

ea

7.2.4 Response of observables in the Glauber model

7.2.4.1 Linearity check

In order to check the applicability of the Taylor expansion in Eq. (7.25) for the different observables O_α introduced in the previous section, we will now compute them for different values of δ ranging between -2 and 2 for a number of modes Ψ_l. We compute $O^+_{\alpha,l} - \bar{O}_\alpha \equiv O_\alpha\left(\bar{\Psi} + \delta\Psi_l\right) - O_\alpha\left(\bar{\Psi}\right)$ and show this quantity as a function of δ in Fig. 7.13 for the initial state (left) resp. final state (right) observables at $b = 0$ fm (top) resp. $b = 9$ fm (bottom) for the Glauber model.[6] Anticipating the

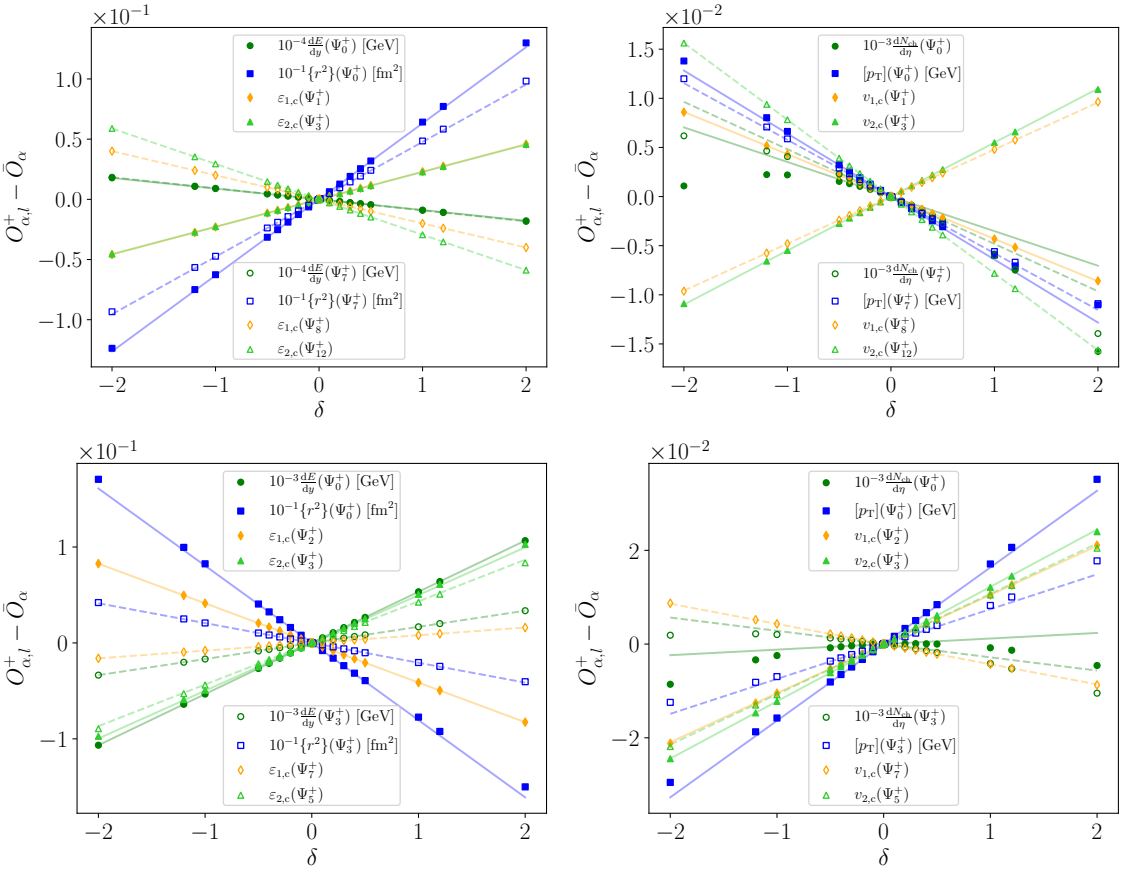

Figure 7.13: $O^+_{\alpha,l}$ for exemplary modes ($\bar{O}_\alpha$ subtracted) as a function of δ in the initial state (left) and final state (right). Closed symbols and full lines correspond to first excitation modes, while open symbols and dashed lines correspond to second excitation modes. The Glauber model was used for impact parameters $b = 0$ fm (top) and $b = 9$ fm (bottom).

results in Sec. 7.2.4.2 we have chosen the modes with the first (full symbols) and second (open symbols) non-vanishing contribution to the observables $\mathrm{d}E/\mathrm{d}y$, $\{r^2\}$, $\varepsilon_{1,c}$, $\varepsilon_{2,c}$ for the initial state resulting in a non-zero response for $\mathrm{d}N_{ch}/\mathrm{d}\eta$, $[p_T]$, $v_{1,c}$ and $v_{2,c}$ in the final state. The straight lines displayed for all observables are linear fits in the range $\delta \in \{0, \pm 0.001, \pm 0.01\}$.

[6] Results for the Saturation model are similar and thus presented in Appendix F.3.1.

For vanishing impact parameter we find that the initial-state observables are mostly linear in δ. An exception is the average square radius $\{r^2\}$, which shows a small deviation from the fit line at large values of $|\delta|$. This deviation is caused by the denominator in Eq. (7.33), which is itself a function of δ, such that the ratio is non linear. The final state flow coefficients are also linear in δ. For the charged hadron multiplicity and the average transverse momentum there is a more pronounced departure from the linear fits, which will be further investigated in the next Section.

At $b = 9$ fm we find similar behaviors for the observables. The initial state non-linearity for $\{r^2\}$ becomes larger than at vanishing impact parameter and we find also a small non-linearity for the eccentricity $\varepsilon_{2,\mathrm{c}}$. In the final state the initial-state nonlinear behavior of $\varepsilon_{2,\mathrm{c}}$ is translated into a nonlinear $v_{2,\mathrm{c}}$. This non-linearity is however not as demonstrative as the one for $\mathrm{d}N_{\mathrm{ch}}/\mathrm{d}\eta$ or $[p_{\mathrm{T}}]$.

7.2.4.2 Linear and quadratic response coefficients

To give a more quantitative characterization of the (non-)linear contributions of the individual modes to the observables, we will discuss the linear and (diagonal) quadratic response coefficients $\{L_{\alpha,l}\}$, $\{Q_{\alpha,ll}\}$ (Eq. (7.25)) computed from Eqs. (7.30)-(7.31) in the following. Here we will only show the results for the Glauber model, as the qualitatively similar results are presented in Appendix F.3.

Figures 7.14 resp. 7.15 show the linear resp. quadratic response coefficients, where the top panels are the values at impact parameter $b = 0$ and the bottom panels at $b = 9$ fm. All initial state quantities are shown on the left and the final state observables are on the right. Response coefficients for dimensionful quantities ($\mathrm{d}E/\mathrm{d}y$, $\{r^2\}$, $[p_{\mathrm{T}}]$) and the multiplicity $\mathrm{d}N_{\mathrm{ch}}/\mathrm{d}\eta$ have been divided by the $\bar{O}_\alpha$ value of the average state observable (and a numerical coefficient) to obtain values which are comparable in one plot with the eccentricity or the flow coefficient response. To simplify the comparison between the two impact parameters, we use the same scale in the upper and lower panel plots, which explains why the upper left plot in Fig. 7.15 (and in Fig. F.11) seem to be empty. This shows that the quadratic response coefficients at $b = 9$ fm (lower left panels) are significantly larger then the ones at vanishing impact parameter. Going back to Eq. (7.25) we see that the response coefficients contribute to an observable either via multiplying an expansion coefficient c_l or its square. We have already seen that the c_l coefficients are of the order 1 and as the linear response (Fig. 7.14) is around one order of magnitude larger than the quadratic response (Fig. 7.15), the linear contribution to the observables is generally larger than the quadratic one.

We start with the initial state quantities at vanishing impact parameter (upper left). In this case we know already that each mode has typically either one eccentricity $\varepsilon_{n,\mathrm{c/s}}$ with a purely linear response, or it changes the energy and the mean square radius.[7] The latter response has also a small quadratic contribution. As an example, let us look at $l = 0$. This mode affects $\mathrm{d}E/\mathrm{d}y$ and $\{r^2\}$, while the

[7] As we have pointed out at the beginning of Sec. 7.1.4, there is an exception ($l = 40$). This mode has a ε_1 and a ε_2 contribution, as it is degenerate with the modes $l = 42$ and 43, which have a ε_2 structure.

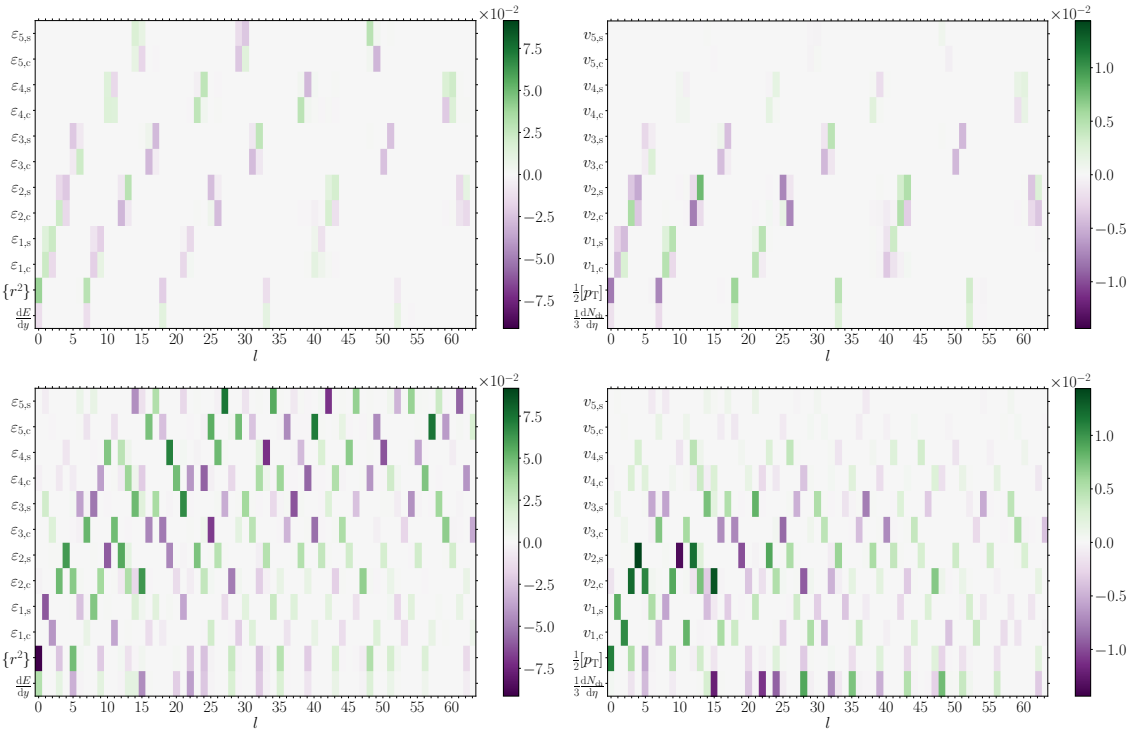

Figure 7.14: Linear response coefficients $L_{\alpha,l}$ for the initial state quantities (upper left) and final state observables (upper right) at $b = 0$ fm in the Glauber model. The same plots for $b = 9$ fm are shown below. All dimensionful observables have been divided by $\bar{O}_\alpha$.

next mode $l = 1$ affects $\varepsilon_{1,\mathrm{c}}$ and $\varepsilon_{1,\mathrm{s}}$. For some modes we do not find a response coefficient, e.g. $l = 19$ or 20, as they have a ε_6, which is not investigated in our study.

The linear response coefficients for $b = 0$ fm directly give the eccentricity of the state $\bar{\Psi} + c_l \Psi_l$ (up to a multiplication with c_l of order 1), as the average state is radially symmetric. For the observables $\mathrm{d}E/\mathrm{d}y$ and $\{r^2\}$ we obtain the relative change being of the order of a few percent of the average state value.

One very obvious feature is the structure of the response in the eccentricities, which shows that two successive modes having $\varepsilon_{n,\mathrm{c}}$ and $\varepsilon_{n,\mathrm{s}}$ for a given n. Three values of these 2×2-structures have the same sign, while the fourth on has the opposite sign. This is due to the rotational symmetry, which allows the symmetry-plane angle Φ_n to be oriented arbitrarily. The only condition is that two degenerate modes have to be rotated by $\pi/2n$, as they would generate the same profile otherwise.[8]

We can see that the contribution of modes with non-vanishing eccentricities to the denominators of Eq. (2.25) is small, as there is no sizable quadratic response coefficient. This fact is also visible on the level of the eigenvectors (Fig. F.5), where the oscillations about zero indicate that the integral of $r^n \Psi_l(r, \theta)$ over θ vanishes if r is fixed.

We will now focus on the linear response of the final state observables at $b =$

[8] One could rotate both modes in such a way that one mode has only a $\varepsilon_{n,\mathrm{c}}$ and the other one a $\varepsilon_{n,\mathrm{s}}$. Then the response coefficients are equal in absolute value. However, if the rotational symmetry is broken, this possibility does no longer exist, such that we will not perform a rotation.

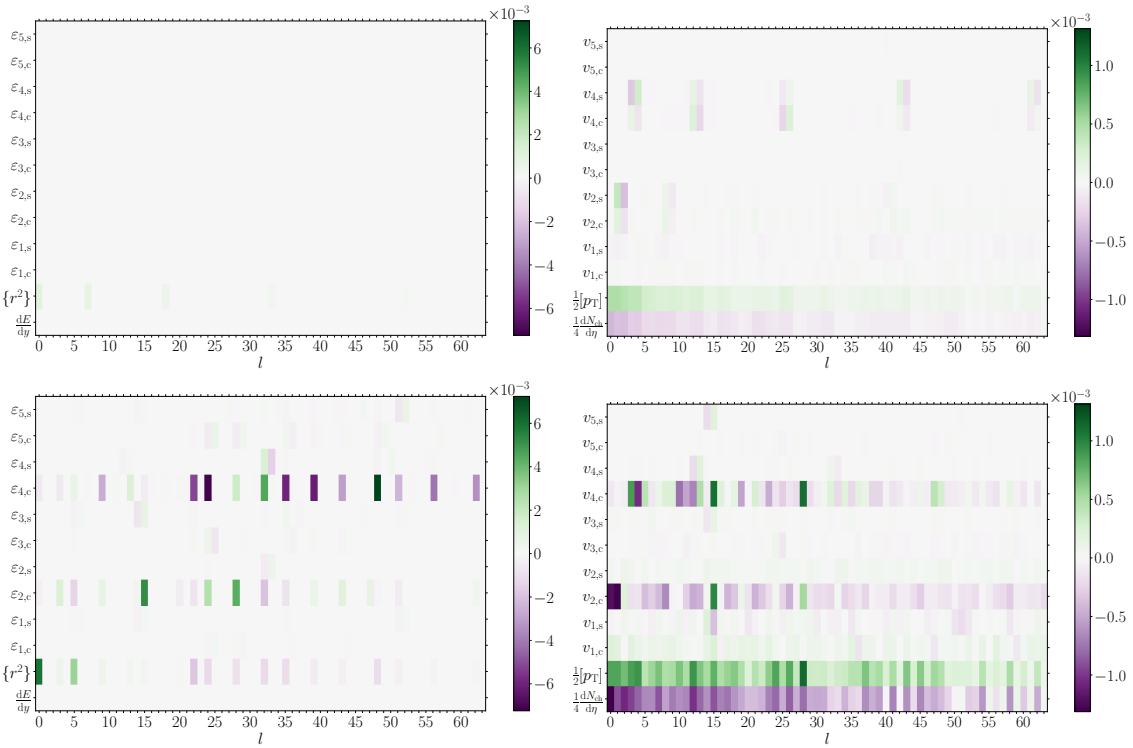

Figure 7.15: Quadratic response coefficients $Q_{\alpha,ll}$ for the initial state quantities (upper left) and final state observables (upper right) at $b = 0$ fm in the Glauber model. The same plots for $b = 9$ fm are shown below. All dimensionful observables have been divided by $\bar{O}_\alpha$.

0 fm (top right panel), which includes also a dynamical response to the initial-state characteristics presented in the upper left panel. There we observe a similar pattern in the final-state responses, as a mode either contributes to the charged hadron multiplicity and the average transverse momentum, or the anisotropic flow harmonics $v_{n,\mathrm{c/s}}$ for a given mode Ψ_l. There is only a linear response to $\mathrm{d}N_{\mathrm{ch}}/\mathrm{d}\eta$ and $[p_{\mathrm{T}}]$ resp. $v_{n,\mathrm{c/s}}$ visible for the modes which have a linear contribution to $\mathrm{d}E/\mathrm{d}y$ and $\{r^2\}$ resp. $\varepsilon_{n,\mathrm{c/s}}$ in the initial state.

Fixing a mode Ψ_l we observe that the linear response of $\mathrm{d}N_{\mathrm{ch}}/\mathrm{d}\eta$ and $\mathrm{d}E/\mathrm{d}y$ has the same sign, while the response for $[p_{\mathrm{T}}]$ and $\{r^2\}$ has opposite sign. This second observation is also true for the Saturation model, but not the first one (see Fig. F.10). For the flow harmonics $v_{n,\mathrm{c/s}}$ we observe the same 2×2-structures as for the initial-state eccentricities. However, we can see that the linear response is significantly weaker for the higher harmonics, especially for $n \geq 3$, reflecting the effect of viscosity, which dampens the finer structures more strongly. This effect of viscosity explains also why the response for lager l is damped, as the modes have finer structures in radial direction for increasing l.

A general observation for the sign of the linear response for the flow harmonics $v_{n,\mathrm{c/s}}$ is, that it is the same as for the eccentricities $\varepsilon_{n,\mathrm{c/s}}$. In the case $n = 1$ this is not true, as the response of ε_1 and v_1 have opposite signs (Fig. 7.14). The sign of ε_1, which has the r^3 weight, determines the sign of v_1 at high p_{T}. This is opposite to the sign of v_1 at low p_{T} to fulfill momentum conservation and thus reflected in the momentum-integrated v_1 [37].

For the quadratic response in the top right panel of Fig. 7.15 we find response coefficients, which are typically smaller than the linear ones. Therefore, there are more sizable quadratic responses visible for the final-state observables, especially for the charged hadron multiplicity $\mathrm{d}N_{\mathrm{ch}}/\mathrm{d}\eta$ (negatively) and the average transverse momentum $[p_{\mathrm{T}}]$ (positively). Thus, we can see again the departure from the linear behavior, which we have already observed for a few modes in Sec. 7.2.4.1 for the two observables (top right panel of Fig. 7.13). In contrast to the linear response coefficients, where only radially symmetric modes contributed to $\mathrm{d}N_{\mathrm{ch}}/\mathrm{d}\eta$ and $[p_{\mathrm{T}}]$, at quadratic order all modes have a contribution. This shows that for most of the modes the first non-vanishing contribution to these two observables is of quadratic order. However, the $\{Q_{\alpha,ll}\}$ is in this case always of the order 10^{-3} or smaller, such that the mode contribution changes the corresponding observable from the average state by a similar relative amount. Additionally, we have to keep in mind that the contribution of the modes decrease in absolute value with increasing l.

We do also observe additional non-linear responses $\{Q_{\alpha,ll}\}$ for the quadratic responses of anisotropic flow coefficients in the harmonic $2n$ to an initial eccentricity in the n-th harmonic, i.e., $v_{2n} \propto \varepsilon_n$. The v_{2n} values from this quadratic response are of the order 10^{-3} or smaller. In real events, which are a superposition of many modes, this response is sub-leading compared to the linear response of v_{2n} to modes with $\varepsilon_{2n} \neq 0$.

Turning now to the case, where the impact parameter is $b = 9$ fm and there is no rotational symmetry, the response coefficients show a more complicated structure. Nevertheless, there are similar trends as for $b = 0$ fm. The most prominent observation is still the viscous damping for the higher-lying fluctuation modes and for the higher anisotropic flow coefficients.

In this case one mode affects multiple observables at linear order in the initial state (bottom left in Fig. 7.14), which is also reflected in the final state linear response coefficients (bottom right in Fig. 7.14) by a one-to-one mapping. Two differences to the response coefficients at vanishing impact parameter are observed. The signs of $\{L_{\alpha,l}\}$ for $\mathrm{d}E/\mathrm{d}y$ and $\{r^2\}$ — and also the corresponding final state correlation resp. anti-correlation between $\mathrm{d}N_{\mathrm{ch}}/\mathrm{d}\eta$ and $[p_{\mathrm{T}}]$ in the Glauber resp. Saturation model (Fig. F.10 bottom right) — does no longer follow a systematics. The second quite obvious observation is that the 2×2-structure of the eccentricities and flow coefficients is no longer present. This is due to the fact that the participant-plane angles Φ_n are preferentially oriented along the direction of the impact parameter, i.e., the x-axis, which results in a finite $\varepsilon_{n,\mathrm{c}}$ and a vanishing $\varepsilon_{n,\mathrm{s}}$, or Φ_n is along the direction $\pi/2n$ from the x-axis, which results in a vanishing $\varepsilon_{n,\mathrm{c}}$ and a finite $\varepsilon_{n,\mathrm{s}}$.

In the final-state linear response coefficients (right panel) on the first look it seems to reflect the responses of the initial state, while we observe a couple of interesting things by taking a closer look. An example are modes $l = 58$ resp 59, which have a sizable $v_{1,\mathrm{s}}$ resp. $v_{1,\mathrm{c}}$, although the corresponding eccentricity in the initial state is very small. At first this seems counterintuitive, but the coefficients $L_{v_1,l}$ measure the v_1 contribution of the modes at order c_l to events of the form $\bar{\Psi} + c_l \Psi_l$, i.e., these events consist of the average state and one of the modes. For a c_l of order 1 these events have a ε_1 of the order 10^{-3}, but a sizable ε_2 from the average state, and a ε_3

from the mode Ψ_l. When this type of initial state is evolved in time, there occurs an interference between the elliptical and triangular geometry, such that there is a non-linear dynamical response

$$v_1\left(\bar{\Psi}+c_l\Psi_l\right) \propto \varepsilon_2\left(\bar{\Psi}\right)\varepsilon_3\left(c_l\Psi_l\right) \tag{7.37}$$

at linear order in c_l.[9] This type of non-linear response

$$v_{|n\pm 2|}\left(\bar{\Psi}+c_l\Psi_l\right) \propto \varepsilon_2\left(\bar{\Psi}\right)\varepsilon_n\left(c_l\Psi_l\right) \tag{7.38}$$

is actually present for all modes at $b = 9$ fm, but cannot be identified for most of the modes, as they have either even or odd eccentricities.

The quadratic response coefficients for the initial state in the bottom left panel of Fig. 7.15 show again sizable non-linear responses for $\{r^2\}$ in cases, where the corresponding mode has also a linear response to $\mathrm{d}E/\mathrm{d}y$ and $\{r^2\}$. In the case $b = 0$ fm there were no further non-linear responses in the initial state. Here we observe sizable non-linear responses $Q_{\alpha,ll}$ mostly for the eccentricities $\varepsilon_{2,\mathrm{c}}$ and $\varepsilon_{4,\mathrm{c}}$. This holds true in the Glauber model, if the modes have at the same time a finite linear response to the same eccentricity, while for the Saturation model it holds true for almost all modes (Fig. F.11 bottom left), even if they have a small $L_{\alpha,l}$ (Fig. F.10 bottom left). These non-linear responses are caused by the denominators in the definition (2.25) and the finite $\varepsilon_{2,\mathrm{c}}$ or $\varepsilon_{4,\mathrm{c}}$ of the average state.

The final-state responses of the observables show that there is a negative resp. positive sizable contribution for $\mathrm{d}N_{\mathrm{ch}}/\mathrm{d}\eta$ and $[p_{\mathrm{T}}]$ in all modes, which we have also seen in the case $b = 0$ fm.[10] A negative quadratic response coefficient $Q_{\alpha,ll}$ is reminiscent of the empirical scaling behavior [131]

$$\frac{\mathrm{d}N_{\mathrm{ch}}}{\mathrm{d}\eta} \propto \left(\frac{\mathrm{d}E}{\mathrm{d}y}\right)^{\frac{2}{3}}. \tag{7.39}$$

This tells us that the initial energy density changes the final-state multiplicity less than linear. We have seen that most of the modes do not change the total energy of the system, but they still change the profile of the energy density distribution, such that there are regions with more (or less) energy than the average state. If we assume that this local change of the energy also results in a local change in the number of emitted particles with a scaling similar to expression (7.39), then the exponent smaller than 1 leads after integration over the whole system to a fluctuation-induced change in the multiplicity, which is less than linear, i.e., $Q_{\alpha,ll} < 0$.

On the other hand, there is an anti-correlation between $\mathrm{d}N_{\mathrm{ch}}/\mathrm{d}\eta$ and $[p_{\mathrm{T}}]$. Since most of the modes do not change the total energy of the system, the decrease in the number of produced particles induces a larger average transverse momentum. The non-trivial part is that it is still true for modes, which change the total energy of the

[9] The notation $\varepsilon_3\left(c_l\Psi_l\right)$ should be substituted by $\varepsilon_3\left(\bar{\Psi}+c_l\Psi_l\right)$, since the energy density used in Eq. (2.25) is $\bar{\Psi}+c_l\Psi_l$. Nevertheless, the used notation emphasizes that only $c_l\Psi_l$ contributes to ε_3.

[10] Opposed to the linear response coefficients, $Q_{\alpha,ll}$ does not change under the transformation $\Psi_l \to -\Psi_l$, which shows, that its sign is meaningful.

system. These modes also change the mean-square radius of the system in the initial state and have a linear order contribution to $\mathrm{d}N_{\mathrm{ch}}/\mathrm{d}\eta$ and $[p_{\mathrm{T}}]$. A disentangling of all these effects is beyond the scope of this work.[11]

We observe that also the quadratic response to $v_{2,\mathrm{c}}$ and $v_{4,\mathrm{c}}$ is sizable for many modes w.r.t the response to the other flow coefficients, which is significantly smaller. The quadratic response to $v_{2,\mathrm{c}}$ and $v_{4,c}$ have different origins, which are entangled. There is a linear response $v_{n,\mathrm{c}} \propto \varepsilon_{n,\mathrm{c}}$ to $\varepsilon_{2,\mathrm{c}}$ and $\varepsilon_{4,\mathrm{c}}$, which is quadratic in c_l (Fig. 7.15 bottom left). Additionally, the modes which have a $\varepsilon_1\left(\Psi_l\right)$ ($\varepsilon_{1,\mathrm{c}}$ or $\varepsilon_{1,\mathrm{s}}$) can lead to a quadratic $v_{2,\mathrm{c}} \propto \varepsilon_1^2$. There is also the possibility of an interference with the ε_2 of the average state to a $v_{4,\mathrm{c}}\left(\bar{\Psi} + c_l\Psi_l\right) \propto \varepsilon_{2,\mathrm{c}}\left(\bar{\Psi}\right)\varepsilon_1\left(c_l\Psi_l\right)^2$. This term also contributes to $v_{2,\mathrm{c}}$ and more generally there are contributions of the form $\varepsilon_{2,\mathrm{c}}\left(\bar{\Psi}\right)\varepsilon_1\left(\Psi_l\right)\varepsilon_3\left(\Psi_l\right)$ or $\varepsilon_{2,\mathrm{c}}\left(\bar{\Psi}\right)\varepsilon_3\left(\Psi_l\right)^2$ (for Ψ_l with odd eccentricities) or $\varepsilon_{2,\mathrm{c}}\left(\bar{\Psi}\right)\varepsilon_2\left(\Psi_l\right)^2$ (for Ψ_l with even eccentricities). Finally, we want to give a further example of a dynamical non-linear response: mode $l = 14$, which has a $\varepsilon_{1,\mathrm{s}}$ (and higher sine harmonics with odd n) and an $\varepsilon_{2,\mathrm{c}}$. When this is dynamically evolved in time, it can produce a $v_{1,\mathrm{s}} \propto \varepsilon_{2,\mathrm{c}}\varepsilon_{1,\mathrm{c}}$, as well as a $v_{3,\mathrm{s}}$ at quadratic order in c_l.[12]

7.2.5 Anisotropic flow response coefficients

We know from a number of studies within either ideal or dissipative hydrodynamics or kinetic theory, that there exist simple relationships between the initial-state eccentricities and final-state anisotropic flow coefficients. In our analysis we use the absolute values of ε_n and v_n [Eqs. (2.25) and (1.6)], and we restrict ourselves to small eccentricities. In this case one finds that the n-th flow harmonic has a linear contribution from ε_n [36–39, 65, 88, 89]

$$v_n = \mathcal{K}_{n,n}\varepsilon_n, \tag{7.40}$$

and also contributions from eccentricities in other harmonics.[13] As we have already seen in Sec. 4.2, the latter contributions are of the form [38, 65, 90, 91]

$$v_n = \mathcal{K}_{n,mp}\varepsilon_m\varepsilon_p \tag{7.41}$$

with $|m \pm p| = n$. Here, we want to discuss how such responses appear on the level of the mode-by-mode analysis.

In the discussion of the response coefficients in the last section we have already related the flow coefficient response to the initial-state eccentricities. We have also seen, that at $b = 9$ fm the sizable ε_2 and ε_4 of the initial state $\bar{\Psi}$ (Tab. 7.1), together with the fact that multiple eccentricities are present for one mode Ψ_l, leads to a complicated interplay between the eccentricities for a given flow harmonic, at the linear and also the quadratic order in the expansion coefficients c_l.

[11] In a planned future extension of this investigation we want to study events at fixed multiplicity, i.e., in centrality classes, instead of fixing the impact parameter. This will make the discussion easier and brings the analysis closer to experiments.

[12] In the case $l = 15$ there is a quadratic $v_{1,\mathrm{s}}$ from $\varepsilon_{2,\mathrm{c}}$ and $\varepsilon_{3,\mathrm{s}}$.

[13] If there is a large ε_2, then a contribution $\propto \varepsilon_2^3$ arises for v_2 [66].

For vanishing impact parameter the situation is much easier, since the average state has radial symmetry and such, the flow signal is only a response to the anisotropy of the modes for events of the form $\bar{\Psi} + c_l \Psi_l$. This asymmetry of the modes contributes to the numerator of the eccentricities $\varepsilon_n \left(\bar{\Psi} + c_l \Psi_l\right)$. There are mostly two cases present. The first one is a linear response as described in (7.40), leading to a non-zero $L_{v_n,l}$, i.e., a linear response of order c_l to Ψ_l with a given ε_n. In this case we compute

$$\mathcal{K}_{n,n} \equiv \frac{v_n \left(\bar{\Psi} + c_l \Psi_l\right)}{\varepsilon_n \left(\bar{\Psi} + c_l \Psi_l\right)}, \tag{7.42}$$

which we present in the left panel of Fig. 7.16. k labels the k-th mode Ψ_l with

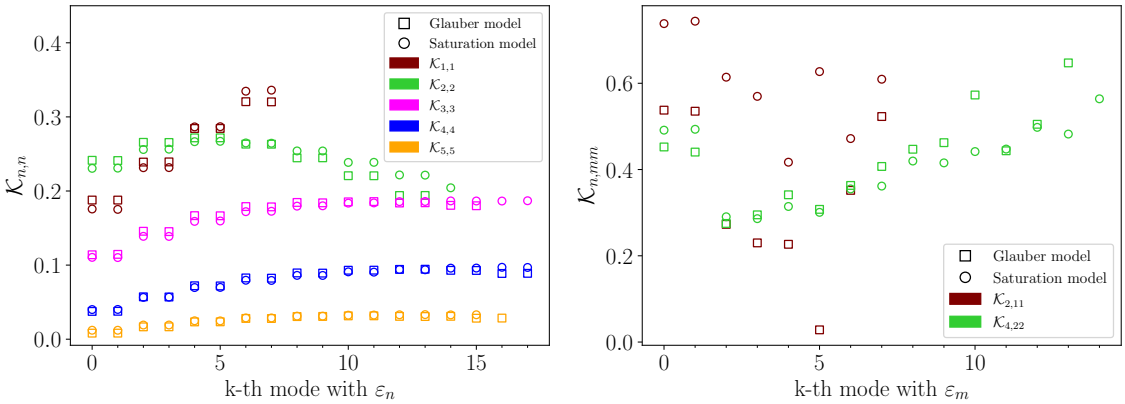

Figure 7.16: Linear flow-response coefficient $\mathcal{K}_{n,n}$ (left) and quadratic response coefficient $\mathcal{K}_{n,mm}$ (right) with $n = 2m$ for modes with $l < 256$ for collisions at $b = 0$ fm within the Glauber (squares) and Saturation (circles) models.

$l < 256$, which has a $\varepsilon_n > 10^{-2}$.[14] The second case is that we find a number of modes with an ε_m in the initial state, where $m = 1$ or 2 leads to a v_n with $n = 2m$ in the final state. This corresponds to Eq. (7.41) with $p = m$. Those modes (with $l < 256$) show a large $Q_{v_n,ll}$ (Fig. 7.15 top right panel) and we show the dynamical response

$$\mathcal{K}_{n,mm} \equiv \frac{v_n \left(\bar{\Psi} + c_l \Psi_l\right)}{\varepsilon_m \left(\bar{\Psi} + c_l \Psi_l\right)^2} \quad \text{with} \quad n = 2m \tag{7.43}$$

in the right panel of Fig. 7.16. In Sec. 7.2.4 we have seen that there exist modes with several sizable eccentricities, which results in "mixed" non linear response (7.41) in the case $m \neq p$. One example would be mode $l = 40$ in the Glauber model, for which we could compute a $\mathcal{K}_{3,21}$, which we did not do. We have constructed the coefficients $\mathcal{K}_{n,n}$ and $\mathcal{K}_{n,mm}$ (Eqs. (7.42)-(7.43)) in such a way that they are positive. In the previous section we have seen that the integrated v_1 has the opposite sign to ε_1, which shows that $\mathcal{K}_{1,1}$ should be negative [91].

For the $\mathcal{K}_{n,n}$ coefficients in the left panel of Fig. 7.16 we find a decrease with n, which is due to the viscous damping in the hydrodynamic evolution of the system.

[14] The numbers l for the two models may differ, especially for the higher modes.

For the quadratic response $\mathcal{K}_{2n,nn}$ this is less visible (right panel), as there might be not enough modes with a sizable ε_1. Once again, we observe that the modes come in doublets, similar to the eccentricities (Fig. 7.5) and the 2×2-structures in the linear response coefficients $L_{\alpha,l}$ (top panels of Figs. 7.14 and F.10).

Both initial-state models show similar values for $\mathcal{K}_{n,n}$, although we have seen that the radial profiles differ. This is also true for the coefficient $\mathcal{K}_{4,22}$, but not for $\mathcal{K}_{2,11}$. For the latter the fluctuation modes with ε_1 in the Saturation model result in a stronger v_2 response compared to the Glauber model. In the case $n = 2, 3, 4$ the coefficient $\mathcal{K}_{n,n}$ is almost constant with increasing mode number l. Only for the $\mathcal{K}_{2,2}$ there might be a decreasing trend, which is rather mild. For the higher modes one would expect that the finer structures along the radial direction lead to a stronger viscous damping. However, this is not seen here.

As the responses are almost constant with increasing l, this gives us the possibility to compare our mode-by-mode results obtained from initial states of the form $\bar{\Psi} + c_l \Psi_l$ to full event-by-event results. In general we find values for $\mathcal{K}_{n,n}$, which are in the same ballpark than the values in the literature:

- $\mathcal{K}_{2,2} \simeq 0.2$–$0.3$ is in good agreement with the findings in hydrodynamical simulations with different setups [65, 66, 113, 132, 133] and in kinetic transport simulations [39, 77, 134].
- $\mathcal{K}_{3,3} \simeq 0.1$–$0.2$ fits most values in the literature [65, 66, 77, 133] apart from Ref. [39], which finds values larger by about a factor 2.
- $\mathcal{K}_{4,4} \simeq 0.05$–$0.1$ is comparable to the results in Refs. [65, 113, 133], although somewhat higher values were found in fluid-dynamical [91] simulations or kinetic theory simulations [39, 84] with $\eta/s = 1/4\pi$.
- In turn, $\mathcal{K}_{5,5} \simeq 0.008$–$0.03$ is twice larger than in Ref. [91], but matches the value in Ref. [133].
- For the last linear coefficient $\mathcal{K}_{1,1}$ the four twofold degenerate values shown in Fig. 7.16 are too few to draw conclusions, yet we find a decent agreement with the results presented in Ref. [37], while the value in Ref. [91] is roughly a factor 2 smaller.

For the quadratic responses we are not aware of any values of $\mathcal{K}_{2,11}$ in the literature, and $\mathcal{K}_{4,22} \simeq 0.3 - 0.6$ (right panel in Fig. 7.16) is significantly larger than the value of 0.1 reported in Ref. [133].

7.3 Comparison to event-by-event simulations

In the following part we want to compare our mode-by-mode predictions to event-by-event simulations of 8192 random events. In Sec. 7.3.1 we will compare $\bar{O}_\alpha$ from the evolution of the average state $\bar{\Psi}$ to the event averaged observables $\langle O_\alpha \rangle$. Then we will discuss the predictions of the mode-by-mode results for the variances and covariances of the observables and compare them to the event-by-event results in Sec. 7.3.2. Finally, in Sec. 7.3.3 we will present results for probability distributions

using linearized Gaussian statistics of the $\{c_l\}$ coefficients and compare them to the full simulations.

7.3.1 Prediction of observables

Now we want to compare the observables of the average states $\bar{\Psi}$ at the two impact parameters to the event-averaged observables using the 1892 randomly sampled events. Our results for the observables, which are not fluctuations, are given in Tab. 7.2.

Table 7.2: Initial and final state quantities for both models at $b = 0$ fm and $b = 9$ fm. For the event-by-event (ebe) simulations we used 8192 events. We compare the ebe simulations with the results by the average state evolution (background). The errors given for the event-by-event results are the standard errors on the mean.

	$\langle \frac{\mathrm{d}E}{\mathrm{d}y} \rangle$	$\{r^2\}$	$\varepsilon_{2,\mathrm{c}}$	$\varepsilon_{4,\mathrm{c}}$	$\langle \frac{dN_{ch}}{d\eta} \rangle$	$[p_T]$	$10^{-2} \cdot v_{2,\mathrm{c}}$	$10^{-3} \cdot v_{4,\mathrm{c}}$
Glauber $b = 0$ fm								
background ($\bar{\Psi}$)	7248	16.29	-	-	2257	0.78	-	-
ebe ($\langle \Phi_i \rangle$)	7247 ± 3	16.30 ± 0.01	-	-	2203 ± 1	0.79 ± 0.0002	-	-
Glauber $b = 9$ fm								
background ($\bar{\Psi}$)	1667	8.72	0.296	-0.094	636	0.75	6.1	4.3
ebe ($\langle \Phi_i \rangle$)	1668 ± 2	8.69 ± 0.02	0.299 ± 0.002	-0.111 ± 0.002	597 ± 1	0.77 ± 0.0003	5.9 ± 0.03	3.7 ± 0.1
Saturation $b = 0$ fm								
background ($\bar{\Psi}$)	6468	17.00	-	-	2119	0.77	-	-
ebe ($\langle \Phi_i \rangle$)	6468 ± 2	17.01 ± 0.01	-	-	2071 ± 1	0.78 ± 0.0002	-	-
Saturation $b = 9$ fm								
background ($\bar{\Psi}$)	1386	7.95	0.406	-0.201	537	0.75	8.5	7.1
ebe ($\langle \Phi_i \rangle$)	1384 ± 2	7.94 ± 0.02	0.410 ± 0.002	-0.220 ± 0.003	493 ± 1	0.79 ± 0.0003	8.2 ± 0.04	6.7 ± 0.2

For a vanishing impact parameter, i.e., an isotropic initial condition we find that the eccentricities and flow coefficients are fluctuations about zero. The initial state quantities $\mathrm{d}E/\mathrm{d}y$ and $\{r^2\}$ show a good agreement between $\bar{O}_\alpha$ and the event average. In the final state there are sizable differences between the two approaches at both impact parameters, especially for $\mathrm{d}N_{\mathrm{ch}}/\mathrm{d}\eta$ and $[p_{\mathrm{T}}]$. We attribute these differences to the non-linearities of these two observables discussed in Sec. 7.2.4.1.

7.3.2 Variances and covariances

In the linear response framework the covariance of two observables is given by Eq. (7.27), which gives us the variance for $\alpha = \beta$. The variance — in the following denoted by $\mathrm{V}(O_\alpha)$ — is a positive definite quantity, while the covariance is not. We will normalize the covariance in the following by the square root of the product of the variances, such that we obtain a quantity quite similar to the Pearson correlation coefficient:

$$\mathrm{C}(\alpha, \beta) = \frac{\langle (O_\alpha - \langle O_\alpha \rangle)(O_\beta - \langle O_\beta \rangle) \rangle}{\sqrt{\mathrm{V}(O_\alpha)\mathrm{V}(O_\beta)}} \tag{7.44}$$

$$= \frac{\sum_l L_{\alpha,l} L_{\beta,l}}{\sqrt{\sum_k L_{\alpha,k}^2 \sum_{k'} L_{\alpha,k'}^2}}. \tag{7.45}$$

The sum over l is cut at a value l_{max}, while for the coefficients k and k' the cut-off is fixed at $k_{\mathrm{max}} = k'_{\mathrm{max}} = 256$ being the highest mode considered in our analysis.

This means that the variances in the latter equation are the end points of the lines in the upper panels of Figs. 7.17-7.18 discussed in the following. The results of the event-by-event simulations are indicated by points in the following, while the covariances are also normalized by the variances of the event-by-event simulations (points in the upper panels of Figs. 7.17-7.18).

We start with the initial- resp. final-state observable variances at $b = 0$ fm, which are displayed in the upper left resp. right panel of Fig. 7.17, either with the linear response coefficients $\{L_{\alpha,l}\}$ (lines) or the random events (points).[15] On

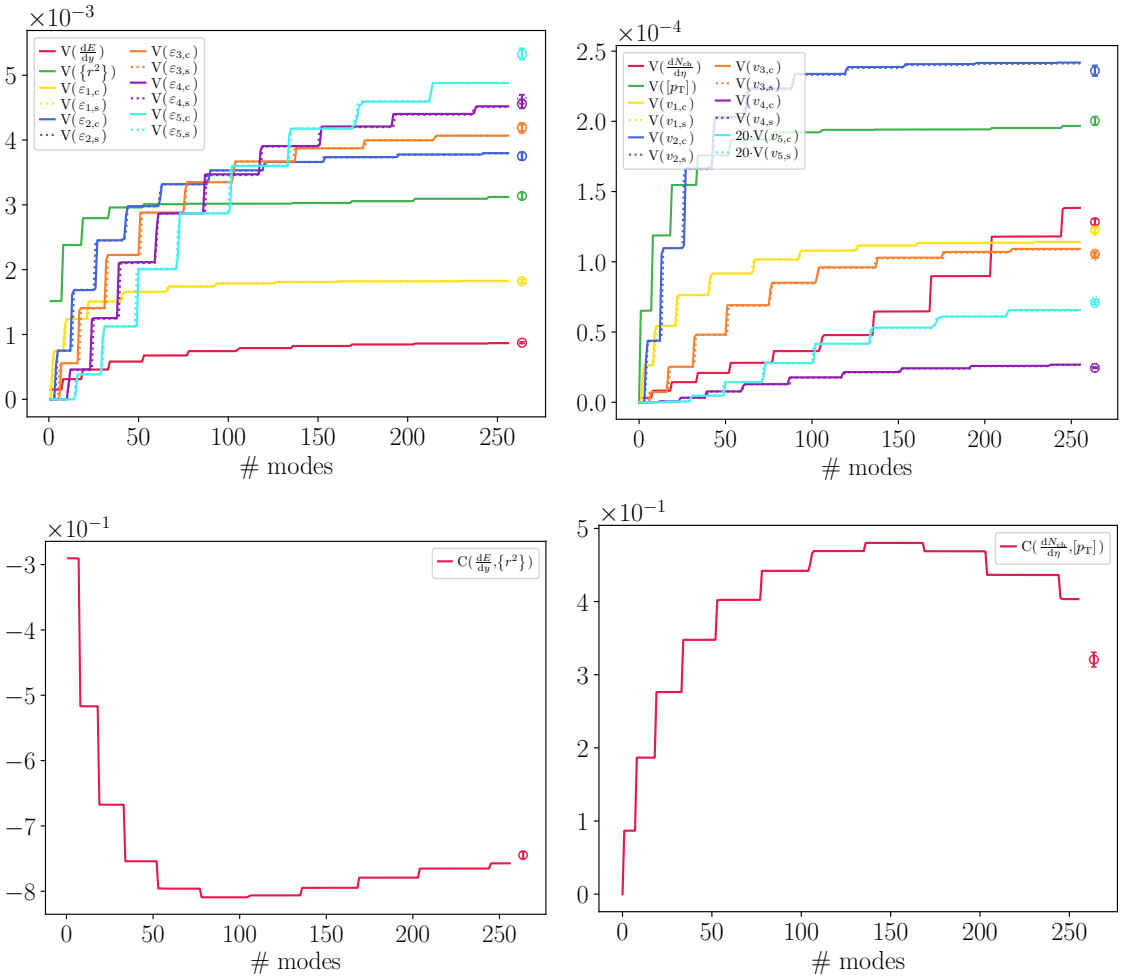

Figure 7.17: Convergence of the variances (top) for the initial state observables (left) and final state observables (right) in the Glauber model at $b = 0$ fm. The modes for which the number of particles changes are $l = (0, 7, 18, 33, 52, 77, \text{etc.})$. At the bottom we see the same for the covariances. All lines show the (co-)variances including the number of modes given at the x-axis. The points on the right are the values computed from 8192 randomly sampled events. For the normalization of the quantity C defined in Eq. (7.45) we used the end points of V for the normalization.

the horizontal axis we indicate the number of modes included in the sum over l in Eqs. (7.27) and (7.45). For the initial-state characteristics (upper left panel) we

[15] The error bars for the points are computed with a delete-d Jackknife algorithm (see Appendix G.3) deleting ten percent of the data points, while generating 10^3 samples.

observe a decent agreement with the variances for the random events. However, for the higher eccentricities (ε_4, ε_5) we find that the lines have not yet converged, which indicates that for these observables more modes should be included. In this work we do not include more then 256 modes, as the computation, especially for the final-state observables would increase the computation time even further. We can also see a general feature of the (co-)variance lines for a given observable, where we observe a step each time a mode has a linear response to this specific observable. Note, that this is also the reason why the steps of the dashed lines, indicating the sine components of the observables, are shifted by one mode. This is due to the fact that the modes appear as rotated pairs (see Sec. 7.2.4.2).

Going now to the upper right panel for the final-state variances of the observables, we find again the same step structure as for the linear responses and we find that the variances are in general by an order of magnitude smaller than for the initial-state characteristics. Additionally, the variances for the eccentricities increased with n, while the behavior is opposite for the flow harmonics.[16] We can attribute the decrease to the fact that the dynamical response coefficients $\mathcal{K}_{n,n}$ decrease with n for ideal fluids and additionally viscosity causes a larger damping for the higher harmonics. The final-state observables show an overall good agreement with the sampled events. Discrepancies between the lines and points are caused by non-linear responses of some observables, especially for $\mathrm{d}N_{\mathrm{ch}}/\mathrm{d}\eta$, where the size of the steps is not decreasing significantly for the higher modes.

In the bottom panels of Fig. 7.17 we show the modified Pearson correlation coefficients C for the initial (left) resp. final state (right) observables with a sizable value. At vanishing impact parameter these are $\mathrm{C}(\mathrm{d}E/\mathrm{d}y, \{r^2\})$ and $\mathrm{C}(\mathrm{d}N_{\mathrm{ch}}/\mathrm{d}\eta, [p_{\mathrm{T}}])$. For the initial state quantities we find a negative correlation between the energy and the average square radius, which has been observed before in Refs. [135–137]. In this case the curve gets close to the value for the random events. The final state quantities have a positive correlation, but the two approaches do not yield the same values. Large step sizes for the highest modes considered here imply, that more modes have to be considered to decide if the two approaches yield the same result.

Going now to impact parameter $b = 9$ fm (Fig. 7.18), the first observation is that there are more steps for the variances in the horizontal direction and their magnitude is smaller. There are also multiple steps in different observables for a given mode. This is caused by the structure of the linear responses (Fig. 7.14 bottom), which is richer and there are multiple eccentricities present for one mode. In the initial state (left panel) we observe that most of the variances in the mode-by-mode approach are too large to converge to the event-by-event results. This can be explained by the fact that at $b = 9$ fm most of the modes contain a sizable amount of energy, reflected in the denominator of ε_n by a change in the average over r^n, making the observable non-linear.

To proof this reasoning we have computed the variances of the numerator and the denominator of the eccentricities separately (Fig. 7.19). The plots shows ratios of the numerator and denominator of an eccentricity ε_n and the event-by-event value for the impact parameter $b = 0$ fm (left panel) resp. $b = 9$ fm (right panel). We find that the numerators and denominators converge nicely to their event-by-event value

[16] An exception is v_1, as the events are re-centered in the initial state.

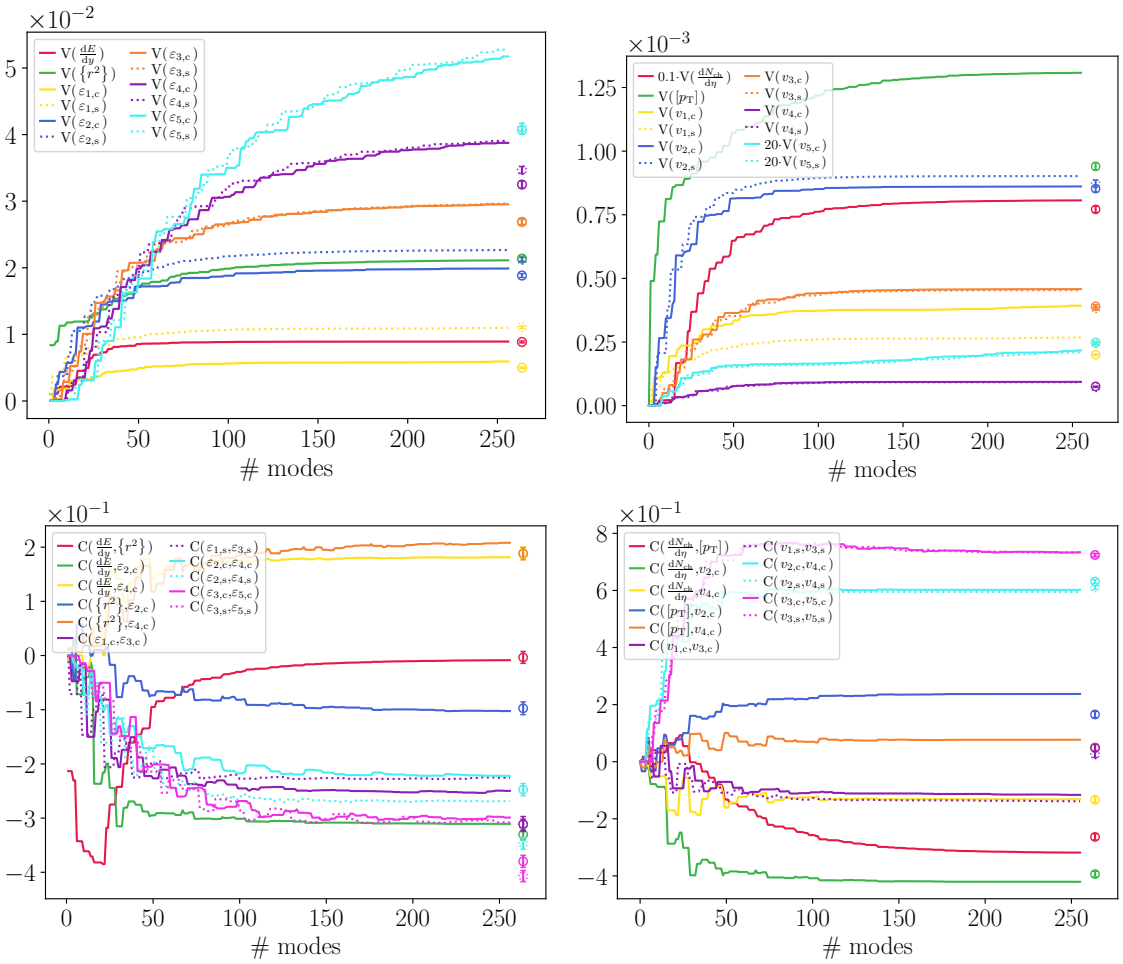

Figure 7.18: Convergence of the variances (top) for the initial state observables (left) and final state observables (right) in the Glauber model at $b = 9$ fm. At the bottom we see the same for the covariances. All lines show the (co-)variances including the number of modes given at the x-axis. The points on the right are the values computed from 8192 randomly sampled events. For the normalization of the quantity C defined in Eq. (7.45) we used the end points of V for the normalization.

or, if they have not converged yet for the 256 considered modes, they are below unity, such that convergence with more modes is not excluded.

In the right panel of Fig. 7.18 we can see again that there are discrepancies between the two approaches, especially for $[p_\mathrm{T}]$, which can be again attributed to the non-linear responses (Fig. 7.15). These non-linearities are stronger in magnitude compared to the $b = 0$ fm case.

As mentioned before, the contributions to $\mathrm{V}(\mathrm{d}N_\mathrm{ch}/\mathrm{d}\eta)$ do not seem to decrease in magnitude for higher modes, e.g., in the top right panel of Fig. 7.17. This can also be attributed to the viscosity of the system — in particular the shear viscosity — since the bulk viscosity is not present in our simulations. In order to verify this, we performed simulations with different values for the shear viscosity to entropy ratio ($\eta/s \in \{0, 0.16, 0.32\}$), which revealed that there is a large viscosity effect for the radial modes with small l, e.g., $l = 0$, damping the effect of the mode on the final state multiplicity considerably. On the other side, modes with large l, e.g., $l = 203$,

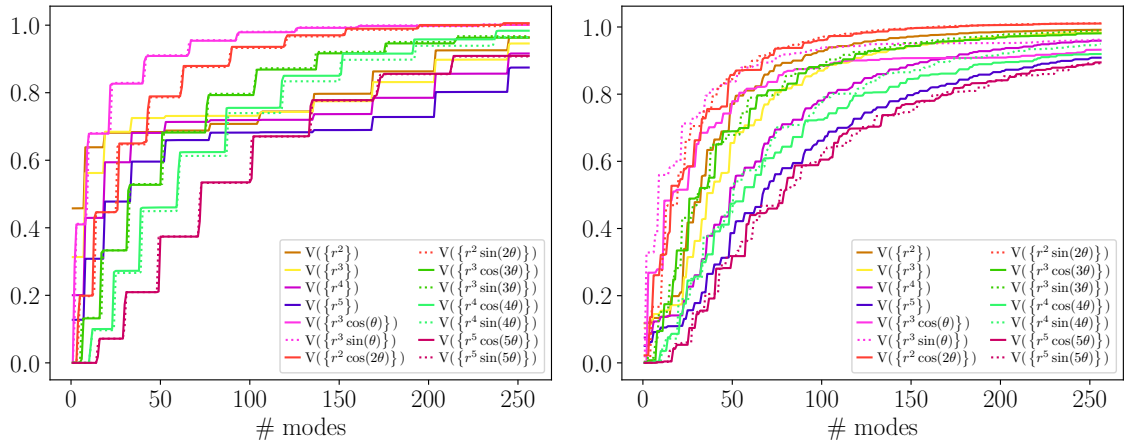

Figure 7.19: Convergence of the variances for the numerators and denominators of the initial state observables in the Glauber model at $b = 0$ fm (left) and $b = 9$ fm (right). The variances are divided by the corresponding values from the randomly sampled events.

are barely affected by the shear viscosity. We also tested the influence of the modes with $l \geq 256$ to check the contributions not included in our analysis. There we have found that the contributions decrease in magnitude, which is expected, since the eigenvalues keep decreasing for the higher modes. This implies that the variance for the particle multiplicity would converge, but it would still not agree with the event-by-event results due to the non-linear behavior of the observable itself.

The lower panels of Fig. 7.18 show the modified Pearson coefficients (Eq. (7.45)) at $b = 9$ fm for the initial state (left) and final state (right) observables. We observe that most of the lines from the mode-by-mode framework seem to converge to a certain value, which however does not coincide with the value from the event-by-event simulations. This might be caused as well by the non-linear behavior present for some of the observables in the initial, as well as the final state (see Fig. 7.15).

Figure 7.20 shows the Pearson coefficient for the Glauber model at $b = 0$ fm. In the upper left resp. right panel we show the initial resp. final state mode-by-mode results and in the bottom panels the same quantities from the event-by-event simulations. The diagonals of the plots are colored in gray, as the values are one by definition. The only sizable anti-correlation is the one for $\{r^2\}$ and $\mathrm{d}E/\mathrm{d}y$ in the initial state (left panels) caused by the fact that radial modes modify both observables, and a correlation of $\mathrm{d}N_{\mathrm{ch}}/\mathrm{d}\eta$ with $[p_{\mathrm{T}}]$. An extended discussion of this finding is presented in Appendix F.5. Comparing the results of the two approaches in the upper and lower panels we find a decent agreement between both. In the lower panels we can see as well some numerical fluctuations for other observables, especially in the final state, which are negligible compared to the afore mentioned (anti-)correlations.

For a finite impact parameter we observe more structures in the Pearson coefficients (Fig. 7.21). We find a good agreement between the mode-by-mode (upper panels) and event-by-event approach for almost all observables. There is a clear anti-correlation for the initial-state eccentricities (left panels) between $\varepsilon_{n,\mathrm{c/s}}$ and $\varepsilon_{n+2,\mathrm{c/s}}$, which becomes stronger for the higher harmonics. Note, that there is also

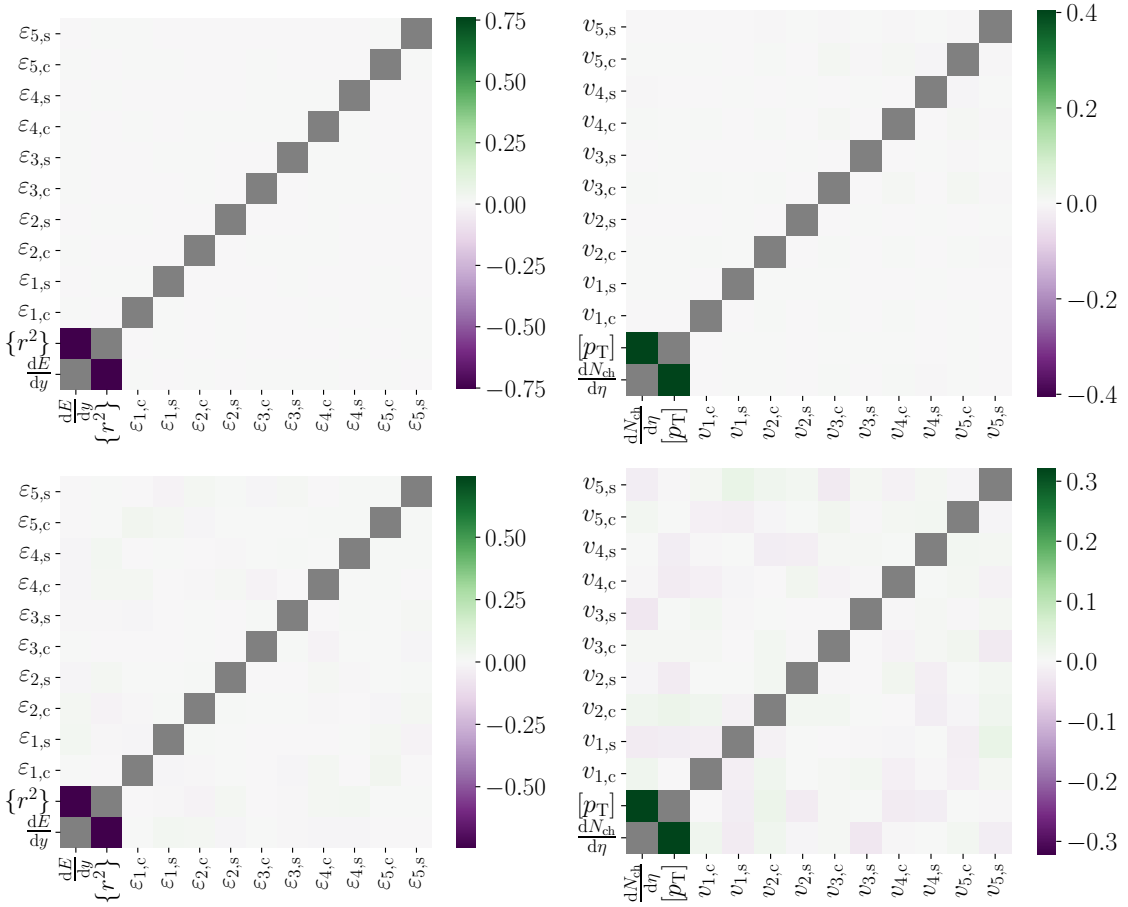

Figure 7.20: Covariances defined in Eq. (7.45) for the Glauber model at $b = 0$ fm from the linear response framework (top) and computed with randomly sampled events (bottom). The left plots show the initial state observables and the right ones the final state observables. The gray squares indicate the values which are not shown, as they are 1 by definition.

a barely visible anti-correlation of $\varepsilon_{n,\mathrm{c/s}}$ and $\varepsilon_{n+4,\mathrm{c/s}}$. The structure for the Pearson correlation between the even resp. odd eccentricities reflects again the structures in the linear response coefficients in Fig. 7.14. In contrast to the case $b = 0$ fm, where only one eccentricity per mode is present, the occurrence of multiple eccentricities per mode can induce correlations. In this case we observe anti-correlations, as the linear responses for a given mode have opposite sign for the n-th harmonic and the one with $n + 2$. Additionally, there is a strong anti-correlation between $\varepsilon_{2,\mathrm{c}}$ and $\mathrm{d}E/\mathrm{d}y$ and a weaker one between $\varepsilon_{2,\mathrm{c}}$ and $\{r^2\}$. For $\{r^2\}$ resp. $\mathrm{d}E/\mathrm{d}y$ there is a correlation with $\varepsilon_{4,\mathrm{c}}$, which is of similar magnitude in both cases. One observation is also the (almost) vanishing anti-correlation of $\mathrm{d}E/\mathrm{d}y$ and $\{r^2\}$ at impact parameter 9 fm, which in contrast was observed in the vanishing impact parameter case. At the moment there is no intuitive explanation for this, such that we leave this as a comment.

In the final state (right panels) we find a similar pattern as for the initial state (left panel). This time the anti-correlation between the eccentricities with $n \geq 2$ turns into a correlation for $v_{n,\mathrm{c/s}}$ and $v_{n+2,\mathrm{c/s}}$, while $v_{1,\mathrm{c/s}}$ and $v_{3,\mathrm{c/s}}$ resp. $v_{5,\mathrm{c/s}}$

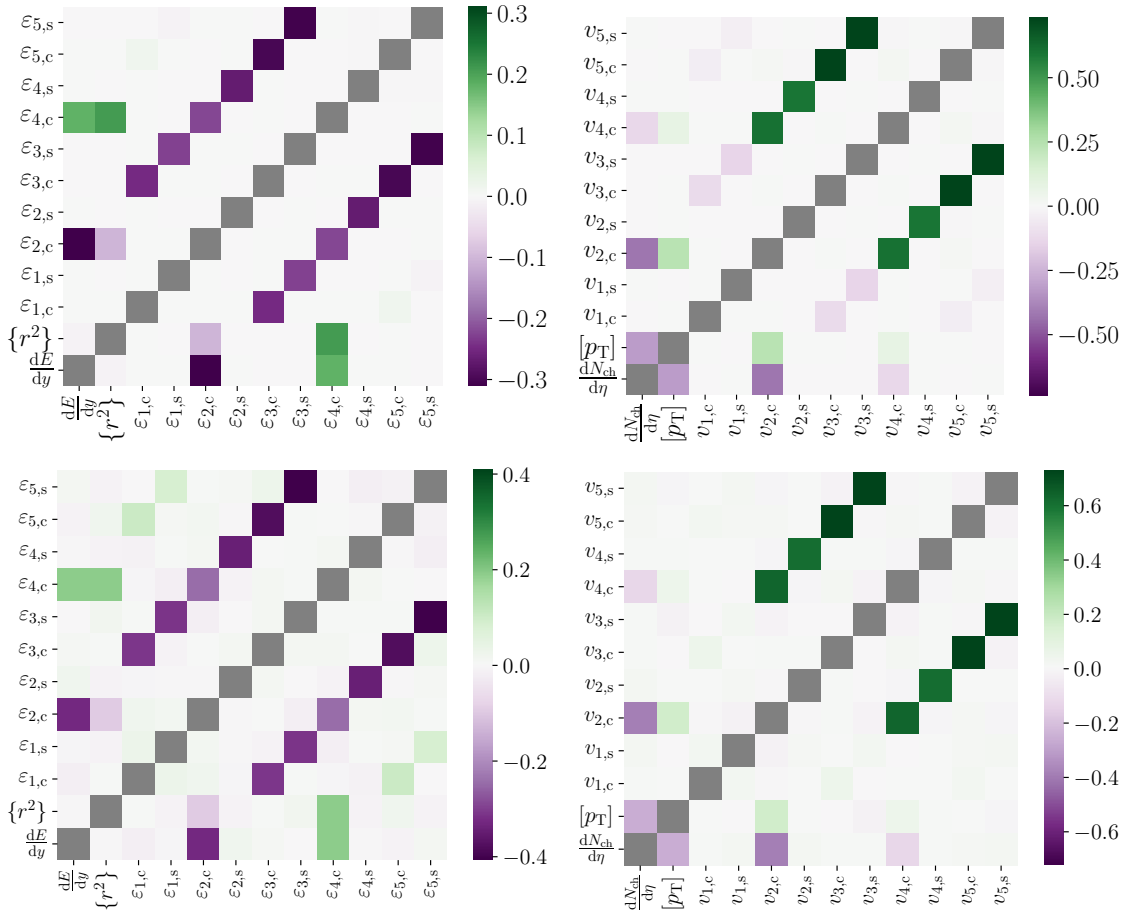

Figure 7.21: Covariances defined in Eq. (7.45) for the Glauber model at $b = 9$ fm from the linear response framework (top) and computed with randomly sampled events (bottom). The left plots show the initial state observables and the right ones the final state observables. The gray squares indicate the values which are not shown, as they are 1 by definition.

are still anti-correlated. From the event-by-event results we obtain a very small and positive signal for the latter Pearson coefficients, which indicates that the non-linear contributions to the observables in the mode response play a significant role here. From the linear response coefficients in the lower right panel of Fig. 7.14 we can see that the responses for the flow harmonics at a given mode number l mainly have the same sign for n and $n+2$ if $n \geq 2$, while this is not true for $v_{1,\mathrm{c/s}}$ and the other flow coefficients present at that mode. This explains why the signs of the Pearson coefficients change in some cases. $\mathrm{d}N_{\mathrm{ch}}/\mathrm{d}\eta$ is found to be anti-correlated with $v_{2,\mathrm{c}}$ and $v_{4,\mathrm{c}}$, while $[p_{\mathrm{T}}]$ is correlated with $v_{2,\mathrm{c}}$. For these observable combinations the non-linear contributions of the responses seem to play a sub-leading role for the sign, but they are important to match the event-by-event results if we compare the lines and points in the lower panels of Fig. 7.18.

Now we will discuss the results for the Saturation model. In Figs. 7.22-7.23 we show the same variances and Perason coefficients as for the Glauber model above (Figs.7.17-7.18). As the results for most of the variances and Pearson coefficients are similar to the Glauber model let us highlight only the differences between the two

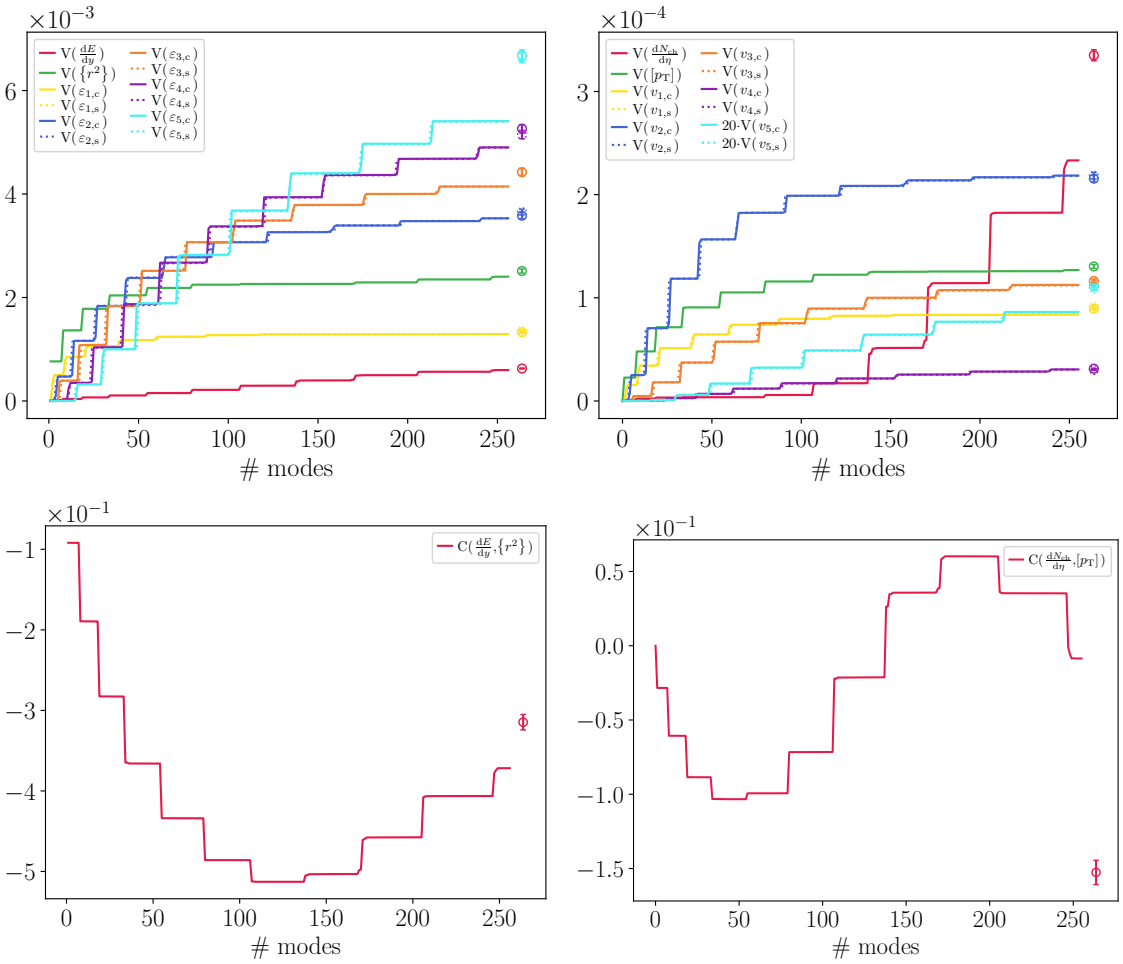

Figure 7.22: Convergence of the variances (top) for the initial state observables (left) and final state observables (right) in the Saturation model at $b = 0$ fm. The modes for which the number of particles changes are $l = (0, 7, 18, 33, 54, 79, 106, 137, 139, 168, 170, 205, 246, \text{etc.})$. At the bottom we see the same for the covariances. All lines show the (co-)variances including the number of modes given at the x-axis. The points on the right are the values computed from 8192 randomly sampled events. For the normalization of the quantity C defined in Eq. (7.45) we used the end points of V for the normalization.

models to keep the discussion short. The variances in both models behave the same way for impact parameter $b = 0$ fm, with the exception that in the Saturation model $\mathrm{V}(\mathrm{d}N_{\mathrm{ch}}/\mathrm{d}\eta)$ computed from the modes is still below the event-by-event value and could in principle still converge when using more modes (upper right panel Fig. 7.22). In the Pearson coefficient (lower panel) we find an anti-correlation between $\mathrm{d}E/\mathrm{d}y$ and $\{r^2\}$ in both models, while between $\mathrm{d}N_{\mathrm{ch}}/\mathrm{d}\eta$ and $[p_{\mathrm{T}}]$ there is a correlation in the Glauber model resp. anti-correlation in the Saturation model. This anti-correlation in the Saturation model (right panels) is small and negative in the mode-by-mode case, as one should include more modes for this Pearson coefficient due to the large step sizes for the higher modes. However, the event-by-event result is clearly negative, which gives us a way to differentiate the two initial state models with an experimentally measurable quantity in principle.

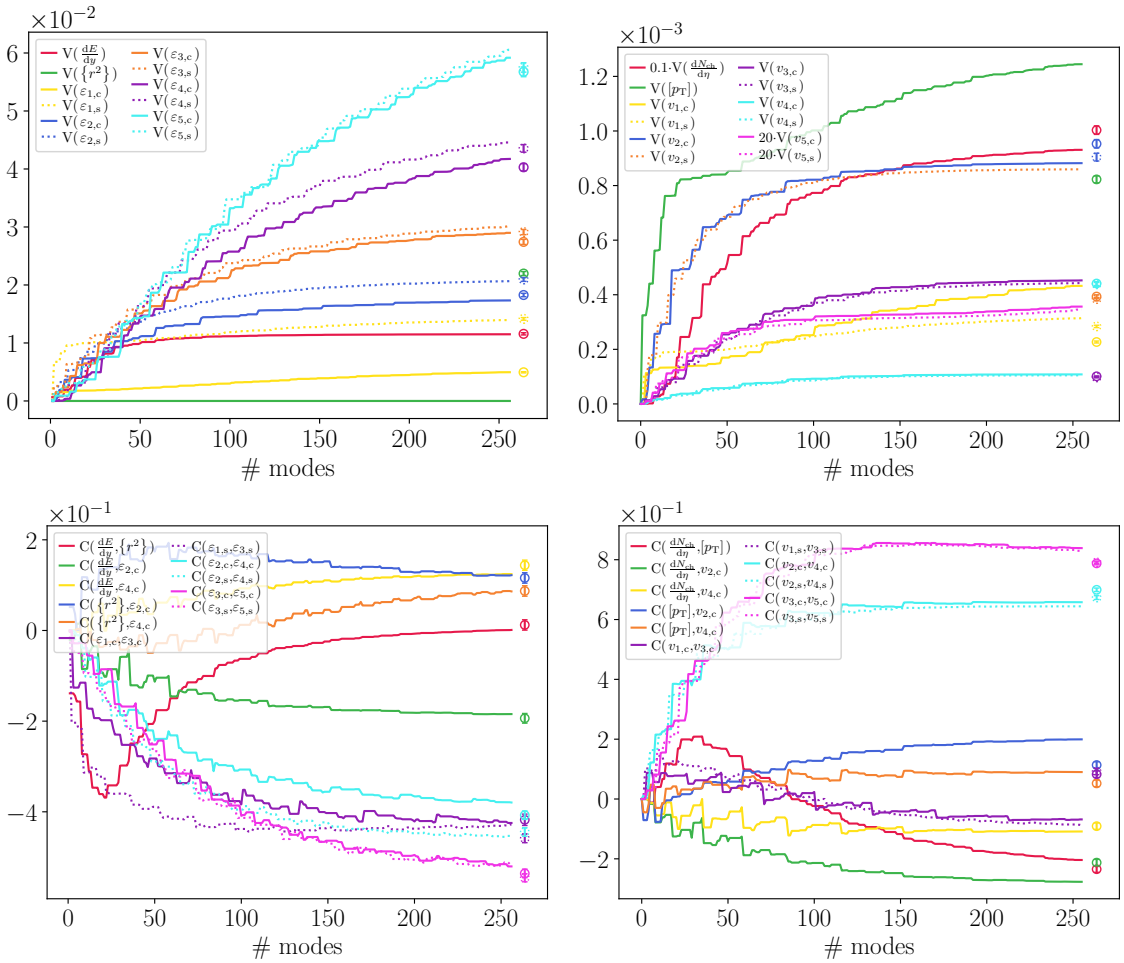

Figure 7.23: Convergence of the variances (top) for the initial state observables (left) and final state observables (right) in the Saturation model at $b = 9$ fm. At the bottom we see the same for the covariances. All lines show the (co-)variances including the number of modes given at the x-axis. The points on the right are the values computed from 8192 randomly sampled events. For the normalization of the quantity C defined in Eq. (7.45) we used the end points of V for the normalization.

For impact parameter $b = 9$ (Fig. 7.23) we obtain a very significant difference in the variance of $\{r^2\}$ between the two approaches (upper left panel), for which we do not have an explanation yet, as this is not present in the Glauber model and the quadratic response coefficients for the observable are of similar magnitude in both models. In the final state there are again more differences between the two approaches due to the influence of non-linear responses, which are not included in the mode-by-mode results. Results for the Pearson coefficients are similar to the Glauber model results, in the sense that the convergence to the event-by-event results could be improved by using more modes and including the quadratic response coefficients as well.

The Pearson coefficients shown in Figs. 7.24-7.25 including 256 modes replicate the findings of the latter convergence plots for both impact parameters. Additionally, we can see that there is indeed no other sizable (anti-)correlation between two

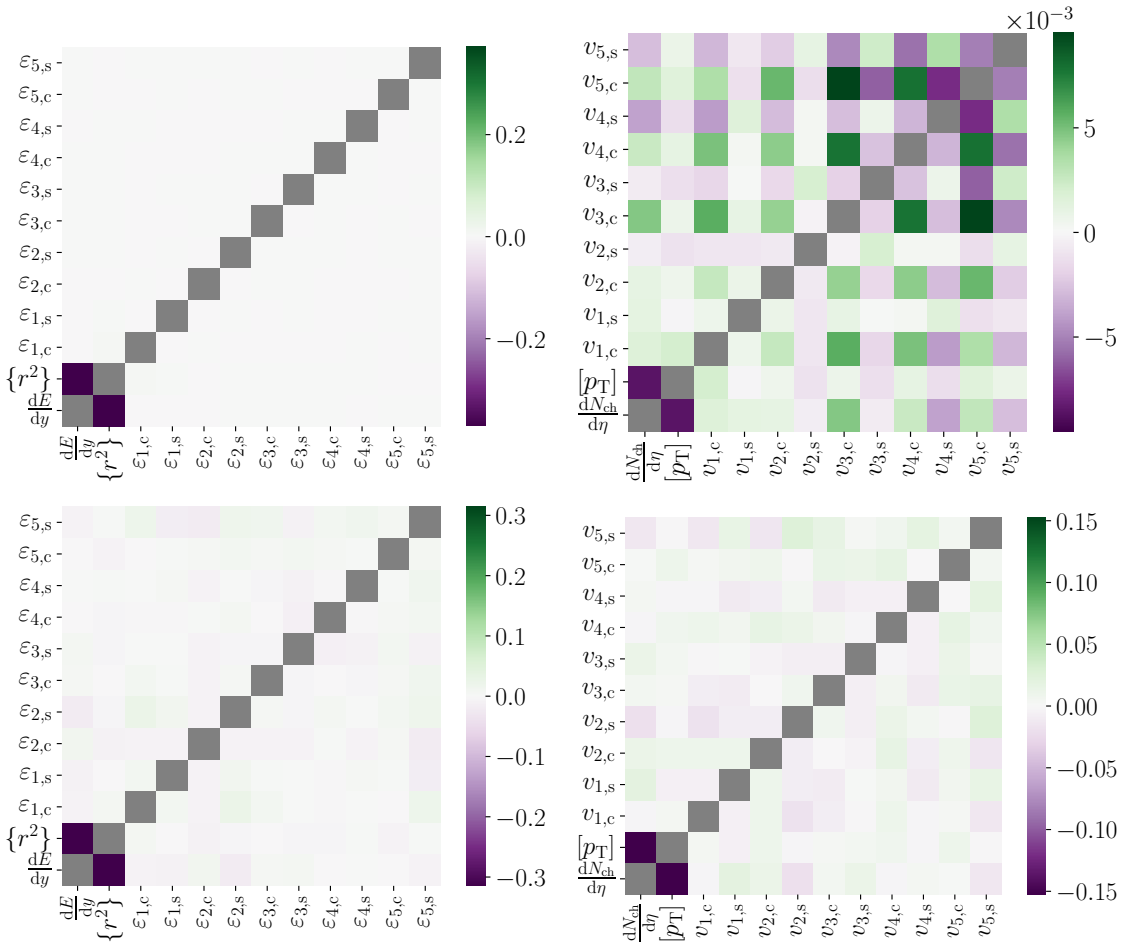

Figure 7.24: Covariances defined in Eq. (7.45) for the Saturation model at $b = 0$ fm from the linear response framework (top) and computed with randomly sampled events (bottom). The left plots show the initial state observables and the right ones the final state observables. The gray squares indicate the values which are not shown, as they are 1 by definition.

observables present, which was not shown in Figs. 7.22-7.23.[17]

7.3.3 Probability distributions

Using the assumption that the $\{c_l\}$-distributions are Gaussian and that the response of the eccentricities and the anisotropic flow coefficients is linear, we can derive a two-dimensional joint probability distribution $p^{\mathrm{G}}_{\beta,\gamma}(O_\beta, O_\gamma)$ for the observables $O_\beta = \sqrt{O^2_{\alpha_1} + O^2_{\alpha_2}}$ and $O_\gamma = \sqrt{O^2_{\alpha_3} + O^2_{\alpha_4}}$ of the form:

$$p^{\mathrm{G}}_{\beta,\gamma}(O_\beta, O_\gamma) = \theta(O_\beta) O_\beta \theta(O_\gamma) O_\gamma \int_0^{2\pi} \mathrm{d}\phi \int_0^{2\pi} \mathrm{d}\psi \; p^{\mathrm{G}}_{\alpha_1,\alpha_2,\alpha_3,\alpha_4}(O_\beta \cos\phi, O_\beta \sin\phi, O_\gamma \cos\psi, O_\gamma \sin\psi). \tag{7.46}$$

[17] The upper right panel of Fig. 7.24 shows that the reported anti-correlation between $\mathrm{d}N_{\mathrm{ch}}/\mathrm{d}\eta$ and $[p_{\mathrm{T}}]$ is of the order of the numerical fluctuations. However, one should include more modes for this observable, as mentioned above.

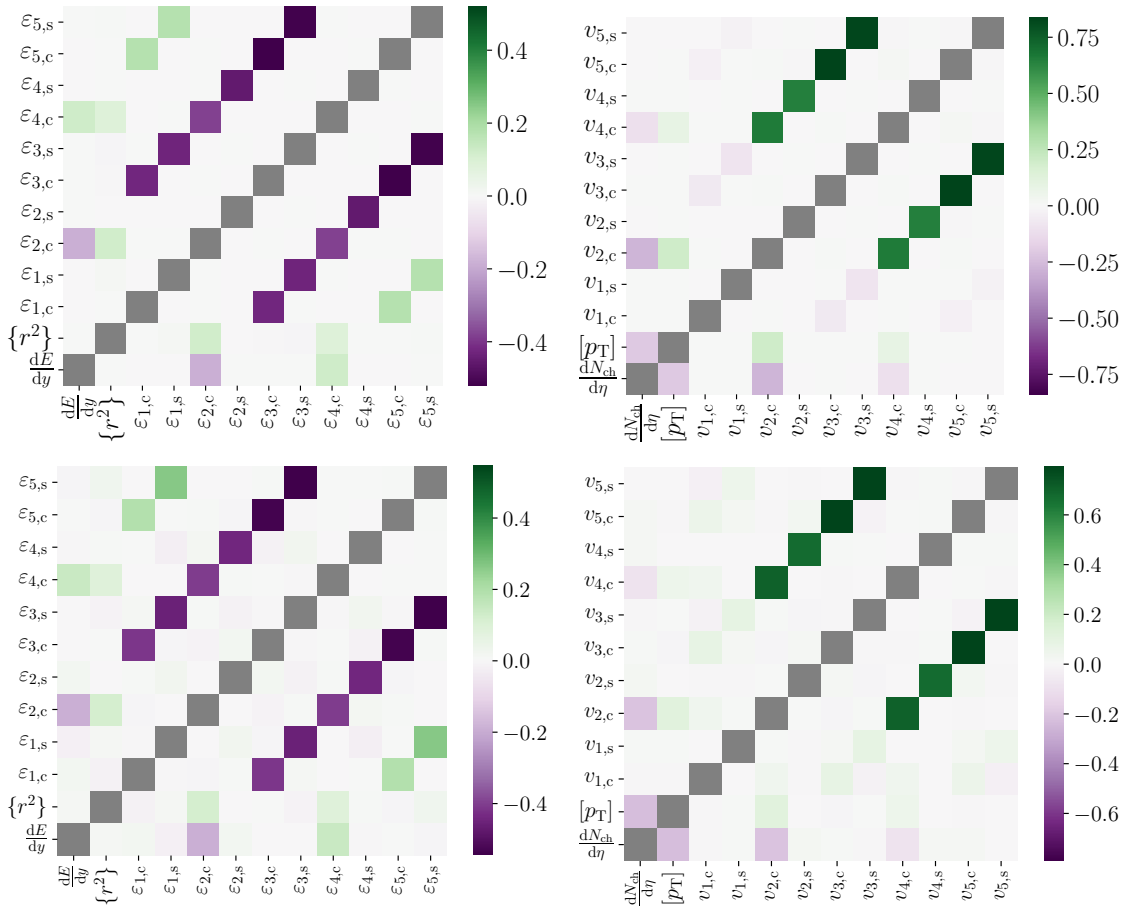

Figure 7.25: Covariances defined in Eq. (7.45) for the Saturation model at $b = 9$ fm from the linear response framework (top) and computed with randomly sampled events (bottom). The left plots show the initial state observables and the right ones the final state observables. The gray squares indicate the values which are not shown, as they are 1 by definition.

The latter expression is derived in Appendix F.4. We can now compare the joint probability distribution $p^{\mathrm{G}}_{\beta,\gamma}(O_\beta, O_\gamma)$ from the linear Gaussian ansatz to the distribution $p_{\beta,\gamma}(O_\beta, O_\gamma)$ obtained from the event-by-event simulations. Distributions for the observables (ε_n, v_n) with $n \in \{1, \ldots, 5\}$ and $(\varepsilon_2, \varepsilon_4)$ are shown in Figs. 7.26-7.29. Indicated by the red cross resp. circle we show the average value of the observables for the event-by-event computation resp. Gaussian statistics. For the event-by-event results the results were smoothed with a Gaussian kernel density estimator (KDE), which is a method to estimate the probability density function of a random variable non-parametrically.[18] For an easier comparison between the distributions we also show the external plots which are the one-dimensional distributions obtained from projecting the two-dimensional distributions onto the corresponding axes. In the case of the one-dimensional distributions we also show the histogram of the observables in the event-by-event simulations, which show a good agreement with the KDE smoothing (blue dotted lines). All Gaussian statistics results include the first 256 modes (orange dashed lines or gray contour lines).

[18] For the KDE we used the implementation in the SciPy library in Python.

For the interpretation of the results let us recall the connections of the flow harmonics to the eccentricities. In the case $n = 1, 2, 3$ there is a linear relation between v_n and ε_n (Eq. (7.40)) and for large impact parameters there is a cubic term of the form $\mathcal{K}_{2,222}\varepsilon_2^3$ in the v_2 signal (Eq. (4.12)). The quadrangular flow v_4 has a linear dependence on ε_4 and a quadratic contribution in ε_2 (Eq. (4.13)), while the pentagonal flow has a linear ε_5 contribution and an additional one from $\varepsilon_2\varepsilon_3$ (Eq. (4.14)).

Starting with the results for vanishing impact parameter, we find that both initial state models (Figs. 7.26-7.27) show a good agreement between the Gaussian statistics and the event-by-event distributions. All averages in the ε_n- and v_n-

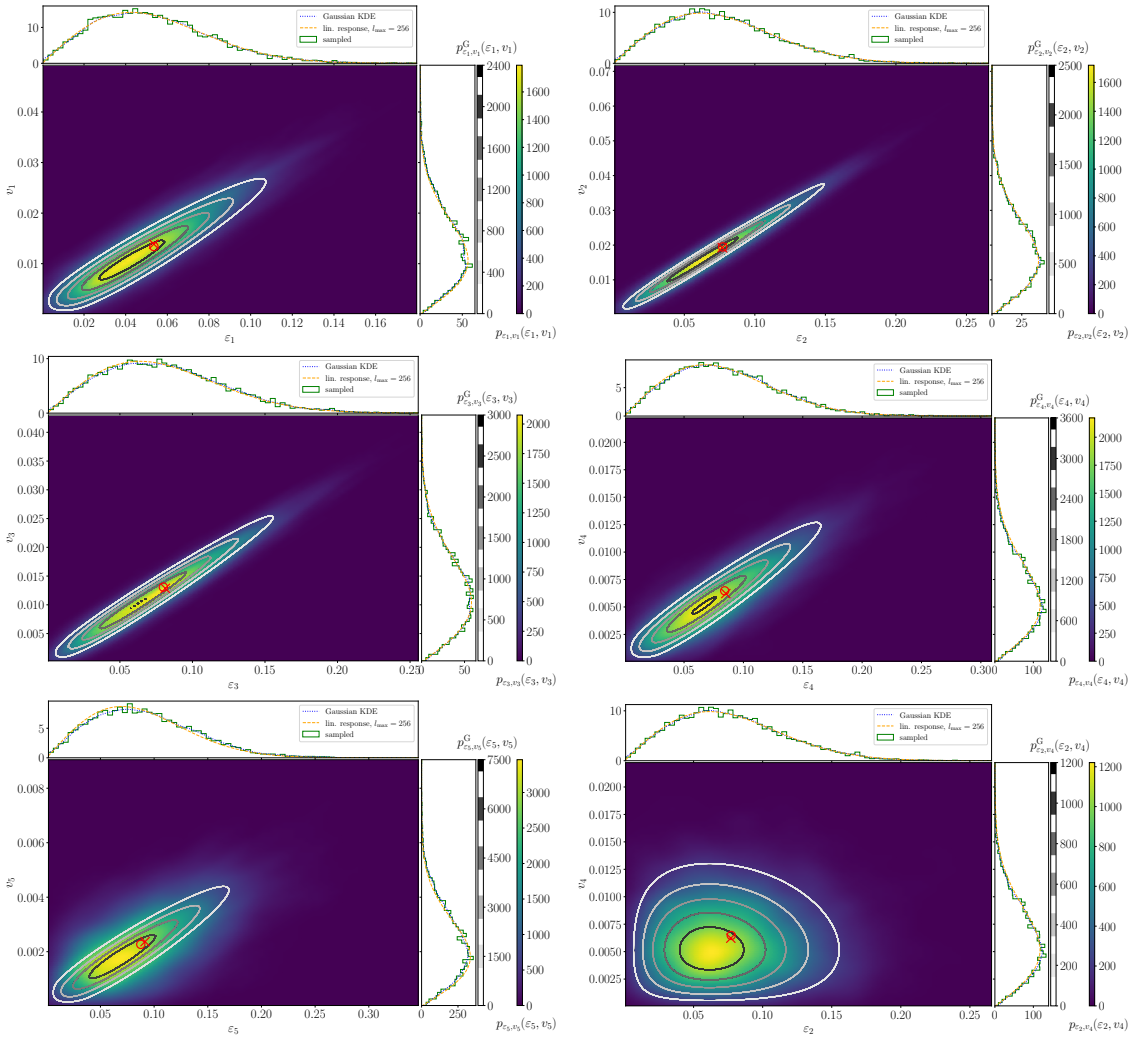

Figure 7.26: Joint probability distributions $p^G_{\beta,\gamma}(O_\beta, O_\gamma)$ (contour lines) from the Gaussian statistics ansatz in the linear response framework at $b = 0$ fm in the Glauber model for different observables. The density plots show the joint probability distributions from the event-by-event evolution $p_{\beta,\gamma}(O_\beta, O_\gamma)$. For both calculations we project the joint probability distribution onto the individual axes. The event-by-event result is shown as a histogram and smoothed by a Gaussian kernel density estimator (KDE). The red cross indicates the average of the distribution in each direction for the event-by-event calculation and the circle the average from the linear response framework.

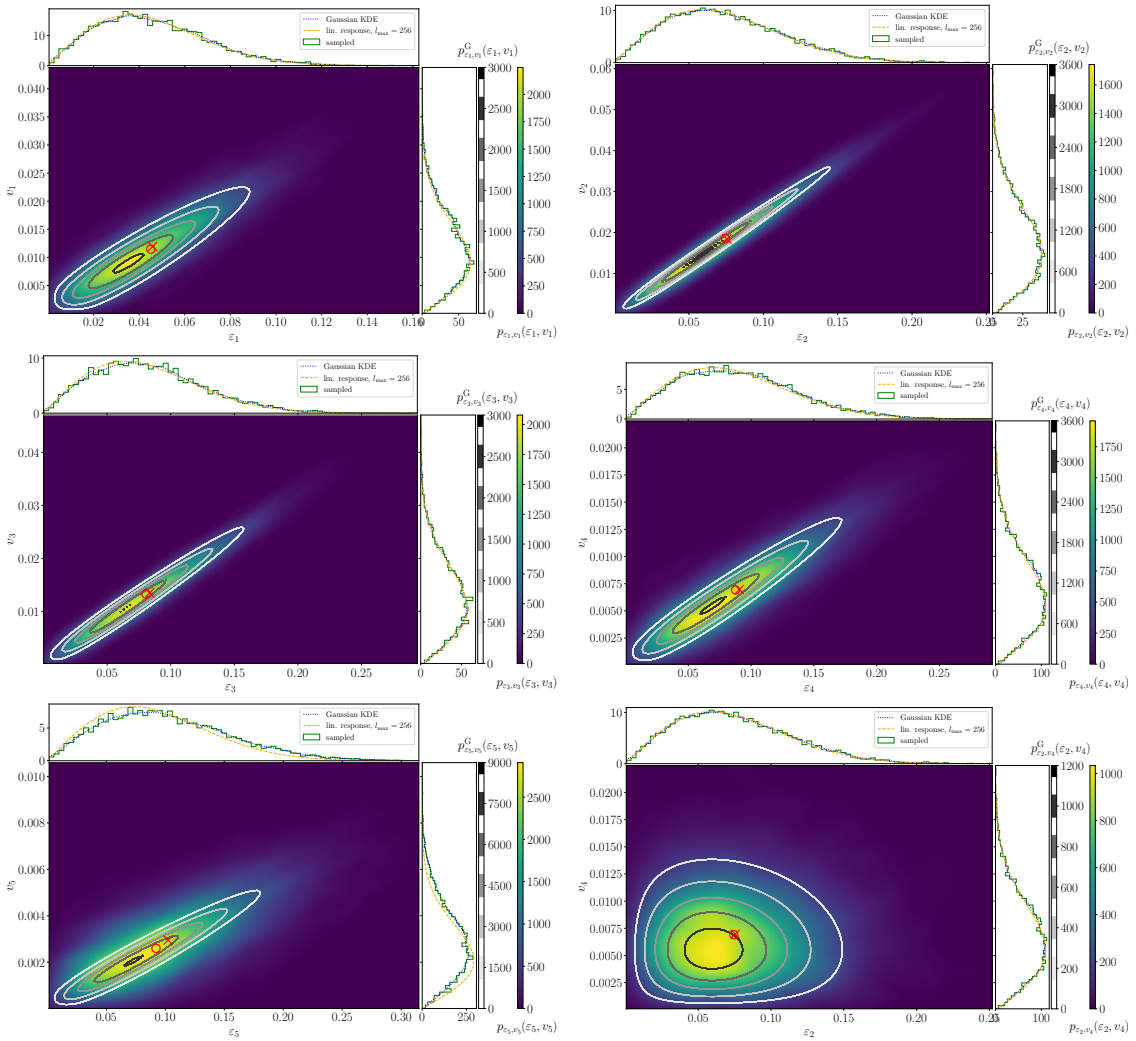

Figure 7.27: Joint probability distributions $p^G_{\beta,\gamma}(O_\beta, O_\gamma)$ (contour lines) from the Gaussian statistics ansatz in the linear response framework at $b = 0$ fm in the Saturation model for different observables. The density plots show the joint probability distributions from the event-by-event evolution $p_{\beta,\gamma}(O_\beta, O_\gamma)$. For both calculations we project the joint probability distribution onto the individual axes. The event-by-event result is shown as a histogram and smoothed by a Gaussian kernel density estimator (KDE). The red cross indicates the average of the distribution in each direction for the event-by-event calculation and the circle the average from the linear response framework.

directions are in good agreement in most of the cases. An exception is found for the combination (ε_5, v_5) in the Saturation model (lower left panel in Fig. 7.28), where the ε_5, and therefore the v_5 signal as well, is larger than the result from the Gaussian statistics. This effect might be caused by the flatter eigenvalue spectrum for the Saturation model enhancing the importance of higher modes compared to the Glauber model such that the cut at $l_{\max} = 256$ in the Gaussian statistics might be too low for this observable in the Saturation model. We observe that the width of the distributions for the combinations (ε_n, v_n) for $n \in \{2, \ldots, 5\}$ increases, which was also observed in Ref. [65]. The (ε_1, v_1) distribution falls out of this scheme, which might be caused by the fact that the densities are re-centered and thus the

ε_1 is computed with an r^3 weight. Looking at the distributions (ε_2, v_4) we see that at $b = 0$ fm the two observables are not correlated, as we have already seen in Sec. 7.3.2. The eccentricities and flow harmonics show the expected linear relation between the two quantities.

When we look at the distributions at impact parameter $b = 9$ fm (Figs. 7.28-7.29) there is in general still a good agreement between the two distributions. However,

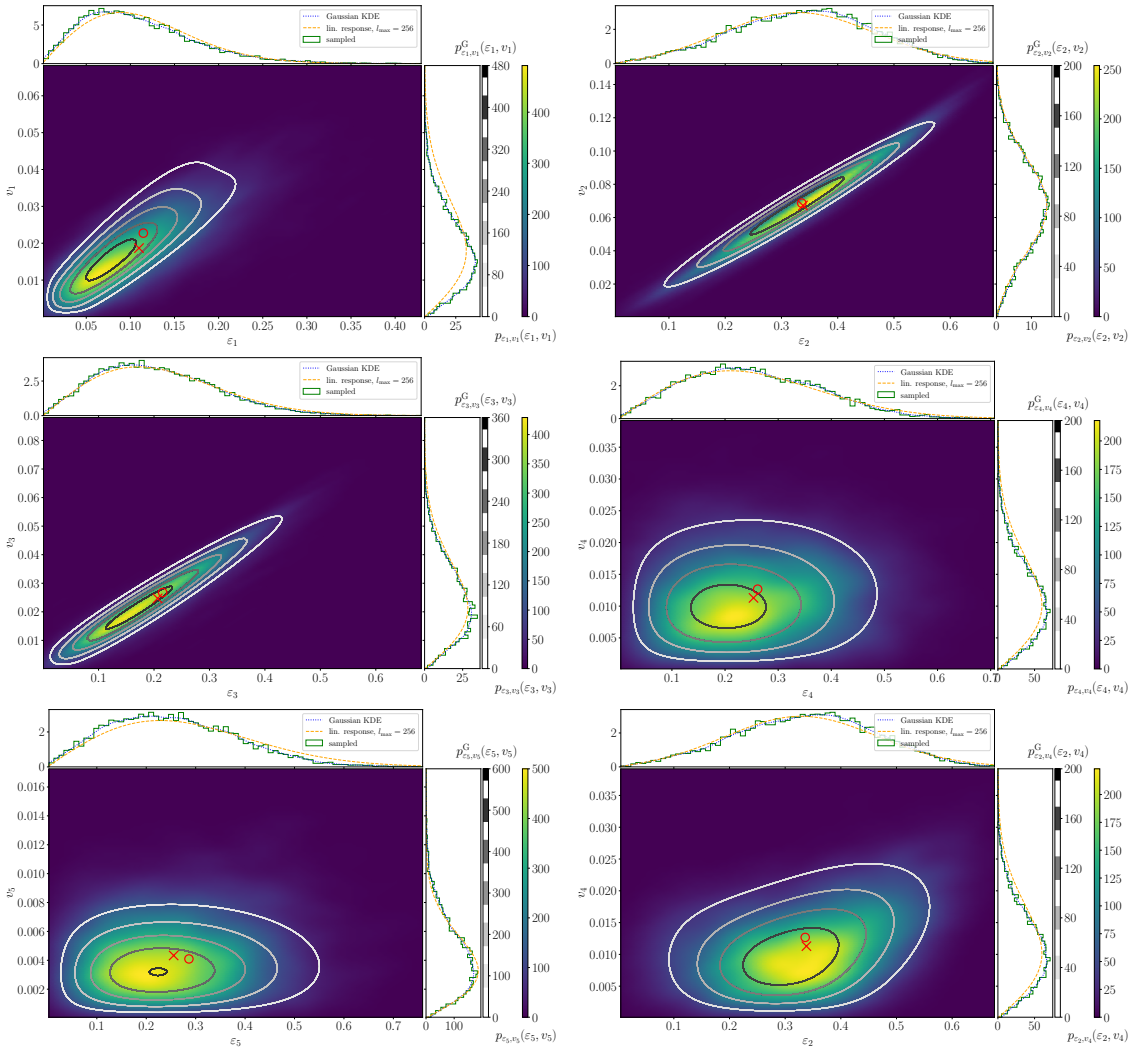

Figure 7.28: Joint probability distributions $p^G_{\beta,\gamma}(O_\beta, O_\gamma)$ (contour lines) from the Gaussian statistics ansatz in the linear response framework at $b = 9$ fm in the Glauber model for different observables. The density plots show the joint probability distributions from the event-by-event evolution $p_{\beta,\gamma}(O_\beta, O_\gamma)$. For both calculations we project the joint probability distribution onto the individual axes. The event-by-event result is shown as a histogram and smoothed by a Gaussian kernel density estimator (KDE). The red cross indicates the average of the distribution in each direction for the event-by-event calculation and the circle the average from the linear response framework.

the deviations are already larger on the level of the average values compared to the vanishing impact parameter case. For the combinations (ε_n, v_n) with $n \in \{1, 2, 3\}$ there is still the linear relation between eccentricities and anisotropic flow coefficients

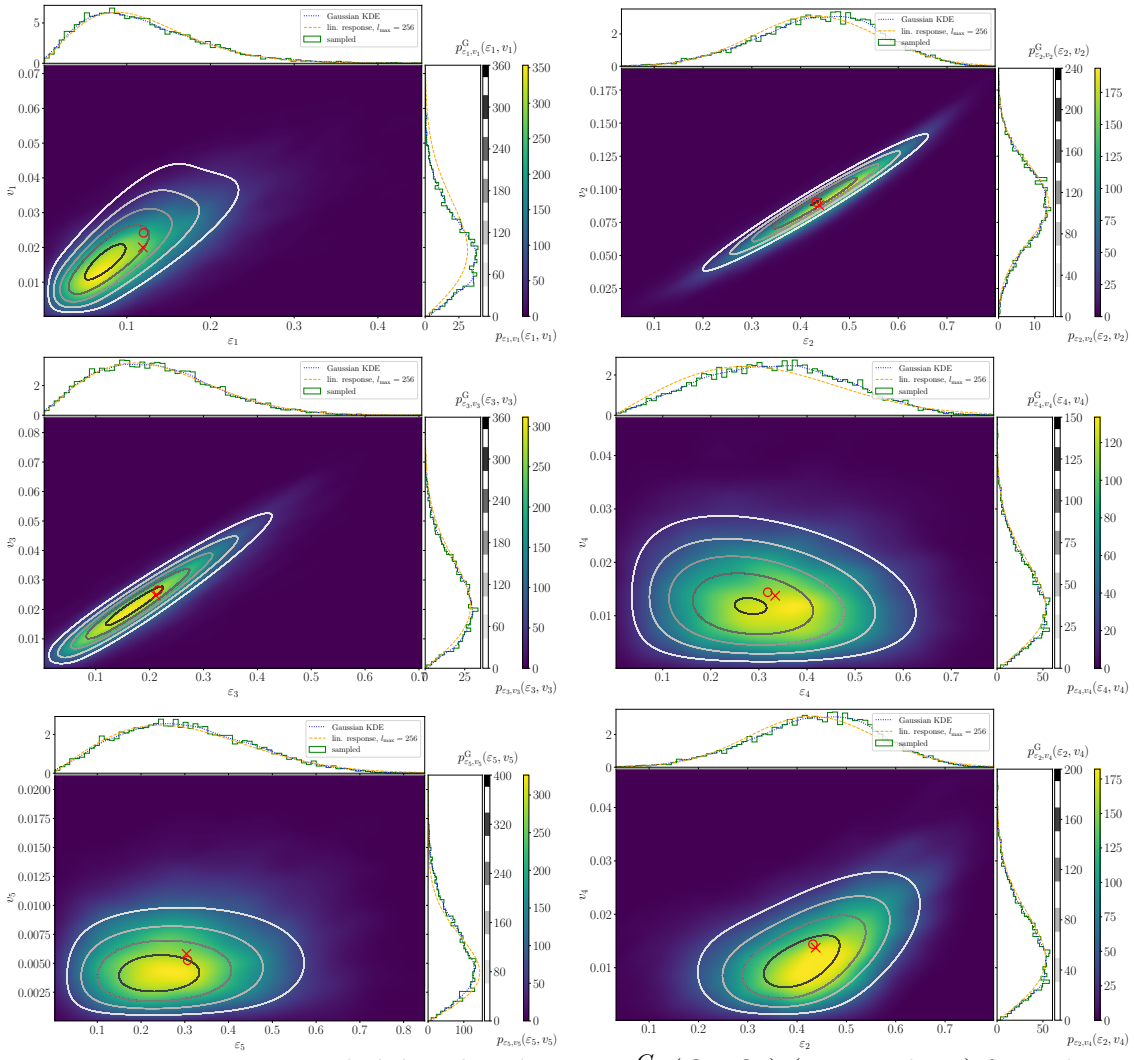

Figure 7.29: Joint probability distributions $p^G_{\beta,\gamma}(O_\beta, O_\gamma)$ (contour lines) from the Gaussian statistics ansatz in the linear response framework at $b = 9$ fm in the Saturation model for different observables. The density plots show the joint probability distributions from the event-by-event evolution $p_{\beta,\gamma}(O_\beta, O_\gamma)$. For both calculations we project the joint probability distribution onto the individual axes. The event-by-event result is shown as a histogram and smoothed by a Gaussian kernel density estimator (KDE). The red cross indicates the average of the distribution in each direction for the event-by-event calculation and the circle the average from the linear response framework.

and additionally we find a cubic part for the v_2 signal as expected in non-central collisions. This cubic part is however only visible in the event-by-event result, as the Gaussian statistics takes only the linear responses into account. In the case (ε_4, v_4) the linear relationship is no longer clearly visible, but we can see in the (ε_2, v_4) distribution there is a contribution from the large ε_2 values at $b = 9$ fm. A linear contribution to v_5 is still not visible in the distributions (ε_5, v_5) shown in the lower left panels of Figs. 7.28-7.29.

Chapter 8

Conclusion

In Ch. 4 we have investigated the anisotropic flow fluctuations and the event-plane angle distributions as a function of the mean number of binary scatterings in the system with massless particles in two dimensions. We have seen that the Elliptic-Power law, which is already an improvement of the Bessel-Gauss distribution, is able to describe the fluctuations of v_3 and also of v_2, as long as the collisions are central enough to have to a good extent a linear relation between initial state eccentricity and final state anisotropic flow. However, when going to more peripheral collisions or even to higher flow harmonics, there are non-linear responses of the flow harmonics to the eccentricities. Using the Elliptic-Power law these fluctuations cannot be described. Therefore, we have introduced a method to look at the fluctuations of the flow coefficients $v_{n,\mathrm{c/s}}$ about the fitted value $\bar{v}_{n,\mathrm{c/s}}$ at the corresponding eccentricity using the relations given in Eqs. (4.10)-(4.12). From these approximations of the conditional probability distributions $p_{v|\varepsilon}(v_{n,\mathrm{c/s}}|\varepsilon_{n,\mathrm{c/s}})$ the first moments were used for the characterization of the flow fluctuations. Additionally, the distributions of the event planes Ψ_2 and Ψ_3 about their participant plane Φ_2 resp. Φ_3 in the initial state were computed. This study of the event-plane angles was extended by looking at the distributions of different combinations of Ψ_2, Ψ_4, Φ_2 and Φ_4, which show an interesting dependence on the impact parameter.

There are five features (see Sec. 4.5) of the above mentioned distributions which are present across all studied impact parameters and therefore appear to be quite robust. First, there is a decrease with $\langle \mathrm{Kn} \rangle^{-1}$ and then an increase in the values of the variance σ_v^2 of the fluctuations of $v_{n,\mathrm{c/s}}$ about the mean $\bar{v}_{n,\mathrm{c/s}}(\varepsilon_{n,\mathrm{c/s}})$. Second, all $v_{n,\mathrm{c/s}}$ distributions are skewed towards zero. When there is an onset of anisotropic flow the skewness takes a sizable value, e.g., the absolute value of the skewness has a value of order 0.5, which decreases then for an increasing number of rescatterings. Third, the $v_{n,\mathrm{c/s}}$ distributions are predominantly more peaked than a Gaussian with the same variance, i.e., they have a positive excess kurtosis, which tends towards zero when the number of rescatterings is increased. The fourth observation is that the event-plane angle distributions about their corresponding initial state participant-plane angle are peaked for $n = 2$ and 3, with a broadening of the peak for the largest value of $\langle \mathrm{Kn} \rangle^{-1}$. The fifth finding is that this is partly true for the fourth harmonic symmetry planes, which have a more complex structure due to correlations between the second and fourth harmonic symmetry planes depending on the impact parameter of the collision.

The above mentioned study of the flow fluctuations from the finite number of rescatterings could be extended in different directions. A first obvious possibility

would be to study more or less rescatterings per particle. In the case of even less rescatterings it would be possible to study the onset of the skewness, or similar the alignment of Φ_2 along Ψ_2, which has the issue of producing smaller flow signals needing more statistics to extract reliable results. Going into the direction of more rescatterings probes the "hydrodynamic limit" in more detail, while checking if the $v_{n,\mathrm{c/s}}$ fluctuations about their mean value become smaller, as expected. It would be interesting to see the evolution of $\Psi_n - \Phi_n$ in this regime as well. Performing simulations in this limit one has to ensure that the system is still dilute enough, such that the Boltzmann equation is applicable.

A second natural extension would be to look at v_4 or v_5 fluctuations or at correlations in fluctuations of different harmonics [62]. Again there is the problem of smaller signals and thus high statistics is needed. Additionally, the higher flow harmonics are affected by the lower-order eccentricities [38, 65, 80, 90, 91], where one needs high statistics for the disentanglement of their effects. It could be interesting as well to look at the fluctuations of the transverse momentum dependent flow $v_n(p_\mathrm{T})$ and the effects of different cross sections.

One way to go into the direction of a phenomenological application of this fluctuation study and a comparison with experiments is to introduce centrality classes instead of fixing the impact parameter. Then the fluctuations caused by the finite number of rescatterings in the system combine with the eccentricity fluctuations inside a centrality class. Most likely the combination of these two sources of fluctuations will lead to a distortion of the non-Gaussianities in the flow fluctuations compared to the eccentricity fluctuations in the centrality bin. As we have seen that the flow harmonic distributions are all skewed towards zero for a fixed eccentricity, we can expect that the v_2 and v_3 distributions in a centrality bin are even more skewed into the same direction than the ε_2 or ε_3 distributions. For more peripheral collisions one can expect a smaller average number of rescatterings leading to an "extra negative skewness" in the v_n distribution, which should be more apparent in the peripheral bins. To confirm (or falsify) these expectations it would be necessary to perform more realistic computations compared to the ones presented in this work.

In Ch. 5 we have studied the early time dynamics of several quantities related to the asymmetry in the transverse plane in position or momentum space for massless particles. For the analysis we have used simulations performed with the transport algorithm described in Secs. 3.4.2-3.4.5 as well as semi-analytical calculations based on a Taylor expansion of the phase space distribution at early times [102]. The results of both calculations were compared within the few-rescatterings regime, as the analytical model is only applicable there. Additionally, simulations over a large interval in Knudsen numbers were performed to map out the early time scaling behavior of the anisotropic flow coefficients from the fluid-dynamical to the few-rescatterings regime, mapping out the transition from $v_n(t) \propto t^n$ in the hydrodynamical regime to $v_n(t) \propto t^{n+1}$ in the few-collisions limit.

Given a system with few rescatterings, we found that the analytical approach and the simulations both exhibit a scaling of $v_n(t) \propto t^{n+1}$, which is also found for the energy-weighted anisotropic flow coefficients $v_n^E(t)$. For quantities like the number of rescatterings over time and the spatial eccentricities $\varepsilon_n^{\mathbf{x}}(t)$, showing a slow departure from their free-streaming behavior, we found a good agreement as well.

Additionally, we have shown that the description of the simulation results by the analytical calculations can be improved when including higher orders in t and/or the cross section σ up to typical times of the order $t/R \approx 0.5$. As every new order in the Taylor expansion introduces many additional terms, it would be a great achievement if one could find a resummation scheme to go to larger times within this description. The results presented in Ch. 5 are not directly related to the description of heavy-ion experiments, but they might be relevant for small systems and for the study of the initial stages of a heavy ion collision [11]. For every prehydrodynamic model — which is not free-streaming — there is a development of a anisotropic flow at early times and it is of interest to know if the model behaves "hydro-like", "few-collisions-like" or even something in between. One possibility would be even to use an initial stage model which uses the scaling law $v_n(t) \propto t^{\gamma_n}$ for the anisotropic flow and similar ones for the other quantities of the system. Then it would be interesting how this affects global Bayesian analyses of medium properties for the QGP created in heavy-ion collisions.

Another area for which this work might be interesting is the search for the existence of dynamical attractor solutions for systems with transverse dynamics [138], as even "late time attractors" have to take into account the different "early time" behaviors. From this point of view it would be of interest to extend the studies into the direction of spatially asymmetric setups, where analytical hydrodynamic results are known [139].

In Ch. 6 we have compared three different setups in kinetic theory. The first one, a simulation with a collision kernel describing elastic binary scatterings, gives the reference to a system, where all rescatterings are considered. In the second realization of the transport algorithm, we introduced a $2 \to 0$ code version to find out which fraction of the anisotropic flow signal is produced by particles which escape the system without undergoing rescatterings. In the third scenario we used analytical calculations within Boltzmann kinetic theory including the loss term for binary collisions only, restricting this approach to the first order in the cross section.[1] These analytical calculations directly provide us with the scaling behavior of the anisotropic flow coefficients at earlier times, confirming the findings from Ch. 5 and they give us the dependence on the initial-state eccentricities. As the analytical approach yields completely different results for even and odd flow coefficients, namely the odd ones have $v_n(t) = 0$, this gives a direct hint that there is a fundamental difference in the production mechanism of even and odd flow harmonics.

The even flow harmonics (v_2, v_4, v_6) are similar within all three approaches if the number of rescatterings is small. For the flow harmonics v_4 and v_6 this holds for the linear response $v_n \propto \varepsilon_n$ and even in the case of non-linear response to the initial-state eccentricities, e.g., $v_4 \propto \varepsilon_2^2$ or $v_6 \propto \varepsilon_3^2$. From this agreement it can be concluded that the even flow coefficients in the few-rescatterings regime are by a large extent produced by particles which escaped the system without any rescattering. The anisotropic escape probability is representing the asymmetric geometry, as advocated for the elliptic flow v_2 in AMPT [111].

This is contrasted by the odd flow harmonics, where the results for the $2 \to 2$ and

[1] This calculation is actually the resummation of the Taylor series approach from Ch. 5 in t at $\mathcal{O}(\sigma)$.

$2 \to 0$ scenarios show significant differences, even in the few-rescatterings regime. While the $2 \to 2$ scenario exhibits a scaling with $N_{\text{resc.}}$, the $2 \to 0$ scenario scales rather with $N_{\text{resc.}}^2$. We have seen that the analytical calculations give $v_3 = 0$ at order σ, while the $2 \to 0$ simulations give a non-vanishing v_3. This is still consistent, as the v_3 signal arises at order σ^2, which can be shown within the Taylor series approach described in Ch. 5. From this discrepancy between the different scenarios we can conclude that for the odd flow harmonics the signal is not driven by the anisotropic-escape probability, i.e., the particles that undergo at least one collision are important for the anisotropic flow signal.

The general conclusion from the work in Ch. 6 is that the "escape mechanism" is not enough to describe the whole anisotropic flow signal, but only the even flow harmonics. Such a difference in the microscopic "origin" of the even and odd flow harmonics has never been discussed before within transport studies. However, it might be relevant for systems with small multiplicity and indeed within a Color Glass Condensate approach a difference between even and odd flow harmonics of two-particle azimuthal correlations was found in proton-nucleus collisions [140]. To put our study within a toy transport model (two-dimensional system, hard spheres) onto a more solid ground, it would be desirable to replicate the results within more realistic transport frameworks, which have then to be "truncated" to also include the $2 \to 0$ collision kernel.

In Ch. 7 we derived a decomposition of a set of initial energy density profiles into an average state and independent fluctuation modes representing the event-by-event fluctuations. This approach seems more appealing from the theoretical point of view than earlier mode decompositions with correlated modes. We have seen that the two initial state models — Glauber and Saturation — have different eigenvalue spectra due to general differences in the structure of the energy density profiles in the models. In the Saturation model the spectrum is flatter, i.e., the higher modes are more important, as there are smaller structures in the density profiles. We observed clear structures for the modes with rotational symmetry at $b = 0$ fm, which are not present at $b = 9$ fm for the broken rotational symmetry and we are able to classify the modes according to their eccentricity and their k-th excitation (radial dependence). Moreover, we performed a Bessel-Fourier decomposition which enables us to reduce the amount of data, which has to be stored for the modes significantly, and it gives us also a natural way to classify the modes according to their azimuthal shape and radial length scales.

We also used a Taylor expansion of the observables (Eq. (7.25)) to characterize the linear and (diagonal) quadratic responses of observables to the modes. While for the rotational symmetric case there is either a linear response to $\mathrm{d}E/\mathrm{d}y$ and $\{r^2\}$ or to one of the eccentricities for a given mode Ψ_l in the initial state, and a response to $\mathrm{d}N_{\text{ch}}/\mathrm{d}\eta$ and $[p_{\text{T}}]$ or one of the flow coefficients in the final state, there are multiple responses for $b = 9$ fm and one specific Ψ_l. In the case of non-linear responses we have seen that they occur due to the non-linearity of the observables themselves or due to a non-linear dynamical response.

Computing the dynamical response coefficients $\mathcal{K}_{n,n}$ and $\mathcal{K}_{n,mm}$ on a mode-by-mode level and comparing our results to full event-by-event results revealed that in general the values are in the same ballpark, even though the values in the literature

are computed within different setups (ideal/dissipative hydrodynamics and kinetic theory).

Comparing the observables from the mode-by-mode approach to event-by-event simulations revealed that there are some observables, e.g., the multiplicity or the mean transverse momentum, whose averages, variances or correlation coefficients would require either more modes or considering more than the linear order in c_l. However, most of the observables can be described with the amount of modes used in our analysis and considering linear response only, especially for central collisions. One of the questions we wanted to answer was if there are any differences between the two initial state models. Within the discussion of the Pearson coefficients we have seen that at $b = 0$ fm we obtain $\mathrm{C}(\mathrm{d}N_{\mathrm{ch}}/\mathrm{d}\eta, [p_{\mathrm{T}}]) > 0$ in the Glauber model and $\mathrm{C}(\mathrm{d}N_{\mathrm{ch}}/\mathrm{d}\eta, [p_{\mathrm{T}}]) < 0$ in the Saturation model. This correlation is in principle measurable in experiments, one thing which has to be checked is if the correlation survives when going to a centrality class dependent description.

Under the assumptions that the expansion coefficients $\{c_l\}$ are Gaussian distributed and there is only a linear response of observables to the mode perturbations, we can predict most of the joint probability distributions $p_{\beta,\gamma}(O_\alpha, O_\gamma)$ from the event-by-event simulations quite well. In some cases, e.g., at $b = 9$ fm for v_2 and ε_2 non-linear relations become visible in the event-by-event distributions, which are not captured in the mode-by-mode approach. This is due to the fact that the assumptions underlying the analytical calculation are only partially fulfilled, such that higher order terms in the expansion of the observables w.r.t. the expansion coefficients should be taken into account.

For the future this mode-by-mode approach could be extended in many different directions. A natural next step is to use centrality classes instead of fixing the impact parameter to come closer to the description of experiments. It would also be very interesting to use the framework for other systems, e.g., deformed nuclei like Ru or Zr, to see how a deviation from sphericity influences the modes. As we perform a Taylor expansion in the coefficients c_l it would be also interesting to investigate higher orders, especially at larger impact parameters or centrality, as we have seen for the moments of the coefficients, that there are modes with sizable skewness and kurtosis. These third and fourth moments are not fixed by construction of the basis of modes like the mean and variance, and thus they leave space for further investigations. In the future one could think of comparing to other initial conditions than the ones used in this work, or extend the framework for three-dimensional initial conditions.

Appendix A

Modeling the initial state of the heavy-ion collision

A.1 Saturation model

In this Section we will present additional calculations for the Saturation model introduced in Sec. 2.3. We will compute in detailed steps the overlap function of two protons (Sec. A.1.1) followed by the gluon spectrum (Sec. A.1.2) and the initial energy deposition (Sec. A.1.3). Afterwards we present a self consistent solution for the computation of the average saturation scale of the nucleus (Sec. A.1.4), which is needed for the computation of the initial energy-density distribution.

Sections A.1.5-A.1.6 show how the number of participants and the effective inelastic parton cross section are computed. They are used in the code to decide whether a collision between two nucleons takes place or not.

A.1.1 p-p overlap

In this Section we compute the overlap function of two protons approximated by Gaussians and separated by **b**:

$$\begin{aligned} T_{pp}(b) &= \int \mathrm{d}^2\mathbf{s}\; T_p^A(\mathbf{s}) T_p^B(\mathbf{s}-\mathbf{b}) \\ &= \frac{1}{4\pi^2 B_G^2} \int \mathrm{d}^2\mathbf{s}\; e^{-\frac{\mathbf{s}^2}{2B_G}} e^{-\frac{(\mathbf{s}-\mathbf{b})^2}{2B_G}} \\ &= \frac{1}{4\pi^2 B_G^2} e^{-\frac{\mathbf{b}^2}{4B_G}} \int \mathrm{d}^2\mathbf{s}\; e^{-\frac{\mathbf{s}^2}{B_G}} \\ &= \frac{1}{4\pi B_G} e^{-\frac{\mathbf{b}^2}{4B_G}}. \end{aligned} \tag{A.1}$$

We find that the function T_{pp} only depends on the distance between the two protons.

A.1.2 Gluon spectrum

In this Section we will solve the momentum integrals for the gluon spectrum. Therefore, we start to plug the unintegrated gluon distribution functions $\Phi_{A/B}$ (Eq. (2.20)) into Eq. (2.21):

$$\begin{aligned} \frac{\mathrm{d}N_g}{\mathrm{d}^2\mathbf{b}\mathrm{d}^2\mathbf{P}\mathrm{d}y} =& \frac{\alpha_\mathrm{S} N_c}{\pi^4 \mathbf{P}^2 (N_c^2-1)} \int \frac{\mathrm{d}^2\mathbf{k}}{(2\pi)^2} \Phi_A(x_A, \mathbf{b}+\mathbf{b}_0/2, \mathbf{k}) \Phi_B(x_B, \mathbf{b}-\mathbf{b}_0/2, \mathbf{P}-\mathbf{k}) \\ =& \frac{g^2 N_c}{4\pi^5 \mathbf{P}^2 (N_c^2-1)} \int \frac{\mathrm{d}^2\mathbf{k}}{(2\pi)^2} 4\pi^2 \frac{(N_c^2-1)}{g^2 N_c} \frac{\mathbf{k}^2}{Q_{s,A}^2} \exp\left(-\frac{\mathbf{k}^2}{Q_{s,A}^2}\right) \\ & \times 4\pi^2 \frac{(N_c^2-1)}{g^2 N_c} \frac{(\mathbf{P}-\mathbf{k})^2}{Q_{s,B}^2} \exp\left(-\frac{(\mathbf{P}-\mathbf{k})^2}{Q_{s,B}^2}\right) \\ =& \frac{N_c^2-1}{g^2 N_c \pi^3 \mathbf{P}^2 Q_{s,A}^2 Q_{s,B}^2} \int \mathrm{d}^2\mathbf{k}\; \mathbf{k}^2 (\mathbf{P}-\mathbf{k})^2 \exp\left(-\frac{\mathbf{k}^2}{Q_{s,A}^2} - \frac{(\mathbf{P}-\mathbf{k})^2}{Q_{s,B}^2}\right). \end{aligned} \tag{A.2}$$

For the sake of brevity we do not write the dependencies of the saturation scales $Q_{s,A/B}$ of the nuclei. Now we go into polar coordinates with $P_x = P$, $P_y = 0$, $k_x = k\cos\phi$ and $k_y = k\sin\phi$, where the integration is easier:

$$\begin{aligned} \frac{\mathrm{d}N_g}{\mathrm{d}^2\mathbf{b}\mathrm{d}^2\mathbf{P}\mathrm{d}y} = \frac{N_c^2-1}{g^2 N_c \pi^3 P^2 Q_{s,A}^2 Q_{s,B}^2} & \int_0^\infty \mathrm{d}k\; k^3 \exp\left(-\frac{k^2}{Q_{s,A}^2} - \frac{P^2+k^2}{Q_{s,B}^2}\right) \\ & \times \int_0^{2\pi} \mathrm{d}\phi\; \left[(P^2+k^2) - 2Pk\cos\phi\right] e^{\frac{2Pk\cos\phi}{Q_{s,B}^2}}. \end{aligned} \tag{A.3}$$

Using the identity [141]

$$I_n(x) = \frac{1}{\pi} \int_0^\pi \mathrm{d}x\; e^{\pm x\cos\phi} \cos(n\phi) \tag{A.4}$$

for the modified Bessel functions of first kind, the ϕ-integration gives us

$$2\pi\left[(P^2+k^2)I_0\left(\frac{2Pk}{Q_{s,B}^2}\right)-2PkI_1\left(\frac{2Pk}{Q_{s,B}^2}\right)\right]. \tag{A.5}$$

In the next step the k-integral can be solved, which leaves us with the following expression for the gluon spectrum:

$$\begin{aligned}\frac{\mathrm{d}N_g}{\mathrm{d}^2\mathbf{b}\mathrm{d}^2\mathbf{P}\mathrm{d}y}=&\frac{N_c^2-1}{g^2N_c\pi^2\mathbf{P}^2}\frac{Q_{s,A}^2Q_{s,B}^2e^{-\frac{\mathbf{P}^2}{(Q_{s,A}^2+Q_{s,B}^2)}}}{(Q_{s,A}^2+Q_{s,B}^2)^2}\\&\times\frac{\mathbf{P}^4Q_{s,A}^2Q_{s,B}^2+\mathbf{P}^2(Q_{s,A}^2-Q_{s,B}^2)^2(Q_{s,A}^2+Q_{s,B}^2)+2Q_{s,A}^2Q_{s,B}^2(Q_{s,A}^2+Q_{s,B}^2)^2}{(Q_{s,A}^2+Q_{s,B}^2)^3}.\end{aligned} \tag{A.6}$$

A.1.3 Initial energy deposition

Using the relation between the integration measure in Milne and Minkowski coordinates, which is $\mathrm{d}\tau\mathrm{d}\eta\mathrm{d}^2\tilde{x}_\mathrm{T}=\frac{1}{\tau}\mathrm{d}t\mathrm{d}z\mathrm{d}^2x_\mathrm{T}$, we can now compute the initial transverse energy density per unit rapidity in a heavy-ion collision via

$$(e\tau)_0=\left(\frac{\tau\mathrm{d}E}{\mathrm{d}^2\mathbf{b}\mathrm{d}z}\right)_0=\left(\frac{\mathrm{d}E}{\mathrm{d}^2\mathbf{b}\mathrm{d}\eta}\right)_0 \tag{A.7}$$

$$=\int\mathrm{d}^2\mathbf{P}\;|\mathbf{P}|\frac{\mathrm{d}N_g}{\mathrm{d}^2\mathbf{b}\mathrm{d}^2\mathbf{P}\mathrm{d}y}\bigg|_{y=\eta} \tag{A.8}$$

$$=2\pi\int\mathrm{d}P\;P^2\frac{\mathrm{d}N_g}{\mathrm{d}^2\mathbf{b}\mathrm{d}^2\mathbf{P}\mathrm{d}y}\bigg|_{y=\eta}. \tag{A.9}$$

The integral over the momentum P can be carried out analytically and gives us

$$(e\tau)_0=\frac{(N_c^2-1)}{4g^2N_c\sqrt{\pi}}\frac{Q_{s,A}^2Q_{s,B}^2}{(Q_{s,A}^2+Q_{s,B}^2)^{5/2}}\left[2Q_{s,A}^4+7Q_{s,A}^2Q_{s,B}^2+2Q_{s,B}^4\right]. \tag{A.10}$$

A.1.4 Self consistent solution for the saturation scale

To obtain the initial transverse energy density from Eq. (2.24) it is necessary to compute the saturation scale $Q_{s,A/B}(x,T_{A/B}(\mathbf{b}))$ of the nucleus self consistently from Eqs. (2.13) and (2.23). Let us rewrite these equations here:

$$x=\frac{Q_{s,A/B}(x,T_{A/B}(\mathbf{b}))e^{\pm y}}{\sqrt{s_{NN}}}, \tag{A.11}$$

$$Q_{s,A/B}^2(x,\mathbf{b})=Q_{s,0}^2x^{-\lambda}(1-x)^\delta\sigma_0T_{A/B}(\mathbf{b}). \tag{A.12}$$

This leads to the Equation

$$x^{1+\frac{\lambda}{2}}-\sqrt{\frac{Q_{s,0}^2\sigma_0T_{A/B}(\mathbf{b})e^{\pm y}}{s_{NN}}}(1-x)^{\frac{\delta}{2}}=0, \tag{A.13}$$

which can be solved for x and then be reinserted into Equation (A.11) to obtain the average saturation scale of the nucleus.

To solve Eq. (A.13) one can use the approximation $x \ll 1$ which leads to the expression

$$x = \left(\frac{Q_{s,0}^2 \sigma_0 T_{A/B}(\mathbf{b}) e^{\pm 2y}}{s_{\mathrm{NN}}} \right)^{\frac{1}{2+\lambda}} \tag{A.14}$$

and an average saturation scale of the nucleus of

$$Q_{s,A/B}^2(x, \mathbf{b}) = Q_{s,0}^2 \left(\frac{Q_{s,0}^2 \sigma_0 T_{A/B}(\mathbf{b}) e^{\pm 2y}}{s_{\mathrm{NN}}} \right)^{-\frac{\lambda}{2+\lambda}} \sigma_0 T_{A/B}(\mathbf{b}). \tag{A.15}$$

This solution is implemented in the code which was used for the simulations in Ch. 7.[1]

A.1.5 Number of participants

Let us now assume that the proton consists of N_g partons with an effective parton-parton cross section σ_{gg}, which is mostly a gluon-gluon cross section. The probability density for partons — which is normalized to 1 — is then given by $p_{\mathrm{parton}}(\mathbf{r}) = \rho_{\mathrm{parton}}(\mathbf{r})/N_g$, where $\rho_{\mathrm{parton}}(\mathbf{r})$ is the three-dimensional parton distribution function (PDF) of the proton. Given the PDF of the proton, we can now define its thickness function by integrating out the z-direction:

$$T_p(\mathbf{s}) = \int \mathrm{d}z \; p_{\mathrm{parton}}(\mathbf{s}, z). \tag{A.16}$$

Note that the thickness function is also normalized to 1 and that the IP-Glasma model assumes it to be of the form given in Eq. (2.15).

The probability for an interaction between two partons with impact parameter $\mathbf{b}$ is given by

$$p_{\mathrm{int.}}(\mathbf{b}) = \sigma_{gg} T_{pp}(\mathbf{b}). \tag{A.17}$$

Following the Poissonian statistics, the probability of n parton-parton interactions in a p+p collision is given by

$$P(n, \mathbf{b}) = \binom{N_g^2}{n} \left[1 - p_{\mathrm{int.}}(\mathbf{b})\right]^{N_g^2 - n} p_{\mathrm{int.}}(\mathbf{b})^n, \tag{A.18}$$

while the average number of parton collisions is given by

$$\langle N_{\mathrm{coll.}}^{gg}(\mathbf{b}) \rangle = \sum_{n=0}^{N_g^2} P(n, \mathbf{b}) n = N_g^2 p_{\mathrm{int.}}(\mathbf{b}) = \sigma_{gg} N_g^2 T_{pp}(\mathbf{b}). \tag{A.19}$$

[1] For a future version of the code there will be a bisection method which solves Eq. (A.13) for x numerically.

Using Eq. (A.19) we can now calculate the probability that there is at least one interaction between partons:

$$1 - P(0, \mathbf{b}) = 1 - \left[1 - p_{\text{int.}}(\mathbf{b})\right]^{N_g^2} \tag{A.20}$$

$$= 1 - \left[1 - \sigma_{gg} T_{pp}(\mathbf{b})\right]^{N_g^2} \tag{A.21}$$

$$\simeq 1 - e^{-\sigma_{gg} N_g^2 T_{pp}(\mathbf{b})}. \tag{A.22}$$

In the last step the optical assumption $N_g \gg 1$ was used.

This gives us now the final ingredient to write the differential probability of a p+p collision at impact parameter $\mathbf{b}$ as [142]

$$\frac{\mathrm{d}p_{pp}}{\mathrm{d}^2\mathbf{b}} = \frac{1 - e^{-\sigma_{gg} N_g^2 T_{pp}(\mathbf{b})}}{\int \mathrm{d}^2\mathbf{b}\; 1 - e^{-\sigma_{gg} N_g^2 T_{pp}(\mathbf{b})}}. \tag{A.23}$$

The quantity $\sigma_{gg} N_g^2$ is the total effective parton cross section $\sigma_{\text{eff}}^{\text{inel}}$ which is optimized in such a way that the denominator becomes the inelastic p+p cross section $\sigma_{\text{NN}}^{\text{inel}}$ for the specific collision energy $\sqrt{s_{\text{NN}}}$. A more extended computation of numerical values is presented in the following part.

A.1.6 Computation of $\sigma_{\text{eff}}^{\text{inel}}$

Similar to Ref. [30] we use the parametrization

$$\sigma_{\text{NN}}^{\text{inel}}\left(\frac{\sqrt{s_{\text{NN}}}}{1\ \text{GeV}}\right) = 25.2 + 0.05 \ln\left(\sqrt{s_{\text{NN}}}\right) + 0.56 \ln^2\left(\sqrt{s_{\text{NN}}}\right) + \frac{45.2}{\sqrt{s_{\text{NN}}}^{0.9}} + \frac{33.8}{\sqrt{s_{\text{NN}}}^{1.1}} \tag{A.24}$$

for the inelastic nucleon-nucleon cross section obtained from fits to total [143] and elastic [144] cross sections to deduce the effective parton cross section at a given center of mass energy $\sqrt{s_{\text{NN}}}$. This is done by solving the integral equation

$$\sigma_{\text{NN}}^{\text{inel}}\left(\sqrt{s_{\text{NN}}}\right) = 2\pi \int_0^\infty \mathrm{d}b\; b \left[1 - e^{-\sigma_{\text{NN}}^{\text{inel}} T_{pp}(b)}\right] \tag{A.25}$$

including the proton-proton overlap function T_{pp} (Eq. (2.17)) at a fixed value of $\sigma_{\text{NN}}^{\text{inel}}$ and $\sqrt{s_{\text{NN}}}$. Then we find the values given in Tab. A.1.

In the code the effective inelastic parton-parton cross sections from Table A.1 are implemented for the fixed energies given there indicated by the data points in the upper panel of Fig. A.1. We have solved Eq. (A.25) for the energies between the data points as well (green line, Fig. A.1 upper panel).

If energies are considered which are not included in Tab. A.1, then we use the parametrization

$$\sigma_{\text{eff}}^{\text{inel}}\left(\frac{\sqrt{s_{\text{NN}}}}{1\ \text{GeV}}\right) = a + b \cdot \ln(\sqrt{s_{\text{NN}}}) + c \cdot \ln^2(\sqrt{s_{\text{NN}}}) + \frac{d}{\ln\left(\sqrt{s_{\text{NN}}}\right)} \tag{A.26}$$

to approximate the $\sqrt{s_{\text{NN}}}$ dependence of the effective partonic cross section. A fit using the cross sections from the green line in the upper panel of Fig. A.1 is shown in the lower panel of the same figure together with the resulting fit parameters.

Table A.1: Inelastic nucleon nucleon cross section $\sigma_{\mathrm{NN}}^{\mathrm{inel}}$ in mb deduced for different energies $\sqrt{s_{NN}}$ from Eq. (A.24) and the corresponding effective parton cross section $\sigma_{\mathrm{eff}}^{\mathrm{inel}}$ in mb.

$\sqrt{s_{\mathrm{NN}}}$ [GeV]	$\sigma_{\mathrm{NN}}^{\mathrm{inel}}$ [mb]	$\sigma_{\mathrm{eff}}^{\mathrm{inel}}$ [mb]
200	41.6	92.6
900	51.6	154.1
2760	60.8	247.2
5020	66.3	328.0
7000	69.6	387.4
13000	75.9	537.1

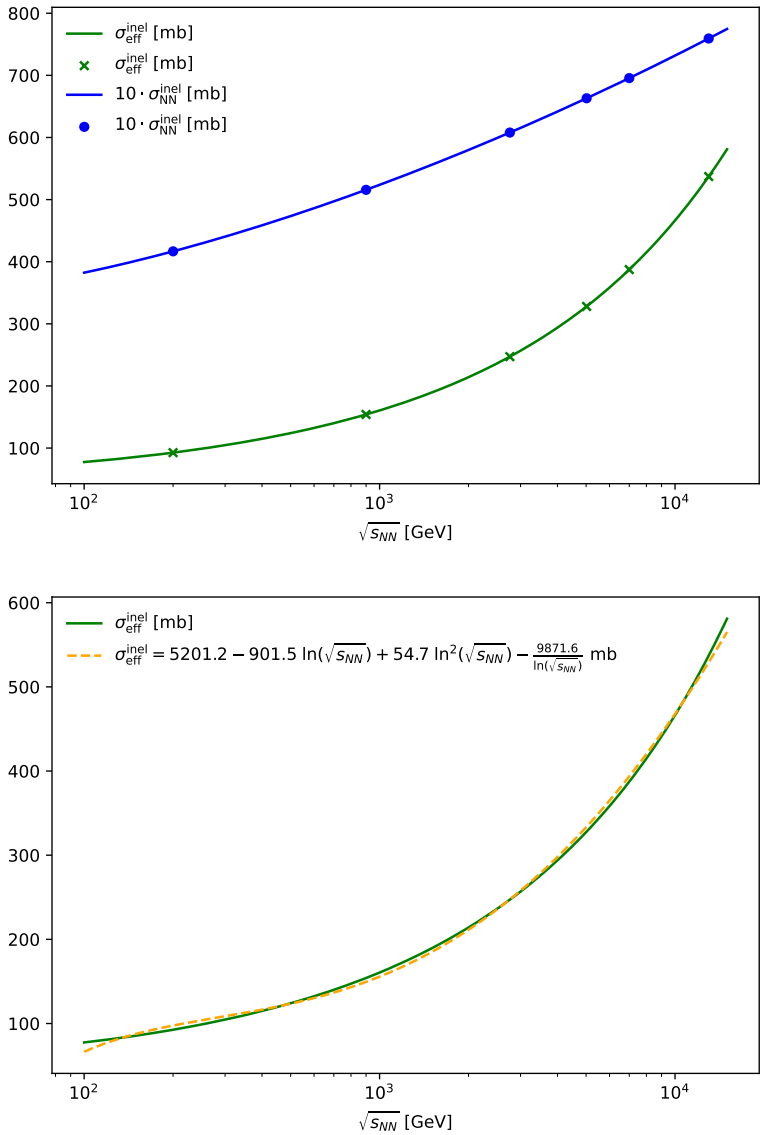

Figure A.1: Top: $\sigma_{\mathrm{eff}}^{\mathrm{inel}}$ extracted by solving Eq. (A.25) (green line) at different $\sqrt{s_{\mathrm{NN}}}$. The blue line shows the $\sigma_{\mathrm{NN}}^{\mathrm{inel}}$ values given by the parametrization (A.24). The points indicate the $\sqrt{s_{\mathrm{NN}}}$ values which are implemented as fixed cases in the code. Bottom: Fit of the extracted effective partonic cross sections with the parametrization (A.26).

Appendix B

Boltzmann equation

In Sec. B.1 we will derive the explicit form of the collision kernel of the classical Boltzmann equation for elastic binary collisions which follows the derivations in [145, 146]. Then we will extend the classical Boltzmann equation to the relativistic one in Sec. B.2.

Additional computations needed for the numerical solution of the Boltzmann equation described in Sec. 3.4 are presented in Sec. B.3.

B.1 Collision kernel of the non relativistic Boltzmann equation

The right hand side of the Boltzmann equation (Eq. (3.8)) encodes the rate of change of the distribution function due to collisions. It can be separated into two parts

$$\left(\frac{\partial f(t,\vec{x},\vec{u})}{\partial t}\right)_{\text{coll}} = \left(\frac{\partial f(t,\vec{x},\vec{u})}{\partial t}\right)_{\text{coll}}^{\text{gain}} - \left(\frac{\partial f(t,\vec{x},\vec{u})}{\partial t}\right)_{\text{coll}}^{\text{loss}}, \tag{B.1}$$

namely the gain and the loss term. Then the expression $(\partial f/\partial t)_{\text{coll}}^{\text{gain}}\ \mathrm{d}^3\vec{r}\mathrm{d}^3\vec{u}\mathrm{d}t$ is the mean number of particles undergoing a collision and one of the two colliding particles will then enter the volume $\mathrm{d}^3\vec{r}\mathrm{d}^3\vec{u}$ around the point $(\vec{r},\vec{u})$ within the time $t+\mathrm{d}t$. The same is true for the loss term but the particle will leave the volume $\mathrm{d}^3\vec{r}\mathrm{d}^3\vec{u}$ around the point $(\vec{r},\vec{u})$ within the time $t+\mathrm{d}t$.

The explicit form of the collision kernel depends on the form of the particle interactions. Here we will only look at elastic binary collisions of particles without internal structure. Additionally we have to make the assumption that the interactions are instantaneous and local. Therefore, under this assumption an external force would have no impact on the collisions.

B.1.1 Loss term of non-relativistic binary collisions

Given two particles with velocities $\vec{u}$ resp. $\vec{u}_1$ which collide, we denote their velocities after their collision by $\vec{u}\,'$ resp. $\vec{u}_1{}'$. The final state velocities can be expressed by the initial ones if the force law of the interaction is known. Describing the interaction in the center-of-mass frame is more convenient. In this system a particle with the reduced mass and moving with the relative velocity of the two particles is deflected from the scattering center. The incoming particle with impact parameter b is then deflected under the azimuthal angle ϕ and polar angle θ. Then the particle flux through an infinitesimal ring $b\,\mathrm{d}b\mathrm{d}\phi$ is given by

$$b\,\mathrm{d}b\mathrm{d}\phi\,|\vec{u}-\vec{u}_1|f(t,\vec{r},\vec{u}_1)\,\mathrm{d}^3\vec{u}_1. \tag{B.2}$$

Multiplying this expression by $f(t,\vec{r},\vec{u})\,\mathrm{d}^3\vec{u}$ gives the number of particle collisions per unit time with particles having a velocity $\vec{u}$. Integration over $\vec{u}_1$ and dividing by $\mathrm{d}^3\vec{u}$ is then the total rate of change of the distribution function induced by scatterings of particles with velocity $\vec{u}$ out of the interval $[\vec{u},\vec{u}+\mathrm{d}^3\vec{u}]$:

$$\left(\frac{\partial f(t,\vec{x},\vec{u})}{\partial t}\right)^{\text{loss}}_{\text{coll}} = \int \mathrm{d}^3\vec{u}_1 \int_0^\infty \mathrm{d}b\; b \int_0^{2\pi} \mathrm{d}\phi\;|\vec{u}-\vec{u}_1|f(t,\vec{r},\vec{u}_1)f(t,\vec{r},\vec{u}). \tag{B.3}$$

It is convenient to introduce the differential scattering cross section

$$\mathrm{d}^2\sigma(\theta,\phi) = b\,\mathrm{d}b\mathrm{d}\phi \tag{B.4}$$

and write the loss term as

$$\left(\frac{\partial f(t,\vec{x},\vec{u})}{\partial t}\right)^{\text{loss}}_{\text{coll}} = \int \mathrm{d}^3\vec{u}_1 \int \mathrm{d}^2\Omega\;\frac{\mathrm{d}^2\sigma(\theta,\phi)}{\mathrm{d}^2\Omega}|\vec{u}-\vec{u}_1|f(t,\vec{r},\vec{u}_1)f(t,\vec{r},\vec{u}) \tag{B.5}$$

with $\mathrm{d}^2\Omega = \sin\theta\;\mathrm{d}\theta\mathrm{d}\phi$.

B.1.2 Gain term of non-relativistic binary collisions

Using the same notations and steps as in the previous subsection we would arrive at the following expression for the gain term of the collision kernel:

$$\left(\frac{\partial f(t,\vec{x},\vec{u})}{\partial t}\right)^{\text{gain}}_{\text{coll}} = \int \mathrm{d}^3\vec{u}_1{}' \int \left(\mathrm{d}^2\Omega\;\frac{\mathrm{d}^2\sigma(\theta,\phi)}{\mathrm{d}^2\Omega}\right)' \left|\vec{u}\,'-\vec{u}_1{}'\right| f(t,\vec{r},\vec{u}_1{}')f(t,\vec{r},\vec{u}\,'). \tag{B.6}$$

Now we can use that the collision is considered as elastic which gives the following conservation relations:

$$\vec{u} + \vec{u}_1 = \vec{u}\,' + \vec{u}_1{}', \tag{B.7}$$

$$\vec{u}^{\,2} + \vec{u}_1^{\,2} = \vec{u}^{\,\prime 2} + \vec{u}_1^{\,\prime 2}. \tag{B.8}$$

Thus, the relation

$$|\vec{u} - \vec{u}_1| = \left|\vec{u}\,' - \vec{u}_1{}'\right| \tag{B.9}$$

is fulfilled and also the identity

$$\mathrm{d}^3\vec{v}_1 \mathrm{d}^3\vec{v} = \mathrm{d}^3\vec{v}_1{}' \mathrm{d}^3\vec{v}\,' \tag{B.10}$$

holds, as the Jacobian of the transformation is one. Additionally, the differential cross section is invariant under time reversal and parity transformation, which is called micro-reversibility, and therefore

$$\mathrm{d}^2\Omega\, \frac{\mathrm{d}^2\sigma(\theta,\phi)}{\mathrm{d}^2\Omega} = \left(\mathrm{d}^2\Omega\, \frac{\mathrm{d}^2\sigma(\theta,\phi)}{\mathrm{d}^2\Omega}\right)' \tag{B.11}$$

holds. Now we can rewrite the gain term from Eq. (B.6) using the upper identities as

$$\left(\frac{\partial f(t,\vec{x},\vec{u})}{\partial t}\right)^{\mathrm{gain}}_{\mathrm{coll}} = \int \mathrm{d}^3\vec{u}_1 \int \mathrm{d}^2\Omega\, \frac{\mathrm{d}^2\sigma(\theta,\phi)}{\mathrm{d}^2\Omega} |\vec{u} - \vec{u}_1| f(t,\vec{r},\vec{u}_1{}') f(t,\vec{r},\vec{u}\,'). \tag{B.12}$$

Combining the gain and loss part of the collision kernel directly gives the full collision kernel written in Eq. (3.9).

B.2 The relativistic Boltzmann equation

The relativistic Boltzmann equation is a quite forward extension of the non-relativistic one. Here we will follow the argumentation in [147].

Scattering processes are characterized by their cross sections which affect the number of interactions in two colliding particle beams. Let us consider these two beams with the densities n and n_1 and the resp. velocities $\vec{u}$ and $\vec{u}_1$. The next step is that we go into the rest frame of beam 1 which gives us the number of interactions in the volume element $\mathrm{d}V$ and in the time interval $\mathrm{d}t$ by

$$\frac{\mathrm{d}N_{\mathrm{interaction}}}{\mathrm{d}^3\vec{x}\mathrm{d}t} = \sigma n n_1 u_{\mathrm{rel}}, \tag{B.13}$$

with the relative velocity u_{rel}. In the rest frame of beam 1 this is just the absolute value of the particles' velocity in the beam with density n. The number of interactions should be Lorentz invariant and thus, we write

$$\frac{\mathrm{d}N_{\mathrm{interaction}}}{\mathrm{d}^3\vec{x}\mathrm{d}t} = \mathcal{A} n n_1, \tag{B.14}$$

with $\mathcal{A}$ in the rest frame of particle 1 given by σu_{rel}. It is important to notice that the cross section measured in the rest frame of one of the beams is an invariant quantity. The same holds true for the relative velocity. We have also seen in Sec. 3.3 that the product $\mathrm{d}^3\vec{x}\mathrm{d}t$ is an invariant quantity. This leads us to the conclusion that the product $\mathcal{A}nn_1$ has to be invariant on its own. The transformation of a density is given by

$$n = \gamma n_{\mathrm{rest}}, \tag{B.15}$$

where n_{rest} is the particle density in their rest frame and $\gamma = \sqrt{1-\vec{u}^{\,2}}$ the Lorentz factor. This can also be expressed in terms of energy E and mass m of the particles by $n = n_{\mathrm{rest}}E/m$ via $E = \gamma m$. Now the invariance of $\mathcal{A}nn_1$ can be recast into the invariance of

$$\mathcal{A}\frac{EE_1}{p^\alpha p_{1,\alpha}} = \mathcal{A}\frac{EE_1}{-EE_1 + \vec{p}\cdot\vec{p}_1} = \text{invariant}, \tag{B.16}$$

where we divided by another invariant quantity $p^\alpha p_{1,\alpha}$. Going now back to the rest frame of beam 1 ($E_1 = m_1$, $\vec{p}_1 = \vec{0}$) shows that $-\mathcal{A}$ is invariant. Additionally, we know that in this reference frame the quantity $\mathcal{A}$ is given by σu_{rel}. Thus, in any reference frame

$$\mathcal{A} = -\sigma u_{\mathrm{rel}}\frac{p^\alpha p_{1,\alpha}}{EE_1} = \sigma u_{\mathrm{rel}}\left(1 - \vec{u}\cdot\vec{u}_1\right) \tag{B.17}$$

is valid.

In the next step we want to express the relative velocity in an arbitrary reference frame. We use the scalar product of the four momenta $p^\mu p_{1,\mu} = -EE_1 + \vec{p}\cdot\vec{p}_1$ and go to the rest frame of particle 1. Thus, we have $\vec{p}_1 = \vec{0}$ and obtain

$$\begin{aligned} p^\mu p_{1,\mu} &= -EE_1 && \text{(B.18)}\\ &= -\gamma m m_1 && \text{(B.19)}\\ &= -\frac{m}{\sqrt{1-\vec{u}_{\mathrm{rel}}^{\,2}}}m_1 && \text{(B.20)} \end{aligned}$$

with $\vec{u}_{\mathrm{rel}}$ the relative velocity between the particles. This quantity is invariant under Lorentz transformations, as well as

$$\begin{aligned} p^\mu p_{1,\mu} &= -\gamma m\cdot\gamma_1 m_1 + \gamma m\vec{u}\cdot\gamma_1 m_1\vec{u}_1 && \text{(B.21)}\\ &= -\gamma\gamma_1 m m_1\left(1 - \vec{u}\cdot\vec{u}_1\right) && \text{(B.22)}\\ &= -m m_1\frac{\left(1-\vec{u}\cdot\vec{u}_1\right)}{\sqrt{(1-\vec{u}^{\,2})(1-\vec{u}_1^{\,2})}} && \text{(B.23)} \end{aligned}$$

in an arbitrary reference frame. Now we can equate the two expressions and solve for u_{rel} which yields

$$\begin{aligned} u_{\mathrm{rel}} &= \frac{\sqrt{(1-\vec{u}\cdot\vec{u}_1)^2 - (1-\vec{u}^{\,2})(1-\vec{u}_1^{\,2})}}{1-\vec{u}\cdot\vec{u}_1} && \text{(B.24)}\\ &= \frac{\sqrt{(\vec{u}-\vec{u}_1)^2 - (\vec{u}\times\vec{u}_1)^2}}{1-\vec{u}\cdot\vec{u}_1} && \text{(B.25)} \end{aligned}$$

by using the identities $(\vec{u}\cdot\vec{u}_1)^2 = \vec{u}^{\,2}\vec{u}_1^{\,2} - (\vec{u}\times\vec{u}_1)^2$ and $(\vec{u}-\vec{u}_1)^2 = \vec{u}^{\,2}+\vec{u}_1^{\,2}-2\vec{u}\cdot\vec{u}_1$.

Going now back to Eq. (B.14) and plugging in the expression for $\mathcal{A}$ from Eq. (B.17) and the relative velocity u_{rel} gives us finally

$$\frac{\mathrm{d}N_{\mathrm{interaction}}}{\mathrm{d}^3\vec{x}\mathrm{d}t} = \sigma n n_1 \sqrt{(\vec{u}-\vec{u}_1)^2 - (\vec{u}\times\vec{u}_1)^2}, \tag{B.26}$$

which is a Lorentz invariant quantity. Let us mention here that the expression $\sqrt{(\vec{u}-\vec{u}_1)^2 - (\vec{u}\times\vec{u}_1)^2}$ is different from the relativistic relative velocity defined in Eq. (B.25). Therefore it has a name on its own, which is Møller velocity $u_{\mathrm{Møller}}$.

If we now consider the case of massless particles with $\vec{u}^{\,2} = 1$ the Møller velocity reduces to:

$$\begin{aligned} u_{\mathrm{Møller}} &= \sqrt{(\vec{u}-\vec{u}_1)^2 - (\vec{u}\times\vec{u}_1)^2} \\ &= \sqrt{\vec{u}^{\,2} + \vec{u}_1^{\,2} \underbrace{-2\vec{u}\cdot\vec{u}_1}_{=(1-\vec{u}\cdot\vec{u}_1)^2-1-(\vec{u}\cdot\vec{u}_1)^2} - \vec{u}^{\,2}\vec{u}_1^{\,2}(1-\cos^2\theta)} \\ &= \sqrt{(1-\vec{u}\cdot\vec{u}_1)^2 + \vec{u}^{\,2} + \vec{u}_1^{\,2} - 1 - \vec{u}^{\,2}\vec{u}_1^{\,2}\cos^2\theta - \vec{u}^{\,2}\vec{u}_1^{\,2} + \vec{u}^{\,2}\vec{u}_1^{\,2}\cos^2\theta} \\ &= 1 - \vec{u}\cdot\vec{u}_1. \end{aligned} \tag{B.27}$$

B.3 Additional calculations for the numerical solution of the Boltzmann equation

The calculations in the following part were originally published in the PhD thesis of C. Gombeaud [57]. We redo them here for the sake of completeness to give an overview over the transport algorithm.[1]

B.3.1 Determining the impact parameter of the test particles

We will now recompute the impact parameter of two particles. Therefore, we assume that particle 1 is at rest and particle 2 moves with a velocity $\vec{v}_2 - \vec{v}_1$ reached by a Galilei transformation with $-\vec{v}_1$. This situation is depicted in Fig. B.1. When particle 2 reaches the line $\mathcal{B}$ then the condition

$$(\vec{x}_2(\tau) - \vec{x}_1)\cdot\vec{v}_1 = 0 \tag{B.28}$$

is fulfilled, with τ being the time when particle 2 reaches $\mathcal{B}$. The position of particle 2 with time dependence is given by

$$\vec{x}_2(t) = (\vec{v}_2 - \vec{v}_1)\,t + \vec{x}_2(0). \tag{B.29}$$

[1] In the original work everything was presented in french language. This is another reason to show the calculations here again.

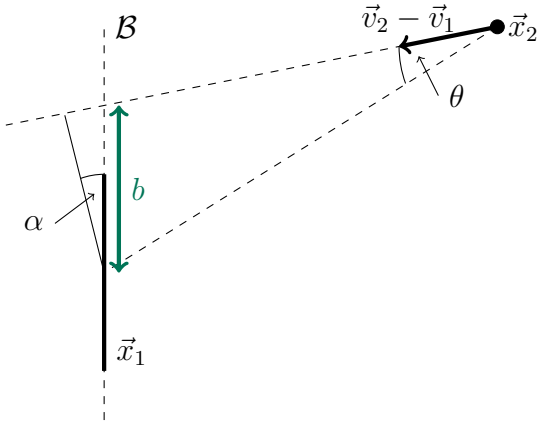

Figure B.1: Schematic representation of the collision of particle 1 and particle 2 in the rest frame of particle 1 [57].

Plugging now Eq. (B.29) into Eq. (B.28) and solving for the time τ leaves us with

$$(\vec{v}_2 - \vec{v}_1) \cdot \vec{v}_1 \tau + (\vec{x}_2(0) - \vec{x}_1) \cdot \vec{v}_1 = 0 \tag{B.30}$$

$$\Leftrightarrow \quad \tau = \frac{(\vec{x}_2(0) - \vec{x}_1) \cdot \vec{v}_1}{(\vec{v}_1 - \vec{v}_2) \cdot \vec{v}_1}, \tag{B.31}$$

which is the time when particle 2 crosses the line $\mathcal{B}$. Reinserting into Eq. (B.29) gives us

$$\vec{x}_2(\tau) = (\vec{v}_2 - \vec{v}_1) \frac{(\vec{x}_2(0) - \vec{x}_1) \cdot \vec{v}_1}{(\vec{v}_1 - \vec{v}_2) \cdot \vec{v}_1} + \vec{x}_2(0). \tag{B.32}$$

Let us recall the definition of an impact parameter b. It is depicted in Fig. B.1 by the green line and it indicates the distance from the center of particle 1 to the center of particle 2 when it crosses the line $\mathcal{B}$. Mathematically it is given by

$$b = |\vec{x}_2(\tau) - \vec{x}_1| \tag{B.33}$$

$$= \left| (\vec{v}_2 - \vec{v}_1) \frac{(\vec{x}_2(0) - \vec{x}_1) \cdot \vec{v}_1}{(\vec{v}_1 - \vec{v}_2) \cdot \vec{v}_1} + \vec{x}_2(0) - \vec{x}_1 \right| \tag{B.34}$$

$$= \left| (\vec{v}_2 - \vec{v}_1) \frac{\vec{r} \cdot \vec{v}_1}{(\vec{v}_1 - \vec{v}_2) \cdot \vec{v}_1} + \vec{r} \right|, \tag{B.35}$$

where we have defined $\vec{r} = \vec{x}_2(0) - \vec{x}_1$.

In the next step we compute the square of b which yields:

$$b^2 = \vec{r}^{\,2} + \frac{(\vec{v}_2 - \vec{v}_1)^2 (\vec{r} \cdot \vec{v}_1)^2}{(1 - \vec{v}_1 \cdot \vec{v}_2)^2} + 2 \frac{(\vec{r} \cdot \vec{v}_2)(\vec{r} \cdot \vec{v}_1) - (\vec{r} \cdot \vec{v}_1)^2}{1 - \vec{v}_1 \cdot \vec{v}_2} \tag{B.36}$$

$$= \vec{r}^{\,2} + 2 \frac{(1 - \vec{v}_1 \cdot \vec{v}_2)(\vec{r} \cdot \vec{v}_1)^2}{(1 - \vec{v}_1 \cdot \vec{v}_2)^2} + 2 \frac{(\vec{r} \cdot \vec{v}_2)(\vec{r} \cdot \vec{v}_1) - (\vec{r} \cdot \vec{v}_1)^2}{1 - \vec{v}_1 \cdot \vec{v}_2} \tag{B.37}$$

$$= \vec{r}^{\,2} + \frac{2}{1 - \vec{v}_1 \cdot \vec{v}_2} \left[(\vec{r} \cdot \vec{v}_2)(\vec{r} \cdot \vec{v}_1) \right], \tag{B.38}$$

where we have used that the particles are massless and therefore $\vec{v}_1^{\,2} = \vec{v}_2^{\,2} = 1$.

We go one step further to show that this expression is indeed covariant by expressing it as a combination of products of four vectors. These are defined by

$$\mathsf{x}_1 = \begin{pmatrix} t_1 \\ \vec{x}_1 \end{pmatrix}, \quad \mathsf{x}_2 = \begin{pmatrix} t_2 \\ \vec{x}_2 \end{pmatrix}, \quad \mathsf{p}_1 = \begin{pmatrix} \gamma m_1 \\ \gamma m_1 \vec{v}_1 \end{pmatrix}, \quad \mathsf{p}_2 = \begin{pmatrix} \gamma m_2 \\ \gamma m_2 \vec{v}_2. \end{pmatrix} \tag{B.39}$$

The square of the vector $\mathsf{x} = \mathsf{x}_1 - \mathsf{x}_2 = (0, \vec{r})$ naturally reproduces the $\vec{r}^{\,2}$ in the first term of Eq. (B.38). For the second term we compute the following products of the four vectors:

$$\mathsf{x} \cdot \mathsf{p}_1 = \gamma m_1 \left(\vec{r} \cdot \vec{v}_1\right), \tag{B.40}$$

$$\mathsf{x} \cdot \mathsf{p}_2 = \gamma m_2 \left(\vec{r} \cdot \vec{v}_2\right), \tag{B.41}$$

$$\mathsf{p}_1 \cdot \mathsf{p}_2 = -\gamma^2 m_1 m_2 \left(1 - \vec{v}_1 \cdot \vec{v}_2\right). \tag{B.42}$$

This gives us the possibility to express b^2 by

$$b^2 = \mathsf{x}^2 - 2\frac{\left(\mathsf{x} \cdot \mathsf{p}_1\right)\left(\mathsf{x} \cdot \mathsf{p}_2\right)}{\mathsf{p}_1 \cdot \mathsf{p}_2}. \tag{B.43}$$

Thus, the quantity is indeed Lorentz invariant.

The second possibility to compute the impact parameter — which is actually equivalent to the one above — uses

$$|\vec{r} \times (\vec{v}_2 - \vec{v}_1)| = |\vec{v}_2 - \vec{v}_1||\vec{r}| \sin\theta \tag{B.44}$$

with the angle θ between $\vec{r}$ and $\vec{v}_2 - \vec{v}_1$. Additionally we can read off in Fig. B.1 that

$$|\vec{r}| \sin\theta = \left|\vec{b}\right| \cos\alpha \tag{B.45}$$

$$\Leftrightarrow \quad \left|\vec{b}\right| = \frac{|\vec{r}| \sin\theta}{\cos\alpha}. \tag{B.46}$$

The $\cos\alpha$ can be obtained via

$$\cos\alpha = \frac{\vec{v}_1 \cdot (\vec{v}_2 - \vec{v}_1)}{|\vec{v}_1||\vec{v}_2 - \vec{v}_1|}. \tag{B.47}$$

Inserting expressions (B.44) and (B.47) in Eq. (B.46) directly gives us

$$\left|\vec{b}\right| = \frac{|\vec{r} \times (\vec{v}_2 - \vec{v}_1)|}{\vec{v}_1 \cdot \vec{v}_2 - 1} = \frac{\vec{\mathsf{e}}_z \cdot [\vec{r} \times (\vec{v}_2 - \vec{v}_1)]}{\vec{v}_1 \cdot \vec{v}_2 - 1}, \tag{B.48}$$

where ${\vec{v}_1}^2 = 1$ for massless particles was used again. Squaring the latter expression one can show that it is equivalent to Eq. (B.38).

B.3.2 Kinematics of a collision

For the final state momenta a schematic picture (Fig. B.2) can be drawn for a rotated frame w.r.t. the laboratory frame, where the calculation is conducted. What has to be determined is the angle θ between $\vec{p}_1$ and the x-axis as well as the absolute

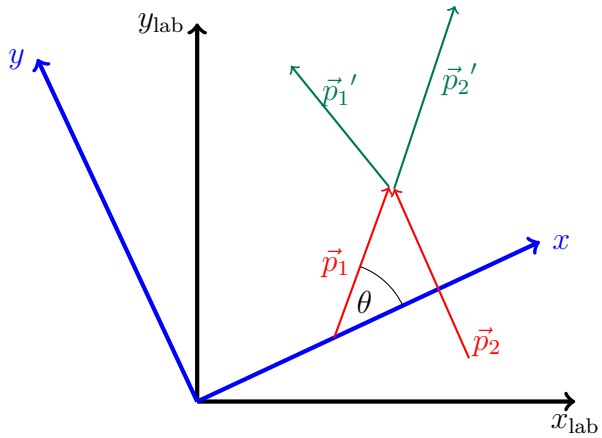

Figure B.2: Schematic representation of a collision for the calculation of the final state momenta [57].

value of $\vec{p}_1\,'$. This final state momentum of particle 1 should be expressed in polar coordinates.

Therefore, we start with the four momentum conservation:

$$\mathsf{p}_1 + \mathsf{p}_2 = \mathsf{p}_1' + \mathsf{p}_2'. \tag{B.49}$$

As we consider massless particles only, we have $\mathsf{p}^2 = -m^2 = 0$ and can rewrite the latter equation to

$$(\mathsf{p}_1 + \mathsf{p}_2 - \mathsf{p}_1')^2 = 0 = (\mathsf{p}_1 + \mathsf{p}_2)^2 - 2\mathsf{p}_1' (\mathsf{p}_1 + \mathsf{p}_2)\,. \tag{B.50}$$

Using the definition of the Mandelstam variables

$$\mathsf{s} = (\mathsf{p}_1 + \mathsf{p}_2)^2\,, \tag{B.51}$$

$$\mathsf{t} = (\mathsf{p}_1 - \mathsf{p}_1')^2\,, \tag{B.52}$$

one quickly finds that they can be rewritten as

$$\mathsf{s} = 2\mathsf{p}_1' \cdot (\mathsf{p}_1 + \mathsf{p}_2)\,, \tag{B.53}$$

$$\mathsf{t} = -2\mathsf{p}_1' \cdot \mathsf{p}_1, \tag{B.54}$$

with the help of Eq. (B.50) and by expanding t.

With the help of the Mandelstam variables we can write

$$-\frac{\mathsf{t}}{2}\mathsf{s} + \frac{\mathsf{s}}{2}\mathsf{t} = 0. \tag{B.55}$$

Then we insert $-\mathsf{t}/2$ in the first term and $\mathsf{s}/2$ in the second one:

$$\mathsf{s}\mathsf{p}_1' \cdot \mathsf{p}_1 + \mathsf{t}\mathsf{p}_1' \cdot (\mathsf{p}_1 + \mathsf{p}_2) = 0 \tag{B.56}$$

$$\Leftrightarrow \quad (\mathsf{s} + \mathsf{t})\, \mathsf{p}_1' \cdot \mathsf{p}_1 + \mathsf{t}\mathsf{p}_1' \cdot \mathsf{p}_2 = 0. \tag{B.57}$$

Separating now the scalar and vectorial parts leads to

$$(\mathsf{s} + \mathsf{t})\, \vec{p}_1\,' \cdot \vec{p}_1 + \mathsf{t}\vec{p}_1\,' \cdot \vec{p}_2 = (\mathsf{s} + \mathsf{t}) \left|\vec{p}_1\,'\right| |\vec{p}_1| + \mathsf{t}\left|\vec{p}_1\,'\right| |\vec{p}_2|. \tag{B.58}$$

In the next step we define a unit vector in $\vec{p}_1{}'$-direction by $\vec{u} = \vec{p}_1{}' / \left|\vec{p}_1{}'\right|$ such that the latter expression can be recast as

$$(\mathsf{s}+\mathsf{t})\,\vec{u}\cdot\vec{p}_1 + \mathsf{t}\vec{u}\cdot\vec{p}_2 = (\mathsf{s}+\mathsf{t})\,|\vec{p}_1| + \mathsf{t}|\vec{p}_2| \tag{B.59}$$

$$\Leftrightarrow \quad [(\mathsf{s}+\mathsf{t})\,\vec{p}_1 + \mathsf{t}\vec{p}_2]\cdot\vec{u} = (\mathsf{s}+\mathsf{t})\,|\vec{p}_1| + \mathsf{t}|\vec{p}_2|. \tag{B.60}$$

We now write $\vec{v} \equiv [(\mathsf{s}+\mathsf{t})\,\vec{p}_1 + \mathsf{t}\vec{p}_2]$ as the vector defining the x-axis of the coordinate system for the collision. The expression

$$\vec{v}\cdot\vec{u} = (\mathsf{s}+\mathsf{t})\,|\vec{p}_1| + \mathsf{t}|\vec{p}_2| \tag{B.61}$$

provides us with the angle θ then.

However, for the definition of the scattering angle it is necessary to know t. The scattering angle is defined in the center-of-momentum frame (indicated by the star) and chosen to be

$$\theta^* = \pi\left(1 + \frac{b}{r}\right). \tag{B.62}$$

This form corresponds to an isotropic differential cross section and it prevents the particles to collide twice. A more detailed discussion of this problem is given in Sec. B.3.3.

Having all ingredients at hand we can now start with the calculation of the final state momenta. This is also the way how collisions are treated in the transport algorithm, where the Cartesian components of the momenta are known for each particle at each step in time. The first part is the change to the coordinate system defined by Eq. (B.61), which corresponds to a rotation around the z-axis by the angle $\beta = \angle(\vec{\mathsf{e}}_x, \vec{v})$. We can write

$$\cos\theta = \frac{(\mathsf{s}+\mathsf{t})\,|\vec{p}_1| + \mathsf{t}|\vec{p}_2|}{|\vec{v}|} \tag{B.63}$$

with the help of Eq. (B.61). Solving this expression for t and going to the center-of-momentum frame, where $\vec{v} = \mathsf{s}\vec{p}_1$, leads to

$$\mathsf{t} = -\frac{\mathsf{s}}{2}\left(1 - \cos\theta^*\right). \tag{B.64}$$

Doing the same for $(\mathsf{s}+\mathsf{t})$ gives

$$(\mathsf{s}+\mathsf{t}) = \mathsf{s}\cos^2\left(\frac{\theta^*}{2}\right). \tag{B.65}$$

In the next step we rewrite Eq. (B.63) by

$$\cos\theta = \frac{w}{|\vec{v}|} \tag{B.66}$$

with $w = (\mathsf{s}+\mathsf{t})\,|\vec{p}_1| + \mathsf{t}|\vec{p}_2|$. Squaring Eq. (B.66) and subtracting one leads us to

$$\cos^2\theta - 1 = \frac{w^2 - |\vec{v}|^2}{|\vec{v}|^2} \tag{B.67}$$

$$= \frac{-2(\mathsf{s}+\mathsf{t})\mathsf{t}\,[-|\vec{p}_1||\vec{p}_2| + \vec{p}_1\cdot\vec{p}_2]}{|\vec{v}|^2}. \tag{B.68}$$

Then we can use the definition of s to rewrite the pseudo scalar product of $\mathsf{p}_1 \cdot \mathsf{p}_2$ as $\mathsf{s}/2$ in the massless case. This leaves us with

$$\cos^2\theta - 1 = \frac{-\mathsf{st}(\mathsf{s}+\mathsf{t})}{|\vec{v}|^2} \tag{B.69}$$

$$= -\sin^2\theta \tag{B.70}$$

and therefore we have

$$\sin\theta = \frac{\sqrt{\mathsf{st}(\mathsf{s}+\mathsf{t})}}{|\vec{v}|}. \tag{B.71}$$

Now we have the cosine and the sine of the scattering angle at hand.

Using the Mandelstam variable t (Eq. (B.54)) can provide us with $\left|\vec{p}_1{}'\right|$:

$$\mathsf{t} = -2\mathsf{p}_1' \cdot \mathsf{p}_1 \tag{B.72}$$

$$\Leftrightarrow \quad -\frac{\mathsf{t}}{2} = -\left|\vec{p}_1{}'\right| \left[|\vec{p}_1| - \vec{p}_1 \cdot \vec{u}\right] \tag{B.73}$$

$$\Leftrightarrow \quad \left|\vec{p}_1{}'\right| = \frac{\mathsf{t}}{2\left[|\vec{p}_1| - \vec{p}_1 \cdot \vec{u}\right]}. \tag{B.74}$$

By the energy momentum conservation laws the other final state momentum components can be determined.

B.3.3 Double collisions

Considering a collision of a point particle with a particle of size $2r$ can lead to some non-physical behavior if the scattering angle θ^* computed from the impact parameter b is chosen in such a way that the particles would collide again immediately. Thus, the sign of θ^* has to be chosen properly, which is depicted in Fig. B.3.

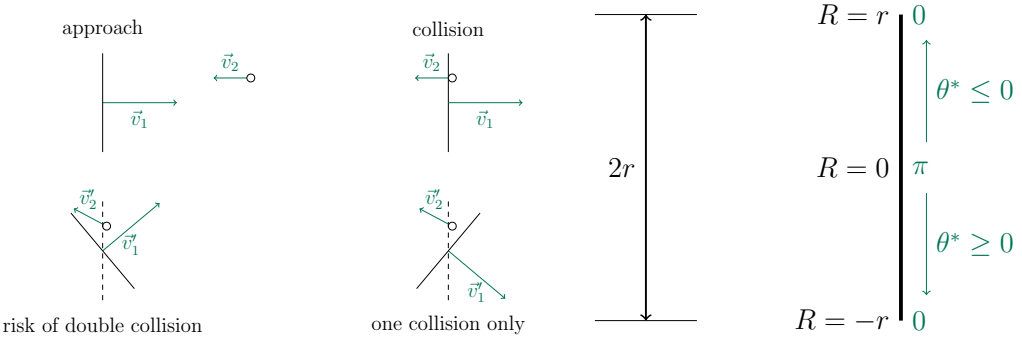

Figure B.3: In the left panel we see that with the wrong choice of the scattering angle a double collision can occur. The right panel shows how to circumvent this problem by choosing the scattering angle as a function of the impact parameter. The figure is adapted from [57].

Appendix C

Fluctuations of anisotropic flow from the finite number of rescatterings

In this appendix additional results for Secs. 4.3-4.4 are presented. In Sec. C.1 will give the remaining probability distributions of anisotropic flow in the initial state of the transport simulation, then the fit parameters for the scatter plots of $v_{n,\mathrm{c/s}}$ and $\varepsilon_{n,\mathrm{c/s}}$ are discussed in Sec. C.2. Then in Sec. C.3 we will briefly discuss what happens in the case of complex eccentricities and flow harmonics in the binning procedure applied to scatter plot mentioned above. Afterwards, in Sec. C.4, the averaged moments for the impact parameters $b = 0$ and 9 fm are given and the corresponding event-plane angle distributions are displayed in Sec. C.5.

C.1 Initial anisotropic flow

For completeness the distributions $p(v_{n,\mathrm{c/s}})$ are presented in the initial state for the impact parameters $b = 0$ and 9 fm. The histograms are shown in Fig. C.1 and their moments are listed in Tab. C.1. All distributions are extremely similar to the ones presented in Sec. 4.3.2 for $b = 0$ fm.

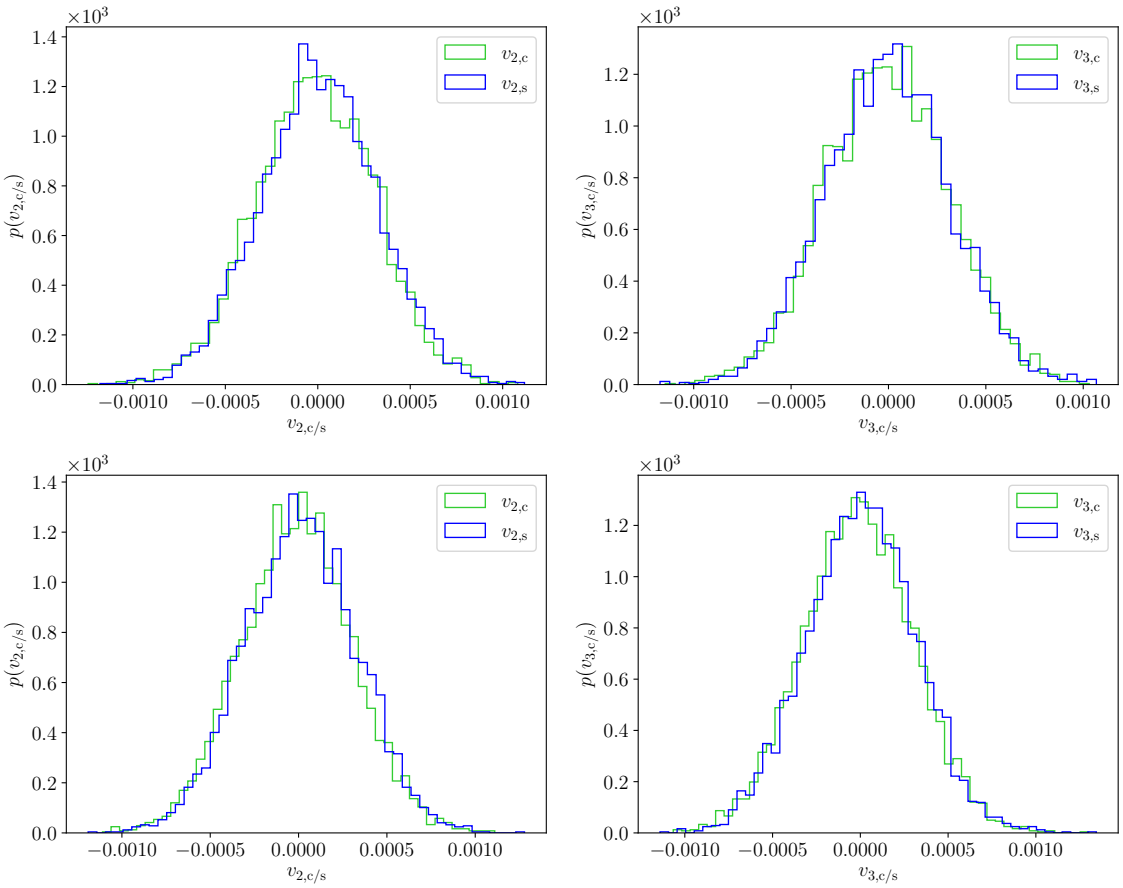

Figure C.1: Initial state probability distributions of $v_{2,\mathrm{c/s}}$ (left) and $v_{3,\mathrm{c/s}}$ (right) including 5000 events at $b = 6$ fm (top), $b = 9$ fm (bottom).

Table C.1: Calculated moments from the probability distributions in Fig. C.1 for $v_{n,\mathrm{c/s}}$ with $n = 2, 3$ at $b = 6, 9$ fm including 5000 events. The variance σ_v^2 was divided by its rough estimate $1/(2N_\mathrm{p})$.

	$\sigma_v^2/(2N_\mathrm{p})^{-1}$	$\lvert\gamma_1\rvert$	γ_2
$b = 6$ fm			
$v_{2,\mathrm{c}}$	1.022 ± 0.020	0.149 ± 0.054	0.000 ± 0.065
$v_{2,\mathrm{s}}$	1.010 ± 0.020	0.032 ± 0.055	0.022 ± 0.067
$v_{3,\mathrm{c}}$	1.006 ± 0.020	0.045 ± 0.052	-0.091 ± 0.055
$v_{3,\mathrm{s}}$	1.002 ± 0.020	0.022 ± 0.056	0.017 ± 0.069
$b = 9$ fm			
$v_{2,\mathrm{c}}$	0.994 ± 0.020	0.013 ± 0.055	0.043 ± 0.066
$v_{2,\mathrm{s}}$	1.002 ± 0.020	0.110 ± 0.054	-0.034 ± 0.071
$v_{3,\mathrm{c}}$	0.994 ± 0.020	0.109 ± 0.056	0.021 ± 0.072
$v_{3,\mathrm{s}}$	0.970 ± 0.020	0.069 ± 0.057	0.084 ± 0.083

C.2 Fit parameters

The Tables C.2, C.3 and C.4 show the parameters of the fit functions used for the scatter plots of the final state $v_{n,\mathrm{c/s}}$ as a function of the initial $\varepsilon_{n,\mathrm{c/s}}$. In all fits a

linear relation between eccentricity and flow harmonic was used, except for $v_{2,\mathrm{c/s}}$ at $b = 6$ and 9 fm, where the non-linear ansatz from Eq. (4.12) was used.

Fixing one condition of impact parameter and $\langle \mathrm{Kn} \rangle^{-1}$ the fit parameters are very similar for the cosine and sine parts. They all increase with $\langle \mathrm{Kn} \rangle^{-1}$ for a given impact parameter. This behavior is already known, but it holds true for the non-linear parameter $\mathcal{K}_{2,222}$ as well, which was reported recently in Ref. [84].

Table C.2: Parameters of the linear-fit functions (4.10)-(4.11) for $v_{2,\mathrm{c/s}}$ and $v_{3,\mathrm{c/s}}$ at $b = 0$ fm.

$\langle \mathrm{Kn} \rangle^{-1}$	$v_{2,\mathrm{c}}$ $\mathcal{K}_{2,2}$	$v_{2,\mathrm{s}}$ $\mathcal{K}_{2,2}$	$v_{3,\mathrm{c}}$ $\mathcal{K}_{3,3}$	$v_{3,\mathrm{s}}$ $\mathcal{K}_{3,3}$
0.30	0.0455 ± 0.0001	0.0455 ± 0.0001	0.0058 ± 0.0001	0.0058 ± 0.0001
3.01	0.1712 ± 0.0003	0.1706 ± 0.0003	0.0920 ± 0.0002	0.0920 ± 0.0002
12.06	0.2133 ± 0.0006	0.2120 ± 0.0006	0.1490 ± 0.0006	0.1490 ± 0.0006

Table C.3: Parameters of the fit functions for $v_{2,\mathrm{c/s}}$ [non-linear fit Eq. (4.12)] and $v_{3,\mathrm{c/s}}$ [linear fit Eq. (4.11)] at $b = 6$ fm.

$\langle \mathrm{Kn} \rangle^{-1}$	$v_{2,\mathrm{c}}$		$v_{2,\mathrm{s}}$		$v_{3,\mathrm{c}}$	$v_{3,\mathrm{s}}$
	$\mathcal{K}_{2,2}$	$\mathcal{K}_{2,222}$	$\mathcal{K}_{2,2}$	$\mathcal{K}_{2,222}$	$\mathcal{K}_{3,3}$	$\mathcal{K}_{3,3}$
0.34	0.0589 ± 0.0001	0.0018 ± 0.0015	0.0565 ± 0.0002	0.0171 ± 0.0065	0.00791 ± 0.00004	0.00782 ± 0.00004
3.43	0.1924 ± 0.0003	0.0182 ± 0.0043	0.1900 ± 0.0005	0.0458 ± 0.0203	0.1069 ± 0.0002	0.1062 ± 0.0002
13.73	0.2382 ± 0.0005	0.0235 ± 0.0082	0.2379 ± 0.0009	0.0539 ± 0.0391	0.1770 ± 0.0005	0.1756 ± 0.0005

Table C.4: Parameters of the fit functions for $v_{2,\mathrm{c/s}}$ [non-linear fit Eq. (4.12)] and $v_{3,\mathrm{c/s}}$ [linear fit Eq. (4.11)] at $b = 9$ fm.

$\langle \mathrm{Kn} \rangle^{-1}$	$v_{2,\mathrm{c}}$		$v_{2,\mathrm{s}}$		$v_{3,\mathrm{c}}$	$v_{3,\mathrm{s}}$
	$\mathcal{K}_{2,2}$	$\mathcal{K}_{2,222}$	$\mathcal{K}_{2,2}$	$\mathcal{K}_{2,222}$	$\mathcal{K}_{3,3}$	$\mathcal{K}_{3,3}$
0.41	0.0662 ± 0.0001	0.0161 ± 0.0007	0.0646 ± 0.0002	0.0081 ± 0.0031	0.00989 ± 0.00003	0.00970 ± 0.00003
4.10	0.1981 ± 0.0002	0.0425 ± 0.0017	0.1976 ± 0.0004	0.0400 ± 0.0086	0.1106 ± 0.0002	0.1091 ± 0.0003
14.42	0.2414 ± 0.0004	0.0456 ± 0.0029	0.2422 ± 0.0008	0.0520 ± 0.0150	0.1697 ± 0.0005	0.1670 ± 0.0005

C.3 Complex eccentricity and elliptic flow at $b = 6$ fm

The dispersion of the complex initial state eccentricity $\varepsilon_2 e^{2\mathrm{i}\Phi_2}$ is shown in Fig. C.2 for 10^4 events at $b = 6$ fm. The impact parameter is still oriented along $\Phi_2 = 0$. Here the same bins as in Fig. 4.6 are indicated by the different colors. The final state complex anisotropic flow is then displayed in Fig. C.3 for the smallest and the largest inverse Knudsen number. Again, the $\varepsilon_{2,\mathrm{c}}$ bins from Fig. C.2 are indicated by the colors. Here it becomes obvious that they do not map into the same bins in $v_2 = \mathrm{Re}\left(v_2 e^{2\mathrm{i}\Psi_2}\right)$ due to fluctuations in the response. A second observation is that events which are indicated by gray points in Fig. C.2 as "outliers" in $\varepsilon_{2,\mathrm{c}}$ and which are sorted out in our $v_{2,\mathrm{c}}$ analysis, are not "outliers" in $\varepsilon_{2,\mathrm{s}}$ direction, and thus they are not the same events which are left aside in the $v_{2,\mathrm{s}}$ analysis.

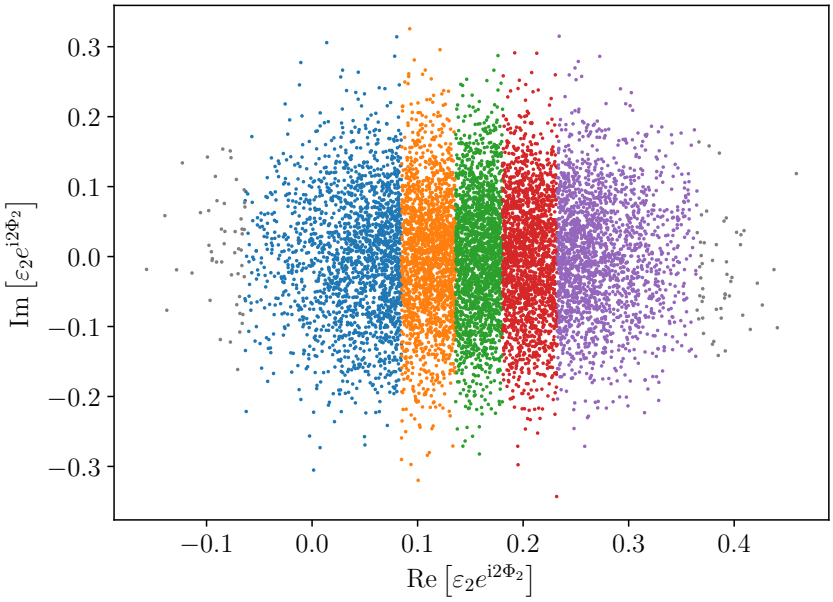

Figure C.2: Scatter plot of the initial complex eccentricity $\varepsilon_2 e^{2\mathrm{i}\Phi_2} \equiv \varepsilon_{2,\mathrm{c}} + \mathrm{i}\varepsilon_{2,\mathrm{s}}$ for 10^4 events at $b = 6$ fm. The bins are the same as in Fig. 4.6.

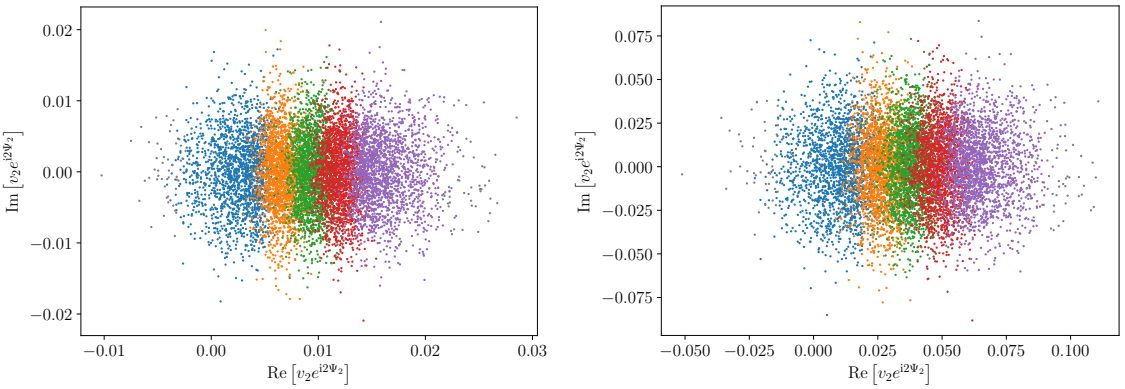

Figure C.3: Scatter plot of the final complex elliptic flow $v_2 e^{2\mathrm{i}\Psi_2} \equiv v_{2,\mathrm{c}} + \mathrm{i}v_{2,\mathrm{s}}$ for 10^4 events at $b = 6$ fm with $\langle \mathrm{Kn} \rangle^{-1} = 0.34$ (left) and $\langle \mathrm{Kn} \rangle^{-1} = 13.74$ (right). The bins are the same ones as in Figs. 4.6 and C.2.

C.4 Averaged moments of the anisotropic flow harmonics

This appendix lists the moments of the distribution $p_{v|\varepsilon}(v_{n,\mathrm{c/s}}|\varepsilon_{n,\mathrm{c/s}})$ about the mean value $\bar{v}_{n,\mathrm{c/s}}(\varepsilon_{n,\mathrm{c/s}})$ for the events at $b = 0$ (Tab. C.5 and C.6) and 9 fm (Tab. C.7 and C.8), as they were not given in Sec. 4.3.3.

Table C.5: Calculated moments of the probability distributions $p_{v|\varepsilon}(v_{2,\mathrm{c/s}}|\varepsilon_{2,\mathrm{c/s}})$ of the flow harmonics in the final state computed for 10^4 events at $b = 0$ fm. We divided the variance σ_v^2 by the linear coefficient from Eq. (4.10).

$\langle \mathrm{Kn} \rangle^{-1}$	$v_{2,\mathrm{c}}$			$v_{2,\mathrm{s}}$		
	$10^4\,\sigma_v^2/\mathcal{K}_{2,2}^2$	$\lvert\gamma_1\rvert$	γ_2	$10^4\,\sigma_v^2/\mathcal{K}_{2,2}^2$	$\lvert\gamma_1\rvert$	γ_2
0.30	1.482 ± 0.049	0.112 ± 0.094	0.161 ± 0.125	1.489 ± 0.049	0.295 ± 0.089	0.091 ± 0.111
3.01	0.905 ± 0.030	0.309 ± 0.092	0.219 ± 0.124	0.908 ± 0.031	0.416 ± 0.095	0.252 ± 0.140
12.06	2.212 ± 0.071	0.372 ± 0.084	0.041 ± 0.100	2.183 ± 0.070	0.081 ± 0.090	0.046 ± 0.120

Table C.6: Calculated moments of the probability distributions $p_{v|\varepsilon}(v_{3,\mathrm{c/s}}|\varepsilon_{3,\mathrm{c/s}})$ of the flow harmonics in the final state computed for 10^4 events at $b = 0$ fm. We divided the variance σ_v^2 by the linear coefficient from Eq. (4.11).

$\langle \mathrm{Kn} \rangle^{-1}$	$v_{3,\mathrm{c}}$			$v_{3,\mathrm{s}}$		
	$10^3\,\sigma_v^2/\mathcal{K}_{3,3}^2$	$\lvert\gamma_1\rvert$	γ_2	$10^3\,\sigma_v^2/\mathcal{K}_{3,3}^2$	$\lvert\gamma_1\rvert$	γ_2
0.30	33.27 ± 1.03	0.313 ± 0.083	-0.024 ± 0.095	37.58 ± 1.15	1.053 ± 0.054	-0.144 ± 0.084
3.01	1.663 ± 0.044	0.074 ± 0.093	0.052 ± 0.128	0.183 ± 0.058	0.875 ± 0.065	-0.080 ± 0.094
12.06	5.488 ± 0.175	0.061 ± 0.088	-0.031 ± 0.109	0.553 ± 0.173	0.407 ± 0.080	-0.064 ± 0.096

Table C.7: Calculated moments of the probability distributions $p_{v|\varepsilon}(v_{2,\mathrm{c/s}}|\varepsilon_{2,\mathrm{c/s}})$ of the flow harmonics in the final state computed for 10^4 events at $b = 9$ fm. We divided the variance σ_v^2 by the linear coefficient from Eq. (4.12).

$\langle \mathrm{Kn} \rangle^{-1}$	$v_{2,\mathrm{c}}$			$v_{2,\mathrm{s}}$		
	$10^4\,\sigma_v^2/\mathcal{K}_{2,2}^2$	$\lvert\gamma_1\rvert$	γ_2	$10^4\,\sigma_v^2/\mathcal{K}_{2,2}^2$	$\lvert\gamma_1\rvert$	γ_2
0.41	3.559 ± 0.149	0.606 ± 0.127	0.551 ± 0.269	2.668 ± 0.133	0.383 ± 0.196	1.334 ± 0.440
4.10	2.376 ± 0.101	0.683 ± 0.130	1.147 ± 0.404	2.423 ± 0.104	0.381 ± 0.157	0.995 ± 0.372
16.42	4.837 ± 0.180	0.404 ± 0.112	0.733 ± 0.267	4.940 ± 0.178	0.219 ± 0.113	0.379 ± 0.187

Table C.8: Calculated moments of the probability distributions $p_{v|\varepsilon}(v_{3,\mathrm{c/s}}|\varepsilon_{3,\mathrm{c/s}})$ of the flow harmonics in the final state computed for 10^4 events at $b = 9$ fm. We divided the variance σ_v^2 by the linear coefficient from Eq. (4.11).

$\langle \mathrm{Kn} \rangle^{-1}$	$v_{3,\mathrm{c}}$			$v_{3,\mathrm{s}}$		
	$10^3\,\sigma_v^2/\mathcal{K}_{3,3}^2$	$\lvert\gamma_1\rvert$	γ_2	$10^3\,\sigma_v^2/\mathcal{K}_{3,3}^2$	$\lvert\gamma_1\rvert$	γ_2
0.41	2.190 ± 0.080	0.138 ± 0.116	0.608 ± 0.251	2.601 ± 0.089	0.942 ± 0.078	0.171 ± 0.125
4.10	0.823 ± 0.034	0.443 ± 0.138	1.262 ± 0.351	1.000 ± 0.038	0.386 ± 0.117	0.548 ± 0.195
16.42	1.304 ± 0.045	0.209 ± 0.098	0.267 ± 0.159	1.499 ± 0.050	0.221 ± 0.100	0.264 ± 0.180

C.5 Event-plane angle distributions with $n = 2, 3$

This appendix shows the event-plane angle Ψ_n distributions in the final state about the corresponding initial state participant-plane orientation Φ_n for the event sets at $b = 0$ fm (Fig. C.4) and $b = 9$ fm (Fig. C.5).

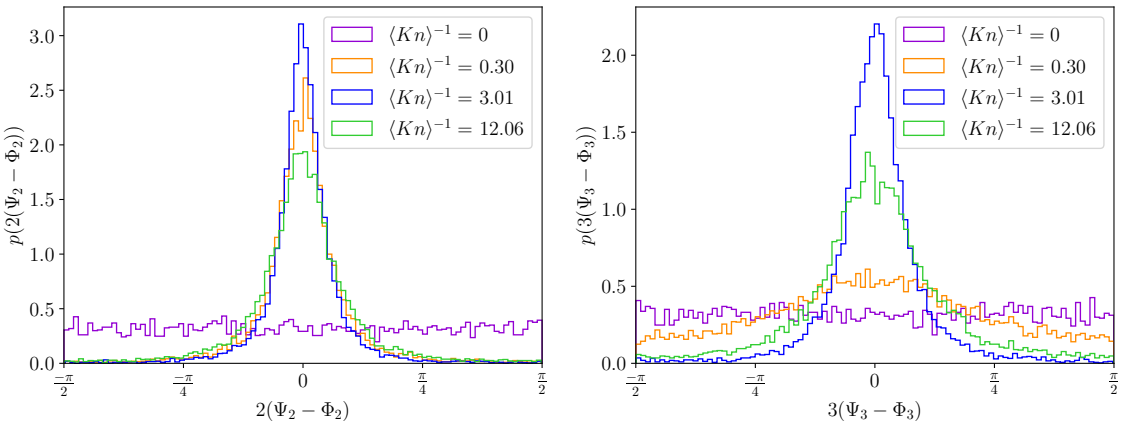

Figure C.4: Probability distributions $p(2(\Psi_2-\Phi_2))$ (left) and $p(3(\Psi_3-\Phi_3))$ (right) for events at $b = 0$ fm for different $\langle \mathrm{Kn}\rangle^{-1}$. The initial state distribution is indicated by the label $\langle \mathrm{Kn}\rangle^{-1} = 0$.

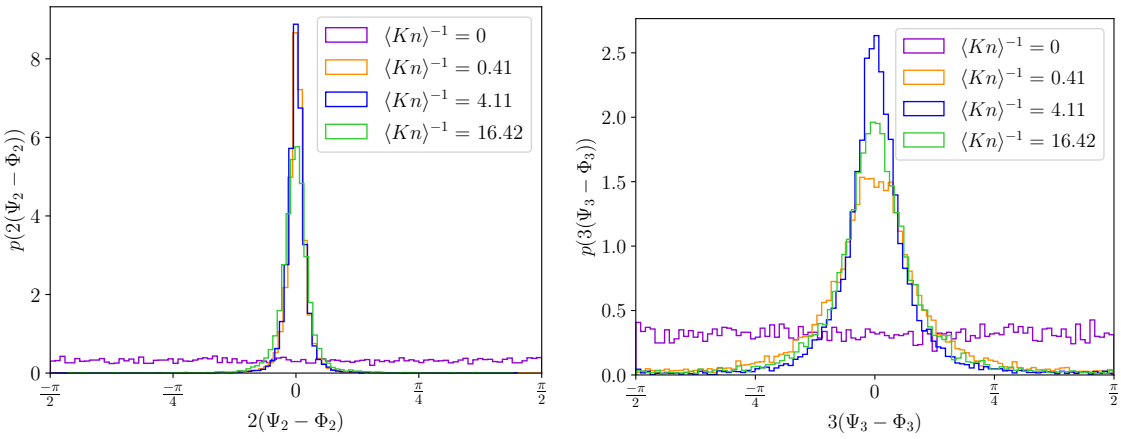

Figure C.5: Probability distributions $p(2(\Psi_2-\Phi_2))$ (left) and $p(3(\Psi_3-\Phi_3))$ (right) for events at $b = 9$ fm for different $\langle \mathrm{Kn}\rangle^{-1}$. The initial state distribution is indicated by the label $\langle \mathrm{Kn}\rangle^{-1} = 0$.

C.6 Event-plane angle distributions with $n = 4$

The distribution of symmetry planes for ε_2 and ε_4 at impact parameter $b = 9$ fm (Fig. C.6) shows a broad peak around zero. For such a large impact parameter it is expected that the symmetry planes of the two eccentricities are aligned for more events in contrast to central collisions, where the two angles are entirely uncorrelated. Induced by this correlation there is also a different behavior for the distributions

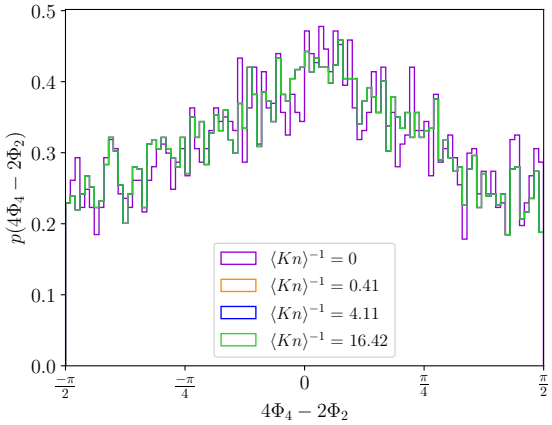

Figure C.6: Probability distributions $p(4\Phi_4 - 2\Phi_2)$ for events at $b = 9$ fm for different $\langle \mathrm{Kn} \rangle^{-1}$. The initial state distribution is indicated by the label $\langle \mathrm{Kn} \rangle^{-1} = 0$.

$p(4(\Psi_4 - \Phi_4))$ and $p(4\Psi_4 - 2\Phi_2)$ (Fig. C.7), which are now both most peaked in the case of the smallest considered number of rescatterings. This correlation is then

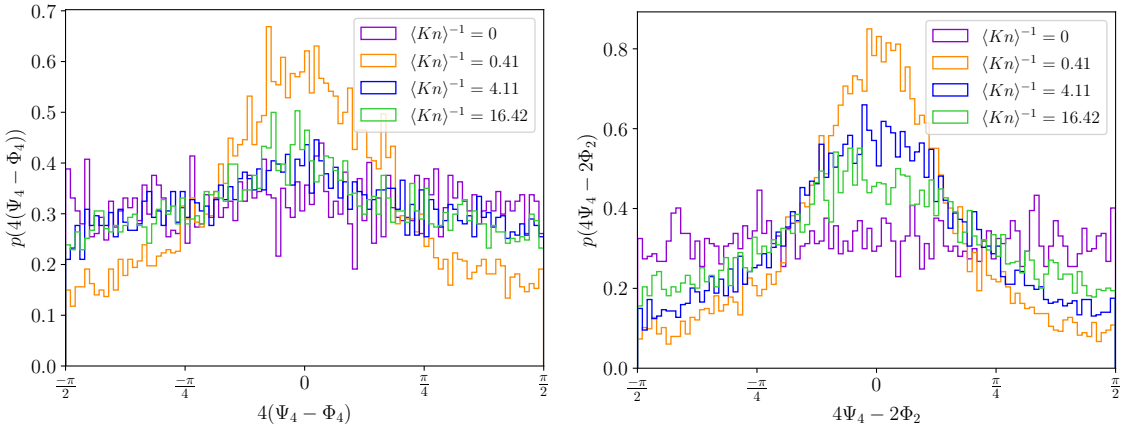

Figure C.7: Probability distributions $p(4(\Psi_4 - \Phi_4))$ (left) and $p(4\Psi_4 - 2\Phi_2)$ (right) for events at $b = 9$ fm for different $\langle \mathrm{Kn} \rangle^{-1}$. The initial state distribution is indicated by the label $\langle \mathrm{Kn} \rangle^{-1} = 0$.

washed out when the number of rescatterings increases, while for the two larger values of $\langle \mathrm{Kn} \rangle^{-1}$ the distributions are not very different from each other.

Appendix D

Early time behavior of spatial and momentum anisotropies in kinetic theory across different Knudsen numbers

We present the analytical calculation of the energy-weighted mean square radius in our simplified setup from Ch. 5 in Sec. D.1. Then we will discuss the early time evolution of the numerator and denominator of $\varepsilon_3^{\mathbf{x}}$ in Sec. D.2 followed by a discussion of $\varepsilon_2^{\mathbf{p}}$ at large times (Sec. D.3) complementing the results presented in Sec. 5.6.

D.1 Energy-weighted mean square radius

In this section we want to follow the derivation of the fact that the mean square radius in a two-dimensional system with massless particles and with a collision kernel in the Boltzmann equation that obeys energy and momentum conservation is independent of collisions in the system.

Energy and momentum conservation of the collision kernel can be formulated as

$$\int p^\mu \mathcal{C}[f] \, \frac{\mathrm{d}^2\mathbf{p}}{E} = 0, \tag{D.1}$$

at any position $\mathbf{x}$ and for all Lorentz indices $\mu \in \{0, 1, 2\}$, where $p^0 \equiv E$ is the energy. Then we can differentiate the expression with respect to time and interchange the

integral with the derivative. We obtain

$$\int p^\mu \partial_t^i \mathcal{C}[f] \, \frac{\mathrm{d}^2\mathbf{p}}{E} = 0 \tag{D.2}$$

for any $j \geq 0$, which is again valid for all points in position space and true for all times, in particular at the initial time.

The Taylor expansion of the distribution function (5.3) multiplied by the energy $E = |\mathbf{p}|$ leads to terms due to collisions at order t^k with $k \geq 1$ of the form

$$\left(-\frac{\mathbf{p}\cdot\nabla_x}{E}\right)^j \partial_t^{k-1-j}\mathcal{C}[f]|_0. \tag{D.3}$$

Calculating the mean square radius with energy weight, which is equal to the denominator of Eq. (2.25) in the case $n = 2$ there are integrals at order t^k of the form

$$\int r^2 \left(-\frac{\mathbf{p}\cdot\nabla_x}{E}\right)^j \partial_t^{k-1-j}\mathcal{C}[f]|_0 \, \mathrm{d}^2\mathbf{x}\mathrm{d}^2\mathbf{p} \tag{D.4}$$

with $k \geq 1$ and $0 \leq l \leq k-1$. One property of f and $\mathcal{C}[f]$ which is used extensively is that they vanish at spatial infinity.

Starting with the case $l = 0$, which is the case for the linear term in t of Eq. (5.3), we obtain an integral over $\mathbf{x}$ of r^2 times an integral of type (D.3) with $j = k-1$ and $\mu = 0$. Due to the energy conservation these terms vanish.

For $l = 1$ integrating over $\mathbf{x}$ in Eq. (D.4) by part once erases the gradient and replaces for instance $x^2 p_x \partial_x$ by $-2xp_x$ in the integrand, while the other term with the integrated part uses $\partial_t^{k-2}\mathcal{C}[f]|_0$ at infinity equals zero. Then the remaining integral is

$$-2\int \frac{xp_x + yp_y}{E}\partial_t^{k-2}\mathcal{C}[f]|_0 \, \mathrm{d}^2\mathbf{x}\mathrm{d}^2\mathbf{p}. \tag{D.5}$$

Looking only at the momentum space integral, it is of the form (D.3) with $\mu = 1$ or 2 and thus vanishes due to momentum conservation.

In the case $l = 2$ one has to integrate by part over $\mathbf{x}$ twice to replace the integrand of Eq. (D.4) $r^2 (\mathbf{p}\cdot\nabla)^2 \partial_t^{k-3}\mathcal{C}[f]|_0$ by $2\left(p_x^2 + p_y^2\right)\partial_t^{k-3}\mathcal{C}[f]|_0$. This gives us

$$2\int \partial_t^{k-3}\mathcal{C}[f]|_0 \, \mathrm{d}^2\mathbf{x}\mathrm{d}^2\mathbf{p}. \tag{D.6}$$

This integral vanishes again due to the energy conservation in Eq. (D.3) with $\mu = 0$.

Considering cases with $l \geq 3$ the transformation of Eq. (D.4) by integrating over $\mathbf{x}$ by parts twice is again possible and the integrated terms still vanish at spatial infinity. This integration by parts replaces terms which look like $r^2(\nabla_x)^l$ by $2(\nabla_x)^{l-2}$ in the integrand. As $l - 2 \geq 1$, there is still an integrand with a spatial derivative which vanishes at $|\mathbf{x}| \to \infty$, such that the further spatial integration gives a zero.

In summary we find that the integrals of the form (D.4) vanish for our setup, which is not the case for massive particles or for $p_z \neq 0$, i.e., three spatial dimensions.

D.2 Early time evolution of the numerator and denominator of the triangularity $\varepsilon_3^{\mathbf{x}}$

Here we want to look at the behavior of the numerator and denominator of the spatial eccentricity $\varepsilon_3^{\mathbf{x}}$, namely the particle-number or energy weighted averages of $-r^3\cos(3\theta)$ and r^3 when rescatterings during the time evolution are considered. The departure from the free streaming values for the two quantities scaled by the initial state values are shown in Figs. D.1 and D.2 at Kn ≈ 25 (left panels) and Kn ≈ 5 (right panels).

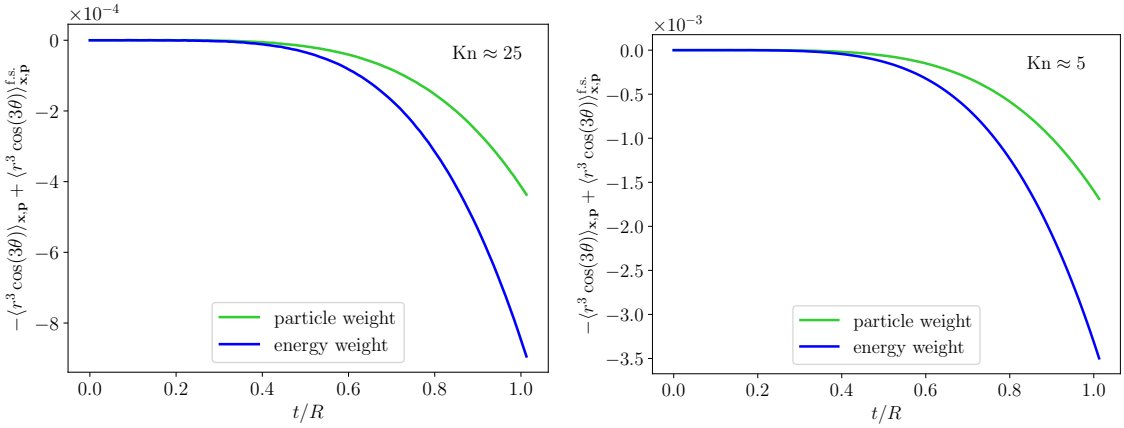

Figure D.1: Time evolution of the departure of $-\langle r^3\cos(3\theta)\rangle_{\mathbf{x},\mathbf{p}}$ with particle-number (green) or energy (blue) weighting from its free streaming value, for simulations with Kn ≈ 25 (left panel) or Kn ≈ 5 (right panel).

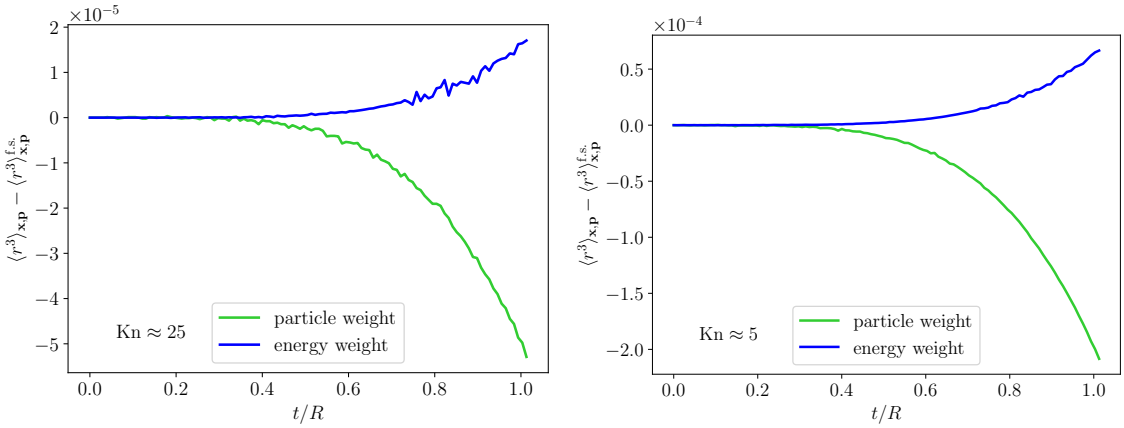

Figure D.2: Time evolution of the departure of $\langle r^3\rangle_{\mathbf{x},\mathbf{p}}$ with particle-number (green) or energy (blue) weighting from its free streaming behavior, for simulations with Kn ≈ 25 (left panel) or Kn ≈ 5 (right panel).

We find that the values at Kn ≈ 5 are approximately 5 times larger than the ones at Kn ≈ 25, such that we can conclude that the relative deviations from the collisionless system scale roughly linear with the number of rescatterings. This coincides with our findings for the second harmonic in Sec. 5.5.

When a fit with the power laws in Eqs. (5.14) and (5.16) is performed we obtain rather inconclusive results in the range 4-5.7, as the signal is small and evolves very slow in time. Thus, we do not know how much we can trust the fits here, as the early-time fits may be dominated by numerical noise, which is also visible in both panels in Fig. D.2.

Comparing with the second harmonic results in Sec. 5.5 we can see that the energy-weighted mean cubed radius deviates from its free streaming behavior and we find indeed in the analytical proof to show that $\langle r^2 \rangle_{\mathbf{x},\mathbf{p}}$ with energy weight is zero, that the arguments do not hold for $\langle r^3 \rangle_{\mathbf{x},\mathbf{p}}$. In the proof in Appendix D.1 we have used twice a twofold integration by parts over position space to eliminate r^2 and two spatial derivatives in the integrand in the cases $l = 2$ and $l \geq 3$. Replacing r^2 by r^3 in the proof leads to the fact that the reasoning used to find that the $l = 2$ part vanishes does no longer work. An interesting finding is also that the rate of growth of $\langle r^3 \rangle_{\mathbf{x},\mathbf{p}}$ with energy weight is increased and the $\langle r^3 \rangle_{\mathbf{x},\mathbf{p}}$ with particle-number weight is decreased by rescatterings. The interpretation here is that the rescatterings redistribute the energy in the system from the inner regions with the largest energy density in the initial state to the outer region, which gives a quite intuitive picture.

D.3 Elliptic momentum anisotropy $\varepsilon_2^{\mathbf{p}}$ at large times

Going beyond the scope of Ch. 5, which is the early-time behavior, a few results on the late time behavior of $\varepsilon_2^{\mathbf{p}}$ are presented here. Figure D.3 compares the long time evolution of $\varepsilon_2^{\mathbf{p}}$, which coincides in our setup with v_2^E, to the particle-number weighted v_2. We show the time evolution for the full $2 \to 2$ collision kernel (full

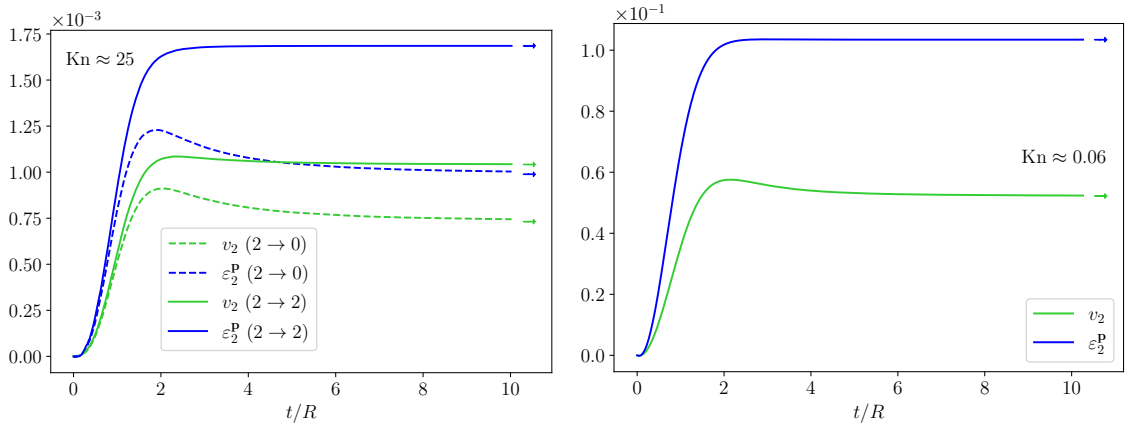

Figure D.3: Evolution of the anisotropic flow coefficient v_2 (green) and the eccentricity $\varepsilon_2^{\mathbf{p}}$ in momentum space (blue) for the $2 \to 2$ and $2 \to 0$ collision kernel in the few collisions limit (top panel) and in the hydrodynamic limit (bottom panel). The arrows indicate the corresponding values at $t/R \approx 30$.

lines) and for the $2 \to 0$ collision kernel (dashed lines) in the few rescatterings regime (left panel: Kn ≈ 25) and in the fluid-dynamical limit (right panel: Kn ≈ 0.06). In the fluid-dynamical limit only the $2 \to 2$ collision kernel gives meaningful results,

thus there are no $2 \to 0$ results shown. For all the curves the initial phase space distribution had an eccentricity of $\varepsilon_2^{\mathbf{x}} \simeq 0.15$.

Comparing $\varepsilon_2^{\mathbf{p}}(t)$ and $v_2(t)$ we find that they have a quite similar behavior: there is a rise until $t/R \approx 2$ and then there is a saturation of the signal or a small decrease (in the $2 \to 2$ scenario). For $v_2(t)$ this result nicely agrees with other results using the same transport algorithm but a different initial profile [83]. The decrease in the $2 \to 0$ scenario, which is about 20% more pronounced, is in greater detail discussed in Ref. [107] (Ch. 6).

Quantitatively the $\varepsilon_2^{\mathbf{p}}$ values are larger than the v_2 values for both collision kernels. Going into the fluid-dynamical regime we find that $\varepsilon_2^{\mathbf{p}} \approx 2v_2$ at late times, which was also found in [82] for a two-dimensional expanding system. Overall the v_2 and the energy-weighted flow $v_2^E = \varepsilon_2^{\mathbf{p}}$ have parallel behaviors in both collision kernel scenarios, which is in contrast to the triangular counterparts v_3 and v_3^E discussed in Secs. 5.4 and 5.6. These behave differently in the $2 \to 0$ scenario.

Appendix E

Different origins of even and odd anisotropic flow harmonics at large Knudsen numbers

We present the proof that the odd flow harmonics vanish identically in the "loss term" scenario (Ch. 6) in Sec. E.1. Afterwards we will present the results for a larger number or rescatterings (Sec. E.2) and we compute the flow harmonics for an alternative distribution function to crosscheck our findings (Sec. E.3).

E.1 Odd flow harmonics in the "loss term" scenario

In this section we want to proof that the odd flow harmonics — v_3, v_5, ... — vanish at all times if only the leading order in the cross section and the loss term in the collision kernel of the Boltzmann equation are considered.

The computation of the anisotropic flow includes the integral over the transverse plane

$$\mathcal{I} \equiv \int f^{(0)}(\mathbf{x} - \mathbf{v}t, \mathbf{p})\, f^{(0)}(\mathbf{x} - \mathbf{v}_1 t, \mathbf{p}_1)\, \mathrm{d}^2\mathbf{x}, \tag{E.1}$$

with the free-streaming distribution function substituted using Eq. (6.5). Changing variables to $\boldsymbol{\xi} \equiv \frac{1}{2}(\mathbf{v} + \mathbf{v}_1)$ directly yields

$$\mathcal{I} = \int f^{(0)}(\mathbf{x} - \boldsymbol{\xi}, \mathbf{p})\, f^{(0)}(\mathbf{x} + \boldsymbol{\xi}, \mathbf{p}_1)\, \mathrm{d}^2\mathbf{x}. \tag{E.2}$$

When assuming that the initial-state phase space distribution factorizes as in Eq. (6.8) into a spatial and a momentum part then only the spatial parts are important for

the $\mathbf{x}$ integration, such that $\mathcal{I}$ contains an integral of the form

$$\mathcal{I}' = \int F(\mathbf{x} - \boldsymbol{\xi}) F(\mathbf{x} + \boldsymbol{\xi}) \, \mathrm{d}^2\mathbf{x}. \tag{E.3}$$

By integration over the whole position space the odd components of the integrand would vanish, such that the integrand can be replaced by the even part:

$$\mathcal{I}' = \frac{1}{2} \int \Big[F(\mathbf{x}-\boldsymbol{\xi}) F(\mathbf{x}+\boldsymbol{\xi}) + F(-\mathbf{x}-\boldsymbol{\xi}) F(-\mathbf{x}+\boldsymbol{\xi}) \Big] \mathrm{d}^2\mathbf{x}. \tag{E.4}$$

Using the even and odd parts of the function F

$$F(\mathbf{x}) = F_+(\mathbf{x}) + F_-(\mathbf{x}) \text{ with } F_\pm(-\mathbf{x}) = \pm F_\pm(\mathbf{x}), \tag{E.5}$$

this can be rewritten. The isotropic part and the even harmonics are encoded in F_+, while the odd harmonics are described by F_-. Now we replace F in Eq. (E.4) by $F_+ + F_-$ and we obtain eight terms, where four terms cancel pairwise and we obtain

$$\mathcal{I}' = \int \Big[F_+(\mathbf{x} - \boldsymbol{\xi}) F_+(\mathbf{x} + \boldsymbol{\xi}) + F_-(\mathbf{x} - \boldsymbol{\xi}) F_-(\mathbf{x} + \boldsymbol{\xi}) \Big] \mathrm{d}^2\mathbf{x}. \tag{E.6}$$

The point where the factorization into a position and momentum part of the distribution function is important is exactly the last step from Eq (E.4) to Eq. (E.6).

It has been found before, e.g., in Ref. [102] within kinetic theory, that a system without initial anisotropic flow of a given harmonic v_n can build up a flow signal by linear response only if there is the n-th harmonic present in the geometry, i.e., $v_n \propto \varepsilon_n$. Or to quadratic order only if the spatial harmonics combine appropriately, i.e. $v_n \propto \varepsilon_k \varepsilon_{n-k}$.[1] The most general form is $v_n \propto \varepsilon_{k_1} \cdots \varepsilon_{k_m}$ with $k_1 + \cdots + k_m = n$. The spatial modulations of even (including the isotropic part) resp. odd harmonics are encoded in F_+ resp. F_-, we find that the combinations F_+F_+ or F_-F_- in Eq. (E.6) can give contributions for v_n caused by ε_n or $\varepsilon_k\varepsilon_{n-k}$ only for even values of n. This means that the integral $\mathcal{I}'$ is independent of the azimuthal angles φ_p and φ_1 of the momenta (which are hidden in $\boldsymbol{\xi}$) such that after multiplying with the Møller velocity and $\cos(n\varphi_\mathrm{p})$ and integrating over the angles no flow signal can arise for odd n.

A last note which should be made is that the proof does not include quantum effects in the collision kernel, but it makes no assumption about the particle mass or the dimensionality of the system under consideration.

E.2 Results for $N_{\text{resc.}} \approx 0.35$

This appendix is supposed to show what happens if the number of rescatterings in the system is no longer small, i.e., $N_{\text{resc.}} \approx 0.35$ such that in the $2 \to 0$ scenario about 70% of the particles disappear during the evolution of the system. Obviously the assumption of the analytical scenario that the phase-space distribution deviates not significantly from the free-streaming distribution with the same initial condition is not fulfilled. We show Results for v_2 (Fig. E.1) and v_4 (Fig. E.2). The two figures

[1] This case is not possible within the analytical approach described in Sec. 6.1.

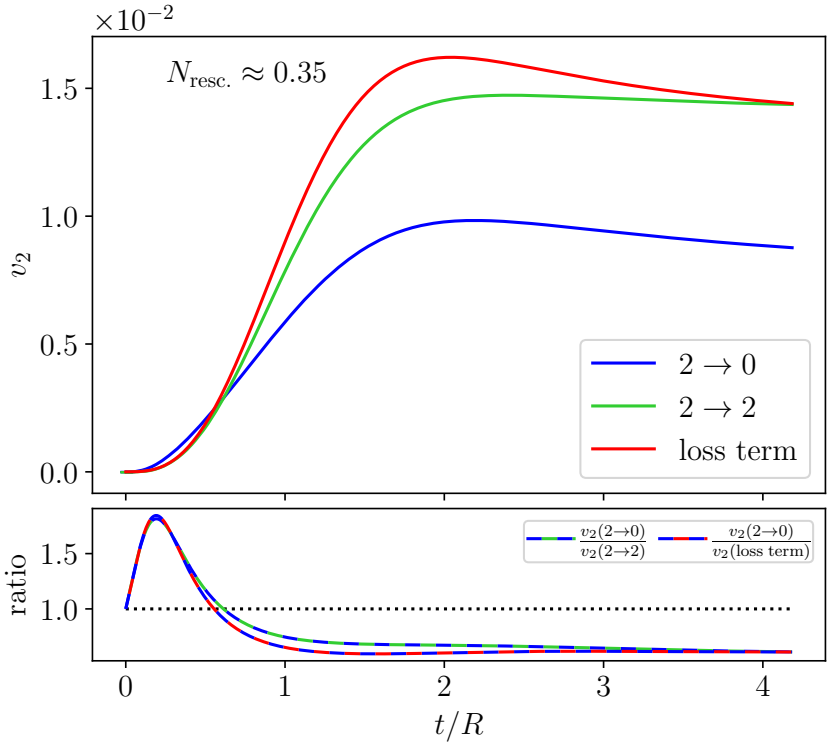

Figure E.1: Time dependence of elliptic flow v_2 in systems with initially $\varepsilon_2 = 0.15$ and on average $N_{\text{resc.}} \approx 0.35$ rescatterings per particle. The green curves are for systems with elastic binary scatterings, the blue lines for the $2 \to 0$ scenario and the red ones show the analytical result (6.12).

show the v_n signal resulting from an initial ε_n with $n = 2$ (Fig. E.1) or $n = 4$ (Fig. E.2). They show similar results, namely the results of the $2 \to 2$ collision kernel (green) and the $2 \to 0$ collision kernel (blue) show significant differences up to $\approx 40\%$ for v_2, while for v_4 even the sign is different. Results from the analytical calculation are quite close to the $2 \to 2$ simulation curves, especially for the end points of the curves. However, this should not be over-interpreted as it might be a coincidence. We have already discussed in Sec. 6.5 that for v_4 at larger values of $N_{\text{resc.}}$ there is no agreement any more, as the $2 \to 2$ results have positive values.

The right panel of Fig. E.2 shows the nonlinear response of v_4 to ε_2^2. Without trying to over-interpret the results we can see a good agreement between all three scenarios.

E.3 Alternative distribution function

To make sure that the results are not just caused by the specific form of the distribution function (6.9), we have computed the anisotropic flow signals in the few-rescatterings regime $N_{\text{resc.}} \approx 0.02$ using a different distribution

$$\tilde{F}(r,\theta) = \frac{N\sqrt{1-\delta_j^2}}{2\pi R^2} \exp\left(-\frac{r^2[1+\delta_j\cos(j\theta)]}{2R^2}\right). \tag{E.7}$$

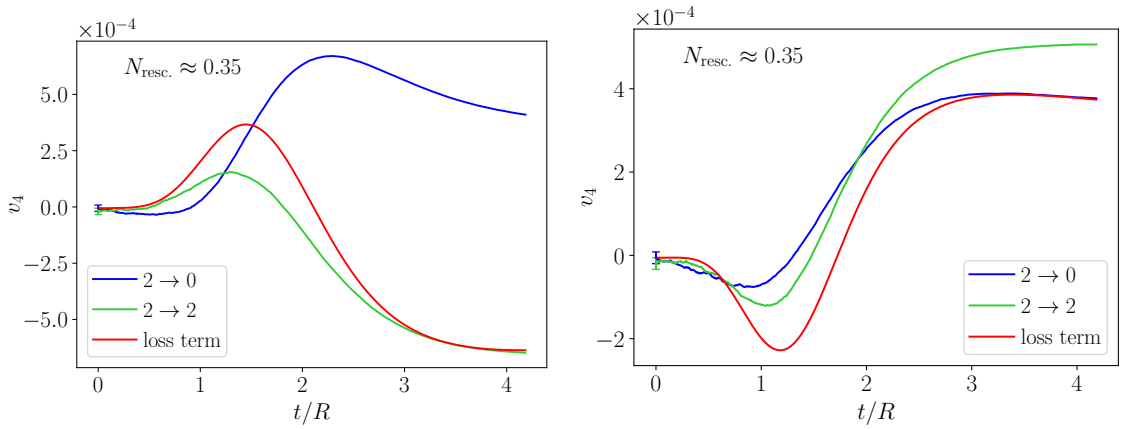

Figure E.2: Time-dependence of quadrangular flow v_4 in systems with $N_{\text{resc.}} \approx 0.35$ rescatterings per particle on average. Left: system with an initial $\varepsilon_4 = 0.15$ and $\varepsilon_2 = 0$; right: system with an initial state $\varepsilon_2 = 0.15$ and $\varepsilon_4 = 0$. The green curves are for systems with elastic binary scatterings, the blue lines for the $2 \to 0$ scenario and the red ones show the analytical results (6.14) (left) or Eq. (6.15) (right).

This distribution was used before for a simulation in the fluid-dynamical regime in Ref. [83]. In contrast to the distribution (6.9) this distribution has several ε_n contributions for a single δ_j, where n is a multiple of j. The advantage of the distribution (E.7) is that it is positive definite for all values of δ_j.

However, the drawback from the analytical point of view is that not all integrals can be computed analytically here, so that we implemented the Vegas Monte Carlo (MC) integration method [148].

In Fig. E.3 we show the flow coefficients $v_n(t)$ for $n \in \{2, 3, 4, 5\}$ computed with the MC integration method. We find that the odd flow harmonics are again zero

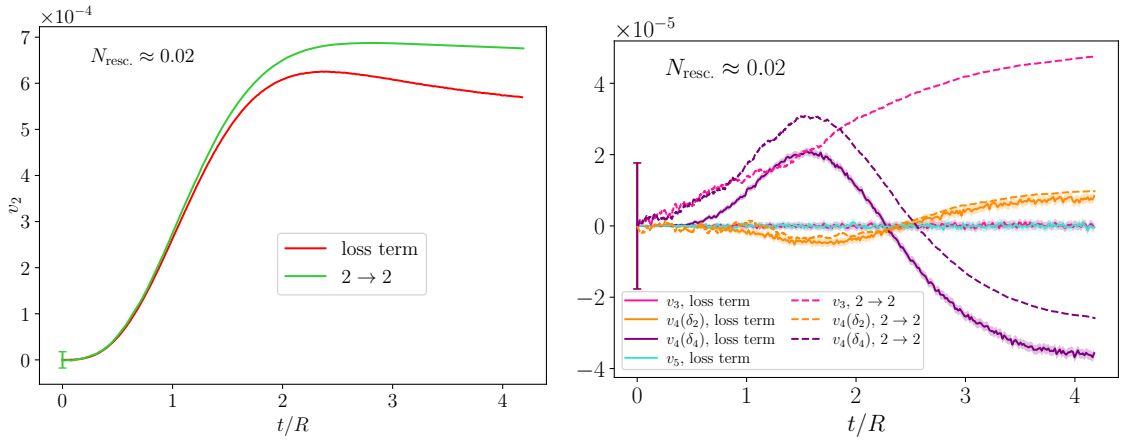

Figure E.3: Time dependence of anisotropic flow harmonics for the initial geometric profile (E.7) in systems with $N_{\text{resc.}} \approx 0.02$. Left: v_2 for $\delta_2 = 0.15$ (green: numerical simulations, red: semi-analytical approach). Right: v_3 for $\delta_3 = 0.15$ (magenta), v_4 (orange: for $\delta_2 = 0.15$, purple: for $\delta_4 = 0.15$), and v_5 (cyan, for $\delta_5 = 0.15$) in numerical simulations (dashed lines) or computed with Vegas (full lines; the color bands show the 3σ error of the MC integration).

within error bars, which matches the results from Appendix E.1. The transport

simulations give a non-vanishing result for $v_3(t)$, while the $v_2(t)$ and $v_4(t)$ resulting from an initial δ_2 signals show a nice agreement between the analytical result and the simulation. If there is an initial δ_4 the $v_4(t)$ agreement is less good. This might be caused by the numerical noise at early times, since the curves are almost parallel at later times. All in all we find that the shapes of the $v_2(t)$ and $v_4(t)$ curves are quite similar to the results found with the other distribution function (6.9) in Secs. 6.3 and 6.5.

Appendix F

Statistical analysis of the intial state and final state response in heavy-ion collisions

In this appendix we will present results complementing the ones in Ch. 7. Section F.1 will give us insight into the statistics of the expansion coefficients $\{c_l\}$ and point out that there are non-Gaussianities if the impact parameter is non-vanishing for the large l modes. Then we will present in Sec. F.2 the first 60 eigenvectors at both considered impact parameters and for both initial state models. Sections F.3.1-F.3.2 will present the results of the linear response for the individual modes for the Saturation model. This complements the results for the Glauber model in Sec. 7.2.4 and allows for a comparison of the two initial state models. In Sec. F.4 we will present an analytical calculation of joint probability distributions of observables under the assumption that the response is purely linear and that the $\{c_l\}$ are Gaussian distributed. Finally, Sec. F.5 will give a more detailed explanation of the signs and magnitudes of the covariances.

F.1 Characteristics of the probability distributions of the expansion coefficients

In this appendix we want to discuss the probability distributions $p(c_l)$ of the expansion coefficients $\{c_l\}$ more quantitatively using the first moments — average μ, variance σ^2, skewness γ_1 and excess kurtosis γ_2 — of the distributions. As we have constructed the basis in such a way that the coefficients obey Eqs.(7.2) and (7.3), the coefficients μ resp. σ^2 should be close to 0 resp. 1. Again, we have used the 8192 events at both considered impact parameters and from both initial state models, similar to Sec. 7.1.3.

Figures F.1 and F.2 show the moments for events at vanishing impact parameter. Here we find that the first four moments have the values of a centered Gaussian with

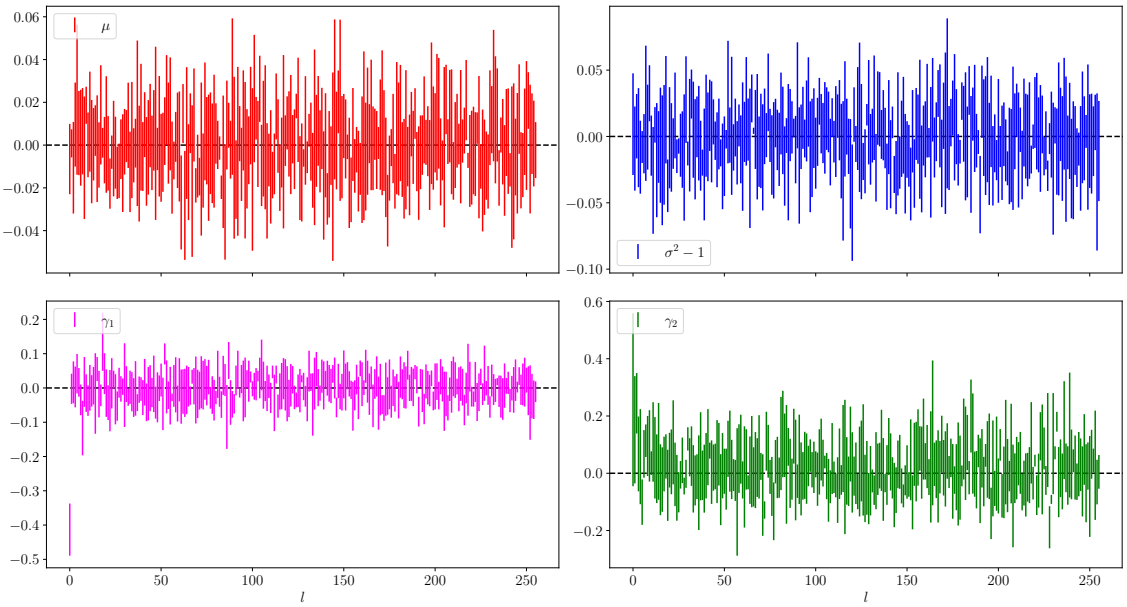

Figure F.1: First four moments (average μ, variance σ^2, skewness γ_1 and excess kurtosis γ_2) of the probability distributions $p(c_l)$ in the Glauber model at $b = 0$ fm.

unit variance ($\gamma_1 = \gamma_2 = 0$) for the majority of the modes. A very obvious exception is the mode $l = 0$ which exhibits a strong negative resp. positive skewness for the Glauber resp. Saturation model. Inspecting the modes with a skewness further reveals that the subsequent modes with a non-zero skewness are $l = 7, 18, 33, \ldots$, which are those with a radial symmetry as well. For these higher modes the effect is less visible. One can understand this non-zero skewness of the radial modes using simple arguments. We will explain this behavior with the help of the Saturation model, for which the mode $l = 0$ is positive in the center of the density distribution (see bottom left plot in Fig. 7.4). If we now consider a random event $\bar{\Psi} + c_0\Psi_0$ with only the zero mode on top of the average state, for the sake of simplicity, there is then a constraint — especially at the position $r = 0$ — on the values of the coefficient c_0 by the positivity of the energy density. Thus, the values of c_0 can not be too negative. On the other hand the values can not be too large and positive to ensure the positivity in regions around $r \approx 0.5R$, which however is the less strict

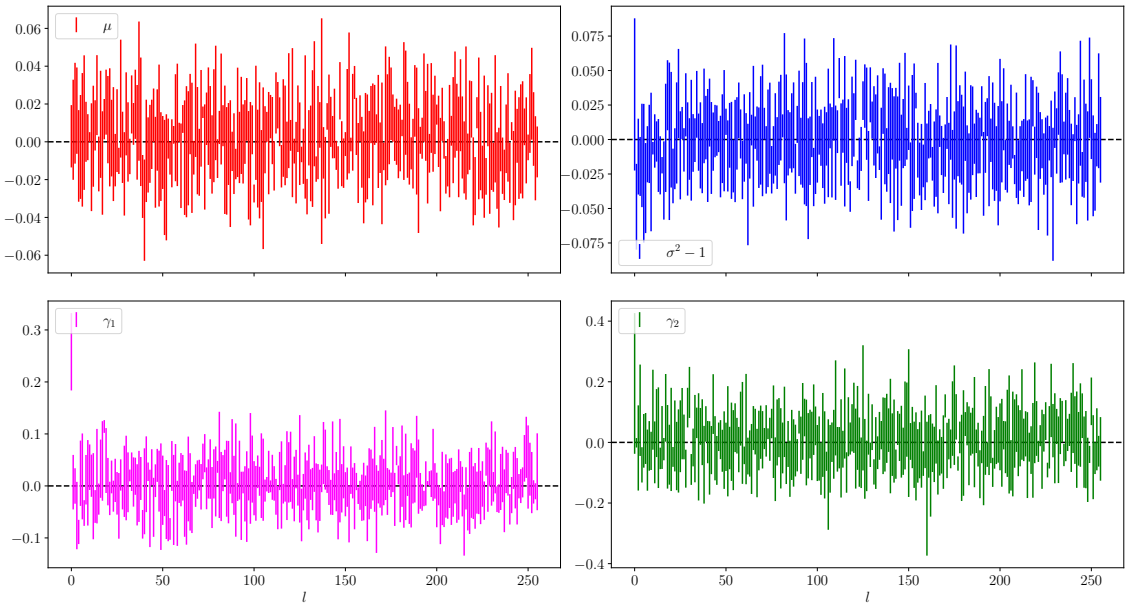

Figure F.2: First four moments (average μ, variance σ^2, skewness γ_1 and excess kurtosis γ_2) of the probability distributions $p(c_l)$ in the Saturation model at $b = 0$ fm.

constraint, in that it allows for larger absolute values $|c_0|$. In general the distribution of c_0 can extend more into the positive direction than into the negative one, i.e., it has a larger tail on the right, thus a positive skewness γ_1.

Turning now to the case of finite impact parameter ($b = 9$ fm), we show the resulting moments in Figs. F.3 and F.4. Both models lead to moments of the c_l

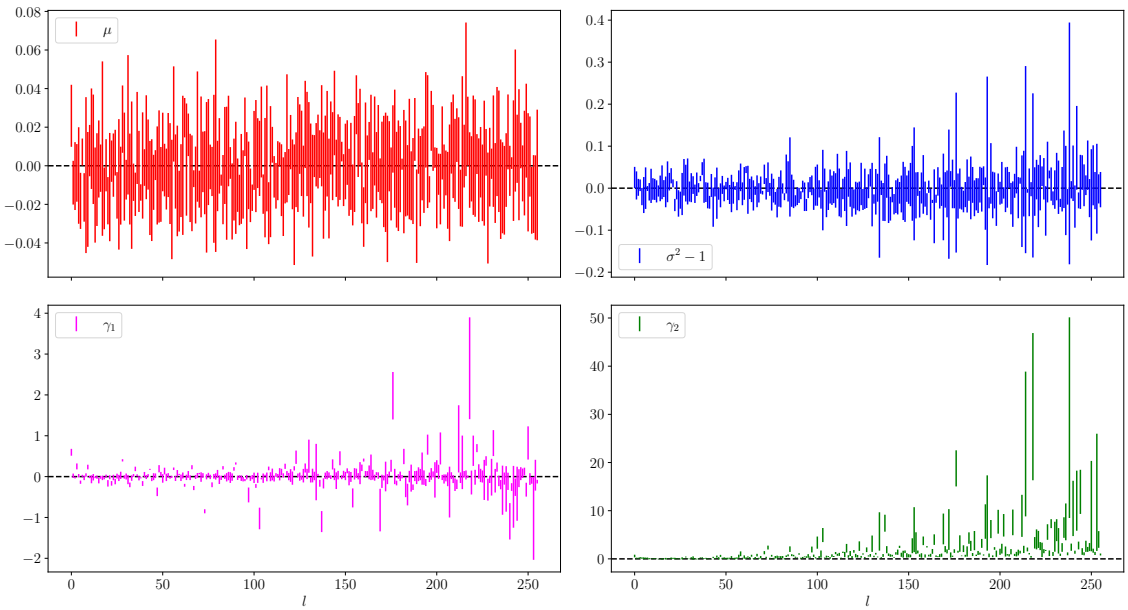

Figure F.3: First four moments (average μ, variance σ^2, skewness γ_1 and excess kurtosis γ_2) of the probability distributions $p(c_l)$ in the Glauber model at $b = 9$ fm.

distributions which deviate more from the Gaussian case than at vanishing impact parameter. The skewness γ_1 of the distributions $p(c_l)$ deviates considerably from

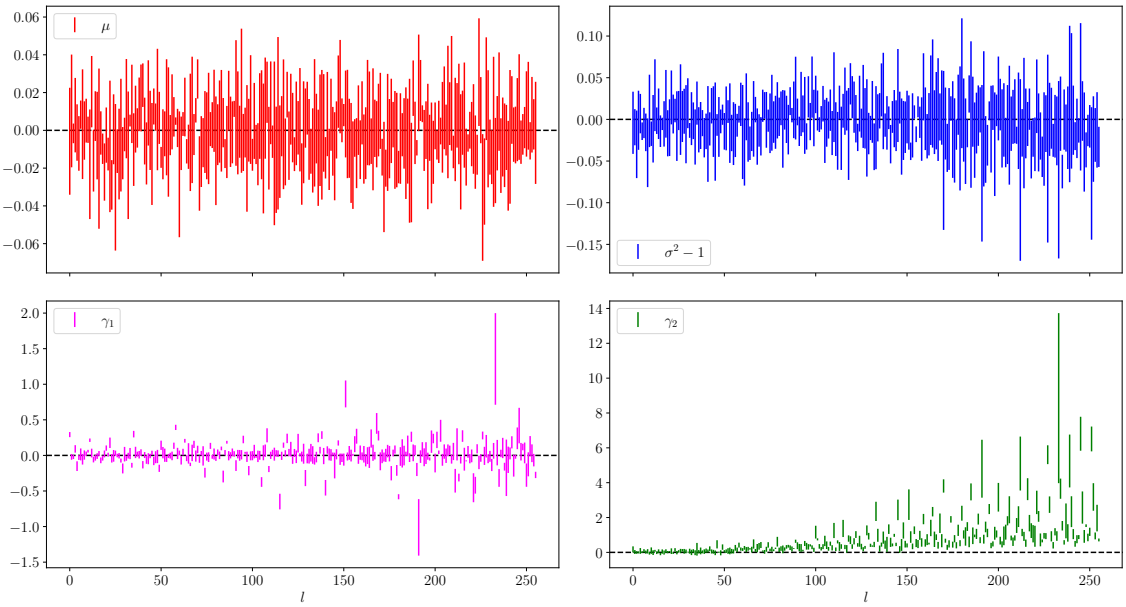

Figure F.4: First four moments (average μ, variance σ^2, skewness γ_1 and excess kurtosis γ_2) of the probability distributions $p(c_l)$ in the Saturation model at $b = 9$ fm.

the Gaussian value for some modes, whereas there is no clear trend. In the case of the excess kurtosis γ_2 there is a clear trend to positive values for increasing l. In summary we find that the broken roataional symmetry at finite impact parameter leads to a small deviation from Gaussian distributed c_l coefficients, which increases for the higher modes.

F.2 Modes for $b = 0, 9$ fm

We show the first 60 orthonormal eigenvectors of the density matrix defined in Eq. (7.9) for the Glauber model (Fig. F.5 at $b = 0$ fm; Fig. F.6 at $b = 9$ fm) and the Saturation model (Fig. F.7 at $b = 0$ fm; Fig. F.8 at $b = 9$ fm). Here the orthonormal eigenvectors and not the $\sqrt{\lambda_l}$-rescaled eigenvectors are shown to make the comparison easier. Otherwise the norm of the Ψ_l decreases with l and thus the higher modes would become too faint.

F.3 Response of observables in the Saturation model

In this appendix we show the linearity check in Sec. F.3.1 and the response of the individual modes in the initial and final state for the Saturation model in Sec. F.3.2. These results complement the ones for the Glauber model in Sec. 7.2.4.

F.3.1 Linearity check

In Fig. F.9 we show similar to Fig. 7.13 the quantity $O^+_{\alpha,l} - \bar{O}_\alpha$ for different values of δ in the Saturation model at $b = 0$ fm (upper panel) and $b = 9$ fm (lower panel).

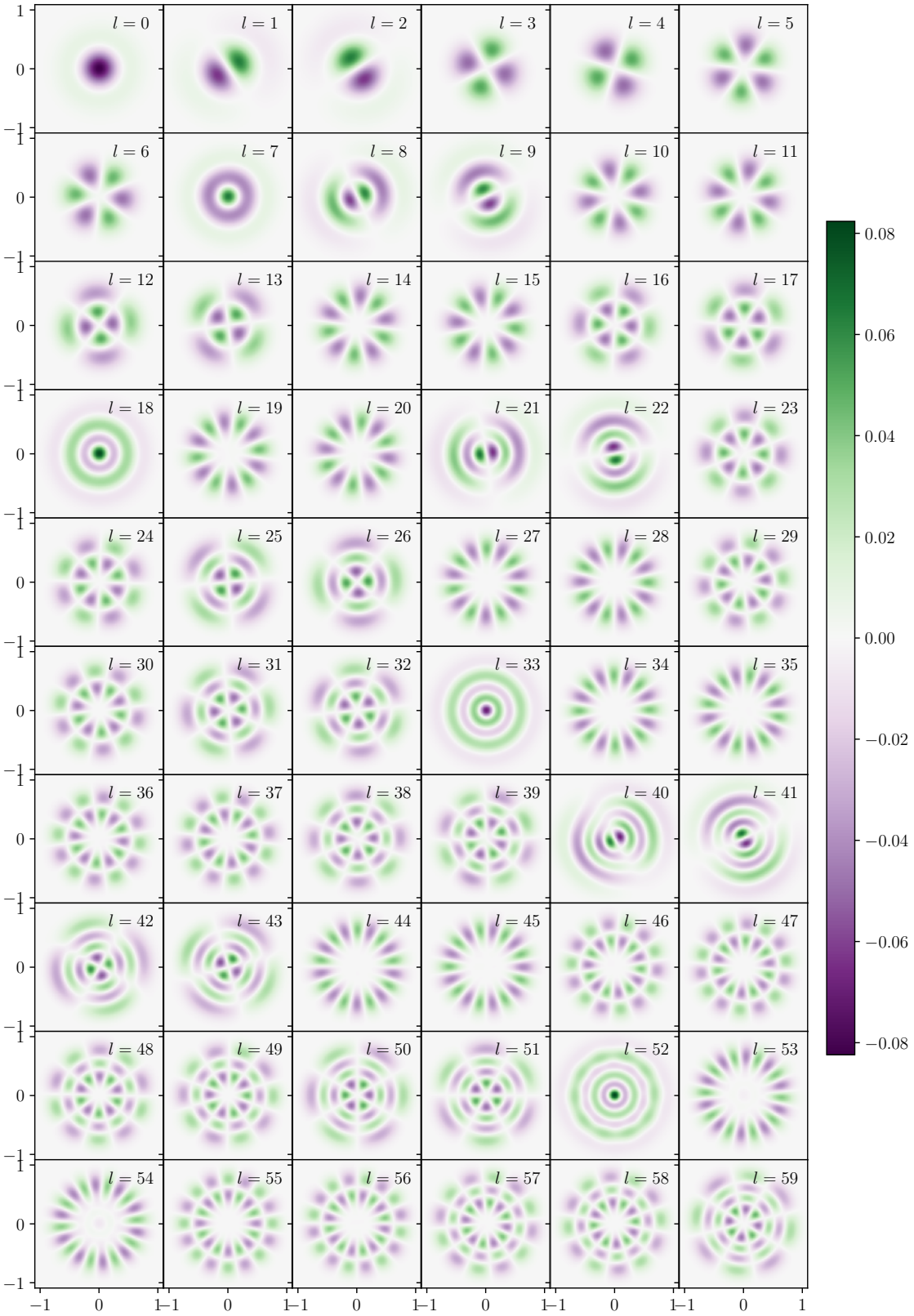

Figure F.5: First 60 orthonormal eigenvectors for the Glauber model at $b = 0$ fm. Both axes are in units of R.

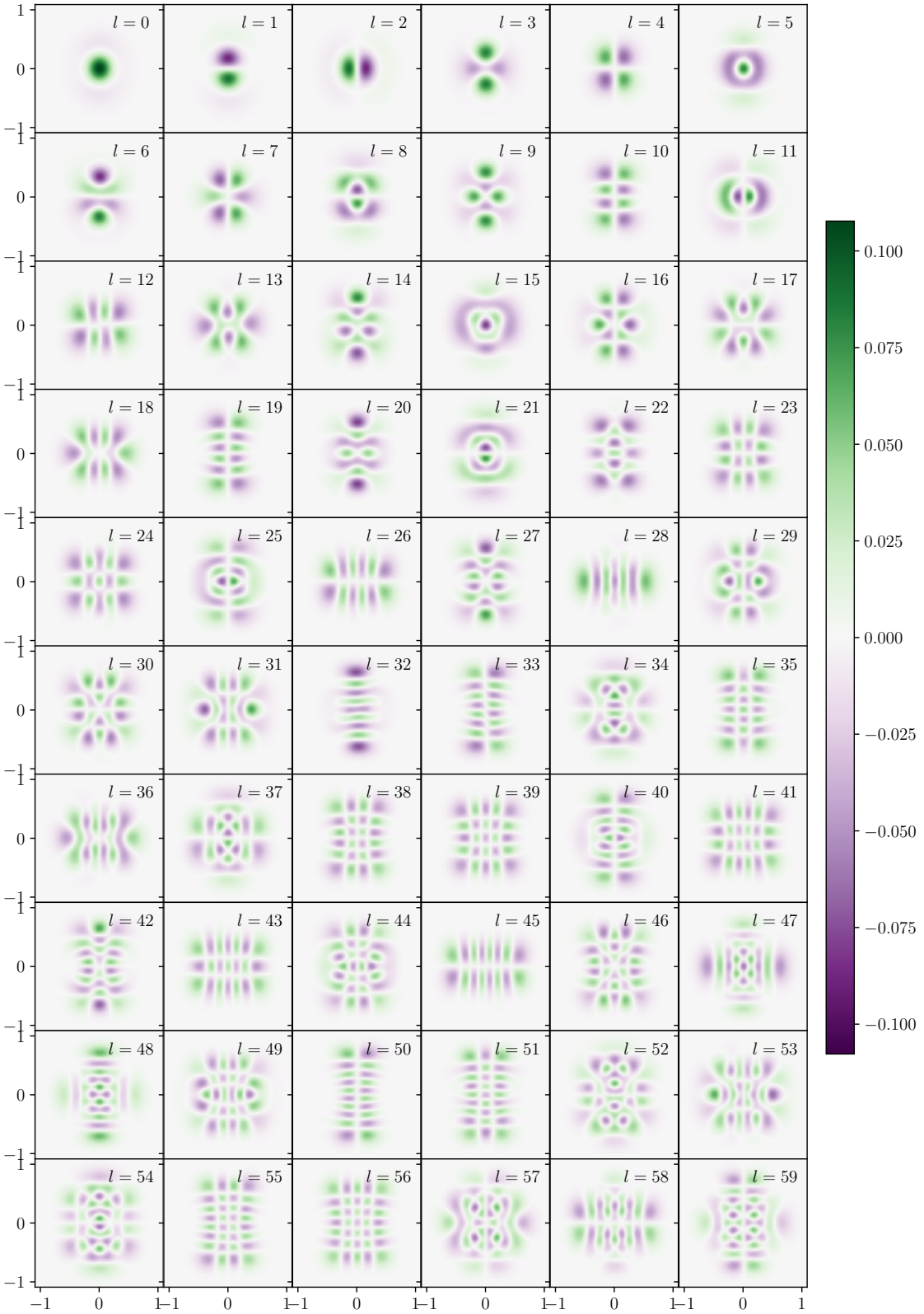

Figure F.6: First 60 orthonormal eigenvectors for the Glauber model at $b = 9$ fm. Both axes are in units of R.

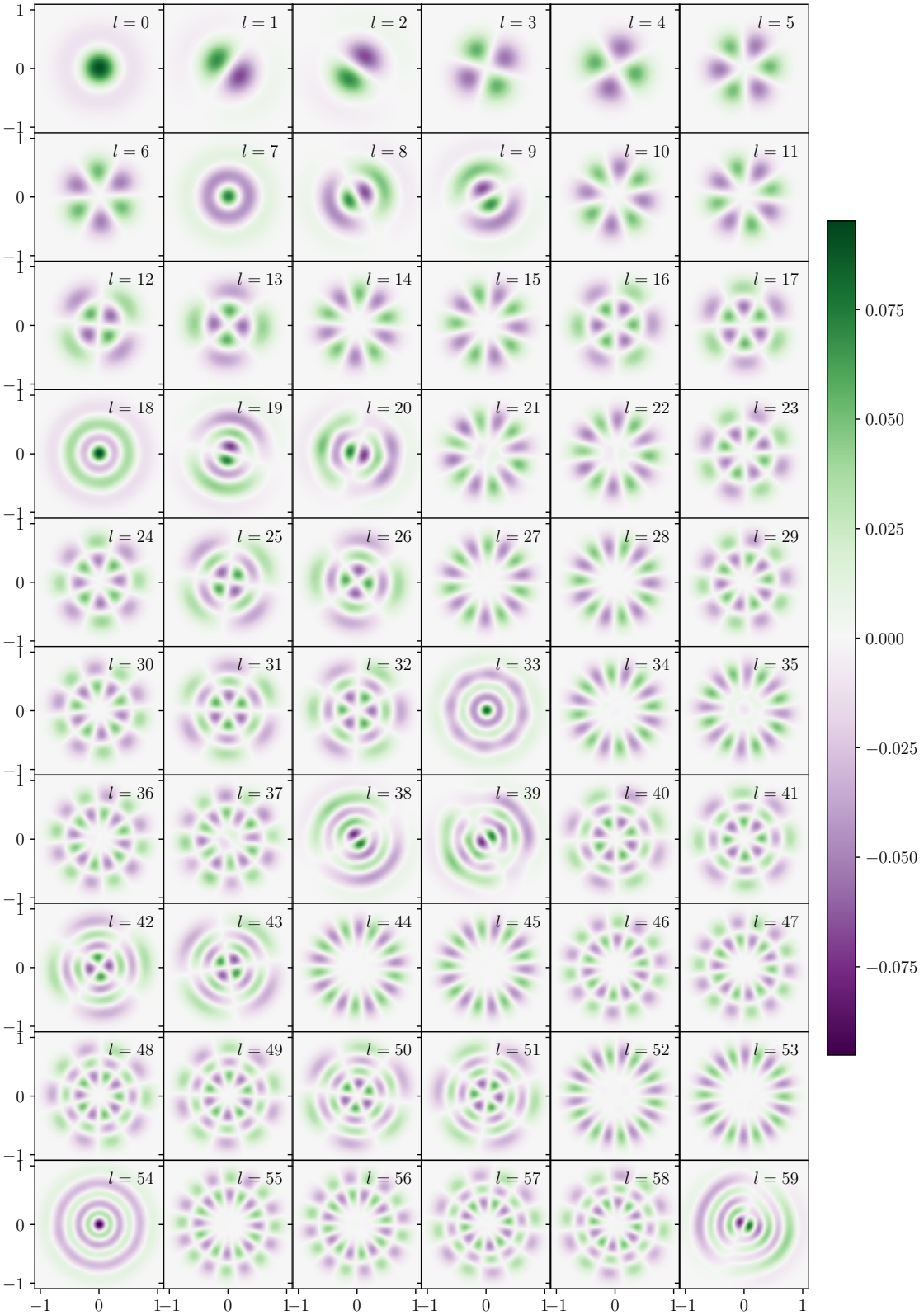

Figure F.7: First 60 orthonormal eigenvectors for the Saturation model at $b = 0$ fm. Both axes are in units of R.

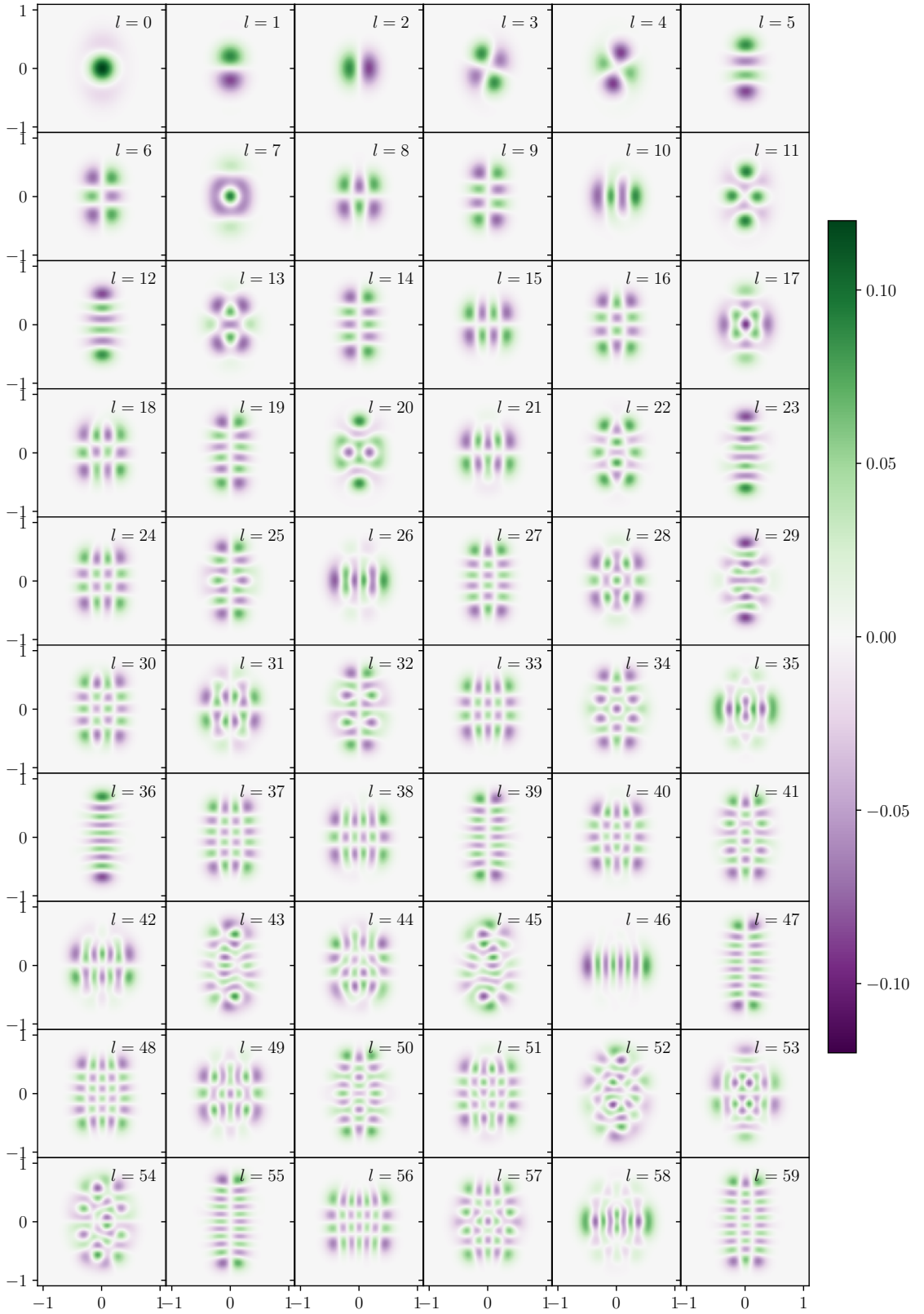

Figure F.8: First 60 orthonormal eigenvectors for the Saturation model at $b = 9$ fm. Both axes are in units of R.

The difference to Fig. 7.13 is that at $b = 9$ fm some different modes were used, as

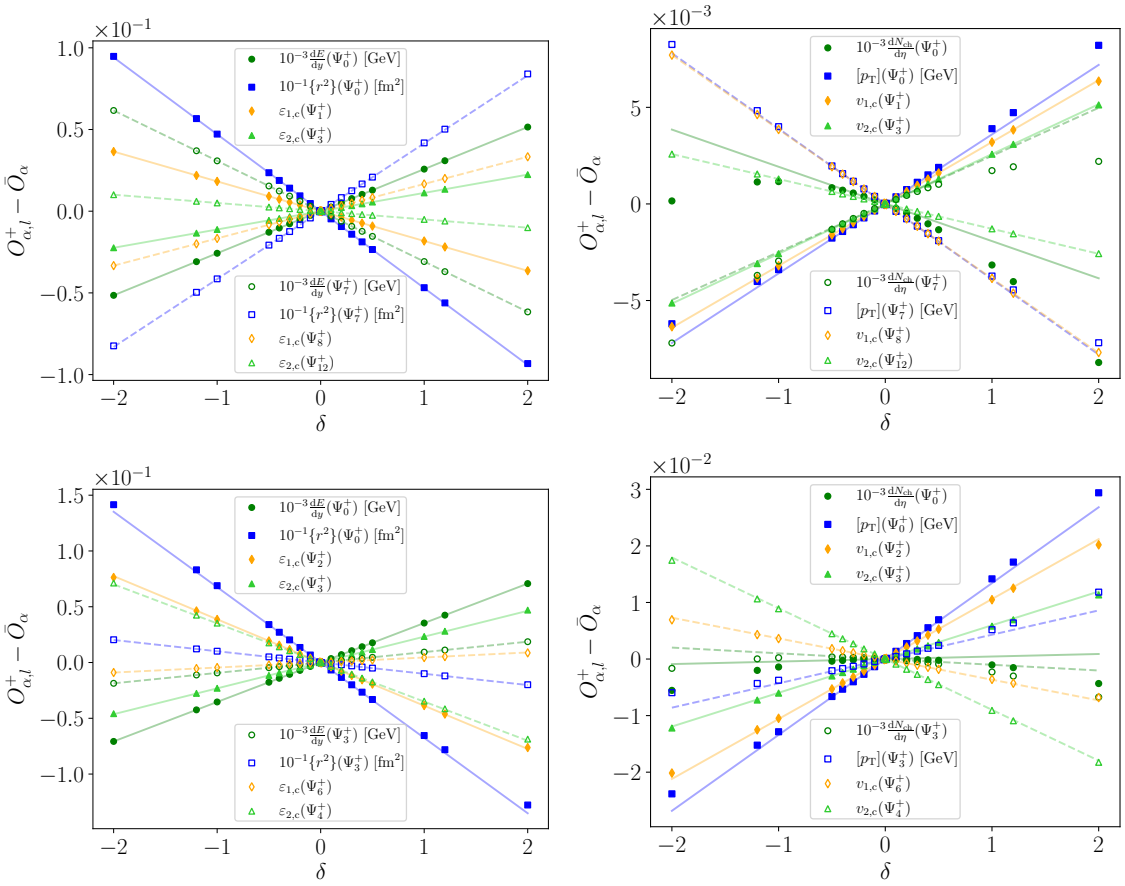

Figure F.9: $O^+_{\alpha,l}$ for exemplary modes ($\bar{O}_\alpha$ subtracted) as a function of δ in the inital state (left) and final state (right). Closed symbols and full lines correspond to first excitation modes, while open symbols and dashed lines correspond to second excitation modes. The Saturation model was used for impact parameters $b = 0$ fm (top) and $b = 9$ fm (bottom).

the order of the modes is different in the two models.

Generally we find the same results as for the Glauber model also for the Saturation model. That is why we will only mention the differences between the two models here. In the initial state we can see already by eye that the observable $\{r^2\}$ is more linear in the Saturation model at $b = 0$ fm compared to the Glauber model. This is also represented in Figs. 7.15 and F.10, where we see that the quadratic response in the Saturation model is even fainter than in the Glauber model.

F.3.2 Linear and quadratic response coefficients

In Figs. F.10-F.11 the linear and quadratic responses of the individual observables to the single mode perturbations are shown for the Saturation model. Qualitatively we observe similar structures comparing the linear and quadratic responses to the ones for the Glauber model.

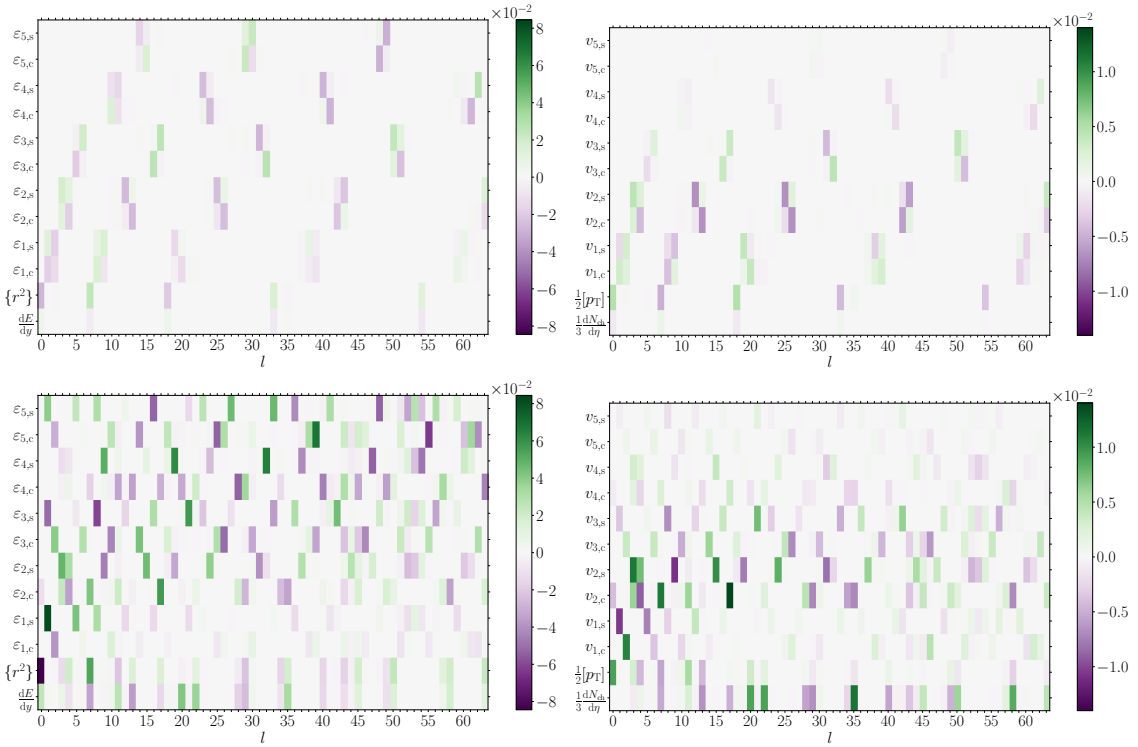

Figure F.10: Linear response coefficients $L_{\alpha,l}$ for the initial state quantities (upper left) and final state observables (upper right) at $b = 0$ fm in the Saturation model. The same plots for $b = 9$ fm are shown below. All dimensionful observables have been divided by $\bar{O}_\alpha$.

F.4 Gaussian statistics in linear response theory[1]

In Sec. 7.1.3 we have seen that the normalized expansion coefficients $\{c_l\}$ follow to a good approximation a Gaussian statistics with unit variance centered around zero. Assuming now that they perfectly follow a Gaussian statistics and that the fluctuations of the observables are linear in the mode fluctuations, one can perform analytical calculations to predict the probability distributions serving as approximation to the true statistical distributions of the corresponding observables. The assumption of linear responses is only valid for some observables, as we have seen in Secs. 7.2.4.1-7.2.4.2. Some observables have constraints which destort their distributions, e.g., they are always positive or they depend on other observables as in the case of the eccentricities $\varepsilon_n = \sqrt{(\varepsilon_{n,\mathrm{c}})^2 + (\varepsilon_{n,\mathrm{s}})^2}$.

We denote by $p(\{c_l\})$ the joint probability distribution of the expansion coefficients. As we have designed the basis in such a way that the modes and therefore also the expansion coefficients are statistically independent, the distribution factorizes as

$$p(\{c_l\}) = \prod_l p_l(c_l). \tag{F.1}$$

Then we introduce the notation $O_\alpha(\{c_l\})$ for the value of an observable O_α given a

[1]The calculations presented in this section were performed by Clemens Werthmann.

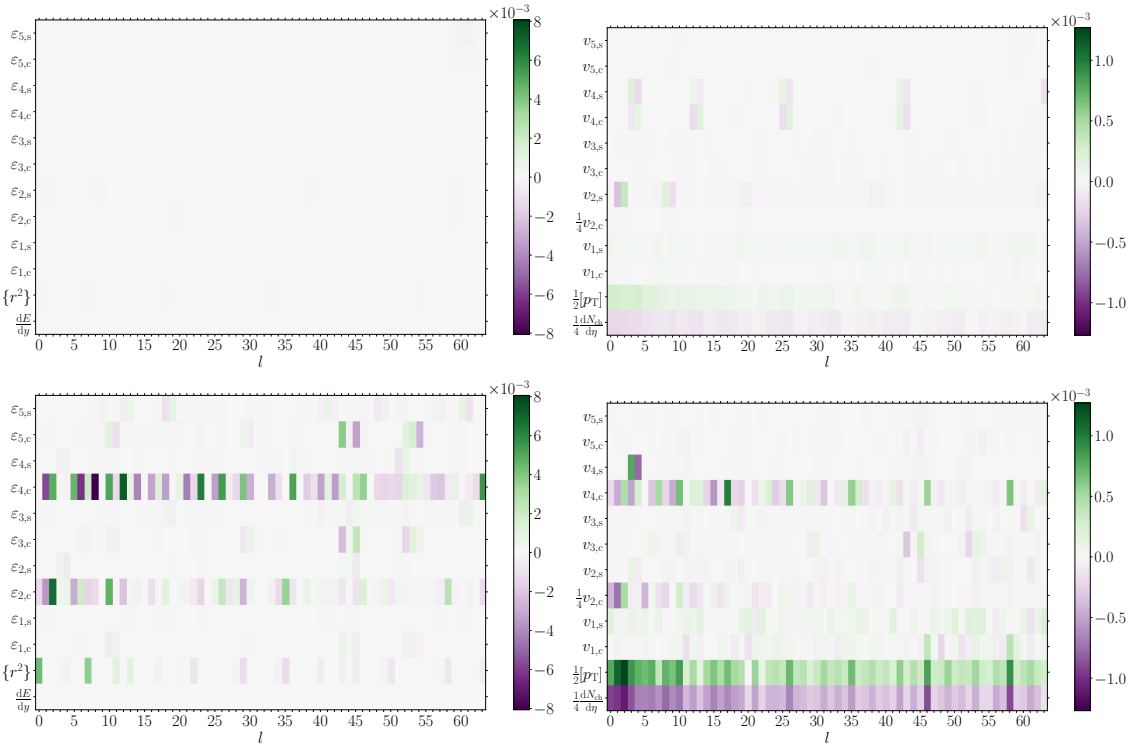

Figure F.11: Quadratic response coefficients $Q_{\alpha,ll}$ for the initial state quantities (upper left) and final state observables (upper right) at $b = 0$ fm in the Saturation model. The same plots for $b = 9$ fm are shown below. All dimensionful observables have been divided by $\bar{O}_\alpha$.

fixed set of coefficients $\{c_l\}$ and we introduce the short notation

$$\int \mathrm{D}c \equiv \prod_l \int_{-\infty}^{\infty} \mathrm{d}c_l. \tag{F.2}$$

Now we can write the probability distribution of O_α as

$$p_\alpha(O_\alpha) = \int \mathrm{D}c \, p(\{c_l\}) \, \delta\left(O_\alpha - O_\alpha(\{c_l\})\right) \tag{F.3}$$

without any approximation. Approximation enter the equation when we assume that the probability distributions $p_l(c_l)$ are Gaussians with unit variance, i.e.,

$$p_l(c_l) \approx \frac{1}{\sqrt{2\pi}} \exp\left(-\frac{c_l^2}{2}\right) \tag{F.4}$$

and when we expand the response in the observable O_α to linear order in c_l:

$$O_\alpha(\{c_l\}) \simeq \bar{O}_\alpha + \sum_l L_{\alpha,l} c_l. \tag{F.5}$$

Note, that in reality we have to cut off the sum at a finite $l_{\max}$, as well as the product in the integral measure Dc. With these assumptions we can now write the linear

response Gaussian approximation of the O_α probability distribution as

$$p_\alpha^{\mathrm{G}}(O_\alpha) = \int \mathrm{D}c\, \frac{\exp\left(-\frac{c_l^2}{2}\right)}{(2\pi)^{l_{\max}/2}}\, \delta\left(O_\alpha - \bar{O}_\alpha - \sum_l^{l_{\max}} L_{\alpha,l} c_l\right). \tag{F.6}$$

Using the identity

$$\delta(x) = \int \frac{\mathrm{d}s}{2\pi}\, \exp\left(\mathrm{i}sx\right) \tag{F.7}$$

we can rewrite the c_l integral in the complex Gaussian form and perform the integration over the expansion coefficients:

$$p_\alpha^{\mathrm{G}}(O_\alpha) = \int \frac{\mathrm{d}s}{2\pi} \int \mathrm{D}c\, \frac{1}{(2\pi)^{l_{\max}/2}} \exp\left[-\frac{c_l^2}{2} - \mathrm{i}s \sum_l^{l_{\max}} L_{\alpha,l} c_l + \mathrm{i}s\left(O_\alpha - \bar{O}_\alpha\right)\right] \tag{F.8}$$

$$= \int \frac{\mathrm{d}s}{2\pi} \exp\left[-\frac{s^2 \sum_l^{l_{\max}} L_{\alpha,l} L_{\alpha,l}}{2} + \mathrm{i}s\left(O_\alpha - \bar{O}_\alpha\right)\right] \tag{F.9}$$

$$= \frac{1}{\sqrt{2\pi C_{\alpha\alpha}}} \exp\left(-\frac{\left(O_\alpha - \bar{O}_\alpha\right)^2}{2C_{\alpha\alpha}}\right). \tag{F.10}$$

In the last step we have used that the contraction of the two linear response matrices is the covariance matrix

$$C_{\alpha\beta} = \sum_l L_{\alpha,l} L_{\beta,l} \tag{F.11}$$

in the linear response case.

We can easily extend the calculation to a formulation for the joint probability distribution of n observables $O_{\alpha_1}, \ldots, O_{\alpha_n}$. Therefore, we just collect the observables, their averages and the linear response matrices into vectors $\vec{O}_{\vec{\alpha}}$, $\vec{\bar{O}}_{\vec{\alpha}}$ and $\vec{L}_{\vec{\alpha},l}$ and we express the n-dimensional Dirac-distribution as a Fourier integral. This integral is then of n-dimensional complex Gaussian form:

$$p_{\vec{\alpha}}^{\mathrm{G}}\left(\vec{O}_{\vec{\alpha}}\right) = \int \mathrm{D}c\, \frac{1}{(2\pi)^{l_{\max}/2}} \exp\left(-\frac{c_l^2}{2}\right)\, \delta^{(n)}\left(\vec{O}_{\vec{\alpha}} - \vec{\bar{O}}_{\vec{\alpha}} - \sum_l^{l_{\max}} \vec{L}_{\vec{\alpha},l} c_l\right) \tag{F.12}$$

$$= \int \frac{\mathrm{d}^n \vec{s}}{(2\pi)^n} \int \mathrm{D}c\, \frac{1}{(2\pi)^{l_{\max}/2}} \exp\left[-\frac{c_l^2}{2} - \mathrm{i}\vec{s}\cdot \sum_l^{l_{\max}} \vec{L}_{\vec{\alpha},l} c_l + \mathrm{i}\vec{s}\cdot\left(\vec{O}_{\vec{\alpha}} - \vec{\bar{O}}_{\vec{\alpha}}\right)\right] \tag{F.13}$$

$$= \int \frac{\mathrm{d}^n \vec{s}}{(2\pi)^n}\, \exp\left[-\frac{\vec{s}^{\,\mathsf{T}} \sum_l^{l_{\max}} \vec{L}_{\vec{\alpha},l} \vec{L}_{\vec{\alpha},l}^{\,\mathsf{T}} \vec{s}}{2} + \mathrm{i}\vec{s}\cdot\left(\vec{O}_{\vec{\alpha}} - \vec{\bar{O}}_{\vec{\alpha}}\right)\right] \tag{F.14}$$

$$= \frac{1}{\sqrt{(2\pi)^n \det(\Sigma_{\vec{\alpha}})}} \exp\left[-\frac{1}{2}\left(\vec{O}_{\vec{\alpha}} - \vec{\bar{O}}_{\vec{\alpha}}\right)^{\mathsf{T}} \Sigma_{\vec{\alpha}}^{-1} \left(\vec{O}_{\vec{\alpha}} - \vec{\bar{O}}_{\vec{\alpha}}\right)\right]. \tag{F.15}$$

Here we have defined the linear order covariance matrix of these observables as

$$\Sigma_{\vec{\alpha}} = \sum_{l}^{l_{\max}} \vec{L}_{\vec{\alpha},l} \vec{L}^{\mathsf{T}}_{\vec{\alpha},l} \tag{F.16}$$

being a submatrix of the full linear order covariance matrix, i.e.,

$$\left(\Sigma_{\vec{\alpha}}\right)_{ij} = C_{\alpha_i \alpha_j}. \tag{F.17}$$

Exploiting Cramer's rule we do not have to specify the covariances any further and can write the inverse of an $n \times n$ matrix A as

$$\left(A^{-1}\right)_{ij} = \frac{(-1)^{i+j}}{\det(A)} \det\left(A_{(j,i)}\right), \tag{F.18}$$

where we denote by $A_{(j,i)}$ the $(n-1) \times (n-1)$ matrix obtained by deleting the j-th row and i-th column from the matrix A. Using this in the expression for $p^{\mathrm{G}}_{\vec{\alpha}}$ we obtain

$$p^{\mathrm{G}}_{\vec{\alpha}}\left(\vec{O}_{\vec{\alpha}}\right) = \frac{1}{\sqrt{(2\pi)^n \det(\Sigma_{\vec{\alpha}})}} \exp\left[-\frac{\sum_{i,j=1}^{n} (-1)^{i+j} \left(\vec{O}_{\vec{\alpha}_i} - \vec{\bar{O}}_{\vec{\alpha}_i}\right)\left(\vec{O}_{\vec{\alpha}_j} - \vec{\bar{O}}_{\vec{\alpha}_j}\right) \det\left(\Sigma_{\vec{\alpha},(j,i)}\right)}{2 \det(\Sigma_{\vec{\alpha}})} \right]. \tag{F.19}$$

We will now turn to observables of the type $O_\beta = \sqrt{O^2_{\alpha_1} + O^2_{\alpha_2}}$ with Gaussian distributed O_{α_1} and O_{α_2}. Then the joint probability distribution can be written as

$$p^{\mathrm{G}}_{\beta}(O_\beta) = \int \mathrm{d}O_{\alpha_1} \int \mathrm{d}O_{\alpha_2}\; p^{G}_{\alpha_1,\alpha_2}(O_{\alpha_1}, O_{\alpha_2})\, \delta\left(O_\beta - \sqrt{O^2_{\alpha_1} + O^2_{\alpha_2}}\right). \tag{F.20}$$

Performing a change of coordinates $O_{\alpha_1} = r\cos\phi$ and $O_{\alpha_2} = r \sin\phi$ makes it possible to solve the radial integral using the Dirac-distribution:

$$p^{\mathrm{G}}_{\beta}(O_\beta) = \int_0^{2\pi} \mathrm{d}\phi \int_0^{\infty} \mathrm{d}r\; p^{G}_{\alpha_1,\alpha_2}(r\cos\phi, r\sin\phi)\, \delta(O_\beta - r) \tag{F.21}$$

$$= \theta(O_\beta) O_\beta \int_0^{2\pi} \mathrm{d}\phi\; p^{\mathrm{G}}_{\alpha_1,\alpha_2}(O_\beta \cos\phi, O_\beta \sin\phi). \tag{F.22}$$

The expression for a two-dimensional joint probability distribution of O_β and $O_\gamma = \sqrt{O^2_{\alpha_3} + O^2_{\alpha_4}}$ can be obtained by performing the latter variable transformation twice:

$$p^{\mathrm{G}}_{\beta,\gamma}(O_\beta, O_\gamma) = \theta(O_\beta) O_\beta \theta(O_\gamma) O_\gamma \int_0^{2\pi} \mathrm{d}\phi \int_0^{2\pi} \mathrm{d}\psi\; p^{\mathrm{G}}_{\alpha_1,\alpha_2,\alpha_3,\alpha_4}(O_\beta\cos\phi, O_\beta\sin\phi, O_\gamma\cos\psi, O_\gamma\sin\psi). \tag{F.23}$$

This integral is in general highly non-trivial, as the distributions $p^{\mathrm{G}}_{\vec{\alpha}}$ contain couplings of all observables $\vec{O}_{\vec{\alpha}}$ induced by their correlations in the argument of the exponential. One case where we can solve the integration analytically is for a one-dimensional probability distribution p^{G}_{β}. Combining Eqs. (F.19) and (F.22) we obtain

$$p^{\mathrm{G}}_{\beta}(O_\beta) = \frac{\theta(O_\beta) O_\beta}{\sqrt{\det(\Sigma_{\alpha_1,\alpha_2})}} \int_0^{2\pi} \frac{\mathrm{d}\phi}{2\pi} \exp\left[-\frac{C_{\alpha_2\alpha_2}\left(O_\beta\cos\phi - \bar{O}_{\alpha_1}\right)^2 + C_{\alpha_1\alpha_1}\left(O_\beta\sin\phi - \bar{O}_{\alpha_2}\right)^2 - 2C_{\alpha_1\alpha_2}\left(O_\beta\cos\phi - \bar{O}_{\alpha_1}\right)\left(O_\beta\sin\phi - \bar{O}_{\alpha_2}\right)}{2\det(\Sigma_{\alpha_1,\alpha_2})} \right] \tag{F.24}$$

The numerator in the exponential of the latter expression can be rewritten by collecting all linear resp. quadratic terms in trigonometric functions into a $\cos(\phi - \theta_1)$-term resp. $\cos(2\phi - \theta_2)$-term and an additional ϕ-independent part:

$$
\begin{aligned}
& C_{\alpha_2\alpha_2}\left(O_\beta \cos\phi - \bar{O}_{\alpha_1}\right)^2 + C_{\alpha_1\alpha_1}\left(O_\beta \sin\phi - \bar{O}_{\alpha_2}\right)^2 \\
& - 2C_{\alpha_1\alpha_2}\left(O_\beta \cos\phi - \bar{O}_{\alpha_1}\right)\left(O_\beta \sin\phi - \bar{O}_{\alpha_2}\right) && \text{(F.25)} \\
= {} & C_{\alpha_2\alpha_2} O_\beta^2 \cos^2\phi + C_{\alpha_1\alpha_1} O_\beta^2 \sin^2\phi - 2C_{\alpha_1\alpha_2} O_\beta^2 \cos\phi \sin\phi \\
& + 2O_\beta\left(C_{\alpha_1\alpha_2}\bar{O}_{\alpha_2} - C_{\alpha_2\alpha_2}\bar{O}_{\alpha_1}\right)\cos\phi + 2O_\beta\left(C_{\alpha_1\alpha_2}\bar{O}_{\alpha_1} - C_{\alpha_1\alpha_1}\bar{O}_{\alpha_2}\right)\sin\phi \\
& + C_{\alpha_2\alpha_2}\bar{O}_{\alpha_1}^2 + C_{\alpha_1\alpha_1}\bar{O}_{\alpha_2}^2 - 2C_{\alpha_1\alpha_2}\bar{O}_{\alpha_1}\bar{O}_{\alpha_2} && \text{(F.26)} \\
= {} & r_1\cos(\phi - \theta_1) + r_2\cos(2\phi - \theta_2) + \frac{1}{2}C_{\alpha_2\alpha_2}O_\beta^2 + \frac{1}{2}C_{\alpha_1\alpha_1}O_\beta^2 \\
& + C_{\alpha_2\alpha_2}\bar{O}_{\alpha_1}^2 + C_{\alpha_1\alpha_1}\bar{O}_{\alpha_2}^2 - 2C_{\alpha_1\alpha_2}\bar{O}_{\alpha_1}\bar{O}_{\alpha_2}, && \text{(F.27)}
\end{aligned}
$$

where we have used

$$
\begin{aligned}
r_1\cos\theta_1 &= 2O_\beta\left(C_{\alpha_1\alpha_2}\bar{O}_{\alpha_2} - C_{\alpha_2\alpha_2}\bar{O}_{\alpha_1}\right), && \text{(F.28)} \\
r_1\sin\theta_1 &= 2O_\beta\left(C_{\alpha_1\alpha_2}\bar{O}_{\alpha_1} - C_{\alpha_1\alpha_1}\bar{O}_{\alpha_2}\right), && \text{(F.29)} \\
r_2\cos\theta_2 &= \frac{1}{2}C_{\alpha_2\alpha_2}O_\beta^2 - \frac{1}{2}C_{\alpha_1\alpha_1}O_\beta^2, && \text{(F.30)} \\
r_2\sin\theta_2 &= -C_{\alpha_1\alpha_2}O_\beta^2. && \text{(F.31)}
\end{aligned}
$$

Using a trick from Ref. [149] with the identity

$$
\exp\left(z^* e^{\mathrm{i}\phi} + z e^{-\mathrm{i}\phi}\right) = \sum_{q=-\infty}^{\infty} e^{-\mathrm{i}q\phi}\left(\frac{z}{|z|}\right)^q I_q\left(2|z|\right) \qquad \text{(F.32)}
$$

we can now write the cosines in the complex exponential representation such that the prefactors of the exponentials are

$$
\begin{aligned}
z_1 &= -\frac{r_1 e^{\mathrm{i}\theta_1}}{4\det\left(\Sigma_{\alpha_1,\alpha_2}\right)}, && \text{(F.33)} \\
z_2 &= -\frac{r_2 e^{\mathrm{i}\theta_2}}{4\det\left(\Sigma_{\alpha_1,\alpha_2}\right)}. && \text{(F.34)}
\end{aligned}
$$

The final expression for the joint probability distribution is then

$$p_\beta^{\mathrm{G}}(O_\beta) = \frac{\theta(O_\beta)\, O_\beta}{\sqrt{\det(\Sigma_{\alpha_1,\alpha_2})}} \exp\left[-\frac{C_{\alpha_2\alpha_2}O_\beta^2 + C_{\alpha_1\alpha_1}O_\beta^2 + 2C_{\alpha_2\alpha_2}\bar{O}_{\alpha_1}^2 + 2C_{\alpha_1\alpha_1}\bar{O}_{\alpha_2}^2 - 4C_{\alpha_1\alpha_2}\bar{O}_{\alpha_1}\bar{O}_{\alpha_2}}{4\det(\Sigma_{\alpha_1,\alpha_2})}\right]$$
$$\times \int_0^{2\pi} \frac{\mathrm{d}\phi}{2\pi} \exp\left[-\frac{r_1\cos(\phi-\theta_1) + r_2\cos(2\phi-\theta_2)}{2\det(\Sigma_{\alpha_1,\alpha_2})}\right] \tag{F.35}$$

$$= \frac{\theta(O_\beta)\, O_\beta}{\sqrt{\det(\Sigma_{\alpha_1,\alpha_2})}} \exp\left[-\frac{C_{\alpha_2\alpha_2}O_\beta^2 + C_{\alpha_1\alpha_1}O_\beta^2 + 2C_{\alpha_2\alpha_2}\bar{O}_{\alpha_1}^2 + 2C_{\alpha_1\alpha_1}\bar{O}_{\alpha_2}^2 - 4C_{\alpha_1\alpha_2}\bar{O}_{\alpha_1}\bar{O}_{\alpha_2}}{4\det(\Sigma_{\alpha_1,\alpha_2})}\right]$$
$$\times \int_0^{2\pi} \frac{\mathrm{d}\phi}{2\pi} \sum_{q_1=-\infty}^{\infty} e^{-\mathrm{i}q_1\phi} \left(\frac{z_1}{|z_1|}\right)^{q_1} I_{q_1}(2|z_1|) \sum_{q_2=-\infty}^{\infty} e^{-2\mathrm{i}q_2\phi} \left(\frac{z_2}{|z_2|}\right)^{q_2} I_{q_2}(2|z_2|) \tag{F.36}$$

$$= \frac{\theta(O_\beta)\, O_\beta}{\sqrt{\det(\Sigma_{\alpha_1,\alpha_2})}} \exp\left[-\frac{C_{\alpha_2\alpha_2}O_\beta^2 + C_{\alpha_1\alpha_1}O_\beta^2 + 2C_{\alpha_2\alpha_2}\bar{O}_{\alpha_1}^2 + 2C_{\alpha_1\alpha_1}\bar{O}_{\alpha_2}^2 - 4C_{\alpha_1\alpha_2}\bar{O}_{\alpha_1}\bar{O}_{\alpha_2}}{4\det(\Sigma_{\alpha_1,\alpha_2})}\right]$$
$$\times \sum_{q=-\infty}^{\infty} \left(\frac{z_1^2 z_2}{|z_1^2 z_2|}\right)^q I_{2q}(2|z_1|) I_q(2|z_2|). \tag{F.37}$$

The function I_q denotes the modified Bessel function of order q. For two cases there is only one term of the sum over q surviving. One is the case where O_{α_1} and O_{α_2} are independent of each other, i.e., $C_{\alpha_1\alpha_2} = 0$, and have the same variance, i.e., $C_{\alpha_1\alpha_1} = C_{\alpha_2\alpha_2}$. Then the variable z_2 is zero and we obtain a Rice distribution of O_β. The other special case is the one where the average observables are vanishing, i.e., $\bar{O}_{\alpha_1} = \bar{O}_{\alpha_2} = 0$, such that $z_1 = 0$.

F.5 Explanation of the covariances

We will discuss parts of the covariance matrices in this Appendix, especially signs and magnitudes thereof. One thing to notice for both models is that $\mathrm{C}([p_\mathrm{T}], \{r^2\})$ is negative (see Figs. 7.20 and 7.24). This is due to the fact that the contribution of each mode at the order of a linear response is negative (see Figs. 7.14 and F.10). Considering an increasing system size leads to a decrease in the pressure — equivalent to gradients which become smaller — such that the mean transverse momentum decreases. For the energy and the charged hadron multiplicity we find a positive correlation for the Glauber model (Fig. 7.14), while it is negative in the Saturation model (Fig. F.10). At first sight the increase in the initial state energy should lead to more particles in the final state according to Eq. (7.39). This equation is however only valid locally such that particles are only generated according to the local energy density, as it is done for example in the freeze-out process. We have seen in Fig. 7.5 that the (radial) modes in the Glauber model have up to a factor of ≈ 3 more energy. Here we have to keep in mind that a given mode does not only change the total amount of energy but also the shape of the energy density distribution. In particular we find $\mathrm{C}(\mathrm{d}E/\mathrm{d}y, \{r^2\}) < 0$ in both models such that the modes which increase the energy of the system decrease its size and vice-versa. For the particle yield this implies that the decrease in $\{r^2\}$ will also decrease $\mathrm{d}N_\mathrm{ch}/\mathrm{d}\eta$. Here are two effects at work which act against each other. First the increase of the total energy in the system and second the decrease in the system size. In the case of

the Glauber model the increase in the energy of a radial mode is larger than in the Saturation model such that it surpasses the effect generated by the change in $\{r^2\}$. In the case of the Saturation model the two effects are of the same order, such that the linear response of the charged hadron multiplicity is small. In Fig. 7.24 we find that $\mathrm{C}\left(\mathrm{d}N_{\mathrm{ch}}/\mathrm{d}\eta, [p_{\mathrm{T}}]\right) \approx 0$ at linear order, while for the randomly sampled events there is a clear negative correlation. This discrepancey between the mode-by-mode and event-by-event approach can be explained by the fact that we inlude only the linear response in the mode-by-mode results. This can be improved qualitatively by including also quadratic terms in the covariance. Then this would be of the form

$$\mathrm{C}(\alpha, \beta) = \sum_l L_{\alpha,l} L_{\beta,l} + \frac{4}{9} \sum_l Q_{\alpha,ll} Q_{\beta,ll}. \tag{F.38}$$

We find for both models that the quadratic contribution is always negative, as already discussed in Sec. 7.2.4.2 and we assumed further that the expansion coefficients $\{c_l\}$ are Gaussian. The quadratic contributions in the Glauber model are much smaller then in the Saturation model, such that we can neglect them for the covariance. However, for the Saturation model the linear and quadratic response is of the same order such that this explains the difference for the observed covariance in Fig. 7.24.

Appendix G

Numerical techniques

G.1 Trapezoidal integration

As we need a two-dimensional integration over the quantities stored on the grid several times in the simulations, we will have a short look at the implementation of a two-dimensional trapezoidal integration. In the code we integrate over the whole grid which is defined in the region $\{(x,y)|a \leq x \leq b, c \leq y \leq d\}$. The number of equally spaced sampling points in x-direction is denoted by m and the one in y-direction by n. Approximating a two-dimensional integral by the trapezoidal rule yields [150]

$$\begin{aligned}\int_a^b \mathrm{d}x \int_c^d \mathrm{d}y\, f(x,y) \approx \frac{1}{4}h_x h_y \Bigg(& f(a,c) + f(b,c) + f(a,d) + f(b,d) \\ & + 2\sum_{j=1}^{n-1} f(a,y_j) + 2\sum_{j=1}^{n-1} f(b,y_j) + 2\sum_{i=1}^{m-1} f(x_i,c) + 2\sum_{i=1}^{m-1} f(x_i,d) \\ & + 4\sum_{j=1}^{n-1}\left(\sum_{i=1}^{m-1} f(x_i,y_j)\right)\Bigg),\end{aligned} \tag{G.1}$$

where h_x, h_y are the integration steps in the corresponding directions. For the simulations this lengthy formula can be shortened to

$$\int_a^b \mathrm{d}x \int_c^d \mathrm{d}y\, f(x,y) \approx h_x h_y \sum_{j=1}^{n-1}\sum_{i=1}^{m-1} f(x_i,y_j), \tag{G.2}$$

as the densities which are stored on the grid vanish within the extent of the grid, such that the boundary terms do not contribute to the integral.

G.2 Bilinear interpolation

Bilinear interpolation is a method to interpolate functions of two variables. The method is based on a very simple idea. First a linear interpolation in one of the directions is performed and then another linear interpolation in the other direction. Because of the two linear interpolations the whole two dimensional interpolation is quadratic. For the interpolation of the point P (see Fig. G.1) we need the four

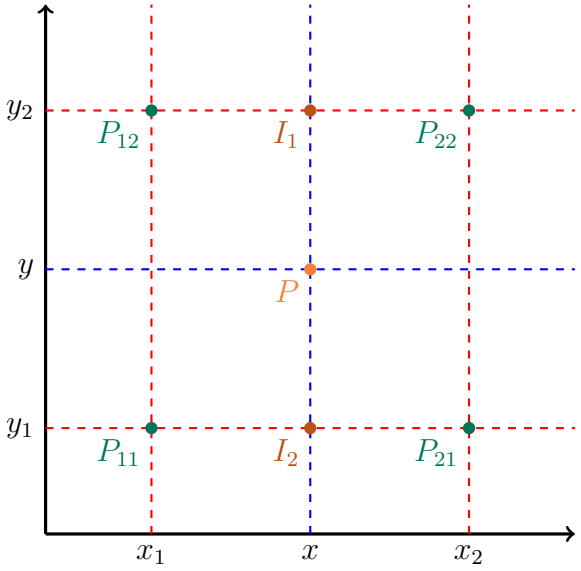

Figure G.1: The green points represent the grid points between which the orange point should be interpolated using a bilinear interpolation.

grid points between which the point lies. These are $P_{11} = (x_1, y_1)$, $P_{12} = (x_1, y_2)$, $P_{21} = (x_2, y_1)$ and $P_{22} = (x_2, y_2)$. First we consider the linear interpolation in x-direction, which yields

$$\begin{aligned} f(x, y_1) &\approx \frac{x_2 - x}{x_2 - x_1} f(P_{11}) + \frac{x - x_1}{x_2 - x_1} f(P_{21}), \\ f(x, y_2) &\approx \frac{x_2 - x}{x_2 - x_1} f(P_{12}) + \frac{x - x_1}{x_2 - x_1} f(P_{22}). \end{aligned} \tag{G.3}$$

Then the interpolation in y-direction is performed and yields

$$f(x, y) \approx \frac{y_2 - y}{y_2 - y_1} f(x, y_1) + \frac{y - y_1}{y_2 - y_1} f(x, y_2). \tag{G.4}$$

Plugging in the interpolation in x-direction, we obtain [151]

$$\begin{aligned} f(x, y) \approx \frac{1}{(x_2 - x_1)(y_2 - y_1)} &[f(P_{11})(x_2 - x)(y_2 - y) + f(P_{21})(x - x_1)(y_2 - y) \\ &+ f(P_{12})(x_2 - x)(y - y_1) + f(P_{22})(x - x_1)(y - y_1)] \end{aligned} \tag{G.5}$$

for the function $f(x, y)$ in the point P.

G.3 Delete-d Jackknife

The Jackknife method as it was reformulated in 1956 by Tukey can be used to construct confidence intervals for many different statistics. In this section we follow the article [152] and the book [153]. Jackknife methods are in general similar to the bootstrap technique, with the difference that the deleted samples are not replaced.

We start with the description of the delete-1 Jackknife. Assuming the n data sets with one deleted element each are given by vectors

$$\vec{X}_{[i]} = (X_1, \cdots, X_{i-1}, X_{i+1}, \cdots, X_n) \tag{G.6}$$

enumerated by i. Then we define the i-th Jackknife sample as the statistics $s(\cdot)$ evaluated for the i-th sample vector:

$$\rho_{(i)} \equiv s\left(\vec{X}_{[i]}\right). \tag{G.7}$$

The standard error is then given by [152]

$$\sigma\left(\rho\right)_{\text{Jackknife}} = \sqrt{\frac{n-1}{n}\sum_{i=1}^{n}\left(\rho_{(i)} - \rho_{(\cdot)}\right)^2}, \tag{G.8}$$

with the average over the Jackknife samples

$$\rho_{(\cdot)} = \frac{1}{n}\sum_{i=1}^{n}\rho_{(i)}. \tag{G.9}$$

As the delete-1 method does not work in all cases, we extend it to a more general case of the delete-d Jackknife, where we randomly delete d elements from the data vector $\vec{Y}$. All $\binom{n}{d}$ Jackknife samples, i.e., the data vectors $\vec{Y}$, can be collected in the set $\mathcal{S}$. The form of the standard error is [152]

$$\sigma(\rho)_{\text{d-Jackknife}} = \sqrt{\frac{n-d}{d\binom{n}{d}}\sum_{i\in\mathcal{S}}\left(\rho_{(i)} - \rho_{(\cdot)}\right)^2}. \tag{G.10}$$

This formula is impractical if d increases. Therefore, we slightly change it to [153]

$$\sigma(\rho)_{\text{d-Jackknife}} = \sqrt{\frac{n-d}{dm}\sum_{i\in\mathcal{B}}\left(\rho_{(i)} - \rho_{(\cdot)}\right)^2} \tag{G.11}$$

where m is the number of Jackknife samples in the set $\mathcal{B}$, which is a subset of $\mathcal{S}$.

Acknowledgments

First of all I would like to thank my supervisor Nicolas Borghini for the great support he has given me over the last years. In his excellent lectures, he awakened my enthusiasm for theoretical physics already during my studies. We had many stimulating and interesting discussions and he was always there (in person or even virtual) to help me with any kind of problem. He gave me the opportunity to expand my knowledge and have a look outside of the box at various conferences, workshops and schools.

Second I would like to thank Hannah Elfner for being my second supervisor within HGS-HIRe and for the many stimulating discussions and comments during our PhD committee meetings. I also thank her for providing me computation time from her own projects at the CSC in Frankfurt.

The third person I would like to thank is Sören Schlichting for his continuous support, his contagious enthusiasm for physics and for motivating me to continue a career in physics.

Then I would like to thank our group in Bielefeld for the nice group seminars, where we discussed many interesting papers and issues with our own research. There are two special persons in our group I want to highlight: Nina Feld and Marc Borrell. Thank you for the amazing collaboration during the last years. It was a very interesting time and we even managed to connect our areas of research such that we produced two publications out of this.

Thanks to my (former) office mates Patric Hölscher, Alexander Klaus, Pascal Kreling, Thorben Mense, Benedikt Bachmann and Marco Mantovanelli for the nice time in D6-150, but also to the rest of the D6/E6 people.

A special thanks goes to Luis Altenkort, Marc Borrell and Marius Neumann for proofreading my thesis.

I am thankful for the administrative support I received from Gudrun Eickmeyer, Irene Kehler and Susi v. Reder during the last years.

Furthermore I acknowledge the support by the Deutsche Forschungsgemeinschaft (DGF, German Research Foundation) through the CRC-TR 211 'Strong-interaction matter under extreme conditions' - project number 315477589 - TRR 211. I thank all the members for the informative and inspiring discussions and colloquia.

Computational resources for the presented simulations have been provided by the Bielefeld GPU Cluster, the Center for Scientific Computing (CSC) at the Goethe-University of Frankfurt and the Paderborn Center for Parallel Computing (PC^2).

Finally, I would like to thank my family for their support over the past years. Without your help I would not have been able to focus on physics with this intensity.

Declaration of authorship

Hereby I declare that I have written this present thesis on my own. The thesis has not been previously submitted to any examination office. Only the sources and literature indicated have been used.

Bielefeld, June 13, 2022

place, date

Hendrik Roch

Bibliography

[1] G. Baym, "Ultrarelativistic heavy ion collisions: the first billion seconds," *Nucl. Phys. A*, vol. 956, pp. 1–10, 2016.

[2] W. Florkowski, *Phenomenology of Ultra-Relativistic Heavy-Ion Collisions*. 3 2010.

[3] A. Chaudhuri, *A short course on Relativistic Heavy Ion Collisions*. IOPP, 9 2014.

[4] M. A. Lisa, "Size matters: Spacetime geometry in subatomic collisions," 2004. Sambamurti Memorial Lecture presented 28 July 2004 at Brookhaven National Lab.

[5] W. Busza, K. Rajagopal, and W. van der Schee, "Heavy Ion Collisions: The Big Picture, and the Big Questions," *Ann. Rev. Nucl. Part. Sci.*, vol. 68, pp. 339–376, 2018.

[6] M. Tanabashi *et al.*, "Review of Particle Physics," *Phys. Rev. D*, vol. 98, no. 3, p. 030001, 2018.

[7] N. Haque, *Some Applications of Hard Thermal Loop Perturbation Theory in Quark Gluon Plasma*. PhD thesis, Saha Inst., 2014-07.

[8] D. J. Schwarz, "Evolution of gravitational waves through cosmological transitions," *Mod. Phys. Lett. A*, vol. 13, pp. 2771–2778, 1998.

[9] "`https://science.osti.gov/-/media/np/nsac/pdf/2015LRP/2015_LRPNS_091815.pdf`." last visit: 14.08.2020.

[10] N. Borghini and C. Gombeaud, "Anisotropic flow far from equilibrium," *The European Physical Journal C*, vol. 71, Apr 2011.

[11] S. Schlichting and D. Teaney, "The first fm/c of heavy-ion collisions," *Annual Review of Nuclear and Particle Science*, vol. 69, p. 447–476, Oct 2019.

[12] W. Florkowski and R. Ryblewski, "Highly anisotropic and strongly dissipative hydrodynamics for early stages of relativistic heavy-ion collisions," *Phys. Rev. C*, vol. 83, p. 034907, Mar 2011.

[13] M. Martinez and M. Strickland, "Dissipative dynamics of highly anisotropic systems," *Nuclear Physics A*, vol. 848, no. 1, pp. 183 – 197, 2010.

[14] C. Blume, "Lecture at international school on quark-gluon plasma and heavy ion collisions: past, present future," mar 2011.

[15] S. Voloshin and Y. Zhang, "Flow study in relativistic nuclear collisions by Fourier expansion of Azimuthal particle distributions," *Z. Phys. C*, vol. 70, pp. 665–672, 1996.

[16] J.-Y. Ollitrault, "Anisotropy as a signature of transverse collective flow," *Phys. Rev. D*, vol. 46, pp. 229–245, Jul 1992.

[17] J.-Y. Ollitrault, "Determination of the reaction plane in ultrarelativistic nuclear collisions," *Phys. Rev. D*, vol. 48, pp. 1132–1139, Aug 1993.

[18] N. Borghini, P. M. Dinh, and J.-Y. Ollitrault, "New method for measuring azimuthal distributions in nucleus-nucleus collisions," *Phys. Rev. C*, vol. 63, p. 054906, Apr 2001.

[19] R. Bhalerao, N. Borghini, and J.-Y. Ollitrault, "Genuine collective flow from lee–yang zeroes," *Physics Letters B*, vol. 580, no. 3, pp. 157 – 162, 2004.

[20] M. L. Miller, K. Reygers, S. J. Sanders, and P. Steinberg, "Glauber modeling in high-energy nuclear collisions," *Annual Review of Nuclear and Particle Science*, vol. 57, no. 1, pp. 205–243, 2007.

[21] K. Reygers, "Optical glauber calculation for pb-pb," 2015. `https://www.physi.uni-heidelberg.de/~reygers/lectures/2015/qgp/glauber.nb`.

[22] R. D. Woods and D. S. Saxon, "Diffuse Surface Optical Model for Nucleon-Nuclei Scattering," *Phys. Rev.*, vol. 95, pp. 577–578, 1954.

[23] D. d'Enterria and C. Loizides, "Progress in the Glauber Model at Collider Energies," *Ann. Rev. Nucl. Part. Sci.*, vol. 71, pp. 315–344, 2021.

[24] C. Loizides, J. Kamin, and D. d'Enterria, "Improved Monte Carlo Glauber predictions at present and future nuclear colliders," *Phys. Rev.*, vol. C97, no. 5, p. 054910, 2018.

[25] H. Holopainen and P. Huovinen, "Dynamical freeze-out in event-by-event hydrodynamics," *Journal of Physics: Conference Series*, vol. 389, p. 012018, nov 2012.

[26] F. Gelis, E. Iancu, J. Jalilian-Marian, and R. Venugopalan, "The Color Glass Condensate," *Ann. Rev. Nucl. Part. Sci.*, vol. 60, pp. 463–489, 2010.

[27] E. Iancu and R. Venugopalan, *The Color glass condensate and high-energy scattering in QCD*, pp. 249–3363. 3 2003.

[28] H. Kowalski and D. Teaney, "An Impact parameter dipole saturation model," *Phys. Rev. D*, vol. 68, p. 114005, 2003.

[29] K. J. Golec-Biernat and M. Wusthoff, "Saturation effects in deep inelastic scattering at low Q**2 and its implications on diffraction," *Phys. Rev. D*, vol. 59, p. 014017, 1998.

[30] L. McLerran and P. Tribedy, "Intrinsic Fluctuations of the Proton Saturation Momentum Scale in High Multiplicity p+p Collisions," *Nucl. Phys. A*, vol. 945, pp. 216–225, 2016.

[31] A. H. Rezaeian, M. Siddikov, M. Van de Klundert, and R. Venugopalan, "Analysis of combined HERA data in the Impact-Parameter dependent Saturation model," *Phys. Rev. D*, vol. 87, no. 3, p. 034002, 2013.

[32] T. Lappi and S. Schlichting, "Linearly polarized gluons and axial charge fluctuations in the Glasma," *Phys. Rev. D*, vol. 97, no. 3, p. 034034, 2018.

[33] J. P. Blaizot, T. Lappi, and Y. Mehtar-Tani, "On the gluon spectrum in the glasma," *Nucl. Phys. A*, vol. 846, pp. 63–82, 2010.

[34] S. Schlichting and V. Skokov, "Saturation corrections to dilute-dense particle production and azimuthal correlations in the Color Glass Condensate," *Phys. Lett. B*, vol. 806, p. 135511, 2020.

[35] J.-Y. Ollitrault, "Relativistic hydrodynamics for heavy-ion collisions," *Eur. J. Phys.*, vol. 29, pp. 275–302, 2008.

[36] B. Alver and G. Roland, "Collision geometry fluctuations and triangular flow in heavy-ion collisions," *Phys. Rev. C*, vol. 81, p. 054905, 2010. [Erratum: Phys.Rev.C 82, 039903 (2010)].

[37] D. Teaney and L. Yan, "Triangularity and Dipole Asymmetry in Heavy Ion Collisions," *Phys. Rev. C*, vol. 83, p. 064904, 2011.

[38] F. G. Gardim, F. Grassi, M. Luzum, and J.-Y. Ollitrault, "Mapping the hydrodynamic response to the initial geometry in heavy-ion collisions," *Phys. Rev. C*, vol. 85, p. 024908, 2012.

[39] S. Plumari, G. L. Guardo, F. Scardina, and V. Greco, "Initial state fluctuations from mid-peripheral to ultra-central collisions in a event-by-event transport approach," *Phys. Rev. C*, vol. 92, no. 5, p. 054902, 2015.

[40] T. Hirano and Y. Nara, "Eccentricity fluctuation effects on elliptic flow in relativistic heavy ion collisions," *Phys. Rev. C*, vol. 79, p. 064904, 2009.

[41] C. E. Coleman-Smith, H. Petersen, and R. L. Wolpert, "Classification of initial state granularity via 2d Fourier Expansion," *J. Phys. G*, vol. 40, p. 095103, 2013.

[42] L. Rezzolla and O. Zanotti, *Relativistic hydrodynamics*. Oxford: Oxford Univ. Press, 1. ed. ed., 2013.

[43] C. Cercignani and G. M. Kremer, *The Relativistic Boltzmann Equation: Theory and Applications*. Progress in Mathematical Physics; 22, Birkhäuser Basel : Imprint: Birkhäuser, 1st ed. 2002. ed., 2002.

[44] F. Reif, *Fundamentals of statistical and thermal physics*. McGraw-Hill series in fundamentals of physics, New York [u.a.]: McGraw-Hill, 1965.

[45] T. Krüger, *The Lattice Boltzmann Method*. Graduate Texts in Physics, Cham: Springer International Publishing, 2017.

[46] M. Mendoza, B. M. Boghosian, H. J. Herrmann, and S. Succi, "Fast lattice boltzmann solver for relativistic hydrodynamics," *Phys. Rev. Lett.*, vol. 105, p. 014502, Jun 2010.

[47] M. Mendoza, B. M. Boghosian, H. J. Herrmann, and S. Succi, "Derivation of the lattice boltzmann model for relativistic hydrodynamics," *Phys. Rev. D*, vol. 82, p. 105008, Nov 2010.

[48] P. Romatschke, M. Mendoza, and S. Succi, "Fully relativistic lattice boltzmann algorithm," *Phys. Rev. C*, vol. 84, p. 034903, Sep 2011.

[49] J. Anderson and H. Witting, "A relativistic relaxation-time model for the boltzmann equation," *Physica*, vol. 74, no. 3, pp. 466–488, 1974.

[50] G. S. Rocha, G. S. Denicol, and J. Noronha, "Novel Relaxation Time Approximation to the Relativistic Boltzmann Equation," *Phys. Rev. Lett.*, vol. 127, no. 4, p. 042301, 2021.

[51] B. Zhang, "Zpc 1.0.1: a parton cascade for ultrarelativistic heavy ion collisions," *Computer Physics Communications*, vol. 109, no. 2, pp. 193 – 206, 1998.

[52] D. Molnár and M. Gyulassy, "New solutions to covariant nonequilibrium dynamics," *Phys. Rev. C*, vol. 62, p. 054907, Oct 2000.

[53] V. Börchers, J. Meyer, S. Gieseke, G. Martens, and C. C. Noack, "Poincaré-covariant parton cascade model for ultrarelativistic heavy-ion reactions," *Phys. Rev. C*, vol. 62, p. 064903, Nov 2000.

[54] D. G. Currie, T. F. Jordan, and E. C. G. Sudarshan, "Relativistic invariance and hamiltonian theories of interacting particles," *Rev. Mod. Phys.*, vol. 35, pp. 350–375, Apr 1963.

[55] Z. Xu and C. Greiner, "Thermalization of gluons in ultrarelativistic heavy ion collisions by including three-body interactions in a parton cascade," *Phys. Rev. C*, vol. 71, p. 064901, Jun 2005.

[56] C. Gombeaud and J.-Y. Ollitrault, "Elliptic flow in transport theory and hydrodynamics," *Phys. Rev. C*, vol. 77, p. 054904, 2008.

[57] C. Gombeaud, *Thermalisation dans les collisions d'ions lourds ultrarelativistes*. PhD thesis, UPMC, Paris (main), 2010.

[58] B. Bachmann, "Numerical investigation of the influence of the gain term in the boltzmann equation," November 2020.

[59] M. Miller and R. Snellings, "Eccentricity fluctuations and its possible effect on elliptic flow measurements," 12 2003.

[60] L. Yan, J.-Y. Ollitrault, and A. M. Poskanzer, "Azimuthal Anisotropy Distributions in High-Energy Collisions," *Phys. Lett.*, vol. B742, pp. 290–295, 2015.

[61] G. Aad *et al.*, "Measurement of the distributions of event-by-event flow harmonics in lead-lead collisions at = 2.76 TeV with the ATLAS detector at the LHC," *JHEP*, vol. 11, p. 183, 2013.

[62] J. Adam *et al.*, "Correlated event-by-event fluctuations of flow harmonics in Pb-Pb collisions at $\sqrt{s_{\rm NN}} = 2.76$ TeV," *Phys. Rev. Lett.*, vol. 117, p. 182301, 2016.

[63] A. M. Sirunyan *et al.*, "Non-Gaussian elliptic-flow fluctuations in PbPb collisions at $\sqrt{s_{\rm NN}} = 5.02$ TeV," *Phys. Lett. B*, vol. 789, pp. 643–665, 2019.

[64] M. Aaboud *et al.*, "Fluctuations of anisotropic flow in Pb+Pb collisions at $\sqrt{\rm s_{NN}} = 5.02$ TeV with the ATLAS detector," *JHEP*, vol. 01, p. 051, 2020.

[65] H. Niemi, G. S. Denicol, H. Holopainen, and P. Huovinen, "Event-by-event distributions of azimuthal asymmetries in ultrarelativistic heavy-ion collisions," *Phys. Rev. C*, vol. 87, no. 5, p. 054901, 2013.

[66] J. Noronha-Hostler, L. Yan, F. G. Gardim, and J.-Y. Ollitrault, "Linear and cubic response to the initial eccentricity in heavy-ion collisions," *Phys. Rev. C*, vol. 93, no. 1, p. 014909, 2016.

[67] H. Petersen, G.-Y. Qin, S. A. Bass, and B. Muller, "Triangular flow in event-by-event ideal hydrodynamics in Au+Au collisions at $\sqrt{s_{\rm NN}} = 200A$ GeV," *Phys. Rev. C*, vol. 82, p. 041901, 2010.

[68] Z. Qiu and U. W. Heinz, "Event-by-event shape and flow fluctuations of relativistic heavy-ion collision fireballs," *Phys. Rev.*, vol. C84, p. 024911, 2011.

[69] C. Gale, S. Jeon, B. Schenke, P. Tribedy, and R. Venugopalan, "Event-by-event anisotropic flow in heavy-ion collisions from combined Yang-Mills and viscous fluid dynamics," *Phys. Rev. Lett.*, vol. 110, no. 1, p. 012302, 2013.

[70] D. Teaney and L. Yan, "Event-plane correlations and hydrodynamic simulations of heavy ion collisions," *Phys. Rev. C*, vol. 90, no. 2, p. 024902, 2014.

[71] L. Ma, G. L. Ma, and Y. G. Ma, "Anisotropic flow and flow fluctuations for Au + Au at $\sqrt{s_{NN}} = 200$ GeV in a multiphase transport model," *Phys. Rev. C*, vol. 89, no. 4, p. 044907, 2014.

[72] H. Niemi, K. J. Eskola, and R. Paatelainen, "Event-by-event fluctuations in a perturbative QCD + saturation + hydrodynamics model: Determining QCD matter shear viscosity in ultrarelativistic heavy-ion collisions," *Phys. Rev. C*, vol. 93, no. 2, p. 024907, 2016.

[73] G. Giacalone, L. Yan, J. Noronha-Hostler, and J.-Y. Ollitrault, "Skewness of elliptic flow fluctuations," *Phys. Rev. C*, vol. 95, no. 1, p. 014913, 2017.

[74] R. S. Bhalerao, G. Giacalone, and J.-Y. Ollitrault, "Kurtosis of elliptic flow fluctuations," *Phys. Rev. C*, vol. 99, no. 1, p. 014907, 2019.

[75] U. Heinz and R. Snellings, "Collective flow and viscosity in relativistic heavy-ion collisions," *Ann. Rev. Nucl. Part. Sci.*, vol. 63, pp. 123–151, 2013.

[76] J. L. Nagle and W. A. Zajc, "Small System Collectivity in Relativistic Hadronic and Nuclear Collisions," *Ann. Rev. Nucl. Part. Sci.*, vol. 68, pp. 211–235, 2018.

[77] H. Roch and N. Borghini, "Fluctuations of anisotropic flow from the finite number of rescatterings in a two-dimensional massless transport model," *Eur. Phys. J. C*, vol. 81, no. 5, p. 380, 2021.

[78] S. Vogel, G. Torrieri, and M. Bleicher, "Elliptic flow fluctuations in heavy ion collisions at RHIC and the perfect fluid hypothesis," *Phys. Rev. C*, vol. 82, p. 024908, 2010.

[79] C. Loizides, J. Nagle, and P. Steinberg, "Improved version of the PHOBOS Glauber Monte Carlo," *SoftwareX*, vol. 1-2, pp. 13–18, 2015.

[80] N. Borghini, S. Feld, and N. Kersting, "Scaling behavior of anisotropic flow harmonics in the far from equilibrium regime," *Eur. Phys. J. C*, vol. 78, no. 10, p. 832, 2018.

[81] A. Kurkela, U. A. Wiedemann, and B. Wu, "Opacity dependence of elliptic flow in kinetic theory," *Eur. Phys. J. C*, vol. 79, no. 9, p. 759, 2019.

[82] R. S. Bhalerao, J.-P. Blaizot, N. Borghini, and J.-Y. Ollitrault, "Elliptic flow and incomplete equilibration at RHIC," *Phys. Lett.*, vol. B627, pp. 49–54, 2005.

[83] B. H. Alver, C. Gombeaud, M. Luzum, and J.-Y. Ollitrault, "Triangular flow in hydrodynamics and transport theory," *Phys. Rev. C*, vol. 82, p. 034913, 2010.

[84] A. Kurkela, S. F. Taghavi, U. A. Wiedemann, and B. Wu, "Hydrodynamization in systems with detailed transverse profiles," *Phys. Lett. B*, vol. 811, p. 135901, 2020.

[85] A. Bzdak, P. Bozek, and L. McLerran, "Fluctuation induced equality of multi-particle eccentricities for four or more particles," *Nucl. Phys. A*, vol. 927, pp. 15–23, 2014.

[86] L. Yan and J.-Y. Ollitrault, "Universal fluctuation-driven eccentricities in proton-proton, proton-nucleus and nucleus-nucleus collisions," *Phys. Rev. Lett.*, vol. 112, p. 082301, 2014.

[87] R. S. Bhalerao, "Collectivity in large and small systems formed in ultrarelativistic collisions," *Eur. Phys. J. ST*, vol. 230, no. 3, p. 3, 2021.

[88] J.-Y. Ollitrault, "Anisotropy as a signature of transverse collective flow," *Phys. Rev. D*, vol. 46, pp. 229–245, 1992.

[89] N. Borghini and C. Gombeaud, "Anisotropic flow far from equilibrium," *Eur. Phys. J. C*, vol. 71, p. 1612, 2011.

[90] N. Borghini and J.-Y. Ollitrault, "Momentum spectra, anisotropic flow, and ideal fluids," *Phys. Lett. B*, vol. 642, pp. 227–231, 2006.

[91] D. Teaney and L. Yan, "Non linearities in the harmonic spectrum of heavy ion collisions with ideal and viscous hydrodynamics," *Phys. Rev. C*, vol. 86, p. 044908, 2012.

[92] C. Lang and N. Borghini, "Dissipative corrections to particle spectra and anisotropic flow from a saddle-point approximation to kinetic freeze out," *Eur. Phys. J. C*, vol. 74, p. 2955, 2014.

[93] N. Borghini, M. Borrell, and H. Roch, "Early time behavior of spatial and momentum anisotropies in kinetic theory across different Knudsen numbers," 1 2022.

[94] R. D. Weller and P. Romatschke, "One fluid to rule them all: viscous hydrodynamic description of event-by-event central p+p, p+Pb and Pb+Pb collisions at $\sqrt{s} = 5.02$ TeV," *Phys. Lett. B*, vol. 774, pp. 351–356, 2017.

[95] W. Zhao, Y. Zhou, K. Murase, and H. Song, "Searching for small droplets of hydrodynamic fluid in proton–proton collisions at the LHC," *Eur. Phys. J. C*, vol. 80, no. 9, p. 846, 2020.

[96] H. Heiselberg and A.-M. Levy, "Elliptic flow and HBT in noncentral nuclear collisions," *Phys. Rev. C*, vol. 59, pp. 2716–2727, 1999.

[97] P. Romatschke, "Azimuthal Anisotropies at High Momentum from Purely Non-Hydrodynamic Transport," *Eur. Phys. J. C*, vol. 78, no. 8, p. 636, 2018.

[98] A. Kurkela, U. A. Wiedemann, and B. Wu, "Nearly isentropic flow at sizeable η/s," *Phys. Lett. B*, vol. 783, pp. 274–279, 2018.

[99] A. Kurkela, U. A. Wiedemann, and B. Wu, "Flow in AA and pA as an interplay of fluid-like and non-fluid like excitations," *Eur. Phys. J. C*, vol. 79, no. 11, p. 965, 2019.

[100] A. Kurkela, A. Mazeliauskas, and R. Törnkvist, "Collective flow in single-hit QCD kinetic theory," *JHEP*, vol. 11, p. 216, 2021.

[101] V. E. Ambrus, S. Schlichting, and C. Werthmann, "Development of transverse flow at small and large opacities in conformal kinetic theory," *Phys. Rev. D*, vol. 105, no. 1, p. 014031, 2022.

[102] M. Borrell and N. Borghini, "Early time behavior of spatial and momentum anisotropies in a kinetic approach to nuclear collisions," 9 2021.

[103] P. F. Kolb and U. W. Heinz, "Hydrodynamic description of ultrarelativistic heavy ion collisions," pp. 634–714, 5 2003.

[104] U. W. Heinz and S. M. H. Wong, "Elliptic flow from a transversally thermalized fireball," *Phys. Rev. C*, vol. 66, p. 014907, 2002.

[105] P. F. Kolb and U. W. Heinz, "Emission angle dependent HBT at RHIC and beyond," *Nucl. Phys. A*, vol. 715, pp. 653–656, 2003.

[106] J. Vredevoogd and S. Pratt, "Universal Flow in the First Stage of Relativistic Heavy Ion Collisions," *Phys. Rev. C*, vol. 79, p. 044915, 2009.

[107] B. Bachmann, N. Borghini, N. Feld, and H. Roch, "Even anisotropic-flow harmonics are from Venus, odd ones are from Mars," 3 2022.

[108] P. F. Kolb, J. Sollfrank, and U. W. Heinz, "Anisotropic transverse flow and the quark hadron phase transition," *Phys. Rev. C*, vol. 62, p. 054909, 2000.

[109] D. A. Teaney, *Viscous Hydrodynamics and the Quark Gluon Plasma*, pp. 207–266. 2010.

[110] N. Borghini and C. Gombeaud, "Anisotropic collective flow of a Lorentz gas," *J. Phys. G*, vol. 38, p. 124172, 2011.

[111] L. He, T. Edmonds, Z.-W. Lin, F. Liu, D. Molnar, and F. Wang, "Anisotropic parton escape is the dominant source of azimuthal anisotropy in transport models," *Phys. Lett. B*, vol. 753, pp. 506–510, 2016.

[112] L. V. Bravina, B. H. Brusheim Johansson, G. K. Eyyubova, V. L. Korotkikh, I. P. Lokhtin, L. V. Malinina, S. V. Petrushanko, A. M. Snigirev, and E. E. Zabrodin, "Hexagonal flow v6 as a superposition of elliptic v2 and triangular v3 flows," *Phys. Rev. C*, vol. 89, no. 2, p. 024909, 2014.

[113] J. Qian, U. W. Heinz, and J. Liu, "Mode-coupling effects in anisotropic flow in heavy-ion collisions," *Phys. Rev. C*, vol. 93, no. 6, p. 064901, 2016.

[114] G. Giacalone, L. Yan, and J.-Y. Ollitrault, "Nonlinear coupling of flow harmonics: Hexagonal flow and beyond," *Phys. Rev. C*, vol. 97, no. 5, p. 054905, 2018.

[115] P. Romatschke and U. Romatschke, *Relativistic Fluid Dynamics In and Out of Equilibrium*. Cambridge Monographs on Mathematical Physics, Cambridge University Press, 5 2019.

[116] C. Gale, J.-F. Paquet, B. Schenke, and C. Shen, "Multimessenger heavy-ion collision physics," *Phys. Rev. C*, vol. 105, no. 1, p. 014909, 2022.

[117] M. Luzum and H. Petersen, "Initial State Fluctuations and Final State Correlations in Relativistic Heavy-Ion Collisions," *J. Phys. G*, vol. 41, p. 063102, 2014.

[118] S. Floerchinger and U. A. Wiedemann, "Mode-by-mode fluid dynamics for relativistic heavy ion collisions," *Phys. Lett. B*, vol. 728, pp. 407–411, 2014.

[119] S. Floerchinger and U. A. Wiedemann, "Characterization of initial fluctuations for the hydrodynamical description of heavy ion collisions," *Phys. Rev. C*, vol. 88, p. 044906, 2013.

[120] S. Floerchinger and U. A. Wiedemann, "Kinetic freeze-out, particle spectra and harmonic flow coefficients from mode-by-mode hydrodynamics," *Phys. Rev. C*, vol. 89, no. 3, p. 034914, 2014.

[121] S. Floerchinger, U. A. Wiedemann, A. Beraudo, L. Del Zanna, G. Inghirami, and V. Rolando, "How (non-)linear is the hydrodynamics of heavy ion collisions?," *Phys. Lett. B*, vol. 735, pp. 305–310, 2014.

[122] S. Floerchinger and U. A. Wiedemann, "Statistics of initial density perturbations in heavy ion collisions and their fluid dynamic response," *JHEP*, vol. 08, p. 005, 2014.

[123] S. Floerchinger, E. Grossi, and J. Lion, "Fluid dynamics of heavy ion collisions with mode expansion," *Phys. Rev. C*, vol. 100, no. 1, p. 014905, 2019.

[124] S. Floerchinger, E. Grossi, and K. V. Yousefnia, "Model comparison for initial density fluctuations in high energy heavy ion collisions," *Phys. Rev. C*, vol. 102, no. 5, p. 054914, 2020.

[125] A. Kurkela, A. Mazeliauskas, J.-F. Paquet, S. Schlichting, and D. Teaney, "Effective kinetic description of event-by-event pre-equilibrium dynamics in high-energy heavy-ion collisions," *Phys. Rev. C*, vol. 99, no. 3, p. 034910, 2019.

[126] B. Schenke, S. Jeon, and C. Gale, "(3+1)D hydrodynamic simulation of relativistic heavy-ion collisions," *Phys. Rev. C*, vol. 82, p. 014903, 2010.

[127] B. Schenke, S. Jeon, and C. Gale, "Elliptic and triangular flow in event-by-event (3+1)D viscous hydrodynamics," *Phys. Rev. Lett.*, vol. 106, p. 042301, 2011.

[128] J.-F. Paquet, C. Shen, G. S. Denicol, M. Luzum, B. Schenke, S. Jeon, and C. Gale, "Production of photons in relativistic heavy-ion collisions," *Phys. Rev. C*, vol. 93, no. 4, p. 044906, 2016.

[129] A. Bazavov *et al.*, "Equation of state in (2+1)-flavor QCD," *Phys. Rev. D*, vol. 90, p. 094503, 2014.

[130] P. Huovinen and H. Petersen, "Particlization in hybrid models," *Eur. Phys. J. A*, vol. 48, p. 171, 2012.

[131] G. Giacalone, A. Mazeliauskas, and S. Schlichting, "Hydrodynamic attractors, initial state energy and particle production in relativistic nuclear collisions," *Phys. Rev. Lett.*, vol. 123, no. 26, p. 262301, 2019.

[132] S. Rao, M. Sievert, and J. Noronha-Hostler, "Baseline predictions of elliptic flow and fluctuations for the RHIC Beam Energy Scan using response coefficients," *Phys. Rev. C*, vol. 103, no. 3, p. 034910, 2021.

[133] P. Liu and R. A. Lacey, "Acoustic scaling of linear and mode-coupled anisotropic flow; implications for precision extraction of the specific shear viscosity," *Phys. Rev. C*, vol. 98, no. 2, p. 021902, 2018.

[134] D.-X. Wei, X.-G. Huang, and L. Yan, "Hydrodynamic response in simulations within a multiphase transport model," *Phys. Rev. C*, vol. 98, no. 4, p. 044908, 2018.

[135] W. Broniowski, M. Chojnacki, and L. Obara, "Size fluctuations of the initial source and the event-by-event transverse momentum fluctuations in relativistic heavy-ion collisions," *Phys. Rev. C*, vol. 80, p. 051902, 2009.

[136] P. Bozek and W. Broniowski, "Transverse-momentum fluctuations in relativistic heavy-ion collisions from event-by-event viscous hydrodynamics," *Phys. Rev. C*, vol. 85, p. 044910, 2012.

[137] P. Bożek and W. Broniowski, "Transverse momentum fluctuations in ultrarelativistic Pb + Pb and p + Pb collisions with "wounded" quarks," *Phys. Rev. C*, vol. 96, no. 1, p. 014904, 2017.

[138] V. E. Ambrus, S. Busuioc, J. A. Fotakis, K. Gallmeister, and C. Greiner, "Bjorken flow attractors with transverse dynamics," *Phys. Rev. D*, vol. 104, no. 9, p. 094022, 2021.

[139] M. Csanad and A. Szabo, "Multipole solution of hydrodynamics and higher order harmonics," *Phys. Rev. C*, vol. 90, no. 5, p. 054911, 2014.

[140] M. Mace, V. V. Skokov, P. Tribedy, and R. Venugopalan, "Systematics of azimuthal anisotropy harmonics in proton–nucleus collisions at the LHC from the Color Glass Condensate," *Phys. Lett. B*, vol. 788, pp. 161–165, 2019. [Erratum: Phys.Lett.B 799, 135006 (2019)].

[141] "*NIST Digital Library of Mathematical Functions*." http://dlmf.nist.gov/, Release 1.1.5 of 2022-03-15. F. W. J. Olver, A. B. Olde Daalhuis, D. W. Lozier, B. I. Schneider, R. F. Boisvert, C. W. Clark, B. R. Miller, B. V. Saunders, H. S. Cohl, and M. A. McClain, eds.

[142] D. d'Enterria, G. K. Eyyubova, V. L. Korotkikh, I. P. Lokhtin, S. V. Petrushanko, L. I. Sarycheva, and A. M. Snigirev, "Estimates of hadron azimuthal anisotropy from multiparton interactions in proton-proton collisions at $\sqrt{s} = 14$ TeV," *Eur. Phys. J. C*, vol. 66, pp. 173–185, 2010.

[143] K. A. Olive *et al.*, "Review of Particle Physics," *Chin. Phys. C*, vol. 38, p. 090001, 2014.

[144] G. Antchev *et al.*, "First measurement of the total proton-proton cross section at the LHC energy of $\sqrt{s}$ =7 TeV," *EPL*, vol. 96, no. 2, p. 21002, 2011.

[145] H. Lee, *Fundamentals Of Theoretical Plasma Physics: Mathematical Description Of Plasma Waves*. World Scientific Publishing Company, 2019.

[146] N. Pottier, *Nonequilibrium Statistical Physics: Linear Irreversible Processes*. Oxford Graduate Texts, OUP Oxford, 2010.

[147] L. D. Landau and E. M. Lifschits, *The Classical Theory of Fields*, vol. Volume 2 of *Course of Theoretical Physics*. Oxford: Pergamon Press, 1975.

[148] P. Lepage, "gplepage/vegas: vegas version 3.5.3," 2020.

[149] N. Borghini, P. M. Dinh, and J. Y. Ollitrault, "Analysis of directed flow from elliptic flow," *Phys. Rev. C*, vol. 66, p. 014905, 2002.

[150] J. Nagel, "Introduction to numerical integration," 2010.

[151] *Numerical recipes in C*. 2. ed., reprint. with corr., corr. to software version 2.10 ed., 2002.

[152] A. I. McIntosh, "The jackknife estimation method," *arXiv: Methodology*, 2016.

[153] J. Shao and D. Tu, *The Jackknife and Bootstrap*. Springer Series in Statistics, 0172-7397, New York, NY :: Springer New York : Imprint: Springer,, 1st ed. 1995. ed., 1995.